Mechanical Behavior of Alternative Multicrystalline Silicon for Solar Cells

To the Faculty of Chemistry and Physics
of the Technische Universität Bergakademie Freiberg
approved

THESIS

to attain the academic degree of

doctor rerum naturalium
Dr. rer. Nat.

submitted
by Dipl. Ing. Teresa Orellana Pérez

born on the 11th of January 1982 in San Fernando (Spain)

Reviewers:
Prof. Dr. Hans-Joachim Möller (TU Bergakademie Freiberg)
Prof. Dr. Jose Ygnacio Pastor Caño (Polytechnic University of Madrid)
Date of the award: 22nd of May 2013

Abstract

The usage of more inexpensive silicon feedstock for the crystallization of multicrystalline silicon blocks promises cost reduction for the photovoltaic industry. Less expensive substrates made out of metallurgical silicon (MG-Si) are used as a mechanical support for the epitaxial solar cell. Moreover, conventional inert solar cells can be produced from upgraded metallurgical silicon (UMG-Si). This feedstock has higher content of impurities which influences cell performance and mechanical strength of the wafers. Thus, it is of importance to know these effects in order to know which impurities should be preferentially removed or prevented during the crystallization process. Solar cell processing steps can also exert a change in the values of mechanical strength of processed multicrystalline silicon wafers until the fabrication of a solar cell.

Bending tests, fracture toughness and dynamic elastic modulus measurements are performed in this work in order to research the mechanical behavior of multicrystalline silicon crystallized with different qualities of silicon feedstock. Bending tests and residual stress measurements allows the quantification of the mechanical strength of the wafers after every solar cell processing step. The experimental results are compared with theoretical models found in the classical literature about the mechanical properties of ceramics. The influence of second phase particles and thermal processes on the mechanical strength of silicon wafers can be predicted and analyzed with the theoretical models.

Metals like Al and Cu can decrease the mechanical strength due to micro-cracking of the silicon matrix and introduction of high values of thermal residual stress. Additionally, amorphous silicon oxide particles (SiO_x) lower the mechanical strength of multicrystalline silicon due to thermal residual stresses and elastic mismatch with silicon. Silicon nitride particles (Si_3N_4) reduce fracture toughness and cause failure by radial cracking in its surroundings due to its thermal mismatch with silicon. Finally, silicon carbide (SiC) and crystalline silicon oxide (SiO_x) introduce thermal residual stresses but can have a toughening effect on the silicon matrix and hence, increase the mechanical strength of silicon wafers if the particles are smaller than a certain size.

The surface of as-cut wafers after multi-wire sawing presents sharp micro-cracks that control their mechanical behavior. Subsequent removal of these micro-cracks by texture or damage etching approximately doubles the mechanical strength of silicon wafers. The mechanical behavior of the wafers is then governed by defects like cracks and particles formed during the crystallization of multicrystalline silicon blocks. Further thermal processing steps have a minor impact on the mechanical strength of the wafers compared to as-cut wafers. Finally, the mechanical strength of final solar cells is comparable to the mechanical strength of as-cut wafers due to the high residual thermal stress introduced after the formation of the metallic contacts which makes silicon prone to crack.

Declaration

I, Teresa Orellana Pérez, hereby declare that I completed the dissertation entitled "Mechanical Behavior of alternative multicrystalline Silicon for solar Cells" without any improper help from a third party and without using any aids than those cited. All ideas derived directly or indirectly from other sources are identified as such.

Part of this work has been submitted in a Bachelor and a Master Thesis carried out in the frame of the investigation of this dissertation:

S. Binti Rahamad, "Mechanical Characterization of Silicon Wafers for Solar Cells," University of Applied Science Augsburg (Germany), Bachelor Final Project 2011

E. M. Tejado Garrido, "Caracterización Mecánica de Sustratos de Silicio Multicristalino para Aplicación en Células Solares," University of Extremadura (Spain), Master Final Project 2011

Teresa Orellana Pérez

Table of Contents

1. Introduction

This chapter describes the state of the art of the production of silicon from quartz for photovoltaic energy conversion. The energy consumption for obtaining silicon feedstock can be reduced by a metallurgical route for purifying silicon which is alternative to the conventional Siemens process. The silicon feedstock obtained by this alternative route is the so called "up-graded metallurgical silicon" (UMG-Si). The usage of UMG-Si promises overall module cost reduction. However, UMG-Si has a higher content of impurities that can be disadvantageous for solar cell efficiency and for the mechanical behavior of silicon wafers. The aim of this work is the investigation of the influence of these impurities on the mechanical behavior of multicrystalline silicon through the whole solar cell value chain.

1.1 Alternative Silicon Feedstock for the Photovoltaic Industry

The reasons why the photovoltaic market is expanding its capacity for electricity generation, reaching the 40 GW worldwide in 2010 [1], are several. First, the sun is an inexhaustible source of energy and it delivers to Earth in one hour the amount of energy used by humans in a year. Also, the energy consumption and emission of pollution gases in the production of silicon together with further solar cell processes and the installation of the final photovoltaic systems is calculated to be "paid back" as emission-free electricity after approximately four to five years out of more than twenty five years of existence [2]. Thus, solar energy is less pollutant than conventional energy. Solar panels have a long lifetime and they require little maintenance and are portable. Another reason is that silicon, the basic material used for photovoltaics (PV), is the best known semiconductor material that has been used by the electronic industry since the late fifties until today. Thus, photovoltaics could profit from the experience and knowledge in the production and manufacturing of silicon for the electronic industry. Silicon is the second most abundant element on Earth's crust after oxygen constituting approximately 26% in weight of the Earth's crust and is considered nontoxic [2]. Therefore, silicon has been the semiconductor material most used for the photovoltaic industry for many years.

Figure 1 depicts the development of the percentage of materials used in the photovoltaic market. Crystalline silicon solar cells made out of monocrystalline, multicrystalline (mc-Si) and string ribbon silicon represents almost 90% of the photovoltaic market share in 2011. On the other hand, thin film solar cells using cadmium telluride, amorphous silicon and copper indium gallium diselenide represent more than 10% of the market share. The prevalence of crystalline silicon over thin film solar cells is due to higher efficiencies reached with crystalline silicon solar cells. Monocrystalline silicon grown via Czochralski

(Cz-Si) technique provides highest solar cell efficiencies (16-22%) but it is expensive in comparison to multicrystalline silicon solar cells with acceptable efficiencies (14-18%) [3]. Current research on multicrystalline solar cells is proving the potential of efficiency gain for this type of cells that can make the reduction of cost production even more beneficial. Therefore, multicrystalline silicon is expected to be the mainstream material in the photovoltaic industry for the next years.

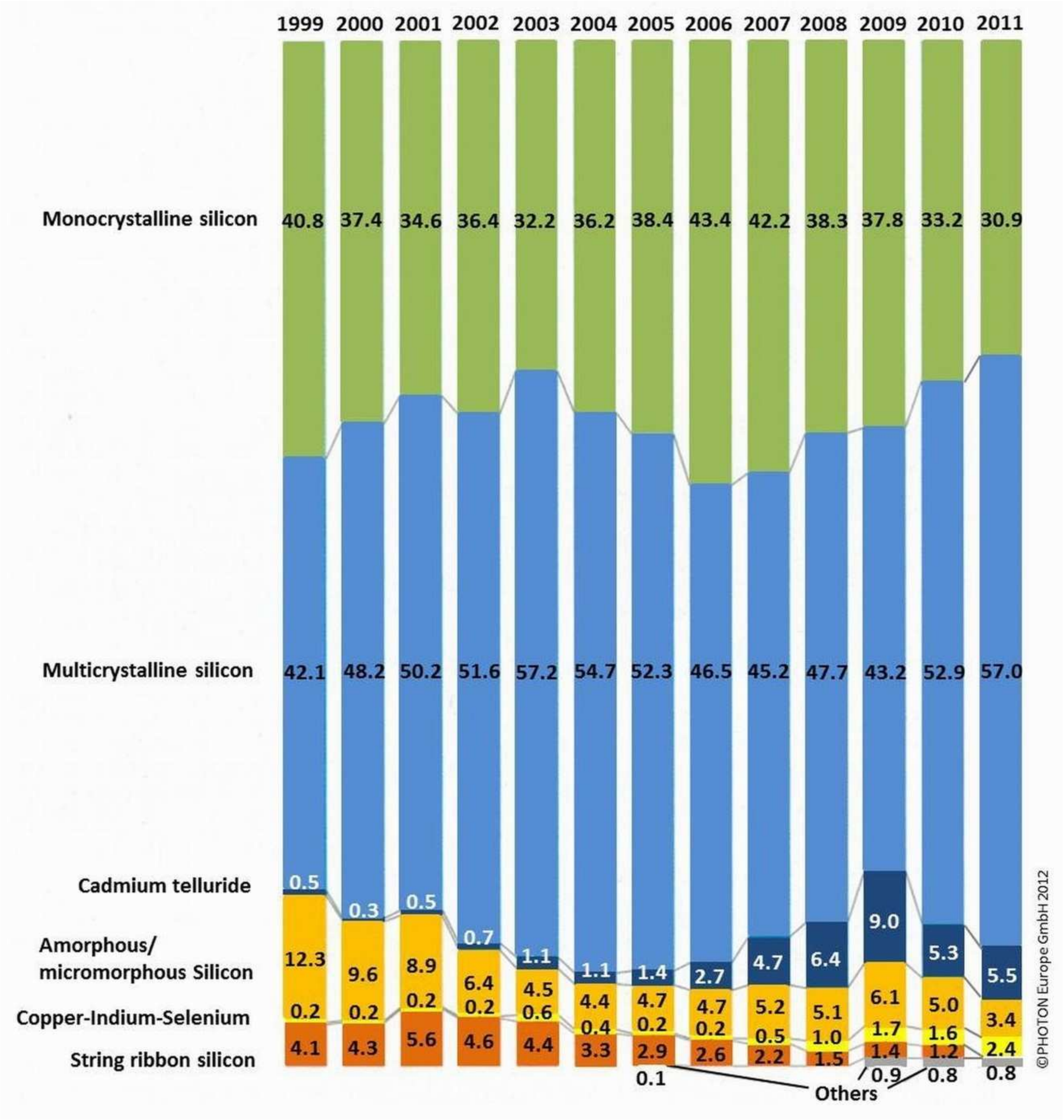

Figure 1 Photovoltaic market share development during the last years after [4]. Crystalline silicon dominates the *photovoltaic market with more than 50% of the market share for multicrystalline silicon from 2010 on.*

The obtaining of silicon starts with the carbothermic reduction of lumpy quartz in an electric arc furnace at high temperature (~2000℃) according to the following simplified reaction:

$$SiO_2(s) + 2C(s) = Si(l) + 2CO(g) \tag{1.1}$$

Carbon monoxide, $CO(g)$, is formed as a reaction co-product and must be further oxidized to carbon dioxide, $CO_2(g)$, in open furnaces in order to be released into the atmosphere. Liquid silicon is drained out from the bottom of the furnace and further refined with oxidative gas and slag-forming additives. When the slag is completely solidified, it is crushed down into small silicon chunks. This silicon is denominated “metallurgical grade silicon” (MG-Si) and has approximately 98.5% purity. Typical impurities within metallurgical grade silicon are carbon, transition and alkali-earth metals, boron and phosphorus. The energy consumption of metallurgical silicon production is in the best case 10 to 11 MW h per metric ton of silicon and 90% silicon yield [2]. The price of metallurgical grade silicon is approximately 1 €/kg.

Metallurgical grade silicon must be further purified to meet the purity level of solar grade silicon (SoG-Si) which is 99.99999% or the so called 5N purity. Metallurgical silicon can be purified either by a chemical route or by a metallurgical route [5]. Purification of silicon by a chemical route provides solar grade silicon. On the other hand, purification following a metallurgical route gives an alternative silicon feedstock known as “up-graded metallurgical silicon”.

The most popular process to purify silicon by the chemical route is the Siemens process. Metallurgical grade silicon is hydrochlorinated in a fluidized bed reactor at 350 ℃:

$$\mathrm{Si(s)} + 3\mathrm{HCl} = \mathrm{HSiCl_3} + \mathrm{H_2} \tag{1.2}$$

Trichlorosilane (TCS) undergoes fractional distillation to be separated from other components and introduced with high-purity hydrogen into a deposition reactor. Large rods of pure silicon grow as the gas within the reactor decomposes onto heated up to 1100 ℃ silicon seed rods. Simplifying, the deposition reaction is as follows:

$$\mathrm{H_2} + \mathrm{HSiCl_3} = \mathrm{Si} + 3\mathrm{HCl} \tag{1.3}$$

The deposition reaction has low yield and the walls of the reactor chamber must be cooled to prevent the deposition of silicon on the inner surfaces of the chamber. Therefore, the Siemens process is a high consuming energy process, 120 kW h per kg of silicon [6]. The purification of metallurgical grade silicon increases the value of silicon by a factor of 30 to 50 [2]. The price of solar grade silicon is approximately 30 €/kg [7].

As the photovoltaic market is dominated by silicon, the industry is very sensitive to the silicon price. The metallurgical route intends to reduce cost by purifying silicon via a series of refining steps like acid leaching and directional solidification. These refining processes are based on the segregation of impurities in the melt leaving a cleaner solid. The equilibrium segregation coefficient, k_0, is the ratio between the concentration of the impurity in the solid, C_s, and the concentration of the impurity in the silicon melt, C_l:

$$k_0 = \frac{C_s}{C_l} \tag{1.4}$$

Impurities with equilibrium segregation coefficients much lower than 1 segregate to the melt. This is the case of most metallic impurities (see Table 1).

Iron and transition metals in metallurgical grade silicon that segregate at grain boundaries forming intermetallic phases with silicon can be dissolved in an acid solution. This is called silicon leaching or hydrometallurgical upgrading. This purifying process cannot refine silicon below the solubility limit of each impurity in the solid silicon.

During directional solidification of multicrystalline silicon, silicon starts solidifying at the bottom of the crucible and impurities with much lower segregation coefficient than 1 segregate to the liquid phase. When the whole block solidifies most of the metallic impurities are in the very top part of the block. This part of the block can be removed and the resulting mc-Si has been refined mostly from metallic impurities [8]. Directional solidification will be further discussed in chapter 3.

Table 1 Equilibrium segregation coefficients, k_0, for some impurities in silicon at the melting point. Most of the data was published by Trumbore [9]. More data can be found in the literature pointed by Ceccaroli and Lohne [2].

Impurity	k_0	Impurity	k_0
O	0.25-1.25	Cu	4×10^{-4}
B	0.8	Ti	3.6×10^{-4}
P	0.35	Cr	1.1×10^{-5}
As	0.3	Mn	1×10^{-5}
C	0.07	Zn	1×10^{-5}
Ga	0.008	Fe	8×10^{-6}
Al	0.002	Ni	8×10^{-6}
N	7×10^{-4}	Co	8×10^{-6}

Impurities like B, P, O and C have segregation coefficients nearer to 1 and therefore they are more difficult to remove from silicon than metallic impurities by acid leaching and directional solidification. One option to reduce this type of impurities in metallurgical grade silicon is the usage of leached quartz selected for its purity and purified carbon black. Another option for the removal of P, B and other impurities is electron beam refining. An electron beam is accelerated towards silicon and owing to the high vacuum in the chamber, elements with higher vapor pressures than that of silicon can be eliminated. The process is performed in a refrigerated copper crucible which does not introduce new impurities in silicon [5]. Plasma refining is very efficient in the removal of B. The plasma, which is composed by argon, helium, water and hydrogen [10], provides oxidizing conditions for B [5]. Boron oxides present a relatively high vapor pressure and they evaporate at the high temperatures achieved by the inductive plasma torch.

Efforts are also being made at present to shift from the rod deposition of silicon in the Siemens process to the decomposition of TCS into silicon granulate in a fluidized bed reactor as an attempt to improve energy efficiency.

The combination of different refining techniques can purify metallurgical grade to solar grade silicon. Typical values of impurity concentration in MG-Si are depicted in Table 2. The values of impurity concentrations for UMG-Si and SoG-Si are levels of impurity concentrations that are expected to be reached after silicon purification via the chemical or the metallurgical route respectively.

Table 2 Target impurity concentration in [ppmw] contained in MG-, UMG- and SoG-Si feedstock [2], [11].

Impurity	MG-Si	UMG-Si	SoG-Si
B	5-70	<30	<1
P	5-100	<15	<5
O	100-5000	<2000	<10
C	5-1500	<250	<10
Ca	20-2000	<500	<2
Mg	5-200	<5	<1
Fe	300-25000	<150	<10
Al	300-5000	<50	<2
Cr	5-150	<15	<1
Ni	10-100	<5	<1
Cu	5-100	<5	<1
Mn	10-300	<5	<1
Mo	1-10	<5	<1
Ti	10-1000	<5	<1
V	1-300	<5	<1

The energy consumption for the refinement of silicon via the metallurgical route is 4 to 5 times lower than the chemical route, reducing the energy consumption down to 25-30 kW h/kg [6]. Moreover, the contaminant chlorinated gases which are expelled during the Siemens process are not produced during the refining steps of the metallurgical route. The price of up-graded metallurgical silicon can be reduced to approximately one third of the price of pure polysilicon, 10 €/kg, which reduces the cost of industry standard crystalline silicon modules by 11% if cell efficiencies are maintained [7]. However, the content of impurities in up-graded metallurgical silicon feedstock is still higher than in solar grade silicon feedstock (see Table 2). The excess of B and P in UMG-Si leads to partial charge carrier compensation and the silicon block obtained after direct solidification starts p-type and can end n-type which leads to poor material yield [6].

The overall module cost gain due to the usage of UMG-Si can be completely lost if cell efficiency is reduced. Therefore, the use of UMG-Si depends on the ability to maintain the electrical quality of silicon with higher content of impurities during solar cell processing.

1.2 Concept and Aim of Research

The photovoltaic market sees a potential for cost reduction in the usage of alternative and inexpensive silicon feedstock as explained in the previous section. The higher concentration of impurities encountered within this silicon feedstock can lower solar cell efficiency [12] and the mechanical strength of the wafers [13].

Impurities, especially transition metals, degrade the minority carrier lifetime and thus the solar cell performance. There is huge research been and being done at this topic and major advances have been achieved in solar cell processing to maintain the efficiency of solar cells made out of UMG-Si.

On the other hand, impurity particles can change the elastic constants of silicon crystals, they can act as propagating crack arrestors or, on the contrary, they can act as stress concentrators where a crack can initiate its propagation. This is a complex topic where some research has been performed in the field of mechanical properties of ceramics and composites. However, the influence of impurity particles on the mechanical properties of crystalline silicon for photovoltaic applications is almost nonexistent until now.

Therefore, the purpose of this work is the quantification of the influence of impurity particles on the overall mechanical behavior of silicon from the crystallization of mc-Si blocks from different feedstock qualities to the final processing of solar cells. Mechanical strength, toughness and elastic modulus were measured at different positions within the mc-Si blocks in order to quantify the impact of impurities segregation on these mechanical properties. The influence of solar cell processing steps on the mechanical behavior of different qualities of mc-Si wafers was also examined via mechanical strength measurements after every solar cell processing step.

The ultimate aim of the work is the identification of impurity particles or precipitates and solar cell processing steps that can be critical for an acceptable mechanical performance of the finished solar cell. The quantification of the influence of these second phase particles and solar cell processing steps on the mechanical properties of mc-Si wafers allows the postulation of failure criteria for the prediction of the mechanical behavior of mc-Si wafers. This knowledge contributes to the clarification of the causes of breakage of silicon wafers and can help wafer manufacturers and solar cell producers to maintain a high yield of wafers survival.

2. Mechanical Properties of Silicon

This chapter presents a complete theoretical description of the mechanical behavior of silicon. Emphasis is done on the mechanical elastic response of silicon as the lifetime temperature performance of solar cells is within the range of temperature where silicon behaves as an elastic material. Special attention is drawn to the different types of defects that can limit the mechanical performance of silicon. The formation of cracks and residual stresses around particles during the crystallization of multicrystalline silicon is explained. Additionally, the intensification of an applied stress in the vicinities of these defects is analyzed. The relationship between defects and the mechanical properties of silicon is presented in detail together with the formulation of failure criteria. This allows the prediction of the mechanical performance of silicon and the correlation of the mechanical performance of silicon with its microstructure. A final picture of the mechanical behavior of a silicon solar cell as a laminated structure and how high temperature processes can influence the status of defects in silicon is visualized at the end of the chapter.

2.1 Elastic Behavior of Silicon

The quantitative study of the mechanical behavior of materials is described by the mathematical description of stress and strain [14]. The stress is the load that a material experiences by unit area, A, and the variable that controls the strain and fracture behavior of a material. The strain is the percentage of deformation that the material experiences under a certain state of stress.

There are two basic types of stresses; normal and shear. Normal stress, σ, is the state of stress that a body experiences when an axial force, F, normal to the faces of the body is applied (see Figure 2 a)). Shear stress, τ, is produced when loads in opposite directions, T, are applied parallel to two parallel faces of the body (see Figure 2 b)).

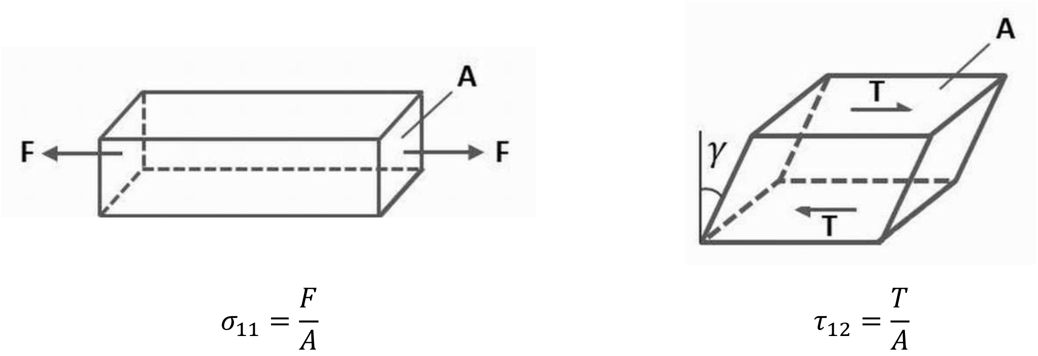

$$\sigma_{11} = \frac{F}{A}$$

a)

$$\tau_{12} = \frac{T}{A}$$

b)

Figure 2 Types of state of stresses. Image a) depicts pure normal tensile stress and image b) depicts shear stress [14].

The stress is a second-rank tensor and thus it has nine possible stress components in three dimensions, σ_{ii} with $i = 1,2,3$ and τ_{ij} with $i = 1,2,3$, $j = 1,2,3$ and $i \neq j$. Actually there are six independent stress components as $\tau_{ij} = \tau_{ji}$.

$$\underline{\underline{\boldsymbol{\sigma}}} = \begin{pmatrix} \sigma_{11} & \tau_{12} & \tau_{13} \\ \tau_{21} & \sigma_{22} & \tau_{23} \\ \tau_{31} & \tau_{32} & \sigma_{33} \end{pmatrix} \tag{2.1}$$

where:

$$\tau_{12} = \tau_{21} \qquad \tau_{23} = \tau_{32} \qquad \tau_{13} = \tau_{31}$$

Normal stresses are the components of the stress tensor expressed as σ_{ii}. A compressive stress is a negative tensile stress. On the other hand, the components of the stress tensor, τ_{ij}, are the shear stresses.

The strain is also a second rank tensor and many of its properties are analogous to the stress tensor. Normal strains are the components of the stress tensor expressed as ε_{ii} and the shear strains, γ_{ij} with $i = 1,2,3$, $j = 1,2,3$ and $i \neq j$, are the angles of distortion that the body experiences when a shear strain is applied (see Figure 2 b)).

$$\underline{\underline{\boldsymbol{\varepsilon}}} = \begin{pmatrix} \varepsilon_{11} & \gamma_{12} & \gamma_{13} \\ \gamma_{21} & \varepsilon_{22} & \gamma_{23} \\ \gamma_{31} & \gamma_{32} & \varepsilon_{33} \end{pmatrix} \tag{2.2}$$

where:

$$\gamma_{12} = \gamma_{21} \qquad \gamma_{23} = \gamma_{32} \qquad \gamma_{13} = \gamma_{31}$$

In the case of the stress state of Figure 2 a) and taking the x axis along the axis of the bar, the stress tensor at any point of the bar is:

$$\underline{\underline{\boldsymbol{\sigma}}} = \begin{pmatrix} \sigma & 0 & 0 \\ 0 & 0 & 0 \\ 0 & 0 & 0 \end{pmatrix} \tag{2.3}$$

Coordinate axes can be taken arbitrarily. For any general tensor there is a set of axes for which the stress tensor only has normal stress components, which are the components in the diagonal of the stress tensor. These axes are called principal axes and the stresses and strains referred to these axes are called principal stresses. Shear stresses and strains for principal directions are zero. A plane that contains a pair of principal axes is thus a principal plane. In the example described by equation (2.3) the x axis is a principal axis and the uniaxial tensile stress is a principal stress.

The calculation of principal stresses is very important as brittle failure at room temperature is controlled by the highest principal tensile stress. The analysis of principal stresses is therefore extremely useful to understand the response of a material to a complex state of stress. The calculation of principal stresses in two dimensions is relatively easy with construction of the Mohr circle [14]. In the case of principal stresses in three dimensions, the analysis is more complicated and stress invariants of the stress tensor must be calculated. If one of the principal planes is known, a two dimensional calculation of the principal stresses can be performed. Most mechanical testing techniques apply simple stress tensors where one principal plane is identified and therefore the calculation of principal stresses is simpler.

The different types of mechanical behaviors are determined by how the material deforms and breaks when a load is applied. Most ceramics exhibit elastic deformation and brittle failure in tension at room temperature. Elastic deformation is defined as a strain that is fully recovered if the applied stress is removed. Normally, elastic strain and applied stress follow a linear correlation and brittle failure occurs at the highest stress reached and is sudden and complete. When a group of similar ceramic samples is broken, it is remarkable that normally the maximum measured tensile stresses disperse (see Figure 3). This is due to the presence of a distribution of flaws with different sizes or nature that exhibit different level of strength control. Fracture mechanics studies the relationship between flaws and stresses and will be discussed in the next two sections.

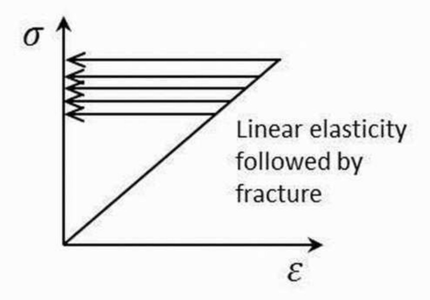

Figure 3 Fracture of samples under the same loading rate adapted from [14]. The arrows point at the maximum tensile stresses under which the samples failed.

This work focuses on the investigation of mc-Si wafers at room temperature, therefore special attention is drawn to the elastic constants that relate stress and strain and therefore govern the mechanical behavior of silicon under the regime of linear elasticity.

In order to understand the physical meaning of the different engineering elastic constants we will consider an isotropic material under the application of simple loads [14]. If the material is subjected to uniaxial tensile load (see Figure 2 a)), the constant of proportionality between stress and strain is the so called "Young´s modulus", E.

$$E = \frac{\sigma_{11}}{\varepsilon_{11}} \tag{2.4}$$

The bar elongates thus in the direction of the tensile loading, ε_{11}, and contracts in directions perpendicular to the tensile stress. The ratio of strains in these two perpendicular directions, ε_{22} and ε_{33}, defines the "Poisson´s ratio" , ν.

$$\nu = -\frac{\varepsilon_{22}}{\varepsilon_{11}} = -\frac{\varepsilon_{33}}{\varepsilon_{11}} \tag{2.5}$$

In the case of applying a pure shear stress (see Figure 2 b)), the "shear modulus", μ, is the relationship between shear stress and strain.

$$\mu = \frac{\tau_{12}}{\gamma_{12}} \tag{2.6}$$

The shear modulus of an isotropic material is related to the Young´s and the Poisson´s modulus by the following expression:

$$\mu = \frac{E}{2(1+\nu)} \tag{2.7}$$

Another important elastic modulus is the "bulk modulus", which describes the response of a material to hydrostatic compression and is related to the Young´s and the shear modulus by the following equation:

$$B = \frac{E\mu}{3(3\mu - E)} \tag{2.8}$$

Equations (2.4) and (2.6) are simple forms of the Hooke´s law that describe the relationship between stresses and strains.

Considering more complex loads and anisotropic crystals, the general form of the Hooke´s law expresses elastic strains as a function of elastic stresses where the proportionality fourth-rank tensor is known as "compliance".

$$\underline{\underline{\boldsymbol{\varepsilon}}} = \underline{\underline{\underline{\underline{\boldsymbol{S}}}}}\,\underline{\underline{\boldsymbol{\sigma}}} \tag{2.9}$$

In the same way stresses can be formulated as linear combinations of strains being the fourth-rank proportionality tensor known as the "stiffness".

$$\underline{\underline{\boldsymbol{\sigma}}} = \underline{\underline{\underline{\underline{\boldsymbol{C}}}}}\,\underline{\underline{\boldsymbol{\varepsilon}}} \tag{2.10}$$

A resumed notation can be adopted, as there are six independent components of stress and strain, in order to reduce the complexity of the expressions that derive from equations (2.9) and (2.10). The stress and strain can be represented as 6×1 matrices instead of 3×3 tensors and the stiffness and compliance as 6×6 matrices instead of 9×9 tensors.

$$\underline{\boldsymbol{\sigma}} = \underline{\underline{\boldsymbol{C}}}\,\underline{\boldsymbol{\varepsilon}} \tag{2.11}$$

$$\begin{pmatrix} \sigma_1 \\ \sigma_2 \\ \sigma_3 \\ \sigma_4 \\ \sigma_5 \\ \sigma_6 \end{pmatrix} = \begin{pmatrix} c_{11} & c_{12} & c_{13} & c_{14} & c_{15} & c_{16} \\ c_{21} & c_{22} & c_{23} & c_{24} & c_{25} & c_{26} \\ c_{31} & c_{32} & c_{33} & c_{34} & c_{35} & c_{36} \\ c_{41} & c_{42} & c_{43} & c_{44} & c_{45} & c_{46} \\ c_{51} & c_{52} & c_{53} & c_{54} & c_{55} & c_{56} \\ c_{61} & c_{62} & c_{63} & c_{64} & c_{65} & c_{66} \end{pmatrix} \begin{pmatrix} \varepsilon_1 \\ \varepsilon_2 \\ \varepsilon_3 \\ \varepsilon_4 \\ \varepsilon_5 \\ \varepsilon_6 \end{pmatrix} \tag{2.12}$$

where:

$\sigma_1 = \sigma_{11}$ $\sigma_2 = \sigma_{22}$ $\sigma_3 = \sigma_{33}$ $\sigma_4 = \tau_{23}$ $\sigma_5 = \tau_{13}$ $\sigma_6 = \tau_{12}$

$\varepsilon_1 = \varepsilon_{11}$ $\varepsilon_2 = \varepsilon_{22}$ $\varepsilon_3 = \varepsilon_{33}$ $\varepsilon_4 = \gamma_{23}$ $\varepsilon_5 = \gamma_{13}$ $\varepsilon_6 = \gamma_{12}$

An analogous formulation can be stated for strains as a function of the stresses with the compliance. As the compliance and stiffness matrices are symmetric their 36 components respectively can be reduced to 21 components, called elastic constants, where $s_{ij} = s_{ji}$ and $c_{ij} = c_{ji}$ for $i \neq j$.

Cubic crystals are not elastically isotropic and have three independent elastic constants. However, electrical, thermal and optical properties are indeed isotropic in the case of cubic crystals. After applying the symmetry of cubic crystals the Hooke´s law remains as follows:

$$\begin{pmatrix} \sigma_1 \\ \sigma_2 \\ \sigma_3 \\ \sigma_4 \\ \sigma_5 \\ \sigma_6 \end{pmatrix} = \begin{pmatrix} c_{11} & c_{12} & c_{12} & 0 & 0 & 0 \\ c_{12} & c_{11} & c_{12} & 0 & 0 & 0 \\ c_{12} & c_{12} & c_{11} & 0 & 0 & 0 \\ 0 & 0 & 0 & c_{44} & 0 & 0 \\ 0 & 0 & 0 & 0 & c_{44} & 0 \\ 0 & 0 & 0 & 0 & 0 & c_{44} \end{pmatrix} \begin{pmatrix} \varepsilon_1 \\ \varepsilon_2 \\ \varepsilon_3 \\ \varepsilon_4 \\ \varepsilon_5 \\ \varepsilon_6 \end{pmatrix} \tag{2.13}$$

The compliance remains also with an analogous structure like the stiffness. The compliance and the stiffness are also related with each other as the following equations indicate [15]:

$$s_{11} = \frac{c_{11} + c_{12}}{(c_{11} - c_{12})(c_{11} + 2c_{12})} \tag{2.14}$$

$$s_{12} = \frac{-c_{12}}{(c_{11} - c_{12})(c_{11} + 2c_{12})} \tag{2.15}$$

$$s_{44} = \frac{1}{c_{44}} \tag{2.16}$$

Equation (2.13) can be expressed in terms of the engineering elastic constants [15]:

$$\varepsilon_1 = \frac{\sigma_1}{E} - \frac{\nu\sigma_2}{E} - \frac{\nu\sigma_3}{E} \tag{2.17}$$

$$\varepsilon_i = \frac{\sigma_i}{\mu} \quad (i = 4{,}5{,}6) \tag{2.18}$$

The elastic engineering constants are related to the material elastic constants as follows:

$$E = \frac{(c_{11} - c_{12})(c_{11} + 2c_{12})}{c_{11} + c_{12}} = \frac{1}{s_{11}} \tag{2.19}$$

$$\nu = \frac{c_{12}}{c_{11} + c_{12}} = -\frac{s_{12}}{s_{11}} \tag{2.20}$$

$$B = \frac{(c_{11} + 2c_{12})}{3} = \frac{1}{3(s_{11} + 2s_{12})} \tag{2.21}$$

$$\mu = c_{44} = \frac{1}{s_{44}} \tag{2.22}$$

Silicon is an anisotropic crystal; therefore, its elastic constants depend on the crystal orientation. Silicon has a cubic symmetry, so the 3-direction-dependent mechanical properties can be described as explained before with a 6x6 matrix with only three independent constants, either stiffness c_{ij} or compliance s_{ij}, for relating stress, σ, with strain, ε, and vice versa, respectively. The elastic constants of silicon are summarized in Table 10 of Appendix A.

Since the mc-Si samples tested in this work are polycrystalline, calculations are based on the assumptions that the material is continuous, homogeneous, and isotropic. Therefore, an isotropic approximation of the elastic modulus for mc-Si is needed as reference value for our silicon wafers. The elastic modulus, can be averaged [15] with the Voigt average method [16], E_V, over the stiffness, c_{11}, c_{12}, c_{44}, and with the Reuss average method [17], E_R, over the compliances, s_{11}, s_{12}, s_{44}. The Voigt approximation assumes plane strain and averages the stress over the grains with random different crystal orientations and the Reuss approximation assumes plane stress and averages the strain over different crystal orientations.

The bulk modulus of cubic crystals is defined by the following relation:

$$B = \frac{1}{3}(c_{11} + 2c_{12}) \tag{2.23}$$

The shear modulus according to Voigt, μ_V, and Reuss, μ_R, is given by:

$$\mu_V = \frac{c_{11} - c_{12} + 3c_{44}}{5} \tag{2.24}$$

$$\mu_R = \frac{5}{4s_{11} - 4s_{12} + 3s_{44}} \tag{2.25}$$

The upper and lower bounds of the elastic modulus of a polycrystal, E_V and E_R, and the Poisson´s ratio, ν_V and ν_R, can be calculated introducing the values of B and μ_V and μ_R respectively in equations (2.7) and (2.8). The arithmetic mean value of the previous ones is a good estimate for converting anisotropic single-crystal elastic constants into averaged engineering elastic constants for quasi-isotropic polycrystalline silicon.

Hashin and Shtrikman [18] also proposed upper and lower bounds for the calculation of the engineering elastic constants of polycrystals. These bounds are more accurate than the Voigt and Reuss bounds. The bulk modulus is given by equation (2.23) and the shear modulus bounds are given by:

$$\mu^- = \mu_1 + 3\left(\frac{5}{\mu_0 - \mu_1} - 4\beta_1\right)^{-1} \tag{2.26}$$

$$\mu^+ = \mu_0 + 2\left(\frac{5}{\mu_1 - \mu_0} - 6\beta_2\right)^{-1} \tag{2.27}$$

where:

$$\beta_1 = -\frac{3(B + 2\mu_1)}{5\mu_1(3B + 4\mu_1)} \tag{2.28}$$

$$\beta_2 = -\frac{3(B + 2\mu_0)}{5\mu_0(3B + 4\mu_0)} \tag{2.29}$$

$$\mu_0 = c_{44} \tag{2.30}$$

$$\mu_1 = \frac{c_{11} - c_{12}}{2} \tag{2.31}$$

The upper and lower bounds of the elastic modulus, $E^+$and E^-, and the Poisson´s ratio, $\nu^+$and ν^-, can be calculated introducing the values of B and μ^+ and μ^- respectively in equations (2.7) and (2.8). As in the case of the Voigt and Reuss approximation, the arithmetic value of the previous ones is a good estimate for engineering elastic constants of polycrystals.

Table 11 to Table 13 of Appendix A summarize all the engineering elastic constants of mc-Si. The average values of both the Voigt and Reuss approximation and the Hashin and Shtrikman approximation point that the elastic modulus of mc-Si is ~162.6 GPa.

2.1.1 Mechanical Strength

Silicon is brittle at room temperature and therefore it exhibits a ceramic mechanical behavior. Ceramics are materials with high mechanical strength; however, their brittleness makes them sensitive to defects. The theoretical and experimental mechanical strength of defect-free ceramics is much higher than the performing mechanical strength of ceramics encountering defects introduced during manufacture and processing. Orowan [19] proposed the following equation for calculating the theoretical tensile breaking stress which is the stress necessary to separate two crystalline planes:

$$\sigma_{theoretical} = \left(\frac{E\gamma}{a_0}\right)^{1/2} \tag{2.32}$$

where a_0 is the plane separation distance in equilibrium and γ is the necessary energy to create a new fracture surface. An approximation of the theoretical strength of Orowan can be given in terms of the Young´s modulus as:

$$\sigma_{theoretical} \approx \frac{E}{\pi} \tag{2.33}$$

Other estimates consider an approximation for the theoretical stress as [20]:

$$\sigma_{theoretical} \approx \frac{E}{10} \tag{2.34}$$

The theoretical strength of silicon is estimated to be ~32 GPa [21].

Analogous to the Orowan analysis is the Frenkel [22] approximation for calculating the theoretical shear breaking stress [21]. This approximation gives the following expression for face-centered cubic materials (FCC):

$$\tau_{theoretical} = \frac{\mu}{2\pi\sqrt{2}} \approx \frac{\mu}{9} \tag{2.35}$$

Thus, the theoretical mechanical strength of silicon under shear stress is ∼7.5 GPa.

The presence of flaws in ceramics lowers the theoretical strength of the material by a factor of 100 or more, which means that the expected mechanical tensile and shear strength of silicon is ∼320 MPa and ∼75 MPa respectively.

2.1.1.1 Cracks

The most detrimental type of flaw is cracks where stresses intensify at the tip of the cracks.

Cracks are mostly introduced in silicon during the multi-wire sawing process of silicon wafers which will be explained in the next chapter. Cracks can be also originated in the surroundings of second phase particles or after high temperature solar cell processes as it will be explained in the next sections.

Fracture mechanics is the brunch of science that analyses failure of materials due to crack propagation when the material is subjected to loads or displacements. Therefore, fracture mechanics is of most importance in order to establish failure criteria that predict fracture stresses of silicon wafers containing different types of flaws.

Griffith [23] derived expressions considering energy assumptions for calculating the stress at the tip of a very sharp crack. In the case of thin plates (plane stress) with an internal crack of length $2a$, the fracture stress can be calculated with the following equation:

$$\sigma_f = \left(\frac{2E\gamma}{\pi a}\right)^{1/2} \tag{2.36}$$

In the case of plane strain the fracture stress is:

$$\sigma_f = \left(\frac{2E\gamma}{\pi(1-\nu^2)a}\right)^{1/2} \tag{2.37}$$

The Griffith criterion is a necessary condition that may be sufficient for fracture.

If attention is drawn to the vicinity of a crack, stress based and energy based analysis can be equivalent. Stress based analysis leads to the Irwin [24] formulation of fracture mechanics with the concept of stress intensity factor. The stress field in the surroundings of a crack is the consequence of one of the three possible modes of loading or of a combination between them (see Figure 4). The stress in the vicinity of the crack can be calculated by equation (2.38) in linear elastic regime.

$$\sigma_{ij} = \frac{K f_{ij}(\theta)}{\sqrt{2\pi r}} \tag{2.38}$$

where r and θ are cylindrical polar coordinates of a point with respect to the crack tip; K is the stress intensity factor which gives a magnitude of the intensification of the stress near the crack tip; and $f_{ij}(\theta)$ is an angular function. The solving of equation (2.38) is complex and can be expanded in a power of series in r and the first term of the series expansion dominates the intensification of stress in a small region near the crack tip.

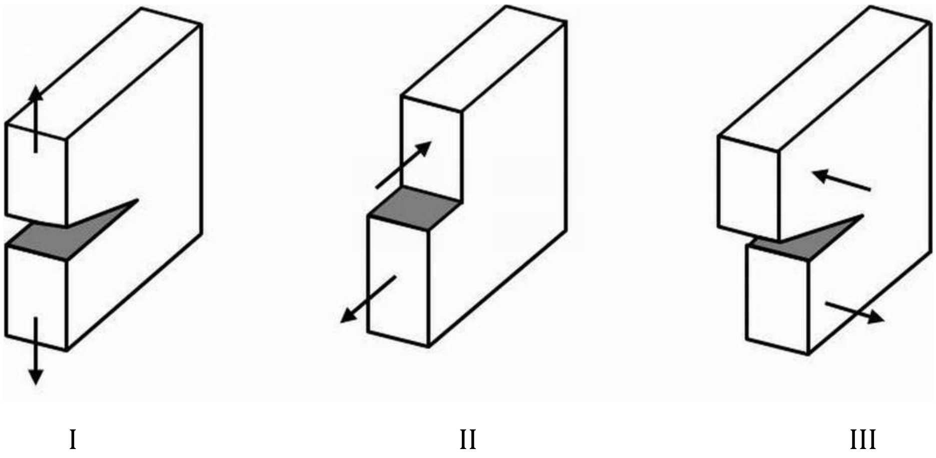

Figure 4 Sketch of the three crack loading modes used in linear elastic fracture mechanics (adapted from [15]): I, uniaxial tensile (opening) mode; II in-plane shear mode; III out-of-plane shear (tearing) mode.

Stress intensity factors can be calculated by easier forms of the general expression described by equation (2.38) for certain specimen shapes, crack configurations and uniform loading:

$$K_i = Y\sigma\sqrt{a} \tag{2.39}$$

where Y is the geometry factor which is a dimensionless parameter that depends on the crack and loading geometries; i represents the loading mode (I, II or III); and a is the length of the crack. Values for Y can be found in handbooks for different cracks and loading configurations [25].

Loading mode I is extremely important in ceramics and is considered to control fracture. Specimen failure with randomly oriented flaws will occur at the largest flaw perpendicular to the largest tensile stress. Thus, the fracture condition assumed by the linear fracture mechanics theory is that there is a critical value of stress intensity factor under loading mode I, K_{IC}, also known as toughness above which rapid crack propagation occurs. The fracture criterion is then:

$$K_I = K_{IC} \tag{2.40}$$

The critical stress intensity factor or toughness is an intrinsic property of every material that can be measured experimentally. Irwin also expressed his fracture criteria in terms of energy which in the cases of plane stress and plane strain is respectively:

$$G_c = \frac{K_{Ic}^2}{E} \tag{2.41}$$

$$G_c = \frac{K_{Ic}^2}{E}(1-\nu^2) \tag{2.42}$$

where G_c is the critical strain energy release rate, which is the amount of stored elastic energy which is released per unit area of the created crack.

If the total strain energy release rate is equivalent to the energy necessary to create the two surfaces of a crack, $2\gamma_f$, and equation (2.39) is introduced in equation (2.41) the failure criteria for plane stress can be expressed depending on the elastic modulus instead of the fracture toughness:

$$\sigma_f = \left(\frac{2\gamma_f E}{Y^2 a}\right)^{1/2} \tag{2.43}$$

To finalize this section a short explanation of the meaning of stored elastic energy is presented for the clearness of this work. Strains occur when a force is applied to a body. That means that the point of application of the force moves and thus a work is done on the body [14]. This energy is stored in the deformed bonds between atoms as an increase in the interatomic potential and is released when the force is removed and can be the driving force for crack propagation. This work per unit volume is known as the stored elastic strain energy density, U.

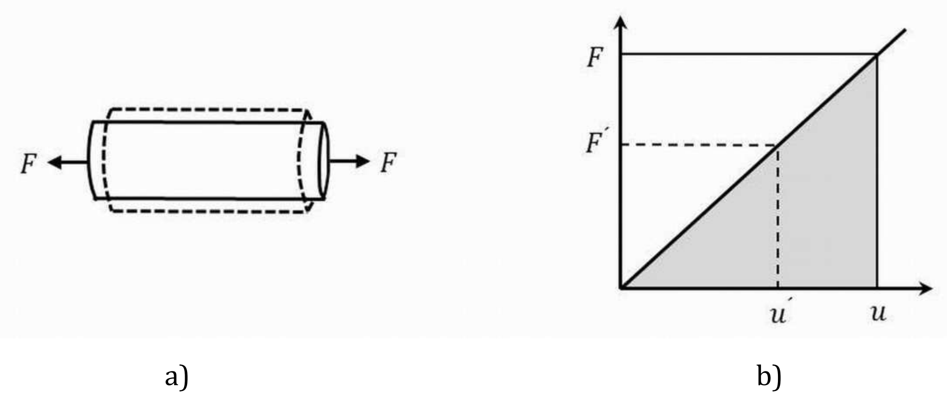

a) b)

Figure 5 Force-displacement behavior of a linear elastic body (adapted from [14]).

Figure 5 depicts a rod that experiences a displacement, u, when a force, F is applied. When the material is linear elastic the applied force is proportional to the displacement. Equation (2.44) is then analogous to equation (2.4):

$$F = ku \tag{2.44}$$

The constant of proportionality, k, depends on the elastic properties of the material and the dimensions of the system. The work done when the full displacement, u, is achieved is then:

$$W = \int_{u'=0}^{u} ku' \mathrm{d}u' = \frac{1}{2}ku^2 = \frac{1}{2}Fu \tag{2.45}$$

The area under the loading curve is thus the elastic work done on the body which is depicted in Figure 5 b) by the shaded triangle. The stored elastic energy per unit volume, U_e, is therefore:

$$U_e = \frac{W}{LA} = \frac{1}{2}\frac{F}{A}\frac{u}{L} = \frac{1}{2}\sigma_{11}\varepsilon_{11} = \frac{1}{2}\frac{\sigma_{11}^2}{E} \tag{2.46}$$

where A is the area of the rod and L is its length.

For more complex states of stress equation (2.46) can be generalized as:

$$U_e = \frac{1}{2}\sum_i \sum_j \sigma_{ij}\varepsilon_{ij} = \frac{1}{2}\sum_i \sum_j \frac{\sigma_{ij}^2}{E} \tag{2.47}$$

2.1.1.2 Particles

Pores and second phase particles in multicrystalline silicon can be also fracture initiators due to elastic and thermal mismatch. Pores or voids intensify significantly the stress in their surroundings when an external load is applied. Pores behave similar to cracks but they are less detrimental due to their lack of sharpness. Second phase particles can be fracture origins due to the thermal residual stresses introduced during processing and to the intensification of stress that occurs when an external load is applied in their surroundings [26].

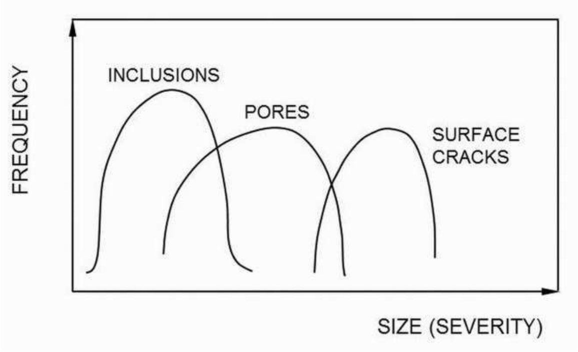

Figure 6 Defects severity chart for ceramics (adapted from [15]).

The presence of second phase particles has the inherent potential problems of inhomogeneous second phase distribution, weak interfacial bonding and misfit thermal and elastic stresses [27]. The stress concentration that occurs at particles is due to thermal expansion and elastic modulus mismatch between the particle and the silicon matrix. Early literature pointed already to particles as frequent fracture initiators, especially at the low strength tail of the strength distribution. Hence, the quantification of the effect of particles on the mechanical strength of silicon is of great importance to enable accurate failure prediction.

Therefore, the important factors that control strength of silicon containing particles are the thermal expansion coefficients and elastic modulus of the matrix and the particles, the particle size and the volume fraction of the particles [28], [29], [30], [31], [32]. The mechanical properties of multicrystalline silicon containing second phase particles can be described by theoretical models proposed for describing the mechanical properties of particle composite materials whose matrix and second phase are also ceramics.

2.1.1.2.1 Thermal Mismatch

Thermal Residual Stress

Residual thermal stresses are a type of stress that remains in the silicon matrix after the crystallization process. They are caused, during the cooling of the multicrystalline silicon blocks, by temperature gradients and the difference in thermal expansion coefficients between the silicon matrix and the second phase particles.

Spherically symmetric thermal stresses, $\sigma_{\theta\theta}$ and σ_{rr}, build around spherical second phase particles in the radial and tangential directions (see Figure 7 and the coordinate system in Figure 11). These thermal stresses in the matrix, which is considered as an isotropic linear elastic continuum, are given by [33] [34]:

$$\sigma_{rr} = P\left(\frac{R}{r}\right)^3 \tag{2.48}$$

$$\sigma_{\theta\theta} = -\frac{P}{2}\left(\frac{R}{r}\right)^3 \tag{2.49}$$

$$P = \frac{(\alpha_p - \alpha_{Si})(T_f - T_{amb})}{\frac{(1+\nu_{Si})}{2E_{Si}} + \frac{(1-2\nu_p)}{E_p}} \tag{2.50}$$

where $\alpha_{Si,p}$, $\nu_{Si,p}$ and $E_{Si,p}$ are the expansion coefficients, Poisson´s ratio and Young´s modulus of silicon and the impurity particle, respectively. T_f is the ductile-brittle transition temperature in silicon (~750℃) [35]. Above T_f silicon can accommodate stresses by creation and movement of dislocations in the silicon matrix. However, below T_f the silicon matrix cannot relax thermal stresses by dislocation movement and residual stresses build up in the silicon matrix. T_{amb} is the ambient temperature, R is the particle radius and r is the distance from the center of the particle. The stress inside the particle, P, is hydrostatic compressive or tensile depending on the sign of the difference in thermal expansion coefficients.

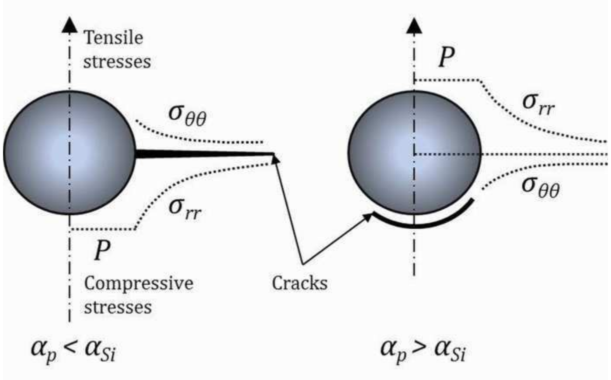

Figure 7 The picture on the left depicts the stress distribution in the vicinity of an impurity particle with a thermal expansion coefficient lower than the one of silicon. The picture on the right depicts the stress distribution in the vicinity of an impurity particle with a thermal expansion coefficient higher than the one of silicon [14].

When the thermal expansion coefficient of the impurity particle is lower than the one of silicon, tangential thermal stresses, $\sigma_{\theta\theta}$, are tensile and radial micro-cracking can occur (see Figure 7, left picture). Lower expansion coefficients of particles leave the particles subjected to compressive internal stresses. When the thermal expansion coefficient of the particle is higher than the one of silicon, radial thermal stresses, σ_{rr}, are tensile and circumferential micro-cracking can occur (see Figure 7, right picture). Higher expansion coefficients of particles leave the particles subjected to tensile internal stresses.

This model holds for the case of a single particle in an isotropic linear elastic matrix. Since thermo-elastic stress diminishes strongly at short distance from the particle, equations (2.48) and (2.49) are a good approximation at low volume fraction of particles [35]. It also has to be noticed that this model corresponds only to spherical particles and other particle geometries can lead to different stress magnitude and distribution around the particles. However, for the purpose of this work spherical particles are assumed and the calculation and interpretation of thermal stresses will be further discussed in section 4.4. Moreover, the evaluation of the fracture of the mc-Si wafers is made considering the thermal stresses built in the silicon matrix as the cause of wafer fracture. The impurity particles can remain under compressive internal stress that can counteract tensile applied stresses or can stand the majority of an applied tensile load causing the fracture of the particle instead of the matrix. Therefore, the consideration of the fracture of silicon due to the thermal stresses built in in the matrix is more appropriate to set a conventional failure criterion for worst case scenario.

Spontaneous Micro-cracking

This section summarizes several models found in the literature for the description of spontaneous micro-cracking of the silicon matrix due to the thermal mismatch between silicon and the particles.

Equations (2.48) to (2.50) show that the value of residual thermal stress does not depend on the impurity particle size. However, experiments observe that micro-cracking after cooling occurs only in the surroundings of particles larger than a critical particle size [36]. Thus, micro-cracking does depend on the size of the particles and on the magnitude of residual thermal stresses [28].

In the case of second phase particles with expansion coefficients higher than the one of silicon, radial thermal stresses are tensile and circumferential micro-cracking of the silicon matrix will occur for values equal or higher than a critical radius size. For particles with lower expansion coefficients than the one of silicon, tangential thermal stresses are tensile and radial micro-cracking of the silicon matrix occurs. This later case is more deleterious than circumferential cracking as micro-cracks from different particles can easily link together and cause the catastrophic failure of the specimen [28].

Davidge et al. [36] proposed a criterion for circumferential micro-cracking due to thermal mismatch. The formation of the circumferential crack requires the existence of a flaw near the particle interface. A supply of energy is also necessary for the flaw to grow. This energy is provided by the elastic stored energy in the particle and in the surrounding silicon matrix. The criteria for crack formation is that the total stored elastic energy, U, must equal or exceed the energy necessary to create a new fracture surface, U_S.

$$U \geq U_S \tag{2.51}$$

The elastic energy, U_e, stored in an element of material subjected to an orthogonal stress field is according to equation (2.47):

$$U_e = \frac{1}{2E}\{(1+\nu)(\sigma_1^2+\sigma_2^2+\sigma_3^2) - \nu(\sigma_1+\sigma_2+\sigma_3)^2\} \tag{2.52}$$

where the strains are expressed as a function of the stresses and the elastic constants as in equation (2.17).

Substituting $-\sigma_1 = 2\sigma_2 = 2\sigma_3 = PR^3/r^3$ in equation (2.52), the elastic stored energy in the silicon matrix can be calculated as:

$$U_{Si} = \int_R^\infty \frac{(1+\nu_{Si})}{2E_{Si}}\frac{3}{2}P^2\left(\frac{R}{r}\right)^6 4\pi r^2 \mathrm{d}r \tag{2.53}$$

$$U_{Si} = \frac{3P^2(1+\nu_{Si})}{4E_{Si}}\frac{4}{3}\pi R^3 \tag{2.54}$$

By substituting $\sigma_1 = \sigma_2 = \sigma_3 = P$ in equation (2.52), then the elastic stored energy within the particle can be calculated as:

$$U_p = \frac{3P^2(1+\nu_p)}{2E_p}\frac{4}{3}\pi R^3 \tag{2.55}$$

The addition of equations (2.54) and (2.55) sums up the total stored elastic energy ($U = U_{Si} + U_p$):

$$U = P^2\pi R^3\left\{\frac{(1+\nu_{Si})}{E_{Si}} + \frac{2(1-2\nu_p)}{E_p}\right\} \tag{2.56}$$

The energy necessary to create a new surface can be expressed proportional to the fracture surface energy of silicon, γ_{Si}, as the formed crack has two faces:

$$U_S = A\gamma_{Si} \tag{2.57}$$

where A is the area of surface formed. Experimental observations pointed that the cracks formed are semi-spherical round the particle. Given that the crack has two surfaces:

$$U_S = 4\pi R^2\gamma_{Si} \tag{2.58}$$

Finally, the critical particle radius for circumferential micro-cracking can be calculated by substituting equations (2.56) and (2.58) in equation (2.51):

$$R_c \geq \frac{8\gamma_{Si}}{P^2\left[\frac{(1+\nu_{Si})}{E_{Si}} + \frac{2(1-2\nu_p)}{E_p}\right]} \tag{2.59}$$

Ito et al. [37] proposed another model to evaluate circumferential micro-cracking due to thermal mismatch. The model is based on the calculation of the strain energy release rate as a function of the particle size and the size of a flaw at the particle´s interface. This function presents a maximum as a function of crack length and particle´s size. Below this maximum value micro-cracking does not occur.

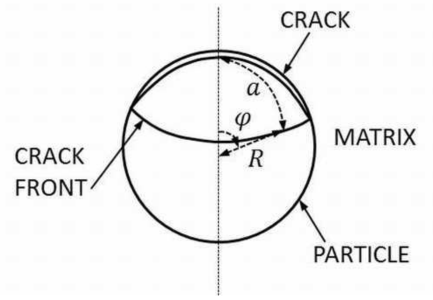

Figure 8 Scheme of the spherical particle and an interfacial crack adapted from [37].

Ito et al. [37] starts his analysis from the expression of the strain energy, U_0, of the uncracked system formed by the particle and the silicon matrix (equation (2.56)). The strain energy of the system decreases when a crack of length $2a$ (see Figure 8) exists at the particle-matrix interface:

$$U = U_0 f(\varphi) \tag{2.60}$$

where $\varphi = a/R$ and $f(\varphi) \leq 1$ is an undetermined dimensionless function.

The strain energy release rate is therefore:

$$G = -\frac{\mathrm{d}U}{\mathrm{d}A} = -U_0 \frac{\mathrm{d}f(\varphi)}{\mathrm{d}A} \tag{2.61}$$

where A is the crack area and $\mathrm{d}A$ is the incremental area change:

$$A = 2\pi R^2(1 - \cos\varphi) \tag{2.62}$$

$$\mathrm{d}A = 2\pi R^2 \sin\varphi \, \mathrm{d}\varphi \tag{2.63}$$

The strain energy release rate can be obtained from equations (2.61) to (2.63) and equation (2.56) for substituting U_0:

$$G = -\left[\frac{1+\nu_{Si}}{2E_{Si}} + \frac{1-2\nu_p}{E_p}\right] P^2 \frac{R}{\sin\varphi} \frac{\mathrm{d}f(\varphi)}{\mathrm{d}\varphi} \tag{2.64}$$

Numerical calculations were conducted in order to calculate the dimensionless function $f(\varphi)$ for relatively small cracks and its derivate [37]:

$$f(\varphi) = -0.56\left(\varphi - \sin\varphi\cos\varphi - \frac{1}{3}\cos^3\varphi + \cos\varphi\right) + 1.38 \tag{2.65}$$

$$\frac{\mathrm{d}f(\varphi)}{\mathrm{d}\varphi} = -1.12\sin^2\varphi + 0.56\sin^3\varphi \tag{2.66}$$

The expression for the strain energy release rate remains then:

$$G = 0.56\left[\frac{1+\nu_{Si}}{2E_{Si}} + \frac{1-2\nu_p}{E_p}\right] P^2 R \sin\varphi\,(2 - \sin\varphi) \tag{2.67}$$

Introducing equation (2.50) for the pressure inside the particle:

$$G = 0.56 \frac{(\Delta\alpha\Delta T)^2}{\left[\frac{1+\nu_{Si}}{2E_{Si}} + \frac{1-2\nu_p}{E_p}\right]} R \sin\varphi\,(2-\sin\varphi) \tag{2.68}$$

Micro-cracking at the particle´s interface will occur when the strain energy release rate reaches a critical value, G_c, at small interfacial defects. The critical strain energy release rate depends on the bonding quality of the interface silicon-particle. However, for the purpose of this work and for simplification of the problem, a plane stress sate will be considered and the stress energy release rate will be expressed in terms of the critical stress intensity factor by equation (2.41):

$$G_c = \frac{K_{Ic}^2}{E_{Si}} \leq 0.56 \frac{(\Delta\alpha\Delta T)^2}{\left[\frac{1+\nu_{Si}}{2E_{Si}} + \frac{1-2\nu_p}{E_p}\right]} R_c \sin\varphi\,(2-\sin\varphi) \tag{2.69}$$

Rearranging equation (2.69), the critical particle size depends on the size of the pre-existing flaw as $\varphi = a/R$ and can be calculated as:

$$R_c \geq 1.79 \left(\frac{K_{Ic}}{\Delta\alpha\Delta T}\right)^2 \frac{\left[\frac{1+\nu_{Si}}{2E_{Si}} + \frac{1-2\nu_p}{E_p}\right]}{E_{Si}\sin\varphi\,(2-\sin\varphi)} \tag{2.70}$$

Evans et al. [26] proposed spontaneous micro-cracking criteria based on approximations of stress intensity factors at pre-existing flaws at or near the interface between a circular particle or inclusion and the silicon matrix. Whether a crack will develop or not depends on the magnitude of the stress intensity factor at small interfacial flaws, K. If the stress intensity factor exceeds the value of toughness for the matrix, K_{Ic}, cracks will propagate [26]. Approximate K values can be calculated as a function of the interfacial flaw size.

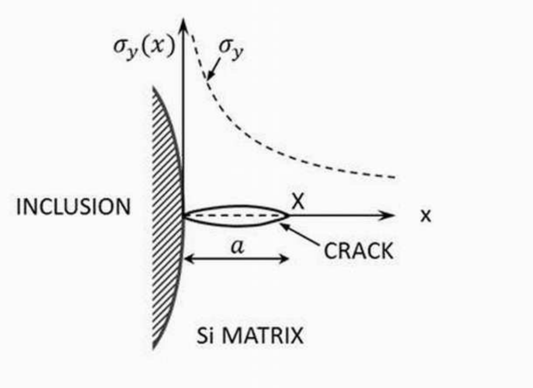

Figure 9 Coordinates to evaluate the stress intensity factor of a flaw in a variable stress field (strip line) adapted from [26].

The stress intensity factor for a crack in a variable stress field, like the stress field in the vicinity of the particles, can be determined directly from the orthogonal stress that existed along the fracture plane before the crack formed [38]. This can be expressed for a through crack of length a with the following equation [39]:

$$K=\left(\frac{2}{a\pi}\right)^{1/2}\int_0^a \frac{\sigma_y(x)x^{1/2}}{(a-x)^{1/2}}\mathrm{d}x \tag{2.71}$$

A much smaller crack size than the specimen size is an assumption for the expression. Approximations of K values can be calculated as suggested in reference [26] by substituting the stress fields around the particles into equation (2.71) and integrating over the crack length. The expression neglects any perturbation of the applied stress field, $\sigma_y(x)$, caused by the crack. Thus, the model is an approximation for small cracks occurring near, or at, the particle´s interface ($a \lesssim 0.2R$).

We have seen in the previous section that when the thermal expansion coefficient of the particle is larger than the one of the matrix, radial residual stresses are tensile and circumferential cracks can form either in the interface or in the matrix. Therefore, cracks propagate at constant stress depending on the location of the defect as a first approximation. A stress intensity factor with thermal origin, K_T, is for this case given by Evans et al. [26]:

$$K_T=\left(\frac{2}{\pi a}\right)^{1/2}(-P)\left(\frac{R}{r}\right)^3\int_0^a \frac{x^{1/2}}{(a-x)^{1/2}}\mathrm{d}x \tag{2.72}$$

where r is the distance from the center of the particle to the position of the defect and $\sigma_y(x)$ is substituted by equation (2.48). Integrating equation (2.72) over the length of the initial flaw gives:

$$K_T\approx\left(\frac{\pi a}{2}\right)^{1/2}(-P)\left(\frac{R}{r}\right)^3 \tag{2.73}$$

When the expansion coefficient of the particle is lower than the one of silicon, tangential thermal stresses are tensile and cracks tend to propagate away from the particle into the silicon matrix. For the calculation of the stress intensity factor for this configuration of thermal stresses, we will consider that the cracks are exposed along their lengths to the tangential thermal stresses at any equatorial plane of the particle. At the end of the crack at the furthest point from the particle, pointed by the letter "X" in Figure 9, and substituting $\sigma_y(x)$ by equation (2.49) and equaling $r = R + x$, equation (2.71) remains:

$$K_T=\left(\frac{2}{\pi a}\right)^{1/2}\frac{P}{2}\int_0^a \frac{(x/R+1)^{-3}x^{1/2}}{(a-x)^{1/2}}\mathrm{d}x \tag{2.74}$$

Expanding $(x/R+1)^{-3}$as a series and calculating the integral [26]:

$$K_T=\frac{P}{2}\left(\frac{\pi a}{2}\right)^{1/2}\left[1-\frac{9}{4}\left(\frac{a}{R}\right)+\frac{15}{4}\left(\frac{a}{R}\right)^2-\frac{175}{32}\left(\frac{a}{R}\right)^3+\cdots\right] \tag{2.75}$$

As the solution for this model is only valid for ($a \lesssim 0.2R$), the terms beyond (a/R) can be neglected:

$$K_T\approx\frac{P}{2}\left(\frac{\pi a}{2}\right)^{1/2}\left[1-\frac{9}{4}\left(\frac{a}{R}\right)\right] \tag{2.76}$$

The interface related cracks propagate when the stress intensity factor reaches its critical value for the silicon matrix, K_{Ic}. These conditions can be found for particles with higher and lower thermal expansion coefficients than the one of silicon respectively by introducing K_{Ic} in equation (2.73) and (2.76). If the initial flaw is exactly located at the particle´s interface and has a length of $0.2R$, then the critical particle radius for particles with higher and lower expansion coefficients is respectively:

$$R_c \geq \frac{10}{\pi}\left(\frac{K_{Ic}}{P}\right)^2 \tag{2.77}$$

$$R_c \geq \frac{10}{\pi}\left(\frac{40}{11}\frac{K_{Ic}}{P}\right)^2 \tag{2.78}$$

Cracks may stop propagating if they extend into a decreasing stress field. Therefore, radial cracks caused by thermal stresses are expected to stop as they extend into the silicon matrix and circumferential cracks may continue propagation until completion of the circumference.

In the case of radial spontaneous micro-cracking Green [40], [41] proposed a cracking criterion for spherical particles with an annular flaw (see Figure 10).

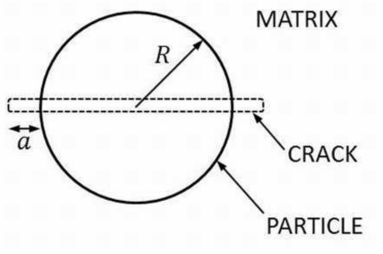

Figure 10 Annular preexisting flaw at spherical particle adapted from [41].

The particle and the crack are considered a penny-shaped crack (with total length $a + R$). The stress acts along the crack surface for $R \leq r \leq (a + R)$. The stress intensity factor for this configuration was proposed by Barenblatt [42] as follows:

$$K_I \cong 2\left(\frac{1}{\pi(a+R)}\right)^{1/2} \int_R^{a+R} \frac{r\sigma(r)\mathrm{d}r}{[(a+R)^2 - r^2]^{1/2}} \tag{2.79}$$

The stress intensity factor for an annular crack due to thermal residual stress can be calculated by introducing Equation (2.49) into Equation (2.79):

$$K_I^T \cong P\left[\frac{a}{\pi}\frac{(\varphi+2)}{(\varphi+1)^5}\right]^{1/2} \tag{2.80}$$

where $\varphi = a/R$ is the normalized crack length.

Spontaneous micro-cracking will occur when $K_I^T = K_{Ic}$, being $R_c = a/\varphi$:

$$R_c \geq \frac{\pi K_{Ic}^2(\varphi+1)^5}{\varphi P^2(\varphi+2)} \tag{2.81}$$

As explained by Davidge and Green [36], the incidence of circumferential micro-cracking at particles increases with increasing particle size. This statement was based on energetic criteria. Evans [26] proposed another explanation for the incidence of both circumferential and radial micro-cracking that relates to the fracture mechanism at particles. An additional size effect on the stress intensity factor can occur if the interface of the particle has statistically distributed initial crack lengths. In that case, an increase in one order of magnitude of the particle size increases the probability of crack extension by 10^2.

2.1.1.2.2 Elastic Mismatch

Stress intensification can occur in the surroundings of a particle when an external load is applied. The difference in elastic constants between the silicon matrix and the second phase particles is responsible for the disturbance of an applied stress field, σ_a, in the vicinity of the particles. These stresses are more complex than thermal stresses and they depend on the angle of orientation, θ, with the applied load (see Figure 11).

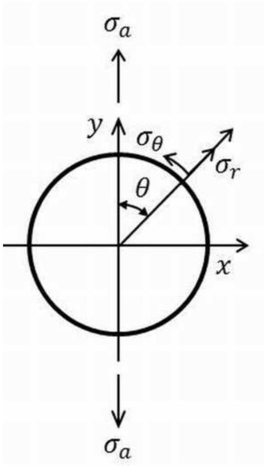

Figure 11 Coordinate system used to evaluate the mechanical stresses around particles adapted from [26].

The matrix is considered infinite, elastic, isotropic and homogeneous solid subjected to uniform applied stress at infinity. The stress disturbance will be confined to the neighborhood of the particle. This means that the applied stress is not modified by more than one percent approximately at a distance of four times the particle diameter. Thus, this model is valid only for particles which are separated a distance at least four times the length of the particles diameter.

The factor of stress concentration is the ratio between the intensified stress due to the presence of the particle and the applied stress. This factor depends on the particle geometry and nature and not on the size of the particle. Particles which are less rigid than the silicon matrix experience higher stress concentration than more rigid particles.

Adding the distribution of stress concentration in the radial and tangential direction to the radial and tangential components of the applied stress respectively, the total distribution of stresses around a particle can be estimated:

$$\sigma_{rr} = \sigma_r + I_{rr} \tag{2.82}$$

$$\sigma_{\theta\theta} = \sigma_\theta + I_{\theta\theta} \tag{2.83}$$

The following equations describe the distribution of stress concentration in the vicinity of the second phase particles [43]. The terms A and B depend on the elastic constants of the silicon matrix and the impurity particle.

$$I_{rr} = 2\sigma_a\left[-A\left(\frac{R}{r}\right)^2 + B\left(\frac{R}{r}\right)^4 - 4\left(\frac{R}{r}\right)^2\right]\cos 2\theta \tag{2.84}$$

$$I_{\theta\theta} = 2\sigma_a\left[-A\left(\frac{R}{r}\right)^2 - 3B\left(\frac{R}{r}\right)^4 \cos 2\theta\right] \tag{2.85}$$

$$A = \frac{(1-2\nu_p)\mu_{Si} - (1-2\nu_{Si})\mu_p}{4[(1-2\nu_p)\mu_{Si} + \mu_p]} \tag{2.86}$$

$$B = \frac{\mu_{Si} - \mu_p}{4[\mu_{Si} + (3-4\nu_{Si})\mu_p]} \tag{2.87}$$

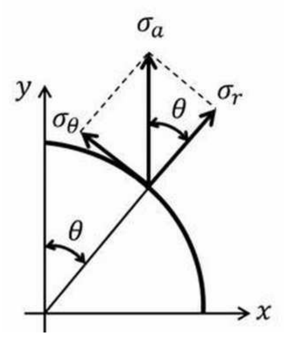

Figure 12 Radial and tangential components of a uniaxial applied stress in the vicinity of a particle in the silicon matrix.

Substituting $\sigma_r = \sigma_a \cos\theta$ and $\sigma_\theta = \sigma_a \sin\theta$ and having into account the half angle formulas:

$$\sigma_{rr} = \frac{\sigma_a}{2}(1+\cos 2\theta) + 2\sigma_a\left[-A\left(\frac{R}{r}\right)^2 + B\left(\frac{R}{r}\right)^4 - 4\left(\frac{R}{r}\right)^2\right]\cos 2\theta \tag{2.88}$$

$$\sigma_{\theta\theta} = \frac{\sigma_a}{2}(1-\cos 2\theta) + 2\sigma_a\left[-A\left(\frac{R}{r}\right)^2 - 3B\left(\frac{R}{r}\right)^4 \cos 2\theta\right] \tag{2.89}$$

As in the case of thermal stresses, the magnitude of stress intensification around second phase particles is independent on the particle radius.

For second phase particles with elastic constants lower than the ones of silicon, tangential stresses, $\sigma_{\theta\theta}$, are tensile and larger than the applied stress, σ_a, at an orientation of $\theta=90°$ with the applied stress. For second phase particles with elastic constants higher than the ones of silicon, radial stresses, σ_{rr}, are tensile and higher than the applied load, σ_a, in the orientation $\theta=0°$. Whereas the tangential stresses, $\sigma_{\theta\theta}$, are still tensile but lower than the applied stress, σ_a, in the orientation $\theta=90°$ [26].

The combination of both residual thermal stress and stress concentration due to thermal and elastic mismatch between the particles and the matrix weakens the mechanical strength of multicrystalline silicon.

In the case of a biaxial stress field acting in the surroundings of the particle, the stress distribution can be estimated by superposing two perpendicular uniaxial stress fields of equal magnitude [30], σ_{a_y} and σ_{a_x} (see Figure 13):

$$\sigma_{rr} = \sigma_{r_y} + I_{rr_y} + \sigma_{r_x} + I_{rr_x} \tag{2.90}$$

$$\sigma_{\theta\theta} = \sigma_{\theta_y} + I_{\theta\theta_y} + \sigma_{\theta_x} + I_{\theta\theta_x} \tag{2.91}$$

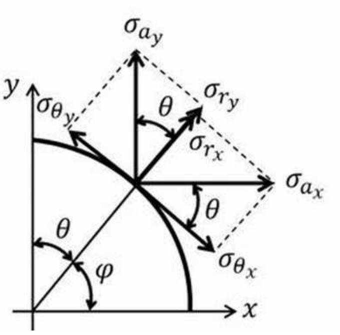

Figure 13 Radial and tangential components of a biaxial applied stress in the vicinity of a particle in the silicon matrix.

Substituting, $\sigma_{r_y} = \sigma_{a_y}\cos\theta$, $\sigma_{r_x} = \sigma_{a_x}\sin\theta$, $\sigma_{\theta_y} = \sigma_{a_y}\sin\theta$, $\sigma_{\theta_y} = \sigma_{a_y}\cos\theta$; $\sigma_{a_y} = \sigma_{a_x} = \sigma_a$ and $\cos 2\varphi = \cos(\pi - 2\theta) = \cos\pi\cos 2\theta + \sin\pi\sin 2\theta = -\cos 2\theta$ in equations (2.90) and (2.91):

$$\sigma_{rr} = \sigma_a + 4\sigma_a\left[-A\left(\frac{R}{r}\right)^2\right] \tag{2.92}$$

$$\sigma_{\theta\theta} = \sigma_a + 4\sigma_a\left[A\left(\frac{R}{r}\right)^2\right] \tag{2.93}$$

Is must be highlighted that in the case of biaxial loading the stress concentration is independent of the angular position.

The intensification of stresses in the tangential direction plays a significant role in the failure of ceramics containing particles as radial cracks extend through the silicon matrix and can link with other particles causing catastrophic failure. For calculating the stress intensity factors of mechanical tangential stresses we will consider that the crack is in the plane of maximum tension at the equator of the particle, $\theta = 90°$. Thus, the stress intensity factor due to intensification of the applied load by the presence of a soft particle, $\mu_{Si} > \mu_i$, can be calculated by introducing equation (2.89) for $\theta = 90°$ into equation (2.71), according to Evans [26]:

$$K_M = \sigma_a\left(\frac{2}{\pi a}\right)^{1/2}\int_0^a \frac{\left[1 + 2A(x/R+1)^{-2} + 6B(x/R)^{-4}\, x^{1/2}\right]}{(a-x)^{1/2}}\mathrm{d}x \tag{2.94}$$

$$K_M = \sigma_a\left(\frac{\pi a}{2}\right)^{1/2}\left[1 + 2A + 6B - 3\left(\frac{a}{R}\right)(A - 6B)\right] \tag{2.95}$$

2.1.1.2.3 Failure Prediction and Fracture Mechanism for Particles

We will suggest in this section a failure prediction for the different types of impurity second phase particles according to the configuration of thermal stresses and intensification of applied stress.

A conservative failure criterion for fracture at particles consists of equaling the particle size to the critical crack length in the Irwin expression [24]. The particle is considered in this case to intensify the stress in its vicinities with the same efficiency as a crack. The stress acting on a particle sized crack is considered to be the addition of the applied intensified load, σ_a, and thermal residual stress σ_{th}. The critical particle radius causing failure would be according to equation (2.39):

$$R_c \geq \left(\frac{K_{Ic}}{Y(\sigma_{th} + \sigma_a)}\right)^2 \tag{2.96}$$

The geometry factor of a scratch-like surface crack, $Y = 1.1\,2/\sqrt{\pi}$, fits best to predict fracture caused by elongated or plate-like sharp particles and the geometry factor of a half-penny-shaped surface crack, $Y = 2.06/\sqrt{\pi}$ [25], fits best to predict fracture caused by circular particles.

Besides a conservative failure criterion, more specific and accurate failure predictions can be formulated analyzing the thermal and mechanical stress distributions around the particles which are dependent of the thermal expansion coefficient and the elastic constants of the particles as seen in the previous sections.

For particles in a silicon matrix with very high thermal expansion coefficients, $(\alpha_p \gg \alpha_{Si})$, circumferential micro-cracking may most probably be present in the silicon matrix due to the high value of thermal stress. When the micro-cracks form a semi-sphere [36] they represent the dominant type of defect limiting the strength of the specimen. These micro-cracks are proportional to the magnitude of the particle radius $a_c = \delta R_c$, being $1 < \delta < 2$ [26]. According to equation (2.39) cracks with the following length cause failure:

$$a_c \geq \left(\frac{K_{Ic}}{Y\sigma_a}\right)^2 \tag{2.97}$$

Depending on the geometry of the originated cracks, the geometry factor for uniaxial tensile loading is $Y = 1.12\sqrt{\pi}$ and $Y = 2.06/\sqrt{\pi}$ [25] for scratch-like and sharp half-penny-shaped surface cracks respectively. In the case of the biaxial loading of a half-penny-shaped surface crack the geometry factor is $Y = 2 \times 1.12/\sqrt{\pi}$ [44].

In the case that spontaneous micro-cracking of the silicon matrix does not occur after directional solidification, cracks can develop in the surroundings of the particles at loads below the fracture stress. Thus, even though the critical flaw is not necessarily found in the as-crystallized silicon wafer, it can develop under the combination of residual thermal stresses and applied stresses [41]. Therefore, extension of micro-cracks at the vicinities of the particle into the silicon matrix due to the overlap of residual thermal stress and applied stress is analyzed in the present section.

Green [41] suggested some expressions to predict critical particle size for radial and circumferential micro-cracking due to an applied stress in the vicinity of a spherical particle with a residual thermal stress field in its surroundings. It is assumed that the matrix and the particle have the same elastic properties and therefore Green´s analysis is only valid for systems where residual thermal stresses are larger than stresses due to elastic mismatch. It was found out that an applied stress of the order of the residual stress reduces significantly the critical particle size below the critical size for spontaneous micro-cracking.

As explained in the previous sections tensile radial stresses are developed in the case of particles with larger thermal expansion coefficients than the one of the matrix. This stress is largest at the particle-matrix interface and defects located in this zone could cause circumferential micro-cracking. The assumed particle-matrix system is depicted in Figure 8. The analysis of this failure criteria starts from the expression of Ito et al. [37] for the strain energy release rate. Substituting the strain energy release rate in equation (2.67) as a function of the toughness for the case of plane stress (equation (2.41)) and equaling the elastic properties of the particle to the elastic properties of the matrix, the stress intensity factor due to radial thermal stress is:

$$K_T = P\left(\frac{0.84R\sin\varphi\,(2-\sin\varphi)}{1+\nu_{Si}}\right)^{1/2} \tag{2.98}$$

Small cracks lengths can be assumed to be penny-shaped with crack length $a = R\varphi$. The geometry factor for a penny-shaped crack is $Y = 2/\sqrt{\pi}$ [25]. Thus, according to equation (2.39) the stress intensity factor of this type of cracks due to the applied stress is [45]:

$$K_M = \frac{2}{\sqrt{\pi}}\sigma_a\sqrt{R\varphi} \tag{2.99}$$

The initial interface flaw will experience then a stress intensity factor which is the addition of the two previous stress intensity factors, $K_S = K_T + K_M$. For small values of φ the sum up of both stress intensity factors, K_S, is:

$$K_S = P\left(\frac{1.68R\varphi}{1+\nu_{Si}}\right)^{1/2} + \frac{2}{\sqrt{\pi}}\sigma_a\sqrt{R_c\varphi} \tag{2.100}$$

Circumferential micro-cracking occurs then when $K_S \geq K_{Ic}$ and the critical particle radius is therefore:

$$R_c \geq \frac{K_{Ic}^2}{\varphi\left(P\left(\frac{1.68}{1+\nu_{Si}}\right)^{1/2} + 1.128\sigma_a\right)^2} \tag{2.101}$$

Radial micro-cracking is expected when the particles have lower thermal expansion coefficients than the matrix. Under this configuration, defects which are perpendicular to the interface are most deleterious. An annular initial flaw of length a is considered in this case. The particle and the crack are considered a penny-shaped crack (with radius $a + R$) (see Figure 10).

The stress intensity factor due to thermal stress can be calculated with equation (2.80). To calculate the stress intensity factor due to the applied load it is assumed that the applied stress acts across the crack faces and thus, equation (2.79) must be solved for $\sigma(r) = \sigma_a$:

$$K_M \cong 2\sigma_a \left[\frac{a\,(\varphi+2)}{\pi\,(\varphi+1)}\right]^{1/2} \tag{2.102}$$

Adding the thermal and stress applied intensity factors, gives the total stress intensity factor acting on the initial flaw at the particle´s interface:

$$K_S \leq P\left[\frac{a\;(\varphi+2)}{\pi\,(\varphi+1)^5}\right]^{1/2} + 2\sigma_a\left[\frac{a\,(\varphi+2)}{\pi\,(\varphi+1)}\right]^{1/2} \tag{2.103}$$

Radial micro-cracking occurs then when $K_S \geq K_{Ic}$ and the critical particle radius is therefore:

$$R_c \geq \frac{\pi K_{Ic}^2(\varphi+1)^5}{\varphi(2\sigma_a(\varphi+1)^2 - P)^2(\varphi+2)} \tag{2.104}$$

Evans [26] proposed expressions for the stress intensity factors of initial flaws in the vicinity of circular particles due to thermal and elastic mismatch. If these expressions are introduced in equation (2.105) a failure criterion for circular particles can be formulated:

$$K_{Ic} \leq K_T + K_M \tag{2.105}$$

K_T is the stress intensity factor that a small interfacial flaw experiences due to the thermal residual stress (see equation (2.76)) and K_M is the stress intensity factor due to the applied mechanical load (see equation (2.95)). If the initial flaw is exactly located at the particle´s interface and has a length of $0.2R$, then the critical particle radius for particles with lower expansion coefficient than the one of silicon is:

$$R_c \geq \frac{10}{\pi}\left(\frac{K_{Ic}}{\frac{11}{40}P + \sigma_a\left(1 + \frac{7}{5}A + \frac{48}{5}B\right)}\right)^2 \tag{2.106}$$

2.1.2 Fracture Toughness

The performance of second phase particles as fracture initiators and its causes have been analyzed in detail in the previous sections. On the other hand, the same second phase particles may represent an obstacle for propagating cracks [46] increasing the fracture toughness of silicon and thus may increase the mechanical strength of the silicon wafers if the particles are well bonded to the silicon matrix.

Fracture energy and toughness of a ceramic can be therefore influenced by second phase particles [47], [48], [49], [50], [51]. Several mechanisms exist for explaining the change in fracture toughness due to particles. For the purpose of this work we will focus on the change of fracture energy and stress intensity factor of a crack approaching a particle due to thermal and elastic mismatch. Stress intensity factors at the crack tips can be influenced by the localized residual stresses and elastic properties of the particle. The crack path can be therefore repelled or attracted by the particles. Generally, a crack propagates in a direction parallel to the axis of the local compressive stress and perpendicular to the axis of the local tensile stress [52]. If the particle has larger thermal expansion coefficient and elastic modulus than the matrix and is in the plane of the crack, the crack is first deflected out of the plane as it approaches the particle and continues its propagation at the particle´s interface (see Figure 14 b)). When the crack tip reaches a position above the particle´s equator it continues its propagation in a direction normal to the radial tensile stress and it extends further in the matrix. When the particles have lower thermal expansion and lower elastic modulus, the crack is attracted and propagates through the particle (see Figure 14 a)).

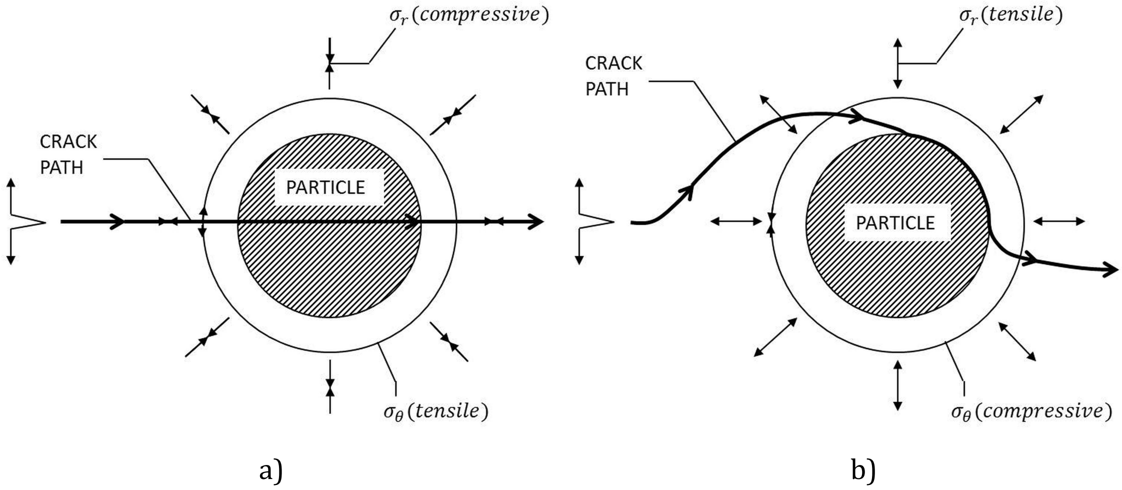

Figure 14 Image a) depicts a crack propagating through a particle ($\alpha_P < \alpha_{Si}$) and ($E_P < E_{Si}$). Image b) depicts the deflection of a crack by a particle ($\alpha_P > \alpha_{Si}$) and ($E_P > E_{Si}$) [52].

The interaction between the crack-tip stress field and the stress concentration developed around a circular particle with different elastic constants and thermal expansion coefficients is analyzed also by Khaund et al. [53]. They provided a simple analytical solution to quantify the change in local crack-driving force ΔK due to an applied biaxial stress field. The toughness that a material experiences when a propagating crack approaches the particle under a biaxial stress field is:

$$K_{Ic}^{(2)} = K_{Ic} + \Delta K = K_{Ic}\left(1 - \frac{2AR^2}{t_d^2}\right) \tag{2.107}$$

The influence of thermal stresses around particles on the local toughness is:

$$K_{Ic}^{T} = K_{Ic} + \Delta K = K_{Ic} - 0.47P\frac{R^3}{t_d^{5/2}} \tag{2.108}$$

where t_d is the distance between the center of the particle and the tip of the crack.

This model shows that the interaction between a particle and a crack tip is influenced by the distance between the particle and the crack tip, the particle size and thermal and elastic misfit stresses.

The parameter A for particles with higher elastic constants than silicon, i.e. stiff particles, is < 0 and therefore, the elastic tangential stress expressed with equation (2.93) is lower than the magnitude of the applied biaxial stress. Thus, the stress intensity factor at the crack tip approaching the particle decreases. The crack is shielded and thus the local effective toughness of the material is increased. A contrary statement applies for particles with lower elastic constants than silicon, i.e. soft particles. In this case $A > 0$ and thus the elastic tangential stress is larger than the applied biaxial stress. Crack growth is accelerated in front of the particle due to an increase of the stress intensity factor of the propagating crack and the toughness is thus diminished.

Particles with larger thermal expansion coefficients than silicon and thus with compressive tangential residual thermal stress in their surroundings also decrease the local stress intensity factor at the crack tip and the local toughness is hence increased. Particles with lower thermal expansion coefficients have tensile tangential thermal stress in their vicinities and therefore the stress intensity factor that a crack tip experiences when the crack is approaching the particle is increased and the toughness is therefore decreased [53].

Li et al. [54] simulated the variation of the energy release rate at the tip of a crack that approaches and penetrates an elastic and circular particle due to a uniaxial stress field.

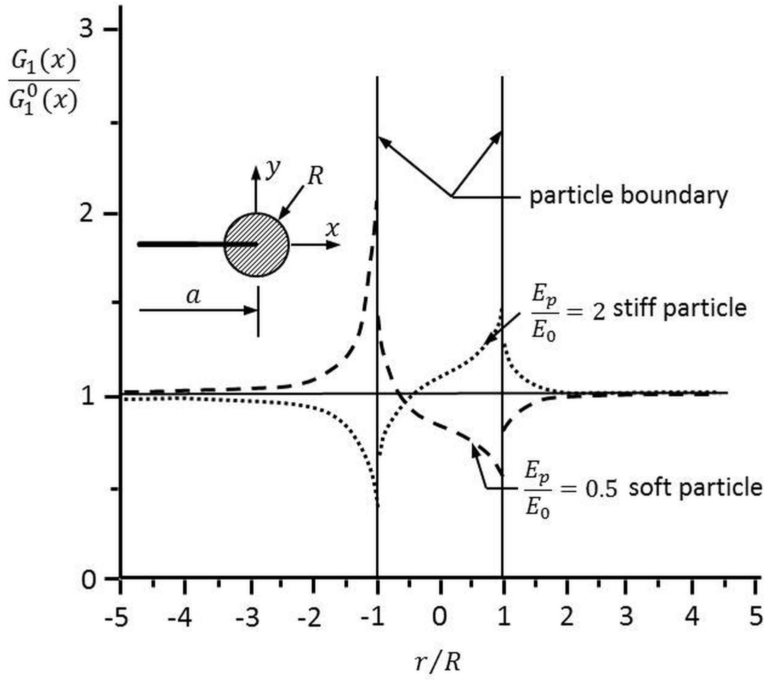

Figure 15 Variation of energy release rate of a crack that approaches and passes a circular particle [54]. The term E_0 in the image states for the elastic modulus of the matrix.

The term $G(x)/G_0\,(x)$ in Figure 15 is the normalized energy release rate where $G(x)$ is the energy release rate of a crack in the presence of a particle and $G_0(x)$ is the energy release rate of the same crack that does not approach any particles.

In the case of a stiff particle, $(E_p > E_{Si})$, the crack is shielded as it approaches the particle and the crack front is decelerated. In the case that the crack cannot deflect and penetrates the stiff particle, the energy release rate of the crack increases (see Figure 15). A soft particle, $(E_p < E_{Si})$, amplifies the energy release rate when the crack approaches the particle and the crack is thus accelerated in the direction of the particle. The energy release rate decreases after the crack penetrates the particle.

The crack senses the particle at a length approximately equal to the length of the particle´s radius from the particle´s interface. Amplification and shielding effects of the energy release rate due to stiff and soft particles vanish rapidly when the crack exits the particle.

Khaund et al. and Li and Chudnovsky analysis of stress intensity factors approaching a particle assume that the particle has a circular form. However, particles can show other geometries. Elongated particles parallel to the crack exert a larger influence on the stress intensity factor at the crack tip than elongated particles located perpendicular to the crack plane [27] [55]. Circular particles exert the least influence on the stress intensity factor.

The particle-crack interaction is also a function of the distribution of the dispersed particles [56]. The energy release rate of a propagating crack is reduced when the crack approaches a cluster of stiff particles. The crack is then shielded and the effective toughness is increased. However, when the crack leaves the cluster the energy release rate is amplified and the effective toughness is reduced [57].

Pre-existing interface flaws, i.e. poor bonding of the particles with the silicon matrix, increase the energy release rate of the propagating crack and therefore attract the crack to the particle [57].

The particles that are more deleterious to toughness are elongated particles with lower elastic constants and thermal expansion coefficient than the ones of silicon with large initial flaws at the particle´s interface and located parallel to the crack plane.

Circular particles most effectively increase fracture toughness, especially when they are smaller than a critical particle radius so that they do not represent a critical defect causing fracture and when they have higher elastic constants and thermal expansion coefficient than silicon.

There is also the possibility that the particle has higher thermal coefficient and lower elastic constants than silicon or vice versa. In that case, the effects of these material parameters on fracture toughness counteract each other and the material parameter that influences the toughness in a larger extent will define if the toughness of silicon increases or decreases.

Concerning the crystalline orientation of silicon, fracture energy and toughness showed little dependence with crystal orientation as for cubic systems. Rice [58] summarized a comparison of ceramic microstructural dependence of fracture energy, toughness and strength.

In the case that spontaneous micro-cracking in the vicinity of the particles occurs, the toughness of silicon can be diminished. Rose [59] proposed an estimation of toughness degradation due to collinear micro-cracks linking up with the advancing main crack. This estimation is based on analytical formulas for the stress intensity factor at the tip of a semi-infinite advancing crack in an infinite body and at a collinear micro-crack (see Figure 16).

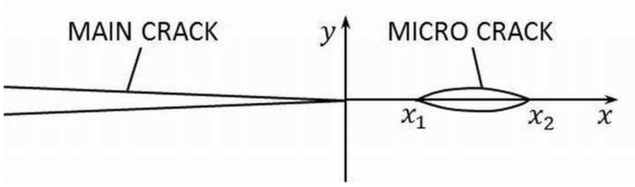

Figure 16 Two-dimensional configuration of a collinear micro-crack ahead of the main crack [59].

The material is considered isotropic and elastic and the cracks randomly distributed. Rose derives K_0 as the value of K_I at which linking up is initiated:

$$\frac{K_0}{\bar{K}_c} = \frac{k}{C} \tag{2.109}$$

Thus, K_0 is an estimate of the effective fracture toughness of the cracked body. $\bar{K}_c$ is the intrinsic fracture toughness of the cracked body which is influenced by the decrease in elastic modulus of the cracked material (which will be explained in the next section). $\bar{K}_c$ can be estimated for plane stress as follows:

$$\bar{K}_c = \sqrt{\frac{\bar{E}}{E}} K_c \tag{2.110}$$

where $\bar{E}$ is the elastic modulus of the cracked body and C is:

$$C = \frac{E(k')}{K(k')} \tag{2.111}$$

where K and E are the complete elliptic integrals of the first and the second kind, respectively, with $k^2 = x_1/x_2$ (see Figure 16) and $k' = \sqrt{1-k^2}$.

The complete elliptic integrals of the first kind and the second kind can be approximated as an expansion of a power of series [60]:

$$\begin{aligned} K(k') = \frac{1}{2}\pi \Bigg[1 + \left(\frac{1}{2}\right)^2 k'^2 + \left(\frac{1\times 3}{2\times 4}\right)^2 k'^4 + \left(\frac{1\times 3\times 5}{2\times 4\times 6}\right)^2 k'^6 + \cdots \\ + \left(\frac{(2n)!}{2^{2n}(n!)^2}\right)^2 k'^{2n} \Bigg] \end{aligned} \tag{2.112}$$

$$\begin{aligned} E(k') = \frac{1}{2}\pi \Bigg[1 - \left(\frac{1}{2}\right)^2 k'^2 - \left(\frac{1\times 3}{2\times 4}\right)^2 \frac{k'^4}{3} - \left(\frac{1\times 3\times 5}{2\times 4\times 6}\right)^2 \frac{k'^6}{5} - \cdots \\ - \left(\frac{(2n)!}{2^{2n}(n!)^2}\right)^2 \frac{k'^{2n}}{2n-1} \Bigg] \end{aligned} \tag{2.113}$$

2.1.3 Elastic Modulus

It is found in the literature that the elastic modulus of materials containing particles or inclusions depends on the elastic properties and volume fraction of the particles [61]. Increasing fraction volumes of stiffer particles increases the elastic modulus of the material.

In the same way, increasing volume fractions of softer particles, or pores and cracks, decreases the elastic modulus of the composite.

Voigt [16] and Reuss [17] were able to predict upper and lower bounds for the bulk modulus [15], B, using stress and strain averaging techniques. This is known as the “Rule of Mixtures” equations:

$$B = B_p V_p + B_{Si} V_{Si} \tag{2.114}$$

$$\frac{1}{B} = \frac{V_p}{B_p} + \frac{V_{Si}}{B_{Si}} \tag{2.115}$$

where $V_{Si,p}$is the volume fraction of silicon and the particle respectively. The same expressions are valid for calculating the shear modulus. The bounds for the elastic modulus can be obtained with the usual relation between elastic constants expressed with equation (2.8). The above theoretical approach can be extended for materials with more than two phases by addition of terms for each new phase.

Hashin and Shtrikman [62] determined bounds for the bulk and the shear modulus based on basic elasticity energy theorems. Assuming that the material is quasi-isotropic and quasi-homogeneous; the effective bulk modulus of the material containing particles can be predicted in terms of the bulk modulus and the volume fractions of the constituting phases (silicon matrix and particles).

$$B^- = B_{Si} + \frac{V_p}{\frac{1}{B_p - B_{Si}} + \frac{3V_{Si}}{3B_{Si} + 4\mu_{Si}}} \tag{2.116}$$

$$B^+ = B_p + \frac{V_{Si}}{\frac{1}{B_{Si} - B_p} + \frac{3V_p}{3B_p + 4\mu_p}} \tag{2.117}$$

$$\mu^- = \mu_{Si} + \frac{V_p}{\frac{1}{\mu_p - \mu_{Si}} + \frac{6(B_{Si} + 2G_{Si})V_{Si}}{5\mu_{Si}(3B_{Si} + 4\mu_{Si})}} \tag{2.118}$$

$$\mu^+ = \mu_p + \frac{V_{Si}}{\frac{1}{\mu_{Si} - \mu_p} + \frac{6(B_p + 2\mu_p)V_p}{5\mu_p(3B_p + 4\mu_p)}} \tag{2.119}$$

The bounds for the elastic modulus can be obtained with the usual relation between elastic constants expressed with equation (2.8).

The Hashin-Shtrikman bounds lie within the Voigt-Reuss bounds and are found to be most reliable possible limits for the bulk modulus, given only the volume fraction and moduli of the constituent phases.

The elastic response of a particle clustered and a non-clustered material is the same. That means that the slope of the stress-deformation curve is the same for both microstructures. Elastic modulus is very sensitive to the volume fraction of reinforcement and less sensitive to the distribution of particles [55].

The presence of well bonded particles can increase the elastic modulus of the material. A decrease in the measured values of elastic modulus indicates non-bonded interfaces or voids [63]. Therefore, special attention should be drawn to the decrease in elastic modulus when spontaneous micro-cracking of the silicon matrix occurs after the crystallization process.

Budiansky and O'Connell [64] proposed a model for predicting the elastic constants of a solid with randomly distributed cracks. The solid is considered isotropic and homogeneous in the large. According to this model the ratio of the bulk modulus of the cracked body, $\bar{B}$, and the uncracked bulk modulus, B, depends on the crack density parameter, ϵ:

$$\frac{\bar{B}}{B} = 1 - \frac{16}{9}\left(\frac{1-(\bar{\nu})^2}{1-2\bar{\nu}}\right)\epsilon \tag{2.120}$$

The relations between elastic constants also yield for the cracked body:

$$\bar{B} = \frac{\bar{E}}{3(1-2\bar{\nu})} \tag{2.121}$$

$$\bar{B} = \frac{\bar{E}\bar{\mu}}{3(3\bar{\mu}-\bar{E})} \tag{2.122}$$

In the case of circular cracks, the elastic modulus, the shear modulus and the crack density parameters are:

$$\frac{\bar{E}}{E} = 1 - \frac{16}{45}\frac{(1-(\bar{\nu})^2)(10-3\bar{\nu})}{(2-\bar{\nu})}\epsilon \tag{2.123}$$

$$\frac{\bar{\mu}}{\mu} = 1 - \frac{32}{45}\left(\frac{(1-\bar{\nu})(5-\bar{\nu})}{2-\bar{\nu}}\right)\epsilon \tag{2.124}$$

$$\epsilon = N\langle a^3\rangle = \frac{45}{16}\frac{(\nu-\bar{\nu})(2-\bar{\nu})}{(1-(\bar{\nu})^2)[10\nu-\bar{\nu}(1+3\nu)]} \tag{2.125}$$

Where N is the number of cracks per unit volume and a is a characteristic linear crack dimension.

It is important to mention that the Poisson´s coefficient of the cracked body, $\bar{\nu}$, is also a decreasing function of the crack density parameter, ϵ. This implies that for all values of ν, when $\bar{\nu} \to 0$ then $\epsilon \to 9/16$ (from equation (2.125)); and consequently $\bar{B}/B$, $\bar{\mu}/\mu$ and $\bar{E}/E \to 0$. This vanishing of the elastic constants is interpreted to be caused by a loss of coherence of the material. This would be produced by an intersecting crack network at the critical value $\epsilon = 9/16$ of the crack density parameter [64].

2.1.4 The Solar Cell as a Laminate Composite

Sections 2.1.1 to 2.1.3 describe the mechanical behavior of silicon wafers containing different types of second phase particles formed in the silicon matrix during the crystallization process of multicrystalline silicon blocks. The presence of these particles makes multicrystaline silicon to behave mechanically as a particle composite. Solar cell processing of silicon wafers deposits thin or thick layers of other materials on the surface of the silicon wafers. Therefore, it is of interest to study the solar cell as a functional structure equivalent to a laminate composite.

2.1.4.1 Thin Film Laminate Composite

2.1.4.1.1 Thin Film Residual Stresses

Residual stresses arise during many solar cell processes where the deposition of a thin film on the silicon wafer occurs at high temperature, as in the case of emitter diffusion and deposition of an antireflection coating. The difference in thermal expansion coefficients between the thin film material and the silicon substrates can induce large thermal stresses within the thin film. Thin film internal stresses also arise during solar cell processing as thin film growth does not take place at thermo-dynamic equilibrium. The addition of thermal and internal stresses defines the magnitude of the residual stress that remains within the thin film [65].

When the volume, i.e. the dimensions of the film, changes elastic strains and stresses develop. The volume of the thin film changes relative to the substrate due to different phenomena. The difference in thermal expansion coefficient between the film and the substrate produces a change in relative volume of the film with a change in temperature. Annihilation of vacancies, dislocations and grain boundaries also induce a change in volume of the film due to a densification of the material. Additionally, phase transformations and composition changes can induce dilatational strains in the film.

In this section we consider a laminate composite and we assume that the film is very thin compared to the substrate and that the lateral dimensions of the laminate composite are much larger than its total thickness [65].

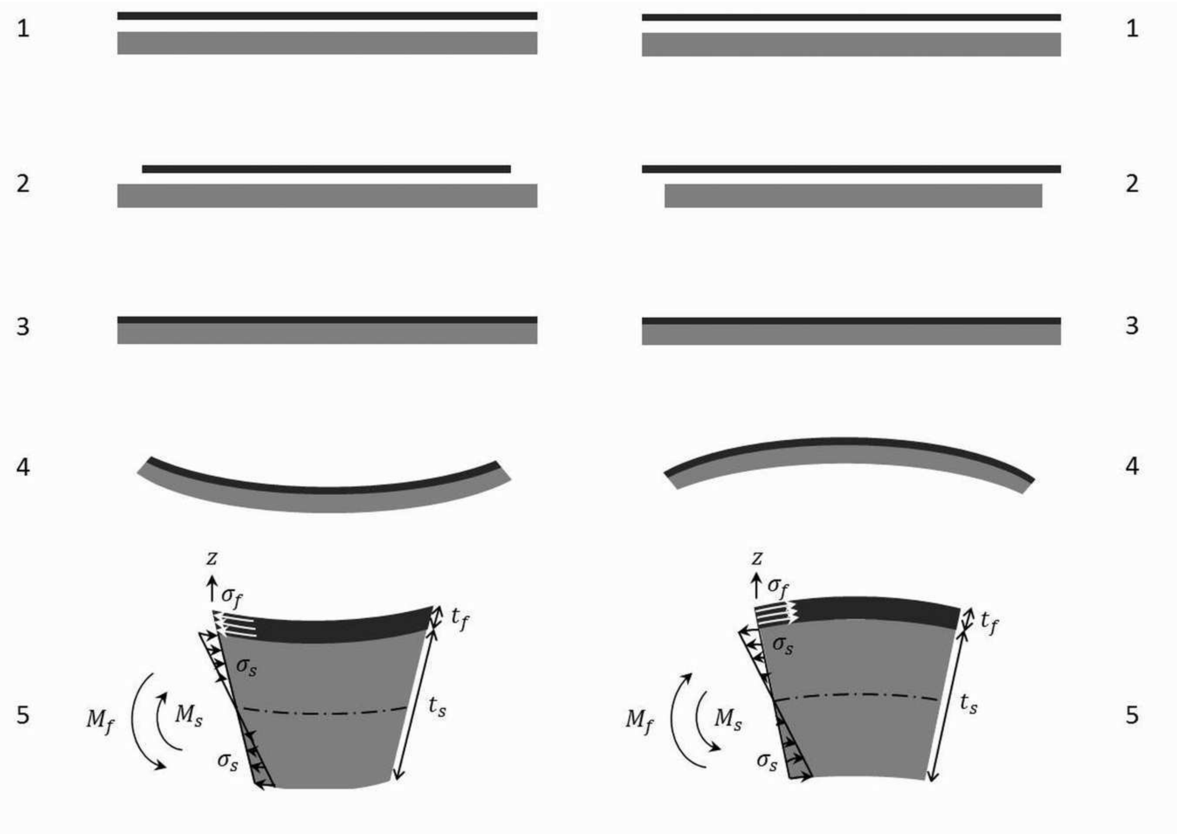

a) b)

Figure 17 Stress distribution and deformation in thin film laminate composites. The sketch is adapted from the literature [65] and [66].The z direction is perpendicular to the x-y plane; $\sigma_{f,s}$, and $t_{f,s}$ are the stress and the thickness of the film and the substrate respectively; and $M_{f,s}$ is the bending moment produced by the stress in the film and by the stress in the substrate respectively.

Next if we consider that the laminate composite is completely free of stress, the lateral dimensions of the film will match exactly the dimensions of the substrate (see Figure 17 a1 and b1). During the cooling from high temperature processing the volume of the thin film can shrink due to, for example, a higher thermal expansion coefficient of the thin film than the thermal expansion coefficient of the substrate (see Figure 17 a2). A uniform volume change is expressed as a dilatational transformation strain of the thin film, e_T. The principal components of a pure dilatational strain are $e_{xx}(T) = e_{yy}(T) = e_{zz}(T) = e_T/3$. If we reattach the film to the substrate a biaxial stress must be imposed on the film to elastically deform until it fits the dimensions of the substrate (see Figure 17 a3). This stress produces elastic strains in the film of the exact magnitude of the corresponding components of the transformation strain:

$$\varepsilon_f = \varepsilon_{xx} = \varepsilon_{yy} = -\frac{e_T}{3} \tag{2.126}$$

The biaxial stress within the film is then according to the Hooke´s law:

$$\sigma_f = \sigma_{xx} = \sigma_{yy} = Y_f \varepsilon_f \tag{2.127}$$

where Y_f is the biaxial elastic modulus of the film. The biaxial modulus of the film for isotropic bodies is:

$$Y_f = \frac{E_f}{1 - \nu_f} \tag{2.128}$$

The biaxial elastic modulus must be calculated according to its crystallographic orientation for anisotropic materials. In the case of cubic single-crystal films the biaxial modulus can be calculated depending on its elastic constants and the crystallographic orientation of the substrate. The biaxial modulus of a cubic single-crystal film in which its crystallographic plane (100) lies parallel to the surface of the substrate is isotropic in the plane of the film and can be calculated as follows:

$$Y_f(100) = c_{11} + c_{12} - \frac{2c_{12}^2}{c_{11}} \tag{2.129}$$

Once the film is attached to the substrate, we assume to remove this biaxial stress necessary for the film to match the dimensions of the substrate. The substrate then bends elastically (see Figure 17 a4), the biaxial normal forces disappear at the edges of the film but shear stresses on the film-substrate interface appear. Normal and shear stresses become zero at an edge or a surface. This phenomenon causes stress redistribution and induces normal and shear stresses at the interface near the edge. The biaxial stress is maintained in the thin film from a certain distance away from the edges. The thin film remains under tensile stress, and the stress distribution within the substrate can be observed in Figure 17 a5. The very top of the substrate is under compressive stress and this stress diminishes its magnitude until the middle of the thickness of the substrate where the neutral plane is. From the neutral plane to the bottom part of the substrate the stress increases and becomes tensile. When thin film tensile stresses are very large they can relieve themselves by micro-cracking of the film [66].

If we consider that the thermal expansion coefficient of the thin film is lower than the thermal expansion coefficient of the substrate, the substrate volume shrinkage during the cooling from high temperature processing is larger than the film volume shrinkage (see Figure 17 b2). It can also be seen as an expansion of the dimensions of the film relative to the dimensions of the substrate. If we reattach the film to the substrate, a biaxial stress must be imposed on the film to elastically deform until it fits the dimensions of the substrate (see Figure 17 b3). Once the film is attached to the substrate, we assume to remove this biaxial stress necessary for the film to match the dimensions of the substrate. The substrate then bends elastically (see Figure 17 b4), the biaxial normal forces disappear at the edges of the film but shear stresses on the film-substrate interface appear. The biaxial stress is maintained in the thin film from a certain distance away from the edges. The thin film remains under compressive stress, and the stress distribution within the substrate can be observed in Figure 17 b5. The very top of the substrate is under tensile stress and this stress diminishes its magnitude until the middle of the thickness of the substrate where the neutral plane is. From the neutral plane to the bottom part of the substrate the magnitude of the stress increases and becomes compressive. Compressive stresses in the thin film can relieve themselves by buckling.

The biaxial modulus of the substrate and the thickness of the film and the substrate define the magnitude of the bending [65] as the properties of the thin film have negligible effect on the bending of the structure due to the thin film approximation. The thin film laminate composite takes the shape of a spherical shell after bending if the elastic biaxial modulus of the substrate, Y_s, is isotropic in its plane.

In equilibrium the bending moment produced by the stress within the film, M_f, must equal the bending moment produced by the stress in the substrate, M_s. The bending moment is calculated as the force times the perpendicular distance and taking the position of the neutral plane as the co-ordinate origin. If the thickness of the thin film laminate is approximated as the thickness of the substrate ($t_s + t_f \approx t_s$):

$$M_f = \sigma_f l t_f \frac{t_s}{2} \tag{2.130}$$

where l is the length of the edge of the thin film laminate composite.

The biaxial stress state of the substrate depending on its distance to the neutral plane is:

$$\sigma_s(z) = Y_s \varepsilon_s(z) = Y_s \frac{z}{r_k} \tag{2.131}$$

where r_k is the radius of the curvature of the composite after bending measured from the neutral plane. $\varepsilon_s(z)$ is the strain in a plane parallel to the surface of the composite at distance z from the neutral plane which can be calculated as z/r_k following a geometrical relation between the dimensions of the system [67]. Thus, the moment produced by the stress in the substrate is:

$$M_s = l \int_{-t_s/2}^{t_s/2} z\sigma(z)\mathrm{d}z = l \int_{-t_s/2}^{t_s/2} Y_s \frac{z^2}{r_k} \mathrm{d}z = Y_s \frac{l t_s^3}{12 r_k} \tag{2.132}$$

The residual stress within the thin film can be obtained by equaling both moments which is known as the Stoney´s equation [67]:

$$\sigma_f = Y_s \frac{t_s^2}{6 r_k t_f} \tag{2.133}$$

where Y_s can be calculated for isotropic and cubic crystal materials with equations (2.128) and (2.129). By measuring the curvature, k, or deflection of the substrate, δ, the curvature radius can be then calculated ($r_k = k^{-1}$) ($r_k = l^2/8\delta$) and the residual stress in the film can be therefore determined.

The stress in the upper plane of the substrate can be approximated as a function of the stress within the thin film and the relation between the thicknesses of the film and the substrate [65]:

$$\sigma_{max,s} \approx -\frac{3t_f}{t_s}\sigma_f \tag{2.134}$$

The smallest the thickness of the film the lower the stress induced in the substrate will be.

As discussed at the beginning of this section, the residual stress within the film is the combination of the thermal and internal stresses of the film:

$$\sigma_f = \sigma_{th} + \sigma_i \tag{2.135}$$

In the case of a thermal mismatch between the film and the substrate there is an elastic strain needed to fit the dimensions of the film to the dimensions of the substrate:

$$\varepsilon_{th} = \left(\alpha_f - \alpha_s\right)(T_0 - T_{amb}) = \Delta\alpha\Delta T \tag{2.136}$$

where $\alpha_{f,s}$ is the thermal expansion coefficient of the film and the substrate respectively; T is the current temperature, usually it is room temperature, and T_0 is the temperature at which the silicon wafer has been processed, i.e. the temperature at which the film and the substrate were in a stress-free state. Thermal stresses are often dominant in the case of thin film depositions at high temperatures [68].

Growth or intrinsic strains are produced when the density of the film changes once it has been bonded or attached to the substrate. Then, the elastic accommodation strain in this case can be expressed as a function of the dilatational transformation strain associated with this change in material density, ε_T. The elastic accommodation strain due to the difference in lattice parameters between the film and the substrate is for epitaxial films grown on thick substrates:

$$\varepsilon_i = -\frac{\varepsilon_T}{3} = \frac{\Delta a}{a} \approx \frac{a_s - a_f}{a_f} \approx \frac{a_s - a_f}{a_s} \tag{2.137}$$

where $a_{f,s}$ is the lattice parameter of the film and the substrate respectively.

Other sources of intrinsic stresses are grain growth, excess vacancy annihilation, shrinkage of grain boundary voids, presence of impurities, phase transformation and precipitation, etc. Growth stresses are strongly dependent on the material properties, on the substrate temperature during processing and on the growth flux and chamber conditions. More detail about these phenomena can be found in the literature [68].

In the case that intrinsic stresses can be simplified to be due to the difference in lattice parameters between the film and the substrate, equation (2.127) can be expressed as:

$$\sigma_f = \sigma_{th} + \sigma_i = Y_f\left[\left(\alpha_f - \alpha_s\right)(T_0 - T) + \frac{a_s - a_f}{a_s}\right] \tag{2.138}$$

2.1.4.1.2 Silicon Substrate Residual Stresses

As the substrates are thick in comparison to the films, the stresses in the substrates are usually small and negligible. However, if the thin film on the silicon substrate remains with very large compressive stresses, the corresponding tensile stresses in the uppermost layer of the silicon substrate can propagate cracks or notches on the surface of the substrate. Thus, fracture through the thickness of the substrate can occur already by the level of thermal residual stress or by the overlap of tensile thermal residual stress and applied stress during further processing, solar cell assembly into modules or loadings during solar cell performance.

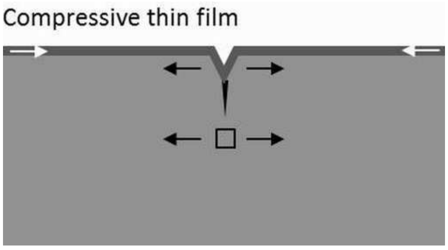

Figure 18 Substrate cracking due to the concentration of tensile thermal stress in a crack in the uppermost layer of the silicon substrate. The sketch is adapted from [65].

Another aspect to be considered, concerning the silicon substrate, is the dependency of its thermal expansion coefficient with the temperature [69].

During solar cell processing silicon wafers are heated up to a temperature between 500 to 1200°C; then the wafers are processed during 30 min approximately and consequently cooled down to room temperature. The outside parts of the wafer tend to be hotter than the inside parts during heating up. And the same occurs during cooling down where the outside parts of the wafer tend to be colder than the inside. Thus, thermal stresses inside the silicon substrate can develop after solar cell processing. The magnitude of the thermal stresses, as explained before, depends on the difference in thermal expansion coefficients between the hottest and the coldest parts of the wafers and on the gradient of temperature of the final rapid cooling after processing at high temperature:

$$\sigma_{th} = \frac{E}{1-\nu} \Delta\alpha \Delta T \tag{2.139}$$

Table 14 of Appendix A summarizes values of the thermal expansion coefficient of silicon within a temperature range from 100 to 1500℃.

2.1.4.2 Thick Film Laminate Composite

When the thickness of the film deposited on the substrate cannot be negligible in comparison to the thickness of the substrate, the elastic constants of the film also play a significant role on the bending of the composite structure. When a laminate composite is subjected to a load, mechanical or thermal, the deformation of the material in each layer is different due to the elastic and thermal mismatch between the different materials composing the layers. When both layers are perfectly bonded shear stresses arises in the interface between the layers in order to exert a deformation that assures the structural integrity of the laminate composite.

The bending that a bilayer composite experiences after the cooling from a high temperature was deduced by Timoshenko [70]. A similar analysis to the one exposed to deduce Stoney´s equation can be conducted for thick film laminate composites by equaling the bending moments and the deformations of the film and the substrate. The magnitude of the bending radius of the laminate can be calculated as follows [70], [71]:

$$\frac{1}{r_k} = \frac{6(\alpha_f - \alpha_s)(T_0 - T_{amb})\left(1 + \frac{t_f}{t_s}\right)^2}{(t_f + t_s)\left[3\left(1 + \frac{t_f}{t_s}\right)^2 + \left(1 + \frac{t_f E_f}{t_s E_s}\right)\left(\left(\frac{t_f}{t_s}\right)^2 + \frac{t_s E_s}{t_f E_f}\right)\right]} \tag{2.140}$$

The bow deflection and the curvature radius are related by $\delta = l^2/8r_k$ when the bending curve is an arc of a perfect circle.

2.1.4.3 Laminate Failure Criteria

2.1.4.3.1 Fracture Mechanics of Interface Cracks

In this section failure criteria are reviewed following the literature on the topic [72], [73], [74] in order to comprehend how fracture of laminated structures occurs and to be able to predict the mechanical strength of such structures.

The first concept to be reviewed in this section is the failure criterion of a planar crack in an isotropic body that is subjected to a mixed mode loading. Considering plane strain conditions, the failure criterion expressed by equation (2.42) can be also expressed in the case that the crack experiences loading under mode I and mode II (see Figure 4):

$$G = \frac{(1 - \nu^2)}{E}(K_I^2 + K_{II}^2) \tag{2.141}$$

Interface cracks tend to propagate in mixed mode by nature. The difference in elastic properties between the layers of the laminate induces some degree of asymmetry even when the geometry of the system and the loading are symmetric. Therefore, the Irwin relation between energy release rate and stress intensity factors must be expressed for a mixed mode of crack propagation.

Stress fields at the tip of an interfacial crack are more complicated than those for the homogeneous body and this issue must be taken into account in the failure criterion. Dundurs [75] proved that these elastic stress fields depend on the material properties through two independent parameters known as the Dundurs mismatch parameters, α_D and β_D:

$$\alpha_D = \frac{\frac{E_f}{(1 - \nu_f)} - \frac{E_s}{(1 - \nu_s)}}{\frac{E_f}{(1 - \nu_f)} + \frac{E_s}{(1 - \nu_s)}} \tag{2.142}$$

$$\beta_D = \frac{1}{2}\frac{\mu_f(1 - 2\nu_s) - \mu_s(1 - 2\nu_f)}{\mu_f(1 - 2\nu_s) + \mu_s(1 - 2\nu_f)} \tag{2.143}$$

α_D represents a mismatch in extensional stiffness and β_D in volumetric stiffness. Both parameters are cero when the materials have the same elastic properties. A complexity of the stresses at the crack tip arises when β_D is non-zero. However, when $\beta_D = 0$ the stresses in the solid are the same as for the homogeneous solid and equation (2.141) can be applied.

Thus, according to equation (2.38) the stress at the interface line can be described like the stress in a homogeneous body if $\beta_D = 0$:

$$\sigma_{22} = \frac{K_I}{\sqrt{2\pi r}} \quad , \quad \sigma_{12} = \frac{K_{II}}{\sqrt{2\pi r}} \tag{2.144}$$

The following equation shows the general relationship between the energy release rate and stress intensity factors for crack propagation in the interface.

$$G = \frac{1-\beta_D^2}{2}\left[\frac{1-\nu_f^2}{E_f} + \frac{1-\nu_s^2}{E_s}\right](K_I^2 + K_{II}^2) \tag{2.145}$$

Since, β_D^2 is much smaller than 0.1, then β_D^2 can be simplified to cero.

There is another parameter to take into account for the description of the mechanical behavior of the interface of a bilayer and it is the relative proportion of mode I and II:

$$\psi = \tan^{-1}\left(\frac{K_{II}}{K_I}\right) \tag{2.146}$$

When $\psi = 0°$ pure mode I controls the stress in the interface and when $\psi = 90°$ pure mode II does. For the crack problem in Figure 19 and $\beta_D = 0$ the stress intensity factors can be introduced in equations (2.145) and (2.146) as a function of the remote stresses:

$$G = \frac{1}{2}\left[\frac{1-\nu_f^2}{E_f} + \frac{1-\nu_s^2}{E_s}\right]\pi a(\sigma_{22}^2 + \sigma_{12}^2) \quad , \quad \psi = \tan^{-1}\left(\frac{\sigma_{12}}{\sigma_{22}}\right) \tag{2.147}$$

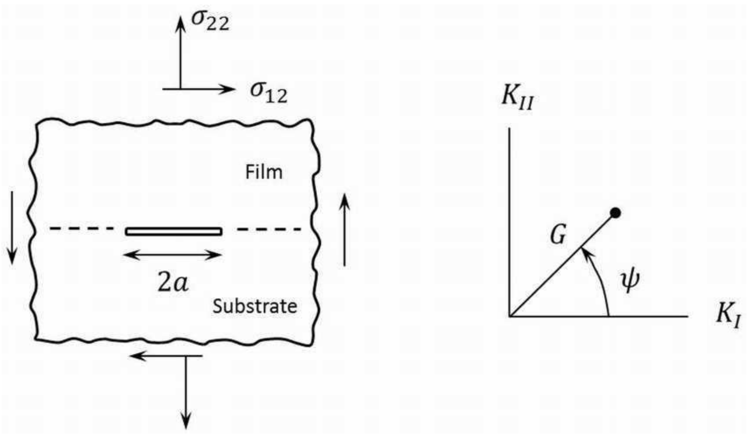

Figure 19 Sketch of an interface crack for a remotely stressed bimaterial adapted from [74].

The interface toughness, which is the critical value of G needed for the crack to propagate through the interface, $G = \Gamma_c$, depends on the relative proportion between the loading modes, $\Gamma_c(\psi)$. Experimental procedures for measuring the interface toughness can be found in the literature as well as experimental values of interface toughness of different materials.

Interfaces described by low values of ψ are dominated by the loading mode I and present low interface toughness. This is the case of brittle materials where the separation of atomic planes, i.e. the strength of the chemical bond, controls the resistance to fracture. Typical values of interface toughness between a brittle substrate and a brittle film approximate to $1\ \mathrm{J/m^2}$.

When the material of the thin film is more ductile, like in the case of most metals, plastic flow and ductile tearing determine more the energy associated with fracture and the loading mode II becomes dominant (larger values of ψ). Typical values of interface toughness between a brittle substrate and a ductile film approximate to $10\ \mathrm{J/m^2}$.

2.1.4.3.2 Specific Solutions for Cracks in Bilayers

Further analysis about the fracture of bilayer laminates will be performed under the concept of the steady-state cracking for simplification. The crack length is considered to exceed approximately twice the thickness of the film, in order to consider the stress at the crack tip independent on the size of the crack. That means that there is a length beyond which the advancing crack front does not “sense” the other end of the crack and therefore the energy release rate is independent on the crack size in the steady-state cracking.

Delamination of Films

Delamination cracks can run through an interface or parallel to the interface in the substrate depending on the material´s properties, geometry of the laminate and stresses.

Equation (2.147) can be formulated for the residual stress acting on an edge crack larger than twice the thickness of the film at the interface whose front is parallel to the edge of the laminate (see Figure 20):

$$G_{SS} = \frac{1}{2}\frac{(1-\nu_s^2)\sigma_f^2 t_f}{E_f} \quad , \quad \psi = \omega(\alpha_D) \tag{2.148}$$

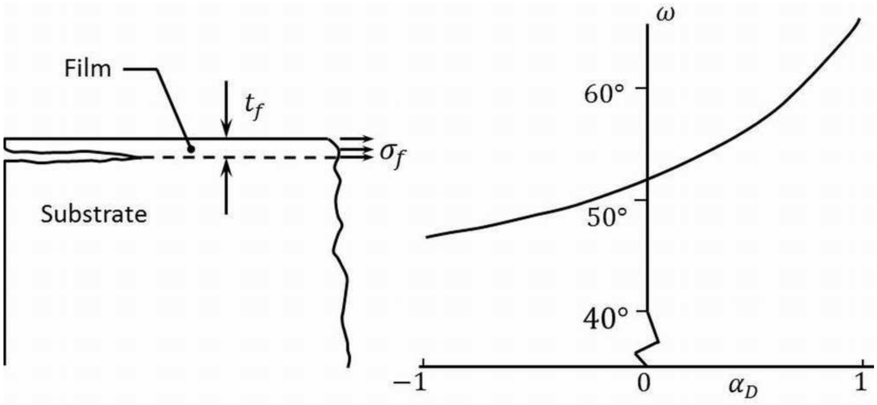

Figure 20 Sketch of an interface crack between a thin film and a substrate adapted from [74].

where G_{SS} is the steady-state energy release rate and the values of ω depending on the first Dundurs parameter can be checked in Figure 20.

Whether a crack will continue its propagation through the interface or will kink out of the interface into the substrate depends on the energy release rate of interface propagation against kinking and on the relative toughness of the interface and the substrate. Moreover, for small a (see Figure 21), the energy release rate of crack kinking depends on the proportion between the loading modes in the film, ψ, the first Dundurs parameter, α_D, and on the crack kink angle, Ω.

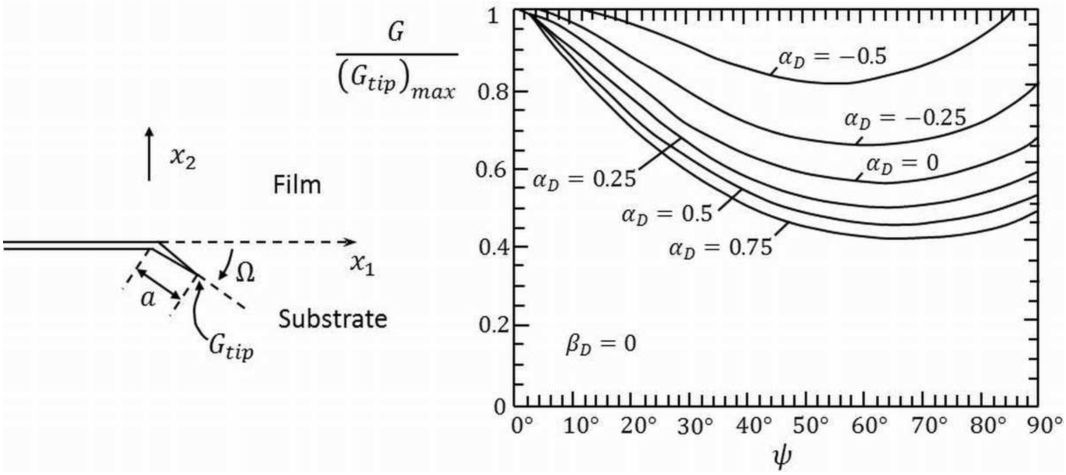

Figure 21 Energy release rate for interface crack propagation relative to the maximum energy release rate needed for crack kinking as a function of mode mixity, ψ, for various Dundurs elastic mismatch parameters α_D, and $\beta_D = 0$. The image is adapted from [74].

There is a value of the kink crack angle that maximizes the energy release rate at the tip of the crack that kinks. Results for different levels of elastic mismatch between the substrate and the film for this value of crack kink angle are depicted in Figure 21. For values of $\alpha_D > -2/3$ the crack kink angle that maximizes the energy release rate makes the kinked crack to propagate at a cero mode mixity, $\psi_{tip} \cong 0$. This can be interpreted as a maximization of the energy release rate of the kinked crack for crack propagation under loading mode I.

Whether the crack kinks or continues its propagation through the interface depends on the toughness of the interface $\Gamma_c(\psi)$ relative to the toughness of the substrate, Γ_c^s:

$$\frac{G}{(G_{tip})_{max}} < \frac{\Gamma_c(\psi)}{\Gamma_c^s} \tag{2.149}$$

Equation (2.149) means that if the energy release rate at the tip of the kinked crack reaches the value of critical energy release rate of the substrate, $(G_{tip})_{max} = \Gamma_c^s$, before the energy release rate for interface crack propagation reaches the interface toughness, $G = \Gamma_c(\psi)$, then the crack will kink into the substrate.

Single Cracks in Films under Tensile Stress

We consider that there is a residual tensile stress, $\sigma_{11} = \sigma_{22} = \sigma_f$ and $\sigma_{33} = 0$, in the film before cracking and that the crack front experiences mode I loading.

The energy release rate in steady-state for this crack geometry (see Figure 22 a)) is:

$$G_{ss} = \frac{\pi}{2}\frac{(1-\nu_f^2)}{E_f}\sigma_f^2 t_f g(\alpha_D, \beta_D) \tag{2.150}$$

The subscript *SS* stays for steady-state and values for g are depicted in Figure 22 b).

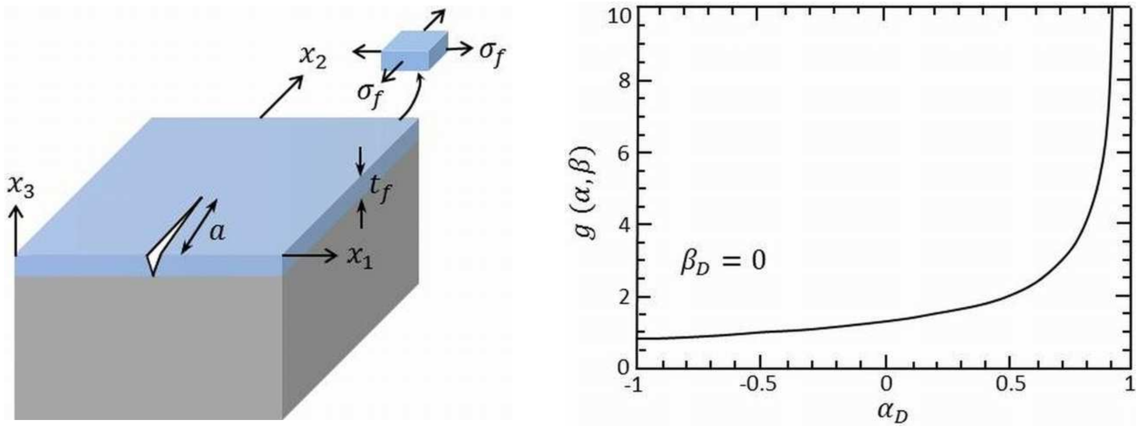

a) b)

Figure 22 Single crack in a film under tensile stress (image a)). Image b) depicts the values of g with respect to the elastic mismatch parameter α_D*. The graph is adapted from [76].*

When the crack propagates through the substrate and reaches the interface, it can penetrate into the film or it can deflect into the interface (see Figure 23). The crack reaches the interface in a perpendicular direction to the interface and is loaded symmetrically under mode I.

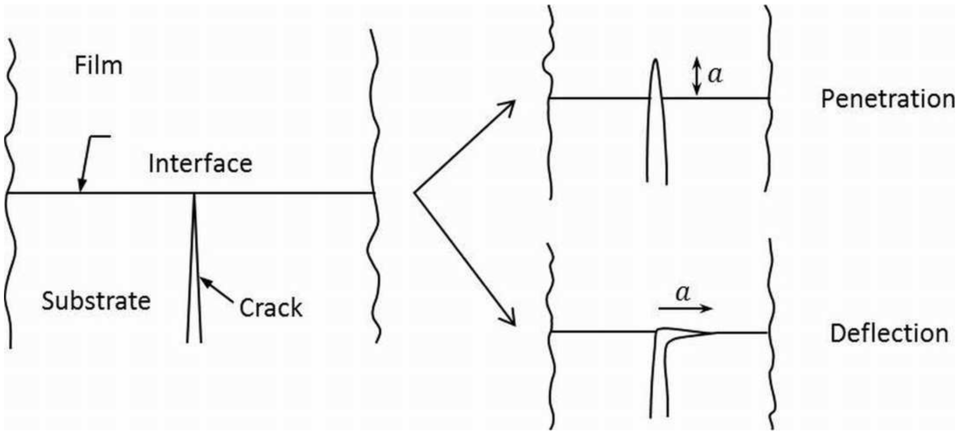

Figure 23 The image depicts a crack that is arrested at an interface under symmetric loading. With increasing loading either the crack penetrates the interface or deflects into the interface. The image is adapted from [74].

Figure 24 depicts the ratio of energy release rates at the tips of the deflected crack, $\left(G_{tip}\right)_d$, and the penetrating crack, $\left(G_{tip}\right)_p$, at equal putative crack lengths, a, for different values of α_D and considering the approximation of $\beta_D = 0$.

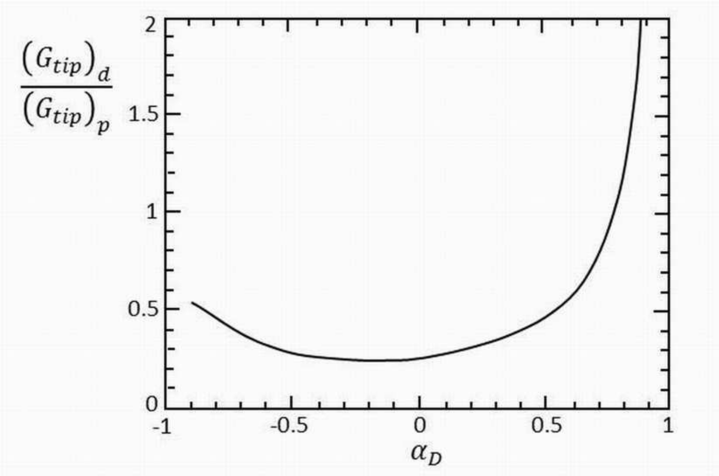

Figure 24 Ratio of energy release rates for crack deflection relative to crack penetration at equal putative crack lengths. The image is adapted from [77].

Whether the crack deflects or penetrates into the film depends on the toughness of the interface $\Gamma_c(\psi)$ relative to the toughness of the film, Γ_c^f:

$$\frac{(G_{tip})_d}{(G_{tip})_p} < \frac{\Gamma_c(\psi)}{\Gamma_c^f} \tag{2.151}$$

Equation (2.151) means that if the energy release rate at the tip of the penetrating crack reaches the value of critical energy release rate of the film, $(G_{tip})_p = \Gamma_c^f$, before the energy release rate of the deflected crack reaches the interface toughness, $(G_{tip})_d = \Gamma_c(\psi)$, then the crack will penetrate into the film. When this condition is not met, the crack will deflect in the interface.

Single Cracks in Films under Compressive Stress

Green [78] analyzed the strengthening of ceramics due to compressive residual stresses in the surface of the specimen. When an applied tensile stress is applied to the specimen, the compressive residual stress opposes to the tensile applied stress. Therefore, failure from surface defects is hindered.

The increase in fracture strength in this case, $\Delta\sigma_{fr}$, is equal to the amount of compressive residual stress, σ_c, when the whole length of the surface defect is subjected to the residual compressive stress:

$$\Delta\sigma_{fr} = -\sigma_c \tag{2.152}$$

In that case, the degree of strengthening $\sigma_{fr}/\sigma_{fr}^0$, can be simply calculated as follows:

$$\frac{\sigma_{fr}}{\sigma_{fr}^0} = 1 + \frac{\sigma_c}{\sigma_{fr}^0} \tag{2.153}$$

where σ_{fr} is the actual fracture strength of the specimen and σ_{fr}^0 is the strength of the body in absence of residual stress.

It can also occur that the depth of the surface defect is larger than the compressive depth zone (see Figure 25). The compressive residual stress closes partially the two surfaces of the crack in the absence of an applied stress. When a tensile stress is applied the crack will begin to open from its back tip to the surface at a critical level of applied stress.

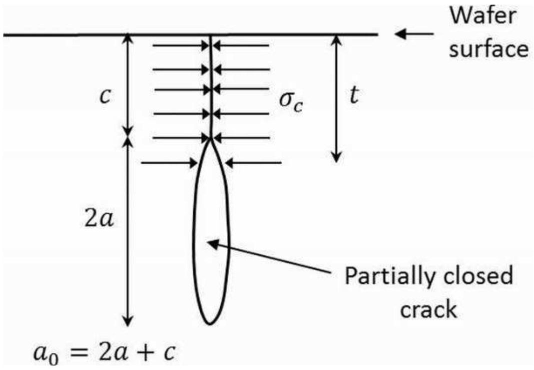

Figure 25 Closure of a surface crack due to the residual compressive stress adapted from [78]. The term "t" refers to the compressive depth zone and "c" states for the crack closure length.

Green [78] suggested determining the crack closure length, c, from a simple expression derived from Barenblatt [42]:

$$\frac{c}{a_0} = \frac{\left(1 + \frac{t}{a_0}\right)\cos\left(\frac{\pi\sigma_a}{2\sigma_c}\right) - \left(1 - \frac{t}{a_0}\right)}{2\cos\left(\frac{\pi\sigma_a}{2\sigma_c}\right)} \tag{2.154}$$

where c is the crack closure length; a_0 is the total crack length; t is the compressive depth zone and σ_a is the applied stress.

The curve described by equation (2.154) is represented in Figure 26 for several ratios of compressive depth zone to total crack length.

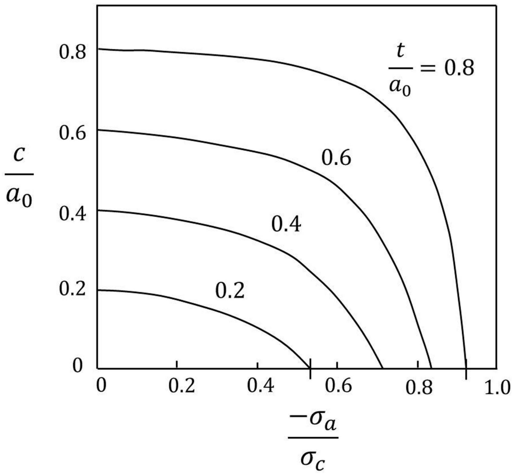

Figure 26 Crack closure length dependence on the depth of the residual compressive stress field and the ratio of applied to compressive stresses taken from [78].

Figure 26 shows how the crack closure length decreases with increasing applied tensile stress. The critical value of applied stress at which the effect of crack closure disappears can be read in the abscissa axis of the graph. For example, if the compressive stress covers only

20% of the surface crack ($t/a_0 = 0.2$), the application of a tensile stress, which is approximately 52% of the residual compressive stress, cancels the closing effect of the compressive stress, i.e. the crack closure length is zero ($c/a_0 = 0$). If the compressive stress acts on 80% of the crack length ($t/a_0 = 0.8$), the crack closure effect is stronger and therefore an applied tensile stress, which is approximately 93% of the compressive stress, is needed to cancel crack closure.

The calculation of the degree of strengthening when the compressive stress does not cover entirely a surface crack is not as straightforward as when it does. Green [78] suggested an expression to evaluate the level of strengthening in this case. He derived an expression for the stress intensity factor of a partially closed crack when a tensile stress is applied. Then he set a conventional fracture criterion and used the resulting equation for calculating the degree of strengthening. The complexity of this mathematical expression is considerable. Therefore, the graph depicted in Figure 27 which is a graphical representation of this expression will be used for the purpose of this work.

Figure 27 shows how the strengthening effect is stronger as the magnitude of the residual compressive stress gets larger than the strength of the specimen without compressive stress. Larger ratios of compressive depth zone to total crack length also leads to higher strengthening effect.

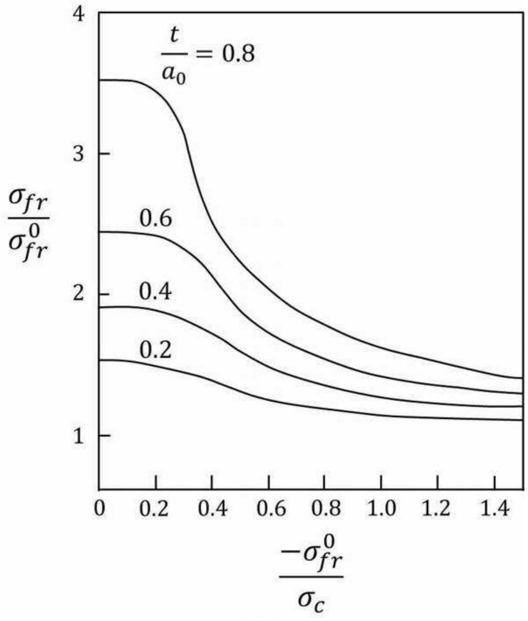

Figure 27 Strengthening due to surface compression in a semi-infinite plate [78].

2.1.4.4 Laminate Spontaneous Cracking under Residual Film Stress

Spontaneous failure of laminated structures is strongly dependent on the residual stress state of the film. Films under tensile residual stress present distinct failure patterns which are different to the failure patterns of films under compressive residual stress. Failure criteria of laminated structures due to residual stress in the film combine certain parameters in a non-dimensional form [74]:

$$\mathrm{Z} = \frac{\left(1 - \nu_f^2\right) t_f \sigma_f^2}{E_f \Gamma_c} \tag{2.155}$$

If the “cracking number”, Z, is lower than a critical value, Z_c, for a specific failure mode, then cracking under that mode can be excluded.

In the case of a single crack under tensile residual stress, σ_f, channel cracking occurs when the energy release rate defined by equation (2.150) exceeds the value of toughness of the film, $G_{SS} \geq \Gamma_c^f$. Equation (2.150) can be written in the form of equation (2.155) in order to formulate a failure criterion due to residual stress:

$$\frac{\left(1 - \nu_f^2\right) t_f \sigma_f^2}{E_f \Gamma_c^f} \geq \frac{2}{\pi g(\alpha_D, \beta_D)} \tag{2.156}$$

where the first term is the critical value for cracking due to the residual stress in the film, $Z_c = 2/\left(\pi g(\alpha_D, \beta_D)\right)$. Thus, channel cracking (see Figure 28) of the film occurs when the condition $Z \geq Z_c$ is met. This failure criterion based on steady-state cracking is conservative because the energy release rate of initial flaws smaller than approximately twice the length of the thickness is always lower than the energy release rate in steady-state cracking.

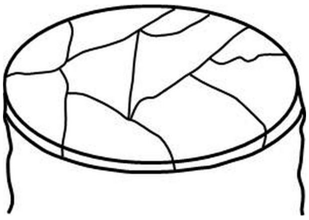

Figure 28 Thin film channel cracking adapted from [74].

An interface crack can also lead to delamination failure due to tensile residual stress, σ_f. Steady-state delamination occurs when the energy release rate defined by equation (2.148) exceeds the interface toughness of the film, $G_{SS} \geq \Gamma_c(\psi)$, and equation (2.148) can be formulated in the form of equation (2.155). The failure criterion for delamination of thin films is thus:

$$\frac{\left(1 - \nu_f^2\right) t_f \sigma_f^2}{E_f \Gamma_c(\psi)} \geq 2 \tag{2.157}$$

It is common that a delamination crack occurs in the substrate below and parallel to the interface when a metal film under residual stress is bonded to a ceramic substrate. In this case, the previous delamination failure criterion can be expressed as follows:

$$\frac{(1 - \nu_s^2) t_f \sigma_f^2}{E_f \Gamma_c^S} \geq 2.93 \tag{2.158}$$

where Γ_c^S is the toughness of the substrate. The substrate cracks at a distance d from the interface (see Figure 29 a)) which shows proportionality with the thickness of the film $d = 2.86 t_f$.

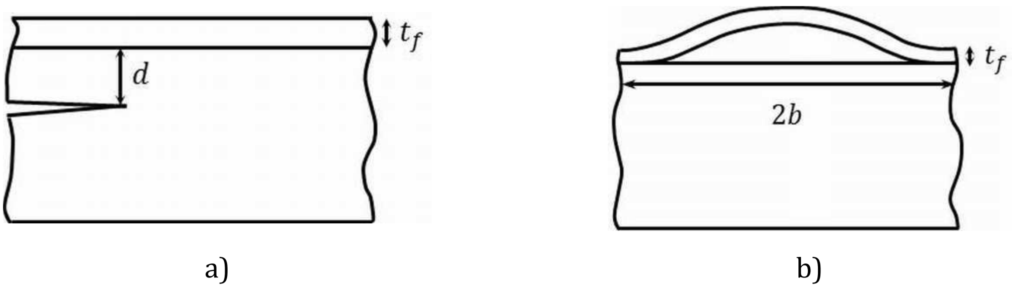

Figure 29 Substrate delamination at a distance d from the interface (image a)) and buckling driven interface delamination (image b)).

A reliable performance is commonly considered to be sufficient when the film remains under compressive residual stress which suppresses cracking through the layer, i.e. crazing. Sensitivity to damage can be also minimized by reducing the thickness of the film. However, failure can also occur when the film is subjected to compressive stress. This is known as buckling driven interface delamination. A detailed analysis of the fracture mechanics of buckling driven delamination is out of the scope of the present work. However, a simple failure criterion for this type of failure is given according to the literature consulted in this section [73], [74]. The failure criterion establishes a critical value of compressive residual stress above which buckling occurs:

$$\sigma_c = \frac{\pi^2}{12} \frac{E_f}{\left(1 - \nu_f^2\right)} \left(\frac{t_f}{b}\right)^2 \tag{2.159}$$

If the residual compressive stress in the film exceeds the value of critical stress for buckling, $\left|\sigma_f\right| \geq \sigma_c$, the film buckles away from the substrate an interface crack length of $2b$ (see Figure 29 b)).

2.2 Plastic Behavior

Another type of mechanical behavior is the one governed by plastic deformation. This type of behavior is typical of metals and can also be observed in ceramics loaded at high temperatures. The total strain is composed by elastic and plastic components. If the stress is removed before fracture occurs, the elastic component of the strain is recovered but not the plastic. The tensile yield strength is a level of stress at which a permanent plastic strain of 0.002 remains after removal of the applied stress (see Figure 30) [14]. This parameter is considered the point of change between elastic and plastic mechanical behavior. Silicon is brittle at room temperature and its transition from brittle to ductile behavior occurs at approximately 60% of its melting point (1412℃) [79]. Temperature life performance of solar cells is within the brittle regime of silicon and therefore this work focuses on the elastic mechanical behavior of silicon at room temperature. However, many solar cell processes heat silicon wafers beyond the brittle-ductile transition temperature and therefore a brief explanation about the concept of plastic behavior will be given in the present section.

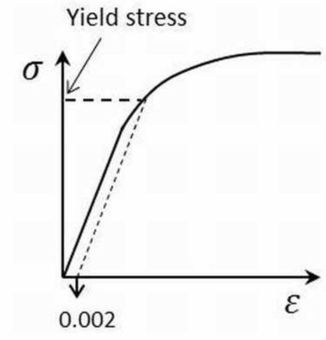

Figure 30 Stress-strain curve for plastic mechanical behavior after [14].

Plastic behavior is defined by the yield stress, τ_y, which is the level of shear stress needed to induce plastic deformation, i.e. dislocation movement. Dislocations are two-dimensional defects in a crystalline lattice. The silicon lattice presents a diamond cubic structure which is a variant of the face-centered cubic structure. Therefore, silicon presents the same slip systems than this latter structure, $\{111\}\langle 110\rangle$. That means that the dislocation moves by the glide on $\{111\}$ family planes with Burger vector in the $\langle 110\rangle$ direction [80].

Yield stress changes with temperature and microstructure. Rabier and Demenet [81] compiled values of yield stress for silicon. The yield stress of silicon at room temperature is approximately 5 GPa and the shear strength is ~75 MPa (see section 2.1.1). Thus, a silicon specimen subjected to an applied stress breaks before plastic deformation can occur. At the brittle-ductile transition temperature the yield stress has approximately the same value than the shear strength and therefore plastic deformation can occur before fracture. At 1000℃ the yield stress of silicon is approximately 10 MPa. That means that thermal or mechanical stresses which are larger than 10 MPa induces plastic deformation in silicon.

Thermal stresses induced on silicon wafers during solar cell processing can be relaxed within the silicon matrix by plastic deformation, i.e. dislocation generation and movement, above the brittle-ductile transition temperature. However, below this temperature dislocation movement is not possible and thermal stresses remain in the silicon crystalline lattice as residual stresses.

Point defects, high dislocation density, grain boundaries and particles can impede dislocation movement and hence increase the yield strength of the material [15].

2.2.1 Thermal Shock Resistance

Temperature gradients can cause the development of stresses when adjacent components constrain the thermal expansion of the specimen. During solar cell processing parts of the ovens were the wafers are being processed can constrain the thermal expansion of the silicon wafers. Additionally, if the wafers are cooled down too fast the outside parts of the wafers tend to be colder than the inside parts. The outside colder parts of the wafers have a lower thermal expansion coefficient than the hotter parts of the wafers and they constrain the thermal expansion of the inside hotter parts of the wafer. Thus, stresses are introduced. These stresses are called thermal stresses and if they are large enough they can cause crack propagation. Specimen failure due to thermal stresses is known as thermal shock.

The maximum allowable temperature difference that a sample can stand without breaking depends on its geometry and the material properties of the sample. A flat plate subjected to a uniform temperature change can survive to in-plane thermal expansion constrain to a maximum temperature difference of [14]:

$$\Delta T_{max} = \frac{\sigma_{fr}(1-\nu)}{\alpha E} \tag{2.160}$$

where σ_{fr} is the fracture strength of the specimen. Equation (2.160) is valid for silicon wafers with sufficient thickness to prevent buckling and states that the higher the fracture strength and the lower the elastic modulus and the thermal expansion coefficient, the larger the maximum temperature difference can be.

Failure provoked by thermal shock may not be always complete and cracks may propagate some distance and stop as the thermal stress stops increasing or disappears. When cracks induced by thermal shock stop their propagation, failure of the specimen may not occur but the fracture strength of the specimen is lowered. Hasselman [82] analyzed this phenomenon and proposed a model for the calculation of the critical temperature difference that would cause incomplete crack propagation and would lower therefore the mechanical strength of the brittle specimen.

Hasselman assumed randomly distributed cracks in a solid body subjected to uniform cooling and being constrained in all directions. Silicon wafers may not be constrain in all directions but in one or two directions and therefore this model would be conservative. The critical temperature difference allowed for short cracks is:

$$\Delta T_C = \left(\frac{\pi\gamma(1-2\nu)^2}{2E\alpha^2(1-\nu^2)}\right)^{1/2} a^{-1/2} \tag{2.161}$$

2.2.2 Change of Microstructure and Failure with High Temperature Processes

When the silicon wafers are heated up during solar cell processing particles may solute according to their phase diagram, especially if their melting point is lower than the processing temperature. The impurities building the particle diffuse into the silicon matrix and the mechanical strength of the silicon wafer may increase as thermal and elastic mismatch between the particle and the wafer disappears. Additionally, the yield strength increases due to solid solution strengthening of the silicon matrix [80]. Finally after cooling another distribution of second phase particles may appear.

If the particle is not dissolved by the high temperature process, residual thermal stress in its vicinities can relax if the processing temperature is higher than the brittle-ductile temperature of silicon but thermal stresses will form again as the wafer cools down to room temperature. High temperature processes may also heal cracks existing already in the material [83] as diffusion of silicon atoms between the two faces of the crack can reduce the sharpness of the crack or heal it completely.

It is also important to discuss that when the silicon is stressed under high temperature and the particles are not dissolved it can behave like a particle reinforced metal-matrix composite. The failure types of this sort of materials are particle fracture [84], interface decohesion and matrix yielding [85].

In the case of rigid interfacial bonding, the particle can fracture when the local stress reaches the fracture strength of the particle. Cracks are prone to appear at bigger particles with high aspect ratio. Smaller particles tend to debond by interfacial decohesion, resulting in voids. Random distribution of particles undergoes less percentage of particle fracture than particle rich clustering microstructure.

Interface decohesion needs the nucleation of a crack and its propagation along the particle-matrix interface. Thermal stresses can propagate small interfacial flaws and allow particle interface decohesion. This can also occur due to matrix yielding. Yielding of the matrix near the outer particles of a cluster can form a big crack and cause failure. In random microstructure every single particle will undergo interface decohesion and this type of failure is less favored [55].

Plastic deformation is affected by microstructure and therefore by the presence of clusters of particles as explained above. The plastic strain that occurs in the matrix near a particle cluster is higher than the plastic strain that occurs in non-clustered composites. During loading, the plastic strain is accumulated around the cluster and there is less transfer of stress inside the cluster region. Thus, particle clusters can cause premature failure by void nucleation at high plastic strains. The matrix failure occurs in three stages. First, some particles fracture or debond at low strength. Second micro voids and cavities nucleate near the broken particles and finally they coalesce and lead to the failure of the matrix.

2.2.3 Failure Criteria after Microstructure Change

After solar cell processing voids caused by yielding of the silicon matrix or cracked and debond particles may be the most important type of defects controlling the mechanical strength of silicon wafers. Therefore, a failure criterion is given in this section for this case.

Green [40] suggested an expression to estimate the stress intensity factor for annular cracks at spherical voids. This expression can be used as a failure criterion for little cavities that may have formed after solar cell processing within the silicon matrix.

According to Goodier [43] the stress near a spherical void without any crack is:

$$\sigma(r) = \sigma_a \left[\frac{4 - 5\nu_{Si}}{2(7 - 5\nu_{Si})} \left(\frac{R}{r} \right)^3 + \frac{9}{2(7 - 5\nu_{Si})} \left(\frac{R}{r} \right)^5 + 1 \right] \tag{2.162}$$

The stress intensity factor of a crack at a spherical void can be calculated by solving equation (2.79) with equation (2.162):

$$K_I' = 2\sigma_a \left(\frac{a(\varphi + 2)}{\pi(\varphi + 1)} \right)^{1/2} \left[\frac{4 - 5\nu_{Si}}{2(7 - 5\nu_{Si})(\varphi + 1)^2} + \frac{3}{2(7 - 5\nu_{Si})} \left(\frac{(\varphi + 1)^2 + 2}{(\varphi + 1)^4} \right) + 1 \right] \tag{2.163}$$

where $\varphi = a/R$. For large φ values equation (2.163) approaches the solution of a stress intensity factor of an internal penny shaped crack. However, for small values of φ the solution for the stress intensity factor of an edge crack in a semi-infinite medium should be approached [86]. Therefore, equation (2.163) must be corrected in order to account the influence of the free surface of the void. For this purpose the spherical void is assumed to be subjected to an internal pressure, P, which gives rise to tensile stresses described by equation (2.49) acting across the crack surface. Substituting equation (2.49) into equation (2.79) gives the correction for the stress intensity factor:

$$K_I'' = P\left[\frac{a}{\pi}\frac{\varphi+2}{(\varphi+1)^5}\right]^{1/2} \tag{2.164}$$

For $P \cong \sigma_a$ and $K_I = K_{Ic}$, the failure criterion for small voids in the silicon matrix ($K_{Ic} = K_I' + K_I''$) stays:

$$\begin{aligned}\left(\frac{a}{\pi}\right)^{-1/2} = \frac{2\sigma_a}{K_{Ic}}\left(\frac{\varphi+2}{\varphi+1}\right)^{1/2}&\left[\frac{4-5\nu_{Si}}{2(7-5\nu_{Si})(\varphi+1)^2}\right.\\ &\left.+\frac{3}{2(7-5\nu_{Si})}\left(\frac{(\varphi+1)^2+2}{(\varphi+1)^4}\right)+1\right]+\frac{\sigma_a}{K_{Ic}}\left[\frac{\varphi+2}{(\varphi+1)^5}\right]^{1/2}\end{aligned} \tag{2.165}$$

where $a = \varphi R$.

3. Experimental Procedure

This chapter summarizes the complete experimental procedure carried out during this research. All processing conditions from the crystallization of multicrystalline silicon blocks until the manufacture of the final solar cells are explained. Material specification as well as the collection and preparation of the samples are described in detail. Next is the presentation of the different techniques for the microstructure characterization of the multicrystalline silicon samples. The final section of this chapter comprises all the techniques performed for the measurement of the most relevant mechanical properties of silicon which are mechanical strength, fracture toughness and elastic modulus. Special attention is drawn to the different bending tests for the measurement of mechanical strength, to the analysis of the values of strength with the Weibull statistical distribution and to post-mortem interpretation of fracture surfaces.

3.1 Production of Multicrystalline Silicon Blocks and Solar Cells

3.1.1 Silicon Feedstock

Five types of silicon feedstock with different purity levels were selected for crystallizing multicrystalline silicon blocks. The concentration of impurities encountered in the silicon feedstock was measured with the inductively coupled plasma optical emission spectrometry (*ICP-OES*) [87] and is summarized in Table 3.

Table 3 Concentration of impurities [ppmw] within the silicon feedstock

Material	Al	B	P	Ca	Mg	Fe	Mn	Cu
4N+Al	3634	36	-	13	1	18	1	2
3N	217	177	-	669	-	370	46	4
B-doped	0.19	154.3	0.49	0.24	0.44	0.21	0.003	<0.001
UMG-Si	0.93	3.3	9.6	0.53	0.52	0.33	0.015	0.123
SoG-Si	0.085	1	1.47	0.54	0.337	0.184	<0.001	<0.001

The *4N+Al* material contained lower concentrations of dopant and metallic impurities than the *3N* material, except for the case of Al content that was extremely high in *4N+Al* silicon feedstock. *B-doped* silicon feedstock came from the top and tail parts of Cz-Si blocks where dopants segregate during the crystallization of monocrystalline silicon. These parts of the Cz-Si blocks are disregarded for solar cell production; thus they were used in this work as inexpensive silicon feedstock. These three types of silicon feedstock are considered like “alternative dirty silicon” which will be used as material´s substrate of “epitaxial wafer equivalents” for the manufacture of epitaxial solar cells. This will be explained better in the next sections. Additional *industry standard* mc-Si and Cz-Si material was tested in this work for comparison of results.

The *UMG-Si* and *SoG-Si* feedstock contained low concentration of impurities, being the content of Al, Fe, Cu and dopants higher in *UMG-Si.* These two types of silicon feedstock were processed from the crystallization of the mc-Si blocks to final solar cells for comparison.

One crystallization process was performed with every type of silicon feedstock. Approximately 80 kg of feedstock was used per experiment, with exception of the *4N+Al* silicon. This feedstock presented a "flake like" form (see Figure 31 a)) and therefore the volume of the crucible was already filled in with only 40 kg of silicon.

The chunks of silicon feedstock were loaded in square quartz crucibles with a base area of $422 \times 422\ \mathrm{mm}^2$ (see Figure 31 b)). The crucibles are coated before they are filled in with the silicon chunks in order to prevent the sticking of the silicon block to the walls of the crucible (see Figure 33 b)) during the crystallization process and to reduce the diffusion of oxygen from the crucible. The composition of the coating was oxygen enriched silicon nitride with a thin layer of silicon dioxide on it [88]. Once the crucible is loaded with the silicon feedstock the crystallization process can take place.

a) b)

Figure 31 Image a) shows the 4N+Al "flake like" feedstock. Image b) depicts a quartz crucible coated with silicon nitride and filled in with silicon feedstock chunks.

3.1.2 Crystallization

The silicon samples tested in this work were provided, like aforementioned, from five multicrystalline silicon blocks crystallized under the same temperature profile and furnace conditions with the Vertical Gradient Freeze (VGF) method; which is a technique that is very often used for the directional solidification of mc-Si in the photovoltaic industry.

A crystallization furnace VGF 632 Si by PVA-Tepla AG was used in the facilities of the SIMTEC laboratory at Fraunhofer ISE [89] (see Figure 32) with the capacity to grow up to 280 kg silicon blocks. This furnace is provided with three heaters, at the bottom, body and cover of the furnace, in order to control the temperature field inside the furnace and therefore the growth conditions. A water cooling system is installed in the base plate of the furnace and a carbon tube introduces argon in the crystallization chamber at the desired moment during growth.

Figure 32 Crystallization furnace in SIMTEC laboratory at Fraunhofer ISE.

The loaded crucible is mounted in the crystallization furnace and a graphite crucible supports the quartz crucible (see Figure 33 a)) as quartz will be soft at the upcoming processing temperatures. The crystallization process starts with heating up of silicon above its melting point. Once the whole amount of silicon is molten, the directional solidification takes place. Heat is extracted from the bottom of the crucible by controlling and cooling the bottom heater with a cooling water system. The created temperature gradient in the melt allows the nucleation of silicon crystals at the bottom of the crucible. These crystals grow vertically, perpendicular to the crystallization front. The temperature of the body heaters is also controlled and kept lower than the temperature of the cover heater in order to keep vertical crystal growth. After the whole silicon has solidified the temperature of the heaters is gradually lowered to cool down the crystallized silicon block. During cooling a temperature of approximately 1200°C is maintained during two or three hours in order to anneal residual stresses in the block. The whole crystallization process can take between two and three days for an 80 kg mc-Si block at a crystallization speed of approximately 7 mm/h.

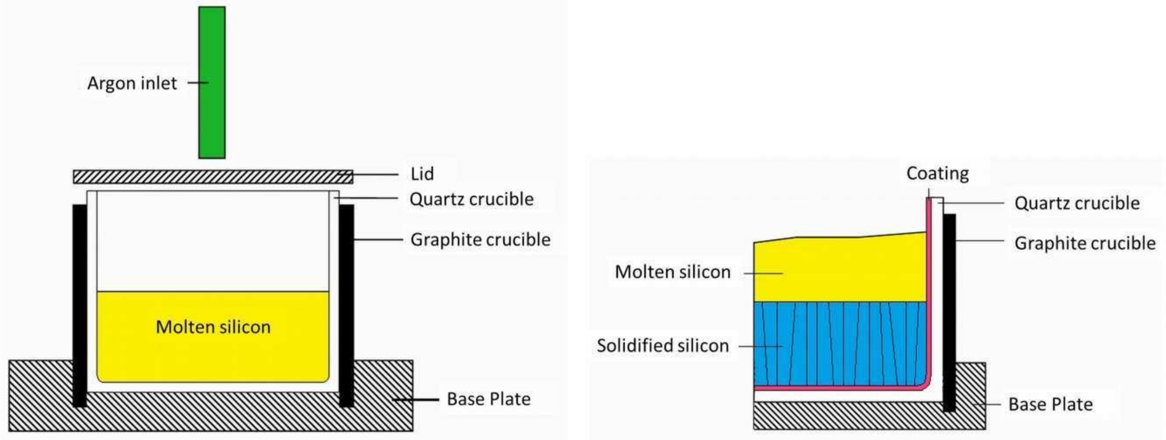

a) b)

Figure 33 Image a) shows a schematic cross section of the VGF oven. Image b) shows a detail of the coating and crucible system.

Figure 34 depicts a photo of every of the crystallized silicon blocks. The sides of the *4N+Al* and the *3N* silicon blocks show a strong reaction with the sides of the crucible which may have been enhanced by the higher content of impurities than within the other three blocks.

a) *4N+Al*   b) *3N*

c) *B-doped*

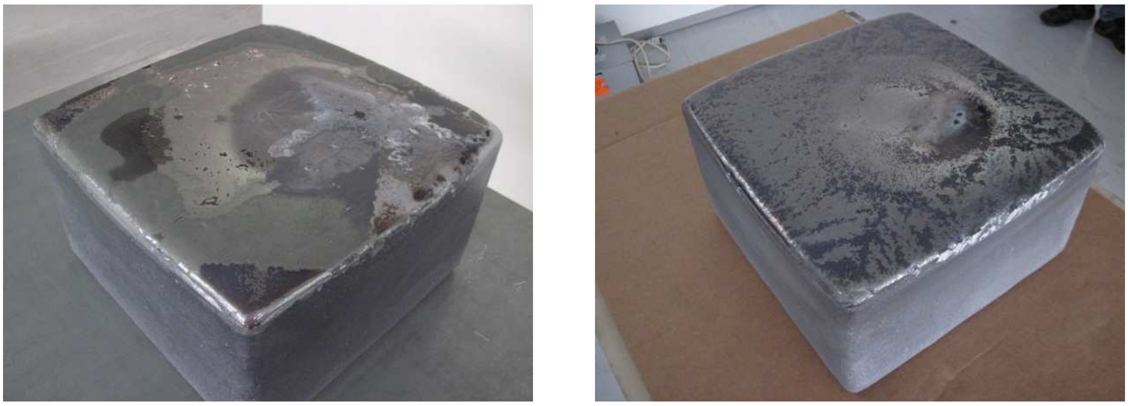

d) *UMG-Si*   e) *SoG-Si*

Figure 34 Multicrystalline silicon blocks crystallized with the different feedstock specified in the previous section.

The main sources of impurities for mc-Si blocks are the silicon feedstock itself, the quartz crucible, the silicon nitride coating and the inside of the crystallization furnace; and the most important defects which remain in the mc-Si blocks, and that could influence the mechanical properties of silicon, are dislocations, grain boundaries including twin boundaries and precipitates [90], [91].

Dislocations are line defects that originate during crystal growth as a result of plastic deformation of the crystal to release stresses. Areas with high density of dislocations present an inhomogeneous pattern within mc-Si blocks [92]. These dislocation clusters originate at the bottom of the block and extend in the growth direction and they become larger as they extend to the top of the block. The origin of dislocation clusters in the bottom of the block is not yet well understood. Possible causes are for example stress concentration at precipitates and mechanical constraint of the neighboring grains. Dislocations in multicrystalline silicon are very often decorated by oxygen and metal atoms. This influences very negatively the electrical properties of solar cells.

Area defects are grain boundaries including twins. The nucleated crystals at the bottom of the crucible grow in different directions during crystallization. When these regions, coincide with one another, they form grain boundaries. Smaller grains are located at the bottom part of the blocks where the nucleation of the crystals took place. Grain boundaries exhibit gettering effect, i.e. impurities diffuse to grain boundaries and gather there. Twin boundaries are grain boundaries that separate two grains which are a mirror image of one another.

Volume defects (e.g. precipitates and micro-cracks) are introduced during the crystal growth, during cooling after growth or during solar cell processes at high temperature. When the concentration of the dissolved impurity, either in the melt or in the solid, exceeds its solubility concentration, second phase particles or precipitates can nucleate. They precipitate normally as compounds of silicon. C and N segregate to the melt during crystallization due to their low segregation coefficients (see Table 1). If their solubility limit in the melt is exceeded large silicon carbide (SiC) and (Si_3N_4) particles can form. The precipitation of SiC and Si_3N_4 is observed inhomogeneous in areas within the middle and the top of the block. O segregates to the solid phase due to its segregation coefficient and therefore it has been observed in areas from the bottom to the middle of the block. The presence of other extended defects like dislocations and grain boundaries can act as proper nuclei for the formation of silicon oxide particles (SiO_x). On the other hand, thermal stresses due to the thermal mismatch between the particles and the silicon matrix can induce the formation of dislocations in their surroundings. This is a complicated topic which is still being researched.

3.1.3 Multi-wire Sawing

The bottom, side walls and the top of the crystallized blocks must be cut off as these parts show high concentration of impurities and therefore have deficient electrical properties. Approximately one to three cm from these parts is cut with a band saw and is disregarded. The band saw consists of a steel blade with incrusted diamond particles. During the cutting process, the blade is cooled down with water. The block then undergoes bricking with the same band saw, i.e. the block is cut into four ingots where the smaller area of the ingot is the size of the surface area of the final wafers (see Figure 35).

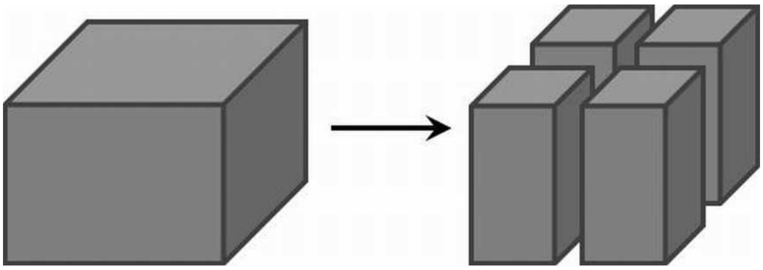

Figure 35 Sketch of a mc-Si block where a slice from the bottom, the side walls and the top has been cut off and disregarded and then the block is cut into four ingots.

After band sawing the bricks are grinded to reduce surface damage and soften edges and corners. Every silicon ingot is then cut into wafers with a multi-wire saw (Meyer-Burger D265). A steel wire is winded in the grooves of the guidance rolls of the multi-wire saw so that a wire web with constant pitch is formed (see Figure 36 a)). The silicon is loaded in the multi-wire saw and the wire web brought to motion. Two nozzles start spreading slurry on the wire web which consists of a suspension of SiC particles in Polyethylene glycol. The silicon block is pushed very slowly against the wire web and the slurry is brought into contact with the silicon thanks to the motion of the wire. When the entire cross section of the ingot has been pushed through the wire web after 6-8 hours the ingot is cut into hundreds of wafers.

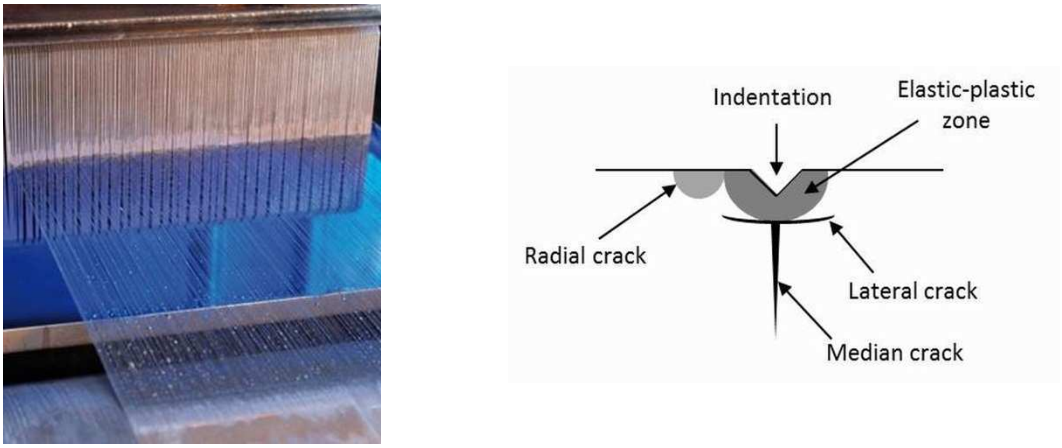

a) b)

Figure 36 Image a) shows an already cut silicon block moving out from the wire web in order to be unloaded from the multi-wire saw. Image b) depicts a sketch of the different types of cracks that can be observed under the indentation of a silicon carbide particle on the surface of a silicon wafer after the multi-wire sawing process. The picture is adapted from the literature [93], [44].

The cutting of silicon blocks into wafers is achieved by the indentation of the abrasive SiC particles on the silicon surface [93]. The particles indent the silicon surface and a remnant plastic impression is generated on the surface known as the elastic-plastic zone. Median cracks are generated beneath the plastic zone, where the stress is highest and radial cracks are generated at the edges of the plastic zone (see Figure 36 b)). When the abrasive SiC particles leave the silicon surface, the residual stress from the elastic-plastic zone can lead to lateral cracks parallel to the surface. When these lateral cracks reach the silicon surface the material is chipped away and the lateral crack disappears but median and radial cracks remain in the silicon surface. If median and radial cracks form in the same plane they may coalesce in a half-penny shaped crack which is visible from the surface [93], [44].

The *4N+Al, 3N* and *B-doped* mc-Si ingots were cut under the same cutting parameters down to approximately 280 µm wafers. *Industry standard* mc-Si and Cz-Si wafers were ~260 µm and *UMG-Si* and *SoG-Si* wafers were ~225 µm.

Additionally, 2 mm thick samples from all crystallized blocks were cut with the multi-wire slurry saw in order to accomplish geometry requirements for mechanical characterization.

After wire-sawing the wafers are dirty with the cutting slurry sticking to the silicon surface. Therefore, they are cleaned immediately after sawing in a cascade of chemical baths with an aqueous solution containing organic surfactants and low concentration of an alkaline etchant [94].

3.1.4 Epitaxial Wafer Equivalent Manufacture

The epitaxial wafer equivalent (Epi WE) is fabricated by depositing an approximately 20 µm crystalline silicon thin film by a rapid thermal chemical vapor deposition process (RTCVD) on a low cost silicon substrate [95] (see Figure 37 a)). The substrate provides a good mechanical strength while the highly pure epitaxial layer is responsible for the electrical performance of the final solar cell. Using silicon as a substrate reduces problems arising from differences in thermal expansion coefficients and misfit of lattice parameters between the substrate and the thin epitaxial layer. Moreover, as the Epi WE is made out of silicon entirely the current highly developed wafer cell technology can be performed. This alternative concept of solar cell allows the saving of the expense of considerable amount of highly pure silicon.

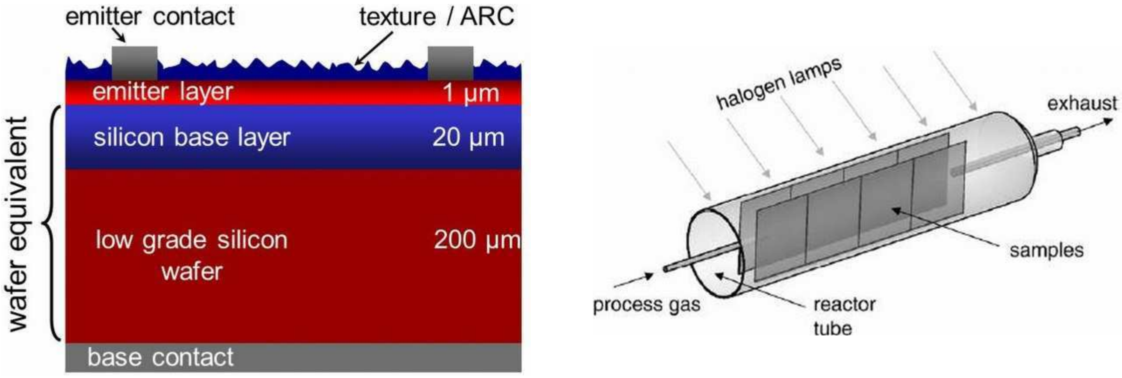

a) b)

Figure 37 Image a) depicts the scheme of an epitaxial silicon thin-film solar cell on low grade mc-Si wafer substrate. Image b) shows the basic principle of function of the RTCVD reactor [95].

Before epitaxial deposition, the *4N+Al, 3N* and *B-doped* mc-Si as-cut wafers were etched with a chemical polishing solution consisting of HF, HNO_3, and CH_3COOH. A silicon layer of approximately 10-15 µm was etched per side of the wafer in order to remove any sub-surface damage from the wire sawing.

Subsequently, the wafers were sized down to 100x100 mm^2 with a laser to process them in the RTCVD reactor [96] for the deposition of an epitaxial crystalline silicon thin film. Two lines of vertical wafers are placed in a quartz carrier which is introduced in a quartz reactor tube (see Figure 37 b)). Then the wafers were heated up optically up to 1150°C within 30 minutes. The process gas (H_2 and $SiHCl_3$) is injected into the chamber and decomposes being silicon deposited on the inner surface of the wafers between the two vertical rows. The deposition takes a few minutes as the deposition rate is 5 µm/min approximately. Finally the wafers are cooled down to room temperature so that the whole process takes one hour approximately. The heating up and cooling down temperature gradients were 100°C/min.

A group of wafers was also processed under the same conditions in the RTCVD reactor without thin film deposition in order to differentiate between the influence of the annealing of the silicon low grade substrate and the deposition of the epitaxial thin film on the mechanical strength of the final Epi WE.

3.1.5 Solar Cell Processes

UMG-Si and *SoG-Si* as-cut mc-Si wafers are processed to conventional solar cells. The term "inert cell" designates a solar cell processed from moderately purified silicon wafers (see Figure 38).

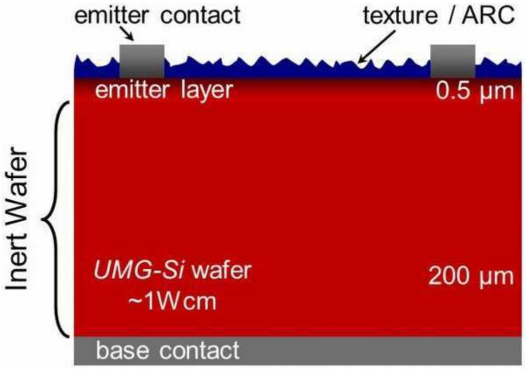

Figure 38 Sketch of an inert cell.

Texture

Solar cell processing [97] starts with the texturing of the silicon wafers. This process serves for removing saw damage, which reduces the mechanical strength of the wafers and increases electrical recombination in its surface, and for enhancing light trapping in the silicon bulk. Multicrystalline silicon is textured with an aqueous solution containing HF, HNO_3. The surface structure of the textured silicon wafers is formed by round concave grooves (see Figure 39).

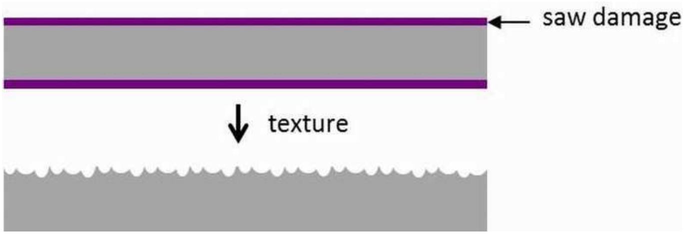

Figure 39 Schematic illustration of the texture of a mc-Si wafers.

Damage etch

Usually, the wafers are not damage etched prior to texture in the standard process sequence. However, damage etch is carried out in this study to compare saw damage removal of damage etch and texture respectively and therefore their influence on the mechanical strength of mc-Si wafers.

As-cut wafers from all the different types of mc-Si tested in this work were etched with a chemical polishing solution consisting of HF, HNO_3, and CH_3COOH. A silicon layer of approximately 10-15 µm was etched per side of the wafer in order to remove any sub-surface damage from the wire sawing. After damage etch defects formed during the crystallization process control the mechanical strength of the wafers.

Emitter Diffusion

The phosphorus emitter diffusion process is meant for the formation of the p-n junction of the solar cell. The wafers are placed in a quartz tube where n-type dopant atoms, P, are diffused at 900°C onto the surface of the p-type mc-Si wafers. Gaseous phosphorus oxychloride, $POCl_3$, and oxygen, O_2, are conducted into the heated quartz tube and phosphorus oxide, P_2O_5, deposits on the silicon surface. On the wafer surface a phosphosilicate glass (PSG) layer of approximately 100 nm is then formed and P atoms from this layer diffuse into the silicon bulk.

Figure 40 Schematic illustration of a mc-Si wafer after emitter diffusion.

Phosphosilicate Glass Etch

A chemical solution containing HF is used to remove the PSG layer. Precaution must be taken so that the emitter layer beneath the PSG layer is not etched away. The depth of the remaining emitter layer is approximately 500 nm.

Antireflection Coating

Cell efficiency is improved by the deposition of an antireflection coating on the silicon surface. This coating enhances light trapping and neutralizes open silicon bindings on the wafer surface. Hydrogenated silicon nitride (SiN_x:H) was deposited on the mc-Si wafers as an antireflection coating because of its optimal refractive index and its excellent bulk and surface passivation. The minority carrier lifetime of silicon is improved since hydrogen passivates the defects and impurities in the bulk silicon. Silicon nitride is deposited on the wafer surface by plasma enhanced chemical vapor deposition, PECVD. The plasma of the processing gasses is created by means of an electromagnetic field. The process is done at low temperature $T < 500°\text{C}$. The deposited silicon nitride layer has a thickness of *75* nm approximately and it infers a dark blue color to the wafer surface.

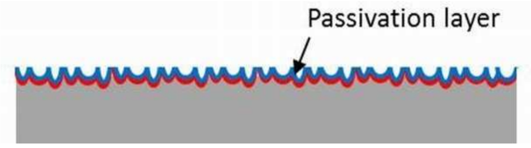

Figure 41 Schematic illustration of a mc-Si wafer after antireflection coating.

Metallization and Firing

Metallization is the formation of the metal contact onto the wafer's surface. The wafers in this work underwent metallization with the conventional screen printing technique.

The front contact consists of bus bars and fingers printed onto the SiN_x:H passivated surface. At the beginning of the metallization of the front contact, an elastic screen and the wafer are in snap off position, which means they are aligned but they are not in contact. A Ag paste is prepared in front of a squeegee on the screen. The screen starts to touch the wafer as pressure is applied to the squeegee. Then the paste is dragged and the openings of the screen are filled with the paste which sticks to the wafer surface. Then the rear side of the wafer is printed with an Al paste which covers the whole wafer surface. Finally, the rear bus bars are printed with an Ag/Al paste.

After screen printing, the front and the rear contacts are fired simultaneously. The firing furnace is provided with IR heaters that heat the wafers up to 900°C. At this temperature Al from the rear side has already melted, the back surface field (BSF) has formed and the front contacts are sintered through the passivation coating to make contact with the emitter layer. After metallization, edge isolation is achieved via laser grooving in order to avoid the short circuit as emitter diffusion also takes place at the edges of the solar cell.

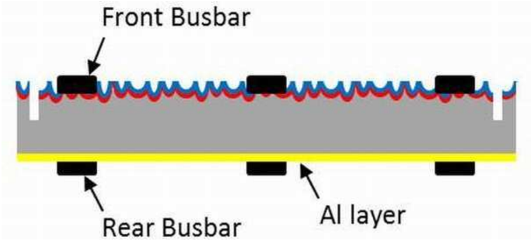

Figure 42 Schematic illustration of a mc-Si wafer after metallization.

3.1.6 Sample collection and preparation

For the mechanical characterization with the ring-on-ring bending test, ten wafers from three different positions within the blocks (top, middle and bottom parts) were collected after multi-wire sawing (see Figure 43). Except in the case of *3N* mc-Si where wafers were taken at four block positions. 10 wafers correspond to a volume of $156 \times 156 \times 3\ \text{mm}^3$

approximately, i.e. within 3 mm of block height mc-Si microstructure and mechanical properties are relatively constant so that the mechanical properties of wafer number 1 should be equal to the mechanical properties of wafer number 10.

These wafers were used for mechanical characterization with the ring-on-ring bending test, for measurement of residual stress and for microstructure inspection.

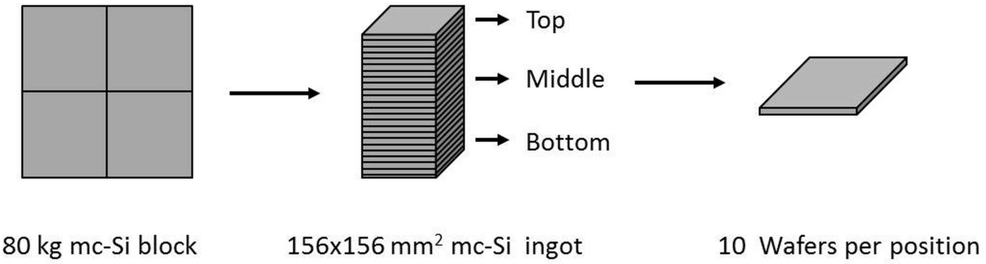

Figure 43 Scheme of the collection of mc-Si wafers for the ring-on-ring bending test.

Each of the wafers was subjected to solar cell processes. In the case of the *4N+Al, 3N* and *B-doped* mc-Si, the wafers underwent multi-wire sawing, damage etch, annealing under the same conditions of epitaxial deposition and thin film epitaxial deposition.

One $156 \times 156\,\mathrm{mm}^2$ wafer after wire saw and damage etch was lasered into 49 round silicon chips (see Figure 44 a)) in order to provide enough silicon chips for a statistical calculation of the mechanical strength with the results of the ring-on-ring bending test. This way one single wafer provides enough silicon samples to measure the mechanical strength of the material. Moreover, the analysis of the experimental data of this work showed the inhomogeneity of microstructure and thus of fractures stresses within different areas of a same single wafer. Therefore, the lasering and bending tests of the round silicon chips gives a spatial resolution of fracture stresses within one wafer.

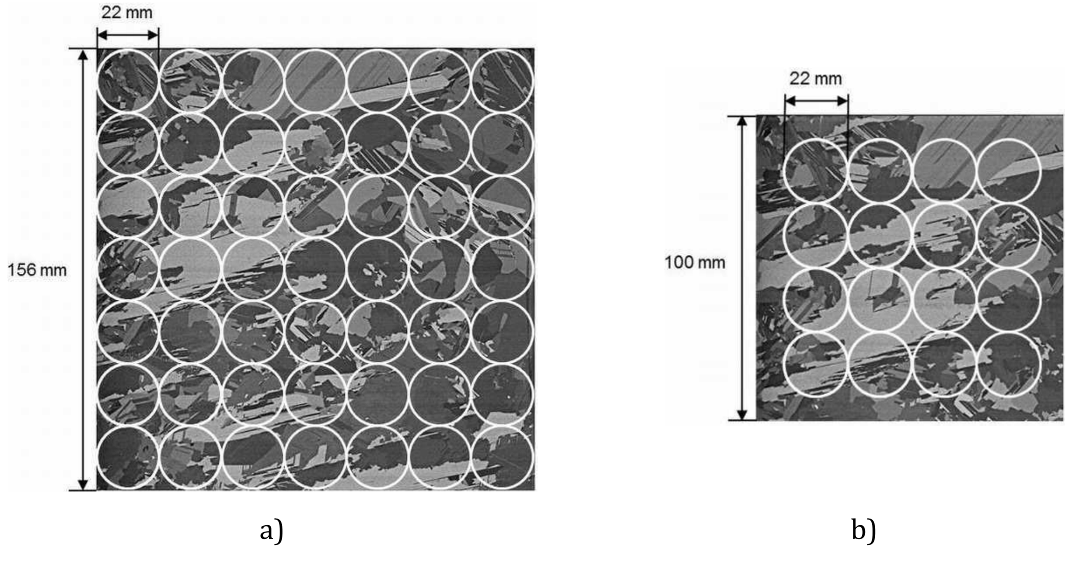

a) b)

Figure 44 Sketch of the lasering into round silicon chips for 156x156 mm² wafers (image a)) and for 100x100 mm² wafers (image b)).

The wafers that were processed in the RTCVD reactor were lasered down to $100 \times 100\,\mathrm{mm}^2$ and therefore only 16 silicon chips could be obtained per wafer (see Figure 44 b)). Thus, two $100 \times 100\,\mathrm{mm}^2$ silicon wafers per block and position underwent annealing and thin film deposition respectively, i.e. 32 round silicon chips were available for the ring-on-ring bending test after annealing and after thin film deposition.

A Nd:YAG laser emitting 1064 nm wavelength from the firm ACR GmbH was used for dicing the wafers. The intensity of the laser beam was 35 A and its frequency was 20000 Hz. It moved at a velocity of 170 mm/s and it followed the laser patterns of Figure 44 five times for cutting a ∼220 µm silicon wafer. The cutting of thicker wafers is achieved by increasing the times that the laser follows the lasering patterns.

UMG and *SoG* mc-Si were processed to conventional solar cells starting from an as-cut wafer, following texture, phosphorus emitter diffusion, PSG etch, antireflection coating and metallization. Another two groups of wafers were added to compare texture with damage etch and to check the influence of the passivation step without the influence of the previous diffusion and PSG etch.

All these wafers were lasered as sketched in Figure 44 a) with exception of the wafers processed until metallization where the metallization pattern on the front and rear sides forced us to choose another lasering scheme (see Figure 45 a)). Three vertical lines of seven circles each were lasered containing the bus bar in the middle of the round silicon chips. Two vertical lines of seven circles each were lasered from the areas between the bus bars, i.e. round chips contained thin metallic fingers but no bus bar (see Figure 45 b)). Two wafers per block and position were processed until metallization so that the mechanical strength of the front side of the solar cell can be tested with one wafer and the mechanical strength of the rear side can be tested with the second wafer.

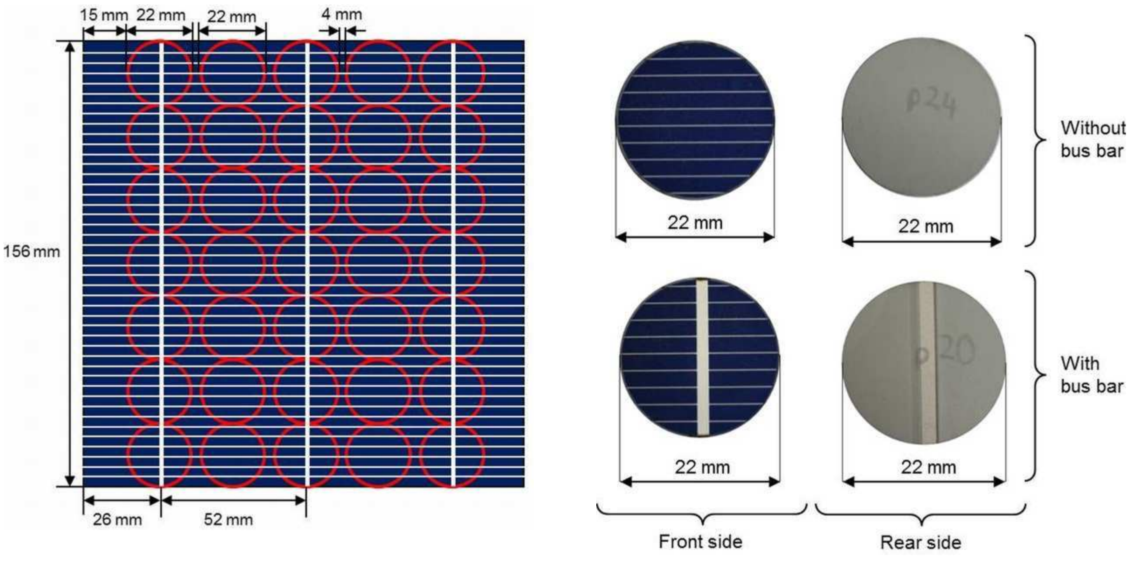

a) b)

Figure 45 Sketch of the lasering into round silicon chips for 156x156 mm^2 wafers after metallization (image a)). Silicon chips showing the front and rear sides are depicted in image b) with and without bus bars.

Other mechanical characterization techniques required thicker silicon samples, e.g. three-point bending test, fracture toughness and dynamic elastic modulus measurements.

Silicon samples with 2 mm thickness were cut with the multi-wire slurry saw from silicon columns coming from the central part of the blocks. Except in the case of *UMG-Si* where the silicon column was taken from a side wall of the block. The columns had an approximate volume of $70 \times 60 \times 200\ mm^3$. After wire sawing one sample was taken from six positions within the block (see Figure 46 a)). The samples had a volume of approximately $70 \times 60 \times 2\ mm^3$ and they were cut into 4-6 pieces with a diamond saw. These final samples had an approximate geometry of $70 \times 10 \times 2\ mm^3$ (see Figure 46 b)). Finally, the samples were strongly etched with a chemical polishing solution consisting of HF, HNO_3, and CH_3COOH in order to remove any sawing damage that lowers the mechanical strength of the samples [98] and to smooth their edges and corners.

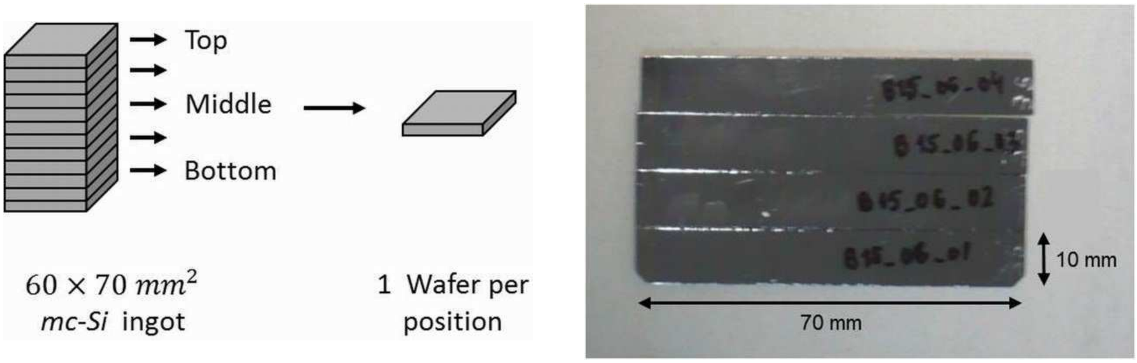

Figure 46 Scheme of the collection of mc-Si samples for the three-point bending test (image a)). 2 mm thick silicon wafer cut into 70x10 mm² samples and subsequently damage etched (image b)).

Further specific preparation of the samples will be explained in the next sections in correlation with every characterization technique.

3.2 Microstructure Analysis

3.2.1 ICP-OES

The content of impurities contained in the silicon feedstock (see Table 3) was measured by Inductively Coupled Plasma/Optical Emission Spectrometry (ICP-OES) [99], [87]. This technique measures the spontaneous emission of photons from atoms and ions that are injected and excited into a radiofrequency (RF)-induced Ar plasma.

The silicon feedstock samples weighing 1.5 g approximately are first dissolved in 20 mL of an HF/HNO_3 solution, i.e. the impurity elements to be analyzed are contained in the solution. This solution is converted into an aerosol and is then injected into a channel that ends up in a torch that contains an Ar plasma. This plasma is induced by the alternating currents inside a Cu coil that is connected to a RF-generator and surrounds the plasma torch. The inductively coupled plasma (ICP*)* sustains a temperature of approximately 10000 K at its core and thus the aerosol is vaporized immediately when it reaches the plasma. The elements contained in the aerosol sample are liberated as free atoms and ions in gaseous state. The collision of the atoms with the plasma provides additional energy to the atoms and ions to reach excited states. When these species relax to ground state they emit a photon. The wavelength of the photons can be used to identify the element by which they were emitted. Additionally the amount of emitted photons is directly proportional to the quantity of impurity elements within the sample, i.e. to their concentrations.

The photons emitted by the ICP are transferred by lenses and focused on a diffraction grating. The photons are at this point separated according to their wavelengths in the optical spectrometer. The intensity of the separated beams is measured in the optical chamber by a photomultiplier tube and converted to an electrical signal by a photodetector. The measured intensities are compared to previously measured intensities of known concentrations and the amount of the impurity elements can be thus determined.

The advantage of the ICP-OES technique relies on its capability to measure accurately more than 70 elements simultaneously at a detection limit of 0.001 ppmw.

3.2.2 Scanning Electron Microscope

The scanning electron microscope (SEM) [100] is one of the most versatile instruments available for the examination and analysis of the microstructure characteristics of solid objects from the nanometer to the millimeter scale. The popularity of the SEM is due to its capability of obtaining three-dimensional images of the surfaces of materials in the magnification range from 20 to 30000 times. The SEM offers therefore the possibility to analyze wafer surface topography, e.g. the presence of second phase particles and their composition, sawing damage morphology, crystal orientation, etc.

In the SEM, the area to be analyzed is irradiated with a finely focused electron beam which is swept across the surface of the specimen to form the image. The types of signals produced from the interaction of the electron beam with the sample include secondary electrons coming from the sample, backscattered electrons, diffracted backscattered electrons and photons (characteristic X-rays). The secondary electron and backscattered electrons emission permits images to be obtained. The three-dimensional appearance of the images is due to the large depth of field of the scanning electron microscope, as well as to the shadow relief effect of the secondary and backscattered electrons contrast. The diffracted backscattered electrons provide information on the crystalline orientation of the sample and the characteristic X-rays on its chemical composition.

The two major components of a SEM are the electron column and the control console. The electron column consists of an electron gun fitted with a tungsten filament cathode and two or more condenser magnetic lenses. The electron gun generates and accelerates electrons in the energy range 0.1-30 keV, and two or more condenser lenses focus the electron beam. The beam travels down a tube and interacts with the specimen to a depth that ranges from the nano- to the micrometer scale depending on the energy of the electron beam and the nature of the sample. The whole electron column works in high vacuum. Secondary and backscattered electrons are collected by a detector and amplified by a photomultiplier for display on a computer monitor or on a cathode ray tube for old models of SEM. The control console consists of the computer or the cathode ray tube viewing screen and the knobs and the computer keyboard that control the electron beam and the movement of the sample.

Silicon samples are enough electrically conductive to be analyzed with the SEM without depositing a conductive layer. All type of silicon samples were checked with the SEM after every solar cell processing step. A top view of the samples and a cross section helped to visualize the topography of the silicon surface.

3.2.3 Energy Dispersive X-ray Spectrometry

Energy Dispersive X-Ray Spectroscopy (EDX) [100] is a chemical microanalysis technique used in conjunction with SEM. As aforementioned in the previous section, the interaction of the electron beam of the SEM with the sample results in the emission of characteristic X-rays. This is due to the emission of electrons from the sample surface as the electron beam hits the sample. The emitted electrons leave holes which are then occupied by electrons from a higher state. Thus, an X-ray is emitted with energy equal to the energy difference between the two electrons' states. The X-ray energy is characteristic of the element that originated the emission. An energy-dispersive detector is used to separate the characteristic X-rays of different elements into an energy spectrum which is analyzed with computer software in order to determine which elements are present in the sample.

3.2.4 Transmitted Light Microscopy

Silicon, like almost all semiconductor materials, is transparent to infrared light (IR). Therefore, it can be inspected with transmitted light microscopy. Second phase particles contained in mc-Si have different optical properties than silicon and thus may not be transparent to IR light. If they absorb IR light they will be visible like dark spots. The absorption contrast between silicon and the particles allows the localization of the second phase particles.

This type of microscopy is based on the transmission of IR light emitted from a source on the back side of the specimen through the same specimen. An IR lamp generates an IR light beam that illuminates a mirror in the base of the microscope. This way the IR light beam is conducted perpendicular to the surface of the sample. After the light passes through the sample, the image of the specimen can be viewed with a charge-coupled device (CCD) camera. The table where the sample rests is motorized in the x and y axis and large areas of the silicon wafers could be scanned. The images taken from one sample were manipulated with the free imaging software “Image J” in order to visualize full $50 \times 50\,\mathrm{mm}^2$ silicon samples.

The samples must be mirror polished on both sides in order to avoid the scattering of the light due to the surface roughness and thus provide sufficient image quality. In the case of *4N+Al, 3N* and *B-doped* mc-Si after damage etch and annealing, silicon chips were lasered down to $50 \times 50\,\mathrm{mm}^2$ and polished to a mirror surface quality for inspection with a $5 \times$ objective lens. The polishing of the samples was achieved in subsequent polishing steps with a SiC paste. The processes started using a 6 µm SiC paste to grind initial rough surfaces and ended with a 1 µm SiC paste for achieving mirror surface quality. Finally the samples are slightly etched with silicic acid and rinsed off with deionized water in order to remove any

SiC particles from the samples´ surface. The inspection of the samples and the analysis of the images were performed in the TU Bergakademie together with Dr. Claudia Funke.

3.2.5 Residual Stress Measurement

Residual stress of damage etched and annealed samples from the *4N+Al, 3N* and *B-doped* mc-Si at different block heights was measured by means of transmission ellipsometry [101] in the TU Bergakademie together with Dr. Claudia Funke. The size of the damage etched samples was lasered down to $50 \times 50\ \text{mm}^2$ while the $100 \times 100\ \text{mm}^2$ annealed samples did not need to be lasered down to a smaller size. The equipment used for this measurement was a SDS-150 polarimeter with a stress resolution less than 1 kPa and $200 \times 200\ \mu\text{m}^2$ space resolution.

The measurement is based on stress-induced birefringence. Cubic crystals like silicon are optically isotropic. However, optical anisotropy, i.e. birefringence, can be induced by elastic stresses (piezo-optical effect).

The beam of an IR laser, with 1.15 µm wavelength, is conducted within the equipment through an optical element that polarizes circularly the laser beam. The circular polarized light has two perpendicular components, the ordinary and extraordinary waves. When the IR laser beam passes through the silicon sample the direction of the ordinary and extraordinary waves rotate in the directions of the two principal components of the residual stress field. The intensity of the light transmitted through the silicon sample is transformed by a rotating analyzer into a periodical sign that is detected by a photodetector. By processing this sign, the phase difference, Δ, between the polarizations along the two principal axes can be obtained. Given the value of phase difference, the maximum difference in refractive indexes, Δn, can be calculated as follows:

$$\Delta n = \frac{\Delta\lambda}{2\pi t} \tag{3.1}$$

where λ is the wavelength of the light and t is the thickness of the wafer. The magnitude of residual stress, $\Delta\sigma = \sigma_{11} - \sigma_{22}$, is proportional to the maximum difference in refractive indexes:

$$\Delta n = C\Delta\sigma \tag{3.2}$$

where C is the photo-elastic constant of the material. The value of the photo-elastic constant depends on the direction of the stress and the direction of light propagation in the crystal. C must be then expressed in terms of the components of the piezo-optical tensor, $\pi_{11}, \pi_{12}, \pi_{44}$, for different crystal orientations. Nevertheless, the calculated photo-elastic constant does not change significantly with crystal orientation [101]. Thus, the calculation of residual stress with equation (3.2) can by simplified by considering a constant value of the photo-elastic constant, $\bar{C} = 1.8 \times 10^{-11}\ \text{m}^2/\text{N}$, which introduces a relative error in the measurement not larger than 11%.

3.3 Mechanical Characterization

3.3.1 Bending Tests

Bend or flexure test is a common technique for determining the strength of a ceramic component [15]. This approach is convenient as simple specimen shapes can be used. This is particularly useful as the silicon samples to be tested can be easily machined from silicon wafers. However, attention must be given to the loading geometry, sample dimensions, friction effects at loading points and alignment.

3.3.1.1 Test Configuration

Uniaxial Bending Test

Silicon samples with 2 mm thickness (see section 3.1.6) were broken with a three-point bending (TPB) test configuration (see Figure 47) in an Instron 5866 electromechanical testing machine following the international standard ISO 14704 [102] in the Polytechnic University of Madrid together with Elena María Tejado Garrido. The sample is placed onto two supporting rods which are resting on top of two balancing semi-cylinders. Following, the loading rod is aligned with the middle point of the span between the supporting rods. The alignment of the system is stabilized by applying a low pre-load. The balancing of the semi-cylinders allows a correct alignment between the loading axis and the sample so that the sample is always perfectly perpendicular to the loading axis. Once the system is aligned, the traverse of the breaking machine in the loading axis moves down at a loading rate of 50 µm/min. The loading rod exerts stress on the sample that bends until fracture. The span between the supporting rods was 20 mm.

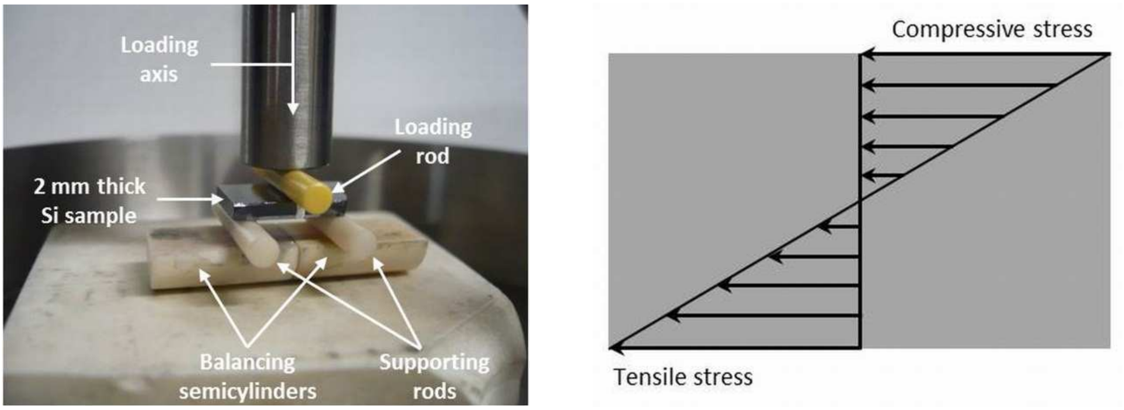

a) b)

Figure 47 TPB test configuration for the measurement of mechanical strength (image a)) and distribution of bending stress through the thickness of the sample during bending.

The thickness of the samples was much higher than the maximum deflection during bending; thus, fracture stresses were calculated with the equations of the linear fracture theory. The maximum tensile stress occurs on the bottom surface and at the center of the span where the load is applied [103]:

$$\sigma_{TPB} = \frac{3FL}{2bt^2} \tag{3.3}$$

where F is the applied load; L is the distance between supports (span); b is the width of the sample and t is the thickness of the sample.

The distribution of the bending stress through the thickness of the sample is depicted in Figure 47 b). The surface of the specimen which is in contact with the supporting rods is under maximum tensile stress (equation (3.3)). The tensile stress diminishes until it disappears at the neutral line of the sample. From the neutral line to the surface of the specimen which is in contact with the loading rod the bending stress is compressive and maximum at the surface of the specimen. The fracture of the specimens broken with a bending test is originated at the surface under maximum tensile stress and finishes at the surface under maximum compressive stress.

As specified in section 3.1.6, five silicon samples with dimensions $70 \times 10 \times 2\ \text{mm}^3$ were available per material and position within the mc-Si blocks. However, for mechanical strength measurement it is recommended to test twenty samples at least. As the length of the samples was considerably larger than the span this issue was possible to solute. The solution consisted of breaking the silicon samples first in the middle into two pieces of approximately 35 mm each. The remaining pieces are still larger than the span and can be broken again (see Figure 48) so that five bending tests could be performed with one silicon sample, i.e. Twenty to twenty-five bending tests could be performed with five silicon samples.

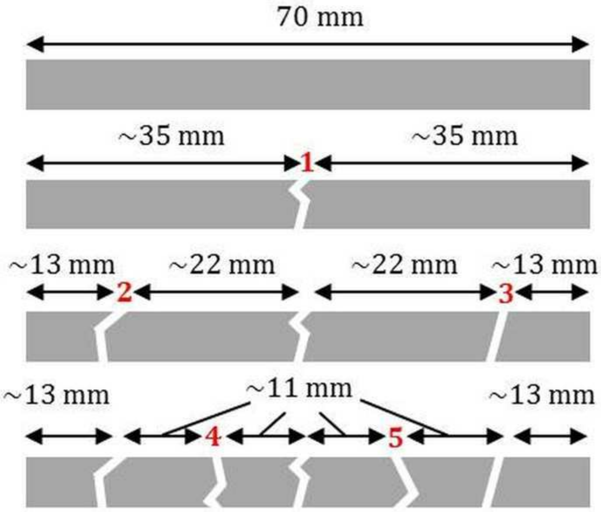

Figure 48 Scheme of the positions within the 2 mm thick silicon samples where the TPB tests were performed. The approximate dimensions of the broken samples are indicated in the image by the arrows. The red numbers indicate the order of the performed TPB tests.

Equibiaxial Bending Test

The silicon round chips (see section 3.1.6) were tested with a ring-on-ring (RoR) bending test configuration (see Figure 49 a)) in a breaking machine DO-FB0.5TS from the Zwick/Roell company following the specifications of the standard ASTM C 1499 [104]. The silicon chip is positioned on a supporting ring and loaded in the center by a coaxial loading ring. The alignment of the coaxial rings and the sample is achieved with two fixed rods on the basis of the supporting ring. In order to induce articulated loading (i.e. passive alignment), like in the case of the TPB test, a sphere is placed central on top of the loading ring, so that the silicon chip is always perpendicular to the loading axis. The diameters of the supporting and loading rings were 18 mm and 6 mm respectively (see Figure 49 b)) and the loading rate was 3 mm/min.

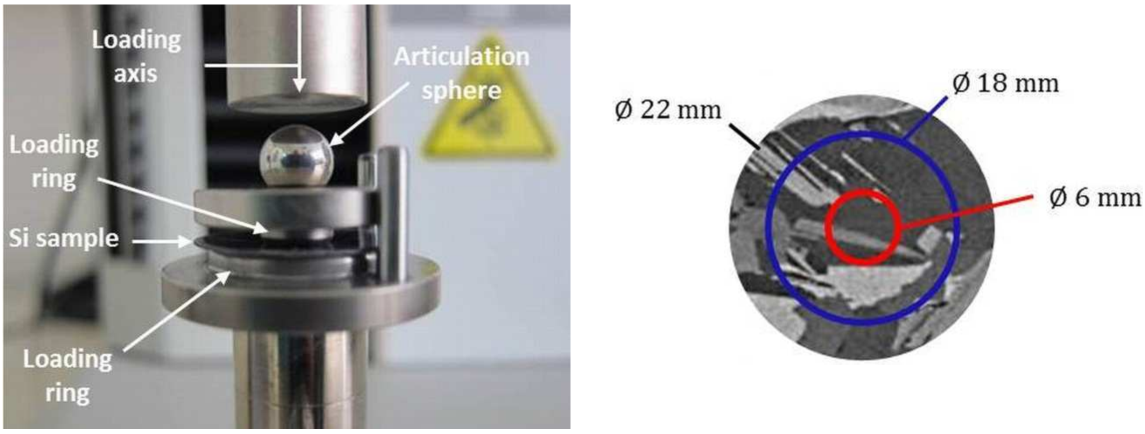

a) b)

Figure 49 RoR test configuration (image a)) and scheme of the alignment of the round silicon chip with the supporting (in blue) and loading (in red) rings (image b)).

This test configuration exerts a constant equibiaxial stress in the area within the loading ring. The surface that is to be tested is oriented to the side of the wafer under tensile stress during bending. The following equation of the linear fracture theory can be used for calculating fracture stresses with the ROR bending test:

$$\sigma_{RoR} = \frac{3F}{2\pi t^2}\left[(1-\nu)\frac{D_S^2 - D_L^2}{2D^2} + (1+\nu)\ln\frac{D_S}{D_L}\right] \tag{3.4}$$

where F is the applied load, t is the thickness of the silicon chip, D_S is the supporting ring diameter, D_L is the loading ring diameter, D is the diameter of the silicon chip and ν is the Poisson´s ratio of the sample.

The thickness of the silicon chips was in the same range of the values of maximum deflections during the bending test. Thus, the equation of the linear fracture theory could not be applied in this work for calculating fracture stresses with the RoR bending test. Instead, the maximum principle stresses at which the wafers broke were calculated from the measured force-displacement curves. For this purpose, the TU Bergakademie Freiberg used the Finite Element program Ansys.

The calculation of the static elastic modulus of the samples tested with the RoR bending test was allowed by the performed Finite Element analysis.

The silicon chips were attached to a sticking plastic film on the side of the samples to be subjected to compressive stress in order to keep all broken pieces together after testing for further fractography analysis of the surface of the samples subjected to tensile stress.

The advantage of the RoR over the TPB test is the avoidance of the loading of the edges of the sample. The influence of the defects at the edges of the samples on the measured mechanical strength is then excluded and only the material surface is tested. Thus, this method is more sensible to the material quality. On the other hand, the loading geometry of the TPB test allows an easier calculation of fracture stresses and an easier localization of the defects causing fracture when performing fractography analysis of the broken samples.

The RoR bending test on the 49 silicon chips lasered from a $156 \times 156\ \mathrm{mm}^2$ silicon wafer gives a spatial resolution of the mechanical strength of the wafers that will be analysed in the next sections.

3.3.1.2 Weibull Statistics

The measured fracture stresses of a group of identical ceramic specimens, i.e. coming from the same material and equally processed, typically scatter considerably. This is due to the scatter in size, position and orientation of the defects causing failure. Moreover, the distribution of fracture stresses is asymmetrical about the mean and therefore fracture stresses do not fit the conventional Gaussian distribution [14].

This issue is handled by statistical treatment of the values of fracture stresses with the two-parameter Weibull distribution [105] based on the weakest-link theory. The basic premises of this model are that all materials contain randomly distributed defects, that fracture initiates at the largest defect, i.e. the weakest-link of material, and that rupture of the weakest-link of material implies the failure of the whole specimen. The probability of failure of a silicon sample according to this model is given by the cumulative Weibull distribution function:

$$P_f = 1 - exp\left(-\frac{\sigma}{\sigma_\theta}\right)^m \tag{3.5}$$

where P_f is the fracture probability of the wafer under an applied load σ. The parameter m is the so called “Weibull modulus” that describes the internal distribution of defect lengths in the material. A high value of m means that the defect lengths, and thus the failure stresses of the tested specimens (silicon wafers), are within a narrow scattering band; while small m values indicate a broad distribution. σ_θ is the “characteristic stress” of the wafers which is given as the load level at which 63% of a group of comparable wafers failed. The characteristic stress is considered to be a representative value for the mechanical strength of the group of tested specimens.

Fracture stresses were fitted to the Weibull distribution by means of the maximum-likelihood method [106], [14]. If n strength measurements with results σ_i $(i = 1, \dots, n)$ are performed, the probability of obtaining a certain σ_i is p_i. Thus, the probability of obtaining the complete set of measurements, P, is:

$$P = \prod_{i=1}^{n} p_i \tag{3.6}$$

The maximum-likelihood estimates, $\hat{m}$ and $\widehat{\sigma_\theta}$, are the ones that maximize *P.* For this purpose we take the logarithm of P which is a monotonically increasing function of P and it is more convenient to maximize.

$$\ln P = \sum_{i=1}^{n} \ln p_i \tag{3.7}$$

At the same time p_i can be calculated by differentiating the cumulative Weibull distribution function with respect to the stress:

$$p_i = \left(\frac{dP_f}{d\sigma}\right)_{\sigma=\sigma_i} = m\frac{\sigma_i^{m-1}}{\sigma_\theta^m} exp\left[-\left(\frac{\sigma_i}{\sigma_\theta}\right)^m\right] \tag{3.8}$$

The logarithm of P as a function of p_i is maximized by taking its partial derivatives with respect to $\hat{m}$ and $\widehat{\sigma_\theta}$ and by equaling them to zero:

$$\frac{\sum_{i=1}^{n} \sigma_i^{\hat{m}} \ln \sigma_i}{\sum_{i=1}^{n} \sigma_i^{\hat{m}}} - \frac{1}{n}\sum_{i=1}^{n} \ln \sigma_i - \frac{1}{\hat{m}} = 0 \tag{3.9}$$

$$\hat{\sigma}_\theta = \left[\left(\sum_{i=1}^{n} \sigma_i^{\hat{m}}\right)\frac{1}{n}\right]^{1/\hat{m}} \tag{3.10}$$

Equation (3.9) can be solved iteratively to obtain the maximum-likelihood estimate of the Weibull modulus, $\hat{m}$. The maximum-likelihood estimate of the characteristic stress, $\widehat{\sigma_\theta}$, can be obtained by introducing the calculated value of $\hat{m}$ into equation (3.10).

The Weibull modulus estimate exhibits statistical bias. This means that if the mechanical testing is repeated many times to create a distribution of values of $\hat{m}$, this distributions is not centered on the true population parameter, m, but is highly biased. The amount of statistical bias decreases with increasing amount of tested specimens. The unbiased estimate of the Weibull modulus, $\hat{m}^U$, is obtained by multiplying $\hat{m}$ by an unbiasing factor (UF) [107]:

$$\hat{m}^U = \hat{m} \times UF \tag{3.11}$$

Table 16 in Appendix B provides the list of UF with respect to the amount of tested specimens.

The calculated characteristic stress estimate is considered already an unbiased estimate of the true population parameter, σ_θ, as its associated statistical bias is minimal. In the case of repeating many times the testing of 20 specimens, $\hat{m}$ shows a statistical bias of $\cong 7\%$ while $\widehat{\sigma_\theta}$ presents a bias $< 0.3\%$.

The values necessary to construct confidence bounds of the maximum likelihood estimates are based on percentile distributions obtained for each maximum-likelihood estimate [107]. The 90% confidence bounds on the Weibull modulus and the characteristic stress are then obtained from the 5 and 95 percentile distributions of q and t respectively. The values of q

and t are listed in Table 17 and Table 18 of Appendix B according to the amount of tested samples.

The upper and lower confidence bounds for $\widehat{m}^U$ and $\widehat{\sigma_\theta}$ are calculated as follows:

$$\widehat{m}_{upper} = \frac{\widehat{m}}{q_{0.05}} \tag{3.12}$$

$$\widehat{m}_{lower} = \frac{\widehat{m}}{q_{0.95}} \tag{3.13}$$

$$\hat{\sigma}_{\theta_{upper}} = \widehat{\sigma_\theta} exp\left(-\frac{t_{0.05}}{\widehat{m}}\right) \tag{3.14}$$

$$\hat{\sigma}_{\theta_{lower}} = \widehat{\sigma_\theta} exp\left(-\frac{t_{0.95}}{\widehat{m}}\right) \tag{3.15}$$

The results of the Weibull analysis of the fracture stresses measured in this work are summarized in detail in Appendix E and F. Weibull parameters with their confidence bounds are presented in table format while the cumulative Weibull distribution function (equation (3.5)) and the experimental values of fracture stresses are presented graphically (see the example depicted in Figure 50). The y axis of the cumulative Weibull distribution function corresponds to fracture or failure probability and the x axis to fracture stresses. The experimental fracture probability associated to the experimental values of fracture stresses is assigned to each sample, after ordering the values of fracture stresses in increasing order, as follows:

$$P_f(\sigma_i) = \frac{i - 0.5}{n} \tag{3.16}$$

Where n is the total number of tested specimens and i is the number of the sample.

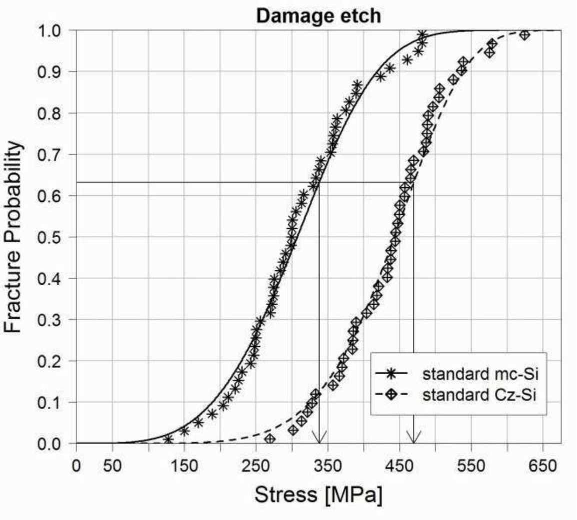

Figure 50 Cumulative Weibull distribution function of standard mc-Si and Cz-Si after damage etching. The points represent the experimental values of fracture probability and stresses while the lines represent the two-parameter Weibull distributions fitted to the experimental values. The arrows indicate the values of their corresponding characteristic stresses.

The nearer the experimental points are to the calculated cumulative Weibull distribution function the better the experimental data fits to the Weibull distribution.

Larger specimens have more probability of containing large defects. Therefore, the calculated characteristic stress is dependent on the volume of material tested, i.e. on the dimensions of the specimen. The standard ASTM C 1683-08 [108] proposes several expressions for calculating size scaled Weibull parameters. This practice allows the comparison of Weibull parameters between groups of specimens with different geometries or dimensions. These calculations were not considered in this work as all samples tested either with the TPB or the RoR bending test had the same dimensions.

The calculation of the Weibull parameters and the graphical representation of the cumulative Weibull distribution functions in this work were performed by two routines written with R [109] (Appendix C and D respectively) in order to optimize the handling of the big amount of data.

3.3.1.3 Fractography

Fractopgraphy is the examination of fracture surfaces to determine the cause and mechanism of failure [14], [110]. Cracks tend to propagate perpendicular to the maximum tensile principal stress. The crack path near the fracture origin provides therefore information on the stress configuration at the moment of failure.

Even though failure starts from a single crack brittle failure usually results in many broken fragments. This is due to the crack branching phenomenon. When the crack starts to grow, the energy release rate of the crack also increases which accelerates crack propagation. When the energy release rate reaches twice the amount of the critical energy release rate of silicon, $G = 2G_c$, the crack splits into two branches. Additionally, at high velocity of crack propagation the stress distribution at the crack tip is disturbed without sufficient time to establish a quasi-static stress field at the crack tip which also enhances crack branching. Strong specimens release more elastic energy when they fracture. Therefore, samples that break into many fragments show high mechanical strength.

Crack branches usually point back to the fracture origin but there are other features of fracture that can be observed on the fracture cross section of the specimen and that can provide information on crack growth direction (see Figure 51).

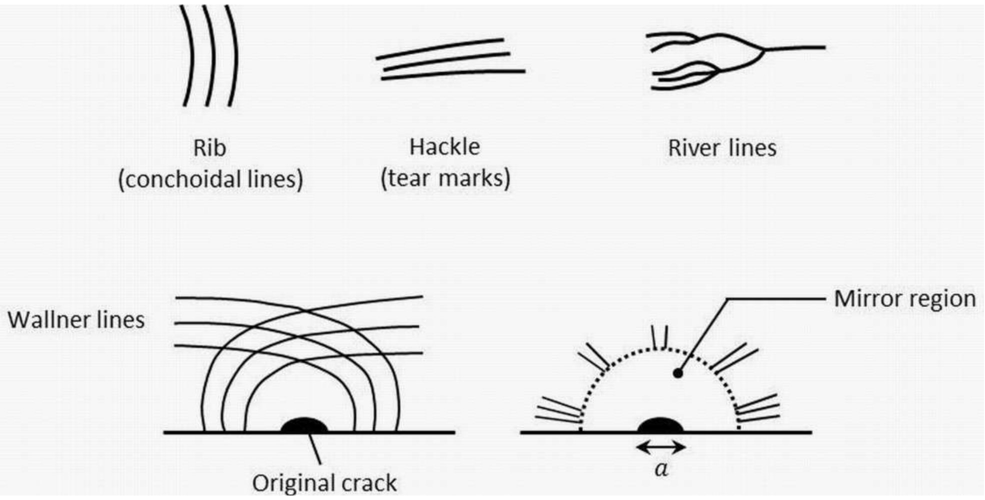

Figure 51 Qualitative features of fracture surfaces in silicon adapted from [111].

“Rib” or conchoidal lines are perpendicular to the direction of crack growth and show instantaneous locations of the crack front. They are always bowed away from the fracture origin and are caused by slight deviations of the crack front away from the plane of fracture [111].

“Hackle” or tear marks are parallel to the crack growth direction and are formed as the propagating crack branches.

Crystals tend to fracture through crystalline planes with low fracture energy; they are cleavage planes. If the cleavage plane is oriented perpendicular to the maximum principal tensile stress the resulting fracture surface is flat. However, if the cleavage plane shows another orientation, fracture still starts along the cleavage plane but the crack may abruptly change direction when it senses the presence of another more favorable cleavage plane for its propagation. When this occurs cleavage steps are formed in the direction of crack growth. When this steps form one after another a “river pattern” can be visible in fractography.

When the crack front is extending it may find other defects. A stress wave is transferred to the material when the crack approaches the defect. The intersection of the stress waves with the crack front leads to a slight disturbance of the principal stresses and therefore, to a slight deviation of the crack path visible as “Wallner lines”.

Flat “mirror surfaces” usually surround the fracture origin. Within this area the crack propagates some extent until it branches and hackle lines are formed pointing at the initial crack.

The measurement of the size of the flaw causing failure can predict the value of fracture stress. A macroscopic failure criterion for samples broken with the TPB test can be applied to fractographical images following Lawn [44]. The premises to consider in order to apply this failure criterion are that fracture is caused by a surface defect, that the defect causing fracture is located at the surface under maximum tensile stress, that the defect exhibits a semicircular shape with radius c, and that processing residual stresses do not exist:

$$K_{Ic} = 1.29\sigma_f\sqrt{c} \tag{3.17}$$

Bansal [112] suggested another failure criterion for samples that fractured due to a semielliptical flaw.

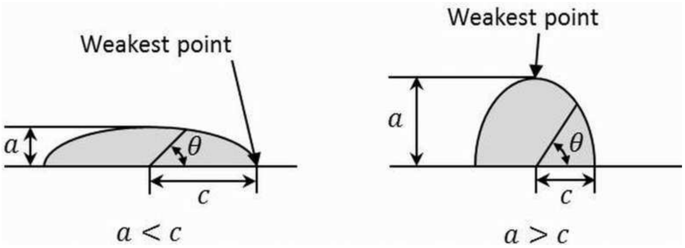

Figure 52 The two types of semielliptical flaws.

The failure criterion of Bansal is derived from the expression of the stress intensity factor of an elliptical flaw proposed by Irwin [113]. This expression assumes that the flaw is much smaller than the dimensions of the specimen and that it exhibits brittle behavior. The stress intensity factor is maximum at $\theta = \pi/2$ for $a < c$ and at $\theta = 0$ for $a > c$. Thus, when the stress intensity factor reaches its critical value fracture occurs at the areas marked as "weakest points" in Figure 52.

The Bansal failure criterion is expressed by the following equation:

$$\sigma_f \approx \frac{1.68}{Y}\frac{K_{Ic}}{A^{1/4}} \tag{3.18}$$

where $Y \cong 2.0$ and $A = \pi ac/2$ is the area of the semielliptical flaw. Equation (3.18) introduces a maximum error of 5% in calculating the fracture stress associated with the semielliptical flaw.

Ritter et al. [114] suggested some modifications of the failure criterion of Bansal in order to take residual stresses and flaw linking into account. In the presence of a localized residual stress a crack may extend on application of an external load and stable crack extension occurs prior to failure [115] [116].The failure stress under these conditions is:

$$\sigma_{fr} = \frac{1.68X}{Y}\frac{K_{Ic}}{A^{1/4}} = X\sigma_f \tag{3.19}$$

where σ_{fr} is the measured fracture stress, σ_f is the fracture stress in the absence of residual stress and X is a constant. X is equal to 0.47 for the residual stress introduced by an ideal indentation crack. X can be larger if partial relief of the residual stress occurs by the formation of lateral cracks or chipping. In the absence of residual stress X is unity.

In many cases flaw linking occurs prior to catastrophic failure so the correlation between strength and flaw size in terms of the extension of an isolated flaw is often inadequate [117]. When the distance between two flaws is in the same order than the flaw size, they may link at a lower stress level than the one necessary to propagate a single flaw. In that case, the fracture stress is determined either by the stress necessary for the flaws to link or by the stress necessary to propagate the larger created flaw.

Two important cases for flaw linking in ceramics must be considered. The first one is the coalescence of flaws in a coplanar array and the second is the linking of a subsurface pore or particle less rigid than the matrix with a surface flaw. In both cases the stress intensity factor of a given flaw is increased:

$$\sigma_{fr} = \frac{1.68}{YI}\frac{K_{Ic}}{A^{1/4}} \tag{3.20}$$

where I is the interacting parameter which can be roughly estimated. For coplanar through cracks [38] and crack spacing less than 50%, I begins to increase considerably. When crack spacing is 10% I can get a value of 2. In the case of sub-surface pores, the factor I can be as high as 4 for pores that are within 10% of their size from the surface [114].

In either case, the flaw-linking stress, σ_L, is governed by the flaw-linking stress intensity factor, K_{Ic}^*:

$$\sigma_L = \frac{1.68}{YI}\frac{K_{Ic}^*}{A^{1/4}} \tag{3.21}$$

3.3.2 Fracture Toughness Measurement

Bending tests of pre-cracked specimens, also known as “three-point bending test single-edge notch beam”, is a common procedure to measure toughness of ceramics. This type of measurement is relevant because there are no measured values of toughness of multicrystalline silicon, containing different types of impurities, in the literature. Samples with 2 mm thickness were broken and prepared in order to measure the toughness of the same multicrystalline silicon samples that that were broken with the TPB test. Thus, toughness was measured in the Polytechnic University of Madrid at six positions within the silicon blocks. A notch was introduced on one side of the samples with a steel-diamond wire (Ø 130 μm). The length of the notches was measured at five different positions with a profile projector with a magnification of 50 × and the medium value was considered as the notch length. This length of the notches varied between 200 and 500 μm, which is not relevant for our purpose. The samples were broken with a TPB where the notch in the sample was carefully aligned with the central loading rod of the rigid ceramic testing device (see Figure 53). The span between the supporting rods was 10 mm so that the largest broken pieces from the TPB of approximately ~13 mm length (see Figure 48) were used for this measurement.

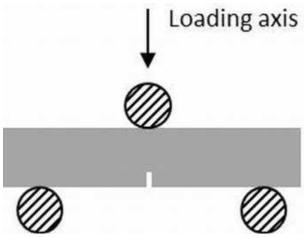

Figure 53 Three point bending test single edge notch beam test configuration for toughness measurement.

Guinea et al. [118] proposed a simple and general expression for calculating stress intensity factors from the values of maximum load and length of the notches. These expression can be used for any crack length and for any span-to-depth ratio (L/t) larger than 2.5.

$$K_I = Y\sigma\sqrt{t} \tag{3.22}$$

where t is the thickness of the sample. For the three-point bending single-edge notch beam test σ can be calculated with equation (3.3). The geometry factor, Y, for any crack length and for any span-to-depth ratio larger than 2.5 can be calculated with the following equation:

$$\begin{aligned} Y = \frac{\sqrt{\Lambda}}{(1-\Lambda)^{3/2}(1+3\Lambda)} \Big\{ & (1.99 + 0.83\Lambda - 0.31\Lambda^2 + 0.14\Lambda^3) \\ & + \frac{4}{\Omega}[(3.89 + 1.24\Lambda + 0.20\Lambda^2 - 0.03\Lambda^3))] \Big\} \end{aligned} \tag{3.23}$$

Where $\Lambda = a/t$ is the crack-to-depth ratio and $\Omega = L/t$ is the span-to-depth ratio; being a the length of the introduced notch in the specimen.

Disagreement between toughness and strength values can be caused by different size scales of the cracks that cause fracture in both types of measurements [58]. Whether increased toughness increases reliability must be thoroughly checked.

3.3.3 Dynamic Elastic modulus Measurement

Elastic constants can be determined by static and by dynamic methods. A static measurement of the elastic modulus can be performed with the TPB or the RoR bending test by calculating the slope of the stress-strain or force-displacement curve. Dynamic methods can achieve a greater accuracy than static methods with relative ease [14]. They comprise resonance and ultrasonic wave propagation and they are a non-destructive technique.

The macroscopic dynamic elastic modulus of the samples was measured in the Polytechnic University o Madrid prior to the bending tests with the resonance method. Elastic materials like silicon show specific mechanical resonant frequencies that are determined by the elastic modulus, mass and geometry of the test specimens. Therefore, the dynamic elastic properties of an elastic material can be calculated if the geometry, mass and mechanical resonant frequencies of the samples can be measured [119]. Resonance methods can be used with any shape of samples but are most often used with flexure and torsion modes of vibration of bars and cylinders.

First the mass and exact dimensions of the samples were measured. The samples then were placed onto two anti-vibration supports and the vibration of the sample is excited by exerting a mechanical impulse with a small steel ball on the middle of the length of the beam (see Figure 54). The resonant frequency of the sample beam is measured by a piezoelectric sensor which is in contact with the sample and recorded in the display of an oscilloscope connected to the sensor. Given the mass, geometry and resonant frequency of the samples the dynamic elastic modulus can be calculated, in the flexural mode of vibration and with the GENEMOD software following the calculations suggested in the ASTM E1876-09 standard [119].

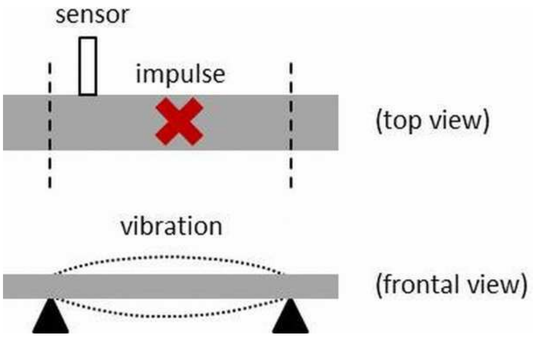

Figure 54 Scheme of the measurement of the mechanical resonant frequency of a multicrystalline silicon sample beam for obtaining the dynamic elastic modulus of silicon.

In the case of flexure resonant frequency of a rectangular bar, the dynamic elastic modulus can be calculated as follows [120]:

$$E = 0.9465 \frac{m_b f_f^2}{b} \frac{L_b^3}{t^3} T_v \tag{3.24}$$

where m_b is the mass of the bar; b is the width of the bar; L_b is the length of the bar; t is the thickness of the bar; f_f is the fundamental resonant frequency of the bar in flexure $[Hz]$; and T_v is the correction factor for the flexure vibration mode.

$$\begin{aligned} T_v = 1 + 6.585(1 + 0.0752v + 0.8109v^2)\left(\frac{t}{L_b}\right)^2 - 0.868\left(\frac{t}{L_b}\right)^4 \\ - \left[\frac{8.340(1 + 0.2023v + 2.173v^2)\left(\frac{t}{L_b}\right)^4}{1.000 + 6.338(1 + 0.1408v + 1.536v^2)\left(\frac{t}{L_b}\right)^2}\right] \end{aligned} \tag{3.25}$$

The material must be considered homogeneous and isotropic for this measurement. The material can be considered homogeneous when the geometrical dimensions of the sample are large with respect to the size of individual grains, particles pores and micro-cracks. The material can be considered isotropic on a macroscopic scale when it is homogeneous and grains, particles, pores and micro-cracks are distributed randomly.

4. Experimental Results I

This chapter focuses on the influence of second phase particles on the mechanical properties of mc-Si. Experimental values of mechanical properties measured at different relative heights within the mc-Si blocks crystallized from alternative silicon feedstock are presented and discussed. Metals segregate at the top of the block, induce spontaneous micro-cracking and introduce high thermal stresses. Amorphous silicon oxide particles at the bottom part of the blocks significantly reduce the mechanical strength and fracture toughness of mc-Si due to both thermal and elastic mismatch with the silicon matrix. On the other hand, silicon oxide crystallites induce a remarkable toughening effect in silicon due to large compressive residual thermal stress in their surroundings and their small size. Silicon nitride particles reduce fracture toughness and cause failure by radial cracking in its surroundings due to its thermal mismatch with silicon. Finally, silicon carbide particles increase fracture toughness and the elastic modulus of mc-Si. Additionally, the mechanical strength of mc-Si can increase when the radius of the silicon carbide particles is smaller than approximately 10 μm.

4.1 Calculation of Fracture Stresses and Stress Distribution

Bending tests provide the values of force at which the silicon samples broke and the displacements of the central point of the samples. The relation between force and displacement is not linear in the case of the RoR tests (see Figure 55 a)) as the thickness of the wafers is in the same order of magnitude than the displacement values, i.e. the wafers bend beyond linear elastic mechanical behavior due to their low thicknesses.

The red force-displacement curve in Figure 55 a) shows a final fracture force of 4.6 N and 62 μm displacement. In this case, the displacement is approximately one fourth of the thickness of the sample and the shape of the force-displacement curve indicates linear fracture behavior. The comparison of the Weibull distributions (see Figure 55 b)) obtained by statistical treatment of fracture stresses calculated with linear fracture equations and finite element analysis corroborates the linear elastic behavior of the sample, i.e. fracture stresses and both Weibull distributions are almost equal.

The solid black line in Figure 55 a) corresponds to a silicon sample that broke at 51 N and 365 μm. The bending of the force-displacement curve (see Figure 55 a)) indicates deviation from linear elastic mechanical behavior. The shift between the Weibull distributions and fracture stresses in Figure 55 b) depicted by the solid lines and the circle symbols respectively proves that calculation of fracture stresses with the equations of the linear fracture theory overestimates the values of fracture stresses due to non-linear elastic behavior. Therefore, the calculation of fracture stresses with finite element analysis at these values of fracture forces, displacements and sample thicknesses is of extreme importance for accurate mechanical characterization of the silicon samples.

The dashed line in Figure 55 a) is the force-displacement curve of a silicon sample that broke at 76 N and 481 µm. The deviation from linear elastic behavior of this curve is even stronger than in the latter case. This is proven by a larger shift between the Weibull distributions and fracture stresses that can be observed in Figure 55 b) depicted by the dashed lines and the square symbols respectively. It is thus, corroborated that larger deflections translates into stronger non-linear elastic behavior of the silicon samples and therefore to more inaccuracy in the calculation of fracture stresses with the equations of the linear fracture theory.

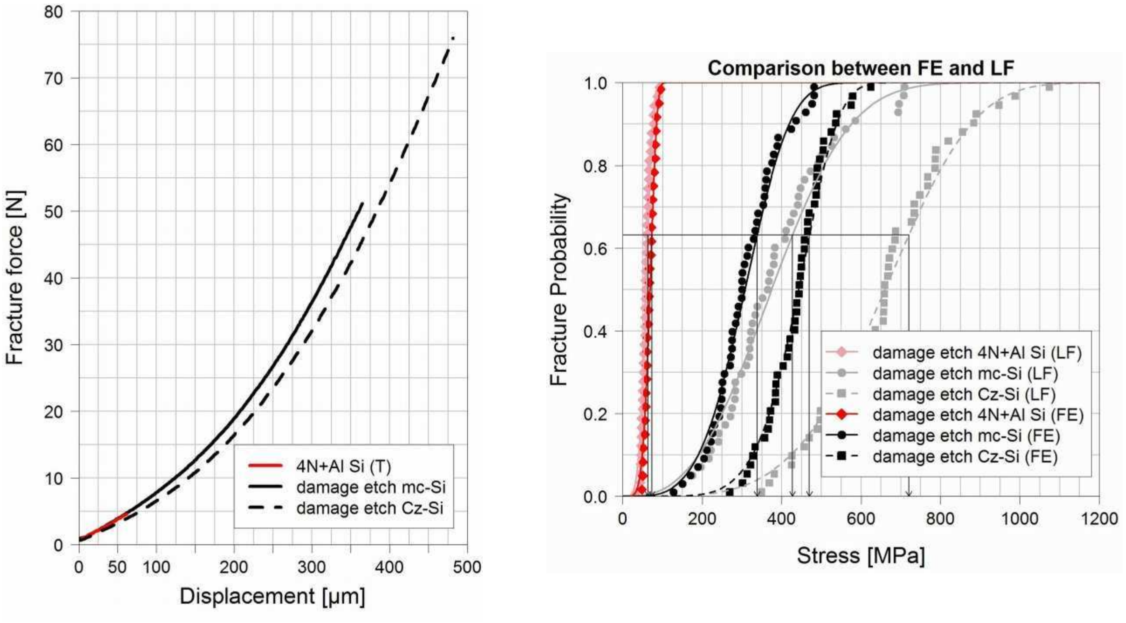

a) b)

Figure 55 Image a) shows typical force-displacement curves of round samples obtained from damage etched industry standard mc- and Cz-Si and top (T) of the 4N+Al silicon block broken with the RoR test. Image b) compares cumulative Weibull distribution functions obtained after linear fracture (LF) and finite element (FE) calculation of equibiaxial stresses of damage etched industry standard Cz- and mc-Si wafers and 4N+Al silicon at the top of the block (T) broken with the RoR test.

Figure 56 a) compares typical force-displacement curves obtained with the TPB and RoR tests. In the case of TPB testing, the samples were 2 mm thick and linear elastic mechanical behavior was preserved.

Fracture forces were larger for TPB than for RoR tests. However, the proper calculation of fracture stresses that takes into account the thickness of the samples and the treatment of fracture stresses by means of the Weibull distribution (see Figure 56 b)) indicate that the same type of material exhibits a higher mechanical behavior when it is tested with the RoR rather than with the TPB test.

Different test configurations can lead to different measured values of mechanical strength as different test configurations exert different stress fields, load different material surface sizes and activate different defect populations. The RoR bending test applies an equibiaxial stress field on the silicon samples that activates only surface defects and the TPB test loads the sample uniaxially and activates surface and edge defects. Therefore, the comparison of mechanical strengths between the RoR and the TPB is not of great meaning but the comparison of different types of materials broken with the same technique.

The advantages of the RoR test are that the mechanical strength of mc-Si can be measured with just one single $156 \times 156\,\mathrm{mm}^2$ wafer and that the material quality can be tested independently to edge defects. However, fracture patters of silicon samples broken with the RoR are extremely complicated to analyze as the samples break into too many pieces being the fracture origin almost impossible to find.

The main advantage of the TPB test is the easiness of fractography analysis as the samples mostly break into two pieces leaving two fracture surfaces. Additionally, fracture criterions are analyzed and developed in much greater detail for uniaxial loading than for equibiaxial loading.

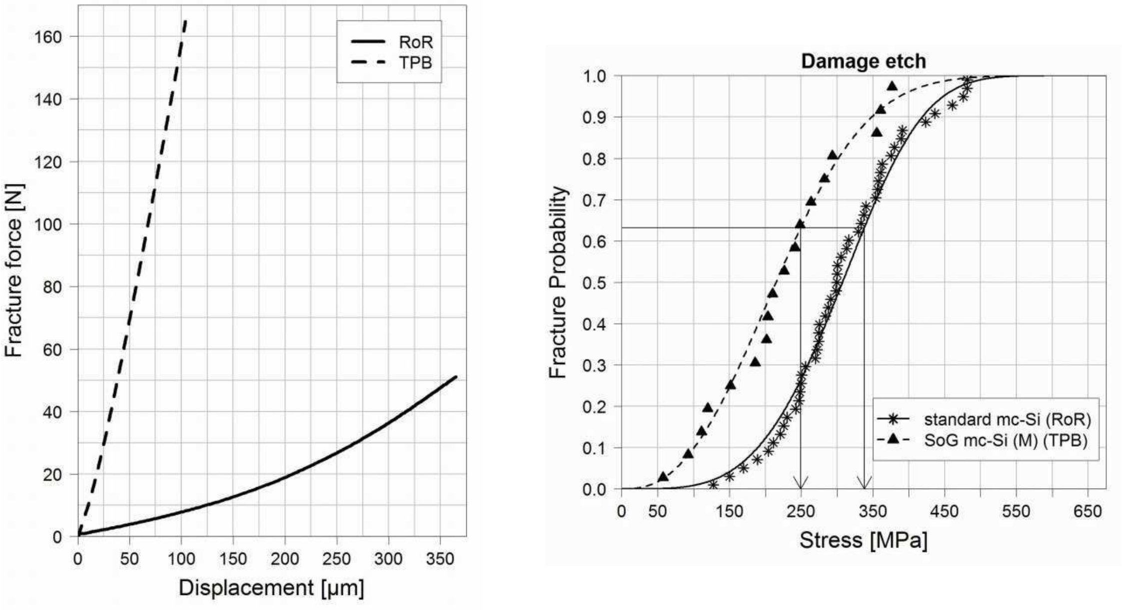

a) b)

Figure 56 The graph in image a) depicts typical applied force during TPB and RoR tests against the deflection at the central point of SoG mc-Si samples after damage etching. Image b) shows the comparison between the cumulative Weibull distribution functions of the SoG mc-Si sample.

As indicated by the Weibull distributions and by the fracture stress map in Figure 57 a), the distribution of fracture stresses within one wafer is broad. The wide distribution of fracture stresses is due to a wide distribution of defect magnitudes. The stress maps of damage etched mc-Si wafers did not reveal a distinct pattern in order to make conclusion statements. However, a slight tendency was observed and it was that silicon samples containing big grains showed higher mechanical strength than silicon samples containing smaller grains and twins [121]. This could be due to the fact that a higher amount of grain boundaries within one silicon sample increases the chances of the presence of residual stresses and particles that could be formed at grain boundaries. Nevertheless, this statement is not robust as the opposite situation, where samples containing big grains that showed lower mechanical strength than samples containing smaller grains and twins, was not the exception.

Figure 57 b) and c) show fracture patters of silicon surfaces that needed high and low energy to break with the RoR bending test and thus their measured fracture stresses were high and low respectively. When the samples can store a high amount of energy until fracture it breaks into many pieces. On the other hand, samples that fracture at low stresses break into a few big pieces.

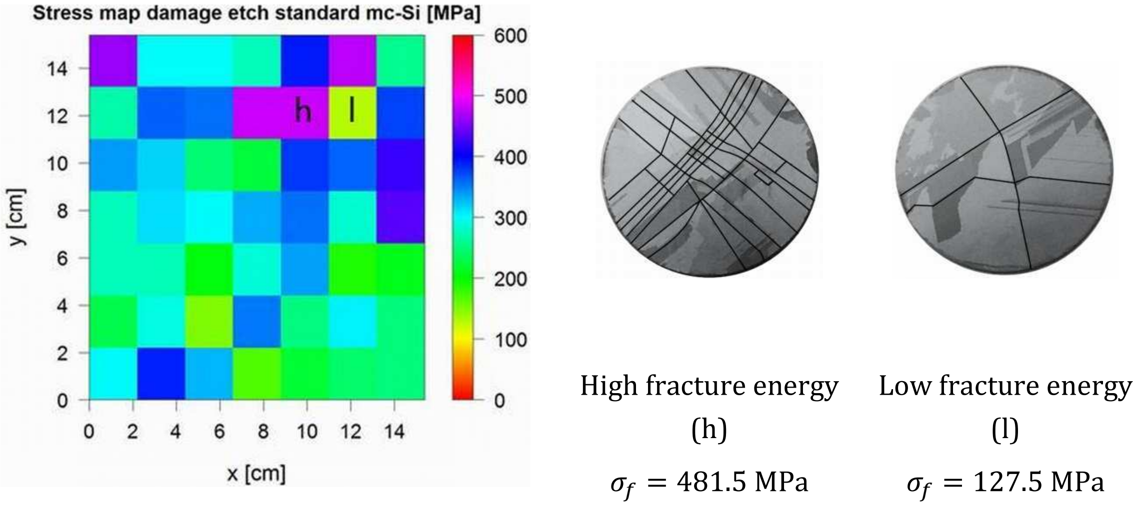

High fracture energy (h) $\sigma_f = 481.5$ MPa

Low fracture energy (l) $\sigma_f = 127.5$ MPa

a) b) c)

Figure 57 Image a) shows the map of fracture stresses of an industry standard mc-Si wafer after damage etch. Images b) and c) are photos of the surfaces under tensile stress of two round silicon chips that broke at high and low stress levels respectively. The black lines are a guide to the eye for the recognition of the fracture pattern.

Mechanical characterization with the RoR test was performed on approximately 12 neighboring wafers per block position. Every wafer underwent different solar cell processes in order to compare the mechanical strength of the wafers after every process. Therefore, it is of interest to check if the defect distribution and thus the mechanical strength of the wafers change within approximately 1 cm of the block height.

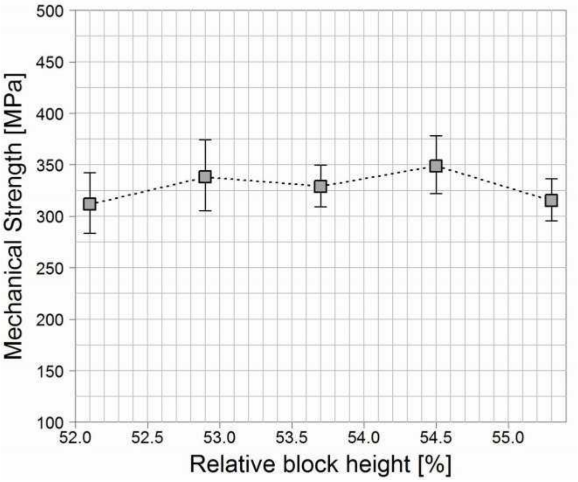

Figure 58 Characteristic stress at five different positions within the UMG mc-Si block.

Figure 58 shows the values of characteristic stress of five mc-Si wafers after damage etch. The first wafer is separated from the last wafer by 14 consecutive wafers, i.e. the distance between the first wafer to the last wafer is 6.4 mm which corresponds to a separation of 3.2% of relative block height. The characteristic stress deviates approximately a maximum range of 30 MPa within 6.4 mm of block height, thus only difference between characteristic stresses after different solar cell processes larger than 30 MPa are relevant.

4.2 Relation between Mechanical Properties and Relative Block Height

As explained in section 3.1.6 five mc-Si blocks were crystallized with different qualities of silicon feedstock. The segregation of impurities during the crystallization process induces the precipitation of different types of second phase particles at certain block heights. Thus, the quality of mc-Si depends on the relative position within the block and its mechanical strength must be tested at different relative block heights. The silicon samples selected for analyzing the influence of the crystallization process on the mechanical properties of mc-Si are damage etched samples where micro-cracks from the sawing process were removed and therefore, the mechanical properties of the silicon samples are governed by the microstructure of the material.

4.2.1 Aluminum Rich Multicrystalline Silicon (*4N+Al* mc-Si)

Results depicted in Figure 59 show the tendencies of mechanical strength, Weibull modulus, toughness and elastic modulus against relative block height in the case of *4N+Al* mc-Si.

Both mechanical strengths, measured with the RoR and the TPB tests, decrease in the direction bottom to top of the mc-Si block, while the Weibull modulus does not exhibit any dependency with the relative block height. The values of the Weibull modulus are relatively low which means that the distribution of defect sizes is wide.

Until approximately 60% of the relative block height the fracture toughness of *4N+Al* mc-Si increases slightly and the elastic modulus remains constant. On the other hand, both mechanical properties decrease significantly at the upper part of the block.

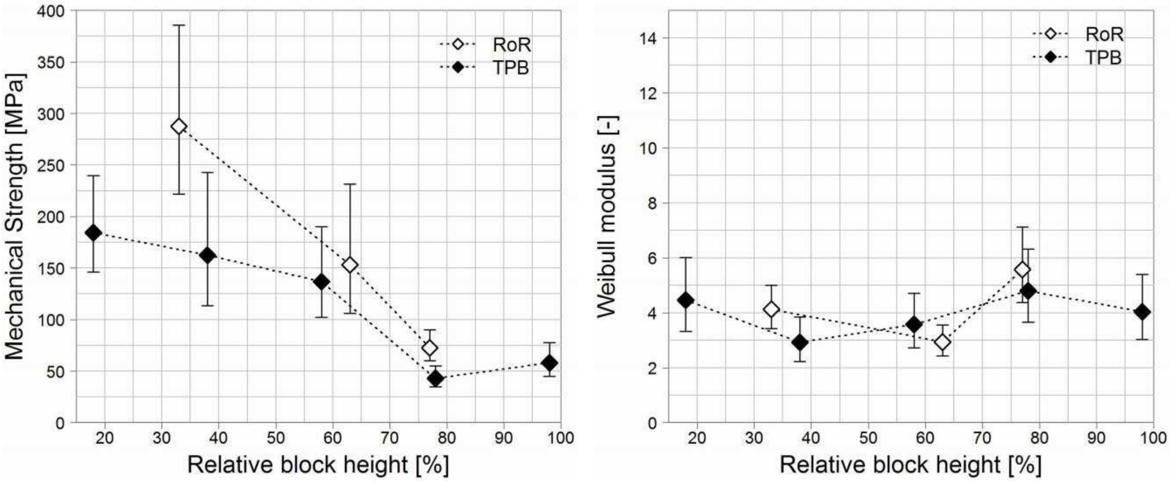

a) b)

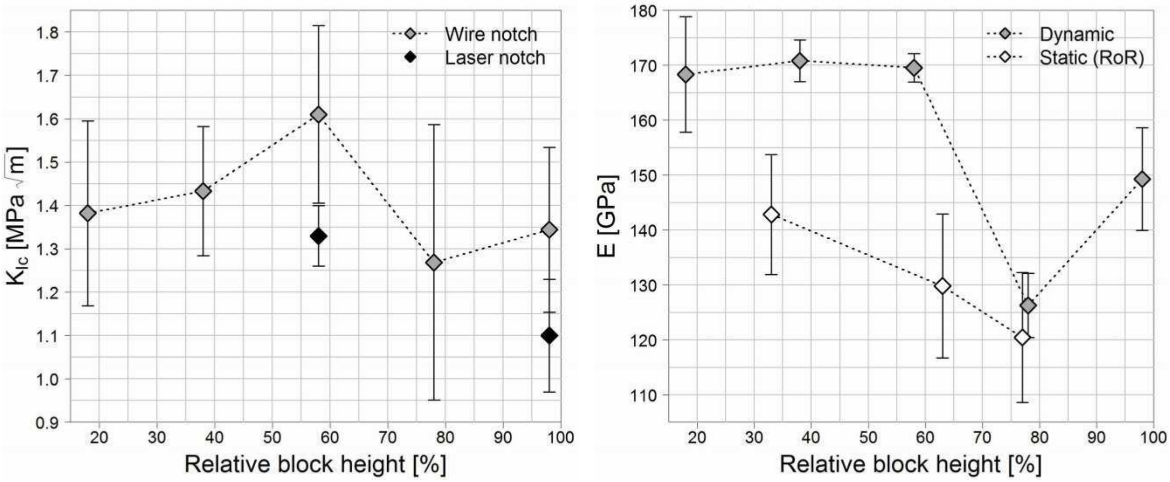

c) d)

Figure 59 Characteristic stress and confidence bounds a), Weibull modulus b), fracture toughness c) and macroscopic elastic modulus d) against relative block height for 4N+Al mc-Si.

The values of fracture toughness measured with the laser introduced notch are approximately 12% lower than the values of fracture toughness measured with the wire introduced notch. The tips of the laser introduced notches were much sharper (approximately two orders of magnitude) than the tips of the wire introduced notches (see Figure 60) and therefore they were more sensible to stress intensification at the notch tip. The roundness of the wire introduced notches is proven to overestimate the measured values of fracture toughness, but the tendency of fracture toughness related to the relative block height can still be contrasted and analyzed.

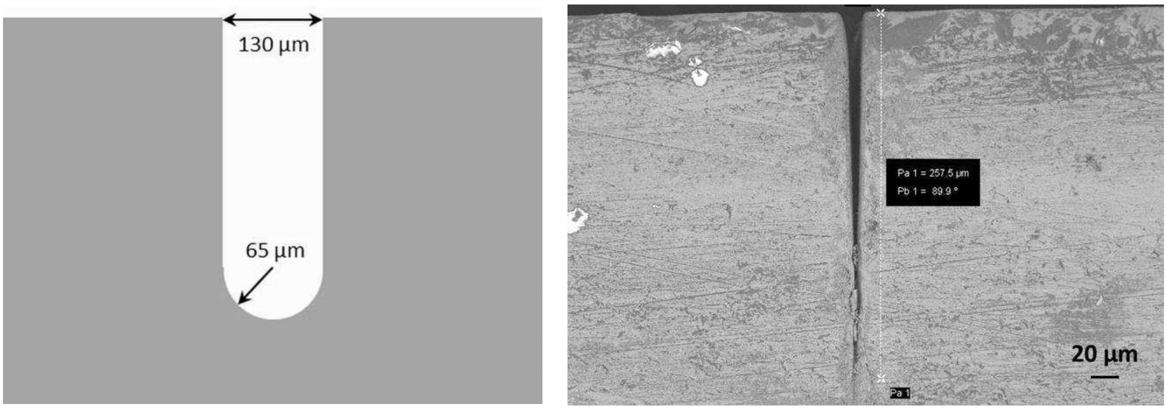

a) b)

Figure 60 Image a) is a sketch of the geometry of a wire introduced notch and image b) depicts a cross section of a laser introduced notch.

The calculated static elastic moduli are also approximately 12% lower than the measured dynamic elastic moduli, an effect dependent on the measurement technique and also reported in the literature.

4.2.2 Metallurgical Grade Multicrystalline Silicon (*3N* mc-Si)

The mechanical strength at the bottom of the *3N* mc-Si block measured with the RoR bending test was considerably lower than the mechanical strength of the upper parts of the block (see Figure 61 a)). A relatively low mechanical strength was also measured at 25% and 79% of the relative block height with the TPB test. As in the latter case, the values of calculated Weibull modulus are low and do not show any dependency with the relative block height.

Low values of fracture toughness are measured at 25% and 40% of the relative block heights (see Figure 61 c)), but these values must be taken carefully as only two samples were available at these block heights for fracture toughness measurements. The highest tested position of the *3N* mc-Si block (79%) experienced a moderate decrease in relative fracture toughness and elastic modulus.

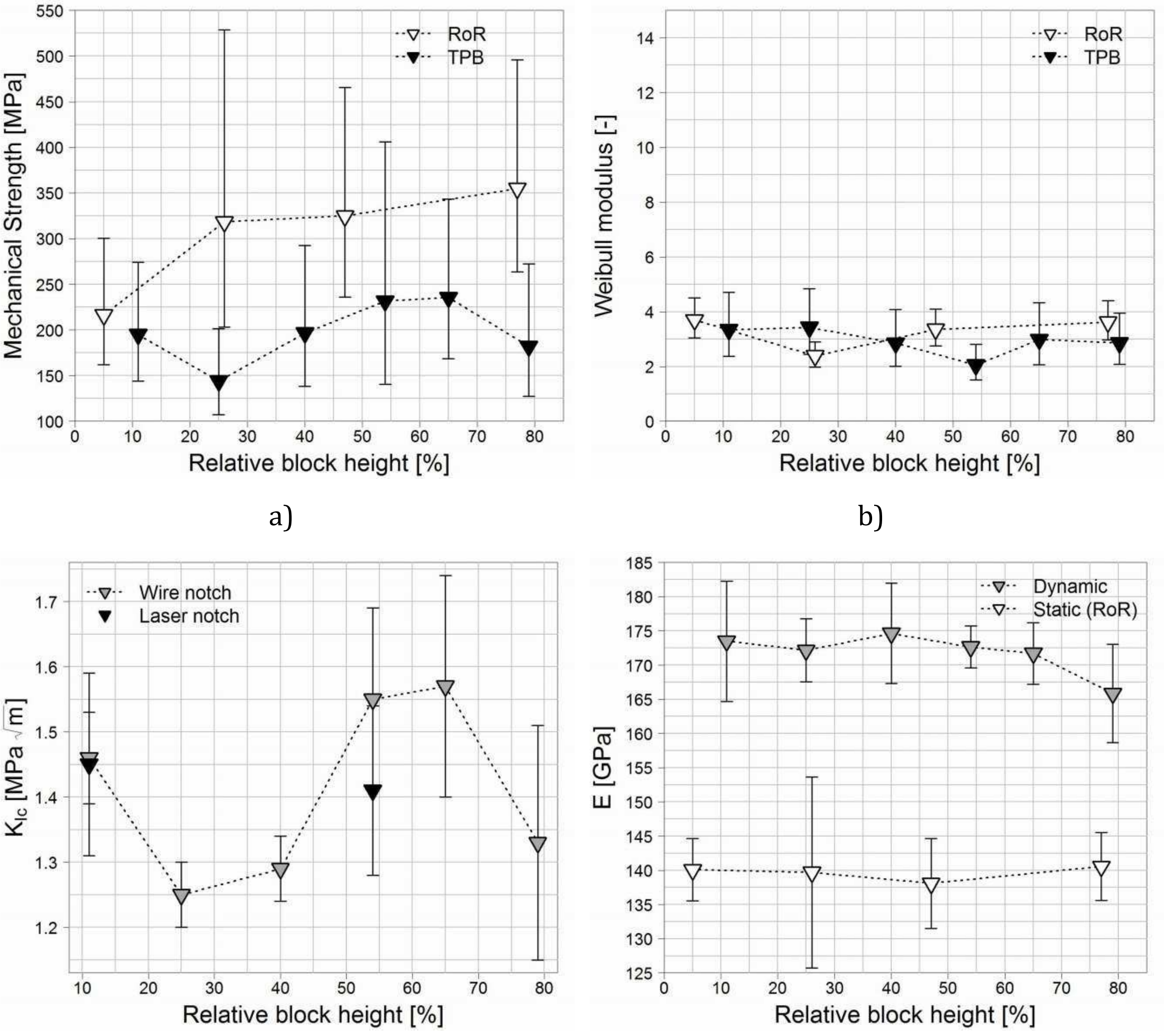

a)

b)

c)

d)

Figure 61 Characteristic stress and confidence bounds a), Weibull modulus b), fracture toughness c) and macroscopic elastic modulus d) against relative block height for 3N mc-Si.

4.2.3 Boron doped Multicrystalline Silicon (*B-doped* mc-Si)

The values of mechanical properties of *B-doped* mc-Si remain high through the whole block height. To be noticed is that the fracture toughness and elastic modulus show opposite tendencies at the top of the block. Additionally, a correlation between mechanical strength and fracture toughness is not observed as it would be expected. Samples with lower fracture toughness show comparable mechanical strength than samples with higher fracture toughness.

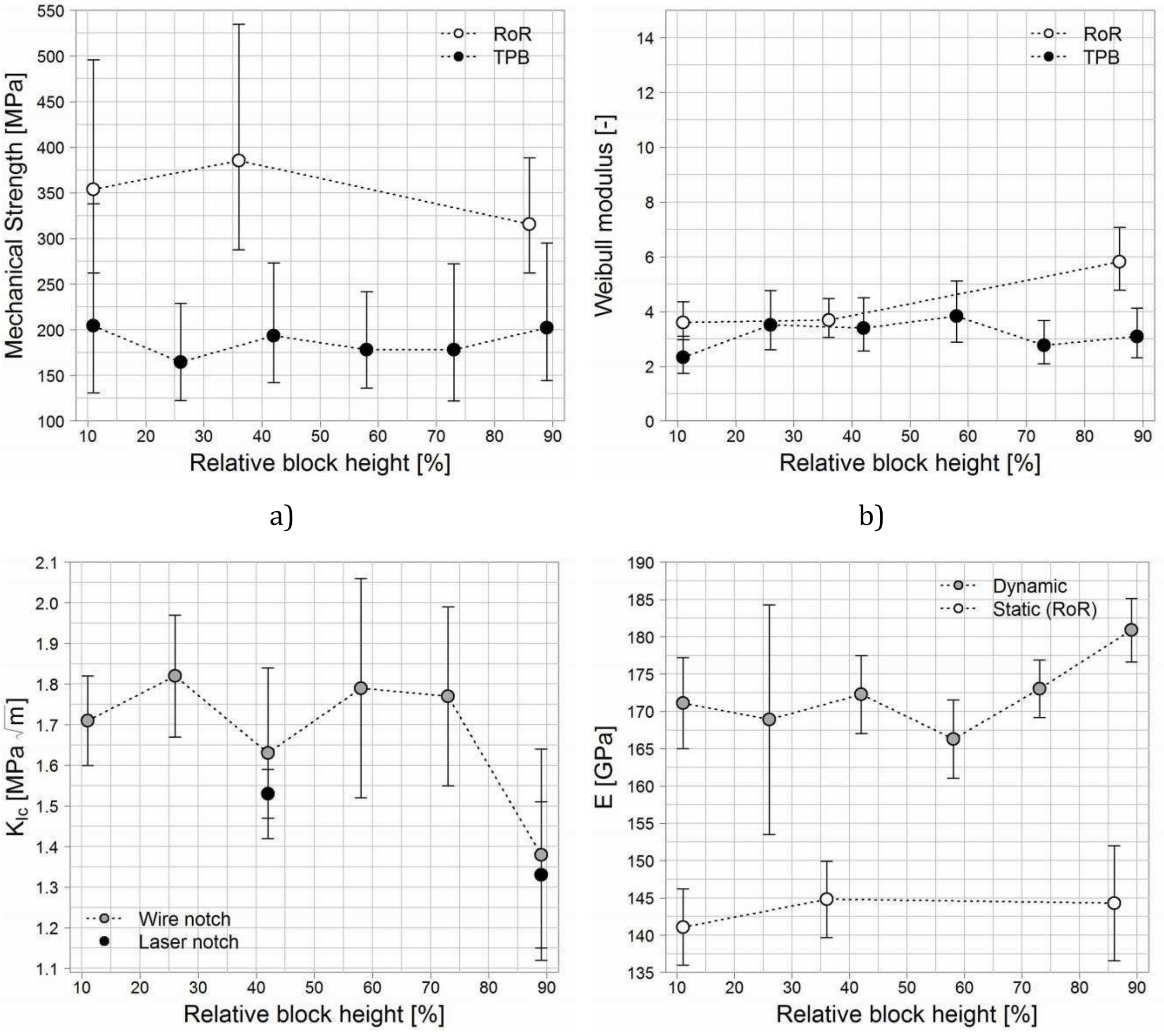

a) b)

c) d)

Figure 62 Characteristic stress and confidence bounds a), Weibull modulus b), fracture toughness c) and macroscopic elastic modulus d) against relative block height for B-doped mc-Si.

4.2.4 Up-graded Metallurgical Multicrystalline Silicon (*UMG* mc-Si)

The mechanical strength of *UMG* mc-Si is slightly lower at 7% of the relative block height for the RoR bending test and at 41% and 93% for the TPB test (see Figure 63 a)). The values of the Weibull modulus remain basically constant through the block height.

The measured fracture toughness of *UMG* mc-Si is low compared to the toughness measured with other mc-Si blocks, while the values of elastic modulus are in general high for silicon.

The decrease in fracture toughness from 41% of the relative block height to the top of the block is very significant (see Figure 63 c)).

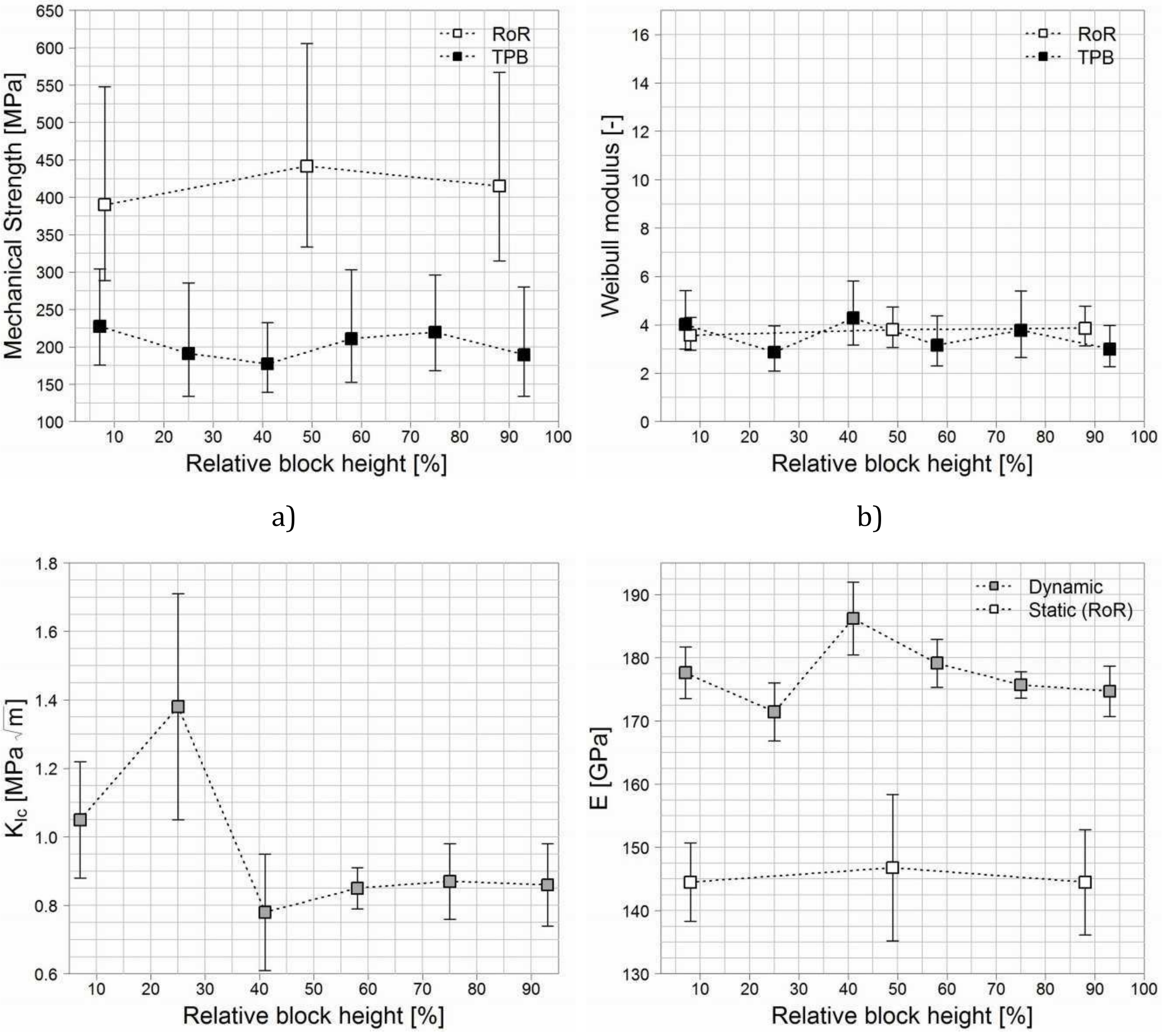

a) b)

c) d)

Figure 63 Characteristic stress and confidence bounds a), Weibull modulus b), fracture toughness c) and macroscopic elastic modulus d) against relative block height for UMG mc-Si.

4.2.5 Solar Grade Multicrystalline Silicon (*SoG* mc-Si)

The mechanical properties of *SoG* mc-Si are very acceptable in comparison with the mechanical behavior of lower quality mc-Si blocks.

The fracture toughness and the elastic modulus exhibit a slight increasing tendency from bottom to the top of the block (see Figure 64 c) and d)). Fracture toughness decreases at the very top of the block (86% of the relative block height) and the mechanical strength slightly increases from the bottom of the block until 38% of the relative block height where it starts decreasing until the very top of the block (see Figure 64 a)).

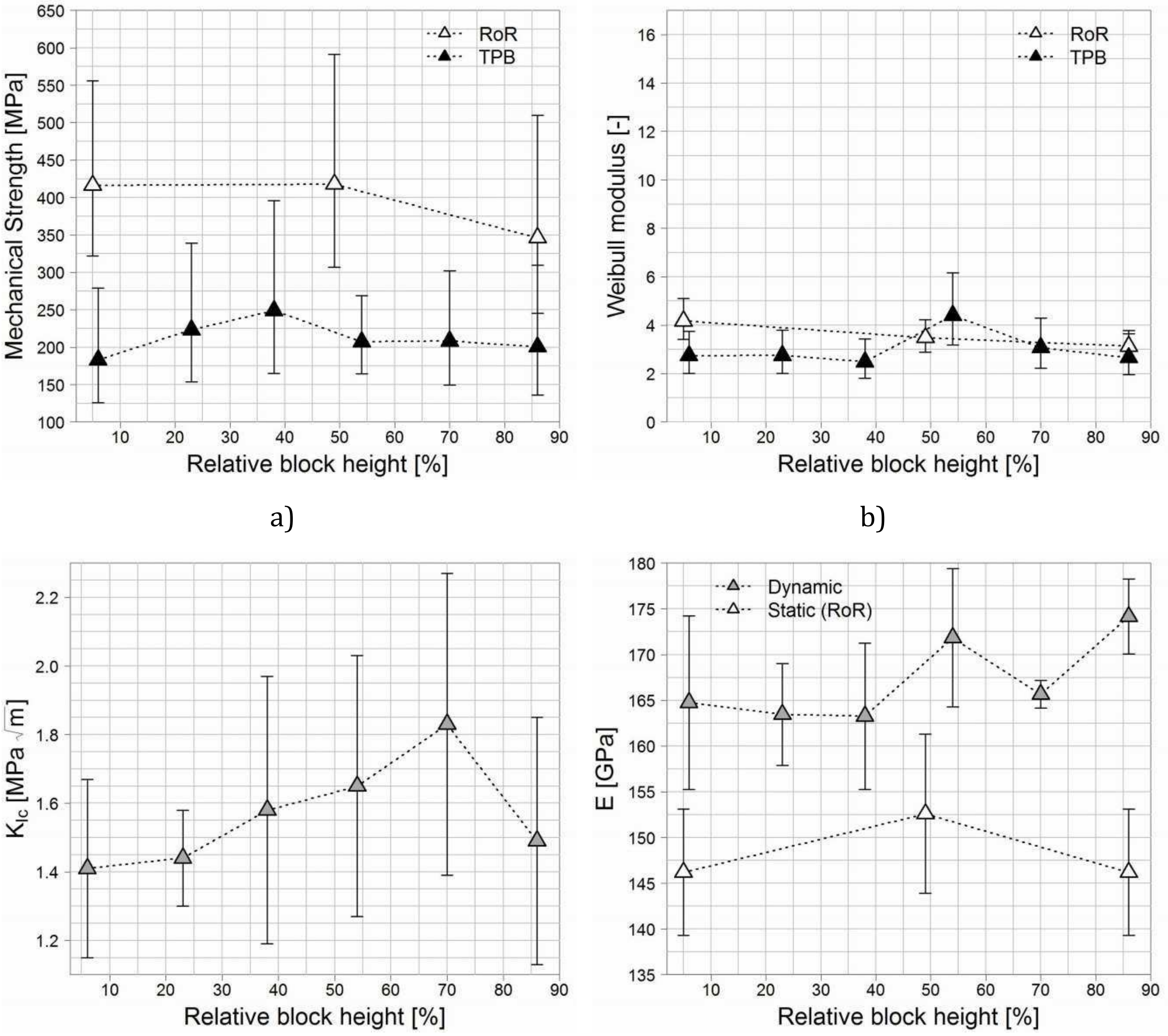

a) b)

c) d)

Figure 64 Characteristic stress and confidence bounds a), Weibull modulus b), fracture toughness c) and macroscopic elastic modulus d) against relative block height for SoG mc-Si.

4.3 Relation between Microstructure and Relative Block Height

4.3.1 Aluminum Rich Multicrystalline Silicon (*4N+Al* mc-Si)

Big sized particles were found within the *4N+Al* mc-Si block throughout the whole block height. During crystallization, aluminum, carbon and nitrogen segregate to the liquid phase and thus to the upper parts of the block. Therefore, SiC and Si_3N_4 precipitation increased in the direction bottom to top of the block as the silicon melt experienced a higher concentration of these impurities in these areas. The nature of the particles is determined by EDX analysis.

The precipitation of SiC and Si_3N_4 could have been enhanced by the decreased solubility of carbon and nitrogen in the silicon melt caused by the high content of aluminum within the melt. Circumferential or radial micro-cracking was not observed with the SEM microscope in the surroundings of SiC and Si_3N_4 particles, which appear well bonded to the silicon matrix (see Figure 65).

The mechanical strength decreases until approximately 60% of the relative block height as the density and size of the SiC and Si_3N_4 particles increases (see section 4.2.1).

The toughness of the silicon samples experience a reverse tendency and increases slightly with the increasing precipitation of SiC and Si_3N_4 particles (see Figure 59 c)). The measured elastic modulus is slightly higher than the theoretical Hill elastic modulus of silicon (162.58 MPa) in these parts of the block where SiC and Si_3N_4 particles are encountered (see Figure 59 d)).

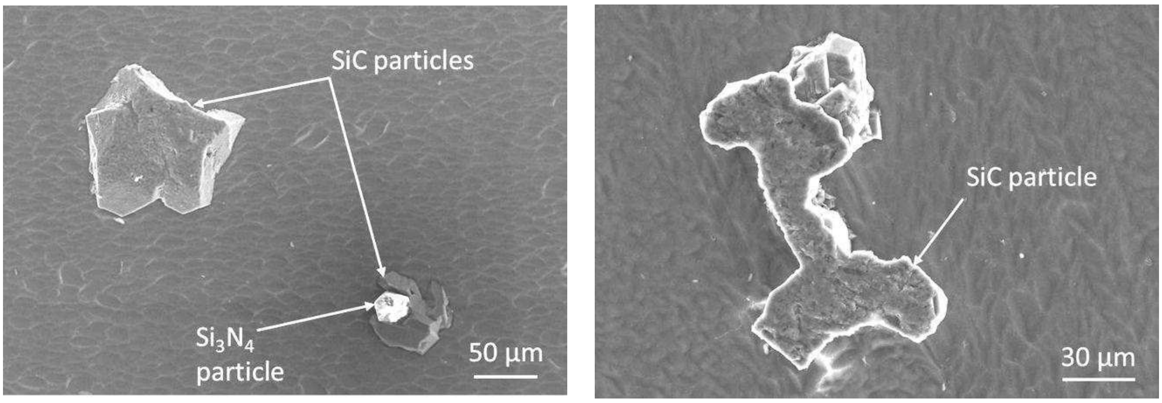

a) b)

Figure 65 SiC particles in the silicon matrix at 63% of the relative block height of the 4N+Al mc-Si.

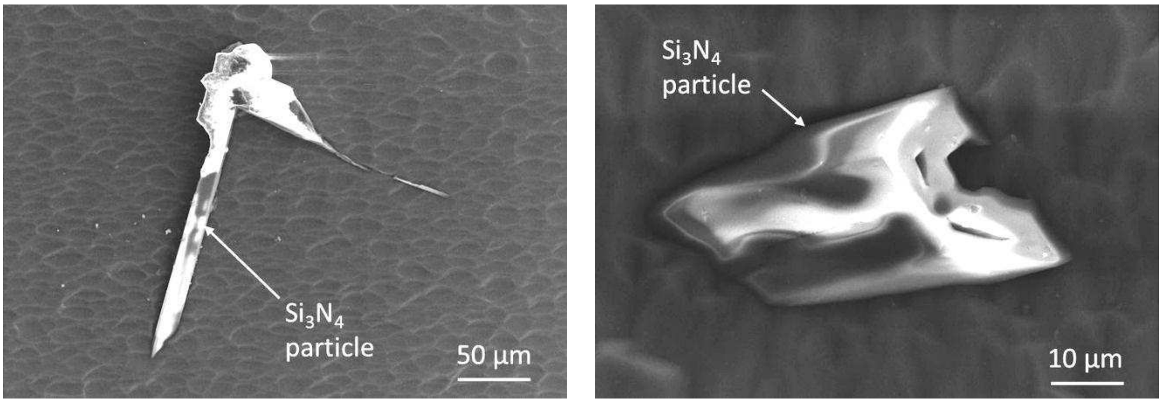

a) b)

Figure 66 Si_3N_4 particles in the silicon matrix at 63% of the relative block height of the 4N+Al mc-Si.

Al segregated to the upper part of the block and Al rich particles started to precipitate at approximately 60% of the relative block height. Micro-cracks in the range of several tens of microns were observed in the surroundings and within the Al rich particles (see Figure 67). The concentration of Al in the silicon melt reached the eutectic concentration for the silicon-aluminum system at approximately 70% of the relative block height. Therefore, an Al eutectic phase precipitated (see Figure 68) with long micro-cracks in its surroundings that reached lengths up to 1 mm. The phase diagram of the Al-Si system can be found in the literature [122].

As Al particles form in the silicon matrix within the upper parts of the blocks all mechanical properties decrease strongly. This is most probably due to the formation of very long cracks in the surroundings of the Al phases. The amount of Al phase is maximum between 70% and 80% of the relative block height where the mechanical properties of the *4-N+Al* mc-Si reach their minimum values (see Figure 59).

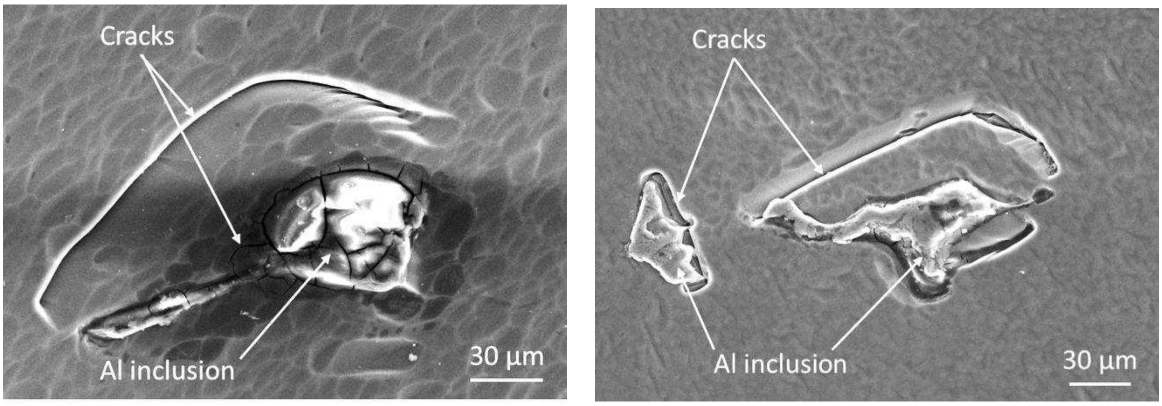

a) b)

Figure 67 Micro-cracks formed in the surroundings of Al rich particles at 63% of the relative block height of the 4N+Al mc-Si.

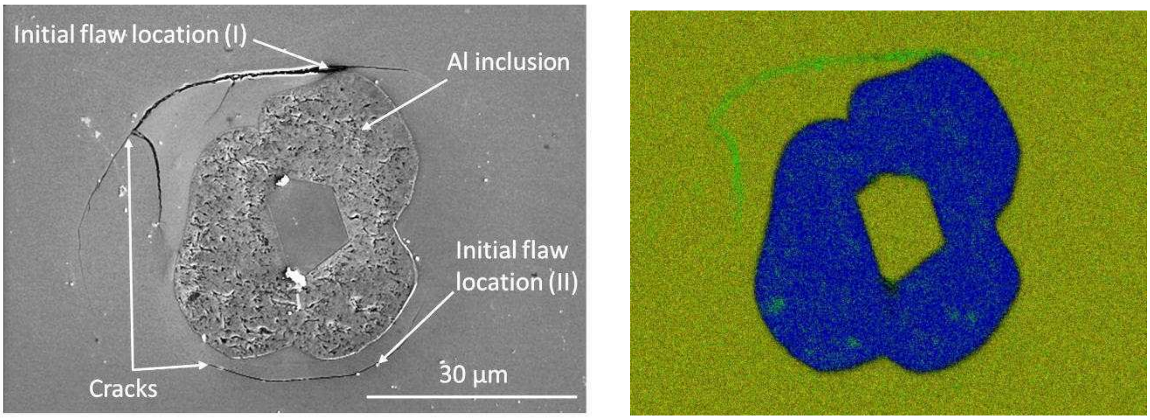

a) b)

Figure 68 Image a) depicts the micro-cracks formed in the surroundings of a eutectic Al phase at 77% of the relative block height of the 4N+Al mc-Si. An EDX map of the Al particle depicted in image a) is shown in image b) where the blue color corresponds to aluminum, yellow to silicon and green to oxygen.

Figure 69 depicts residual stress maps of middle and top *4N+Al* mc-Si samples. At 63% of the relative block height there are areas of material with low level of residual stress which is below 5 MPa and areas of material where a higher stress field of 10 MPa is dominant. Within this latter area small volumes of material reach residual stress values between 15 MPa and 20 MPa. The state of residual stress is increased as silicon samples from higher positions within de mc-Si blocks are examined. Figure 69 shows that areas with low residual stress in *4N+Al* mc-Si samples at 77% of the relative block height are smaller and that local residual stresses can reach values up to 25 MPa.

Even though an increase in the residual stress state of the silicon samples is measured with increasing block height, the residual stress state of the samples and its increase is underestimated. Maximum stresses surrounding the SiC, Si_3N_4 an Al particles are expected to be much larger than the measured values but they are located at the matrix-particle interface and decrease rapidly with increasing distance from this interface (see the discussions in section 4.4). Every pixel of the stress map corresponds to a measurement of residual stress in a surface area of size 0.6 × 0.6 mm^2 so that the measured stress value of every pixel is an averaged value within this area. Therefore, pixels that depict residual stress values as high as 25 MPa may underestimate the residual stress at the particle-matrix interface.

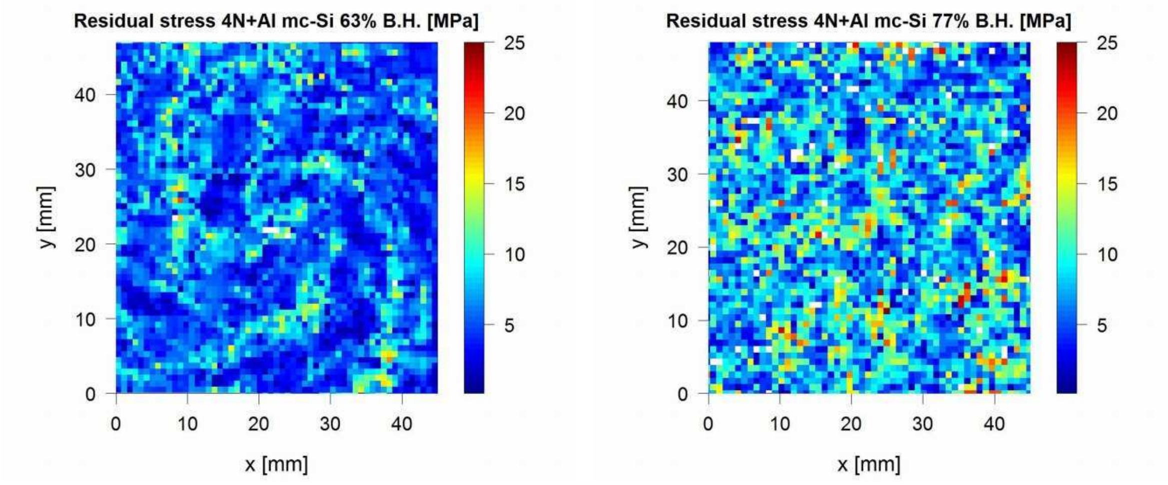

a) b)

Figure 69 Residual stress map at 63% of the relative block height (image a)) and at 77% of the relative block height (image b)) of the 4N+Al mc-Si.

Figure 70 shows the transmitted light image of a 50 × 50 mm^2 *4N+Al* mc-Si sample at 77% of the relative block height. The sample broke during polishing as it can be appreciated in image a). Second phase particles are revealed as dark spots and are depicted with more magnification in images b) and c).

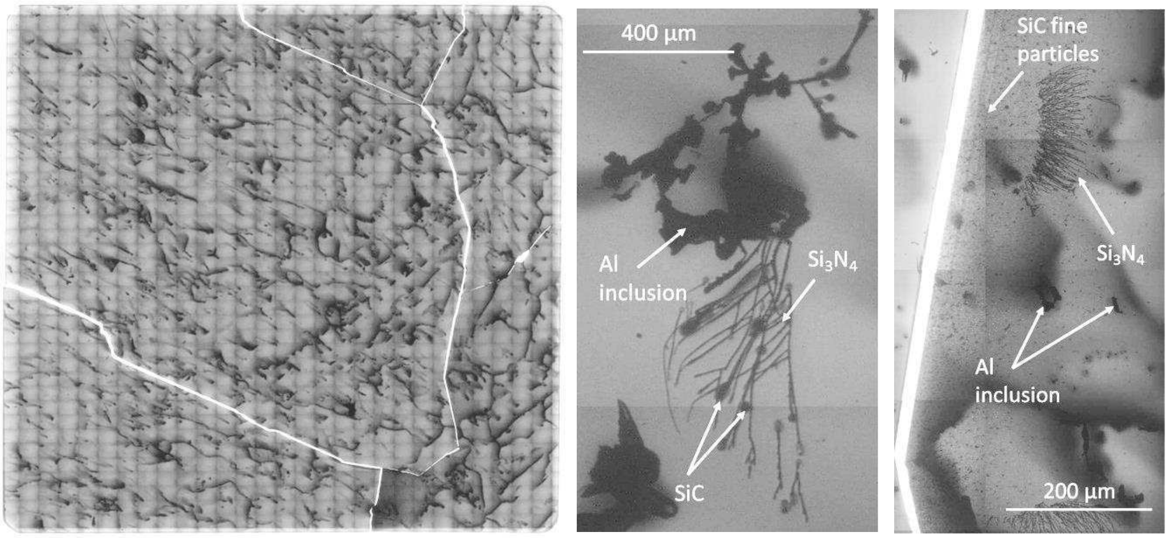

a) b) c)

Figure 70 Transmitted light images taken at 77% of the relative block height of the 4N+Al mc-Si.

4.3.2 Metallurgical Grade Multicrystalline Silicon (*3N* mc-Si)

The SEM images taken at the very bottom of the *3N* mc-Si revealed a relatively high density of SiO_x particles. The presence of SiO_x particles could be observed with the SEM on polished mc-Si samples. Damage etched samples were not suitable for this purpose as the acidic etching solutions also removed the SiO_x particles. Two types of particles were possible to distinguish with the scanning electron microscope. On the one hand, spherical and amorphous 1-2 µm SiO_x particles [123] precipitated at grain boundaries (see Figure 71). On the other hand, bigger particles sometimes appearing in a dendritic form [124] were found in the silicon bulk (see Figure 72 b)). EDX analysis revealed the presence of Cu with the SiO_x particles which points to the possibility that Cu enhanced the precipitation of SiO_x particles [125].

The mechanical strength measured with the RoR bending test at 5% of the relative block height of the *3N* mc-Si is considerably smaller than the mechanical strength of the upper parts of the block (see Figure 61 a)). It was not possible to measure the mechanical strength at this block position with the TPB test. However, relatively low mechanical strength was also measured at 25% of the relative ingot height. The toughness values measured at this block height is low (see Figure 61 c)) in comparison with the toughness values of other parts of the block which could be the cause of the low mechanical strength.

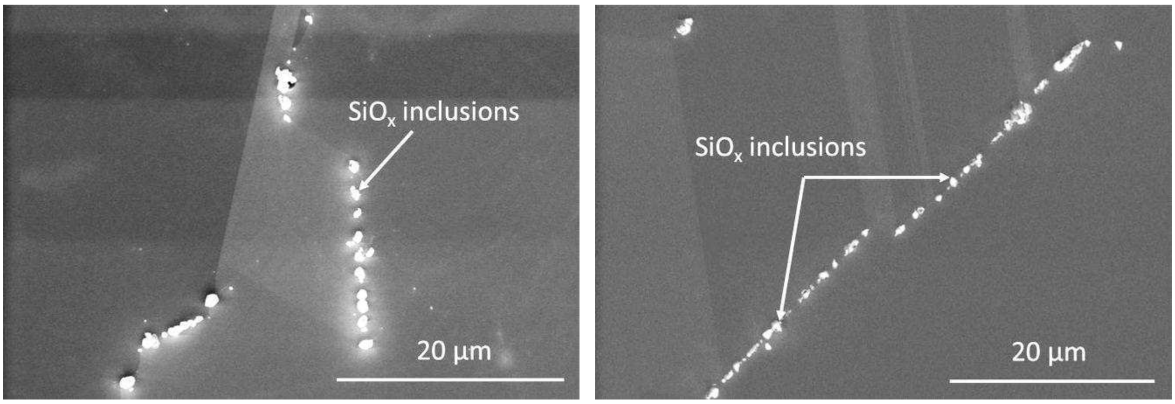

a) b)

Figure 71 Silicon oxide particles at grain boundaries in 3N mc-Si at 5% of the relative ingot height.

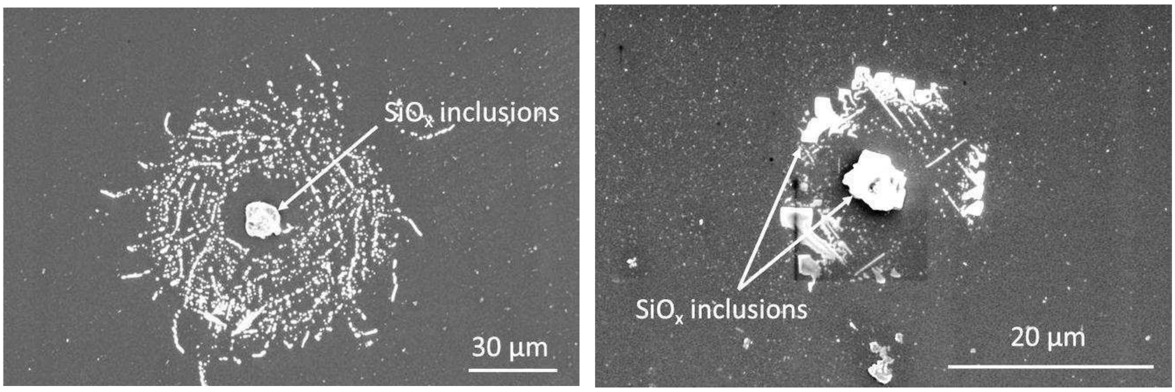

a) b)

Figure 72 Silicon oxide particles in 3N mc-Si at 5% of the relative ingot height.

SiC particles were also found throughout the whole block height with increasing density in the upper parts of the block (see Figure 73 a)). The measured values of dynamic modulus stayed beyond the Hill value of the elastic modulus of silicon and are relatively constant throughout the whole block height but the very top part of the block. A low density of particles with moderate micro-cracking in their surroundings (see Figure 73 b)) was observable at the top of the *3N* mc-Si. EDX analysis revealed the presence of oxygen, carbon and metals at these particles. Thus, micro-cracking is interpreted to occur as metals segregate to silicon carbide or silicon oxide particles where they can getter. Micro-cracking at the vicinities of particles is most probably the cause of the low mechanical strength, toughness and elastic modulus measured at the top of the block.

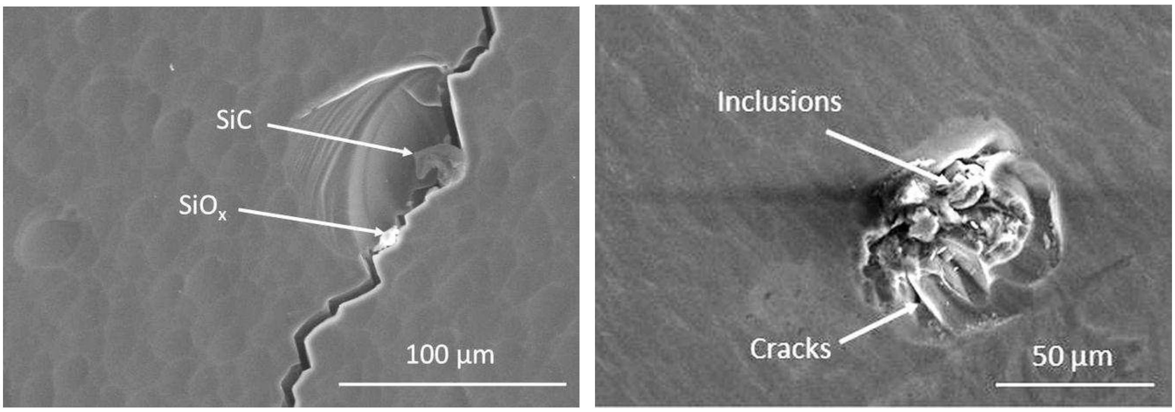

a) b)

Figure 73 Image a) depicts a SiO_x and a SiC particle in a broken mc-Si sample and image b) shows micro-cracking in the surroundings of particles at the top part of the 3N mc-Si block.

The level of residual stress measured with the *3N* mc-Si samples is low (see Figure 74). At the bottom of the block (%5 relative block height) grains are small and residual stress do not reveal the grain pattern clearly. In upper positions of the silicon block as grains are enlarged, there are grains in more stress free state than others (see Figure 74 b)).

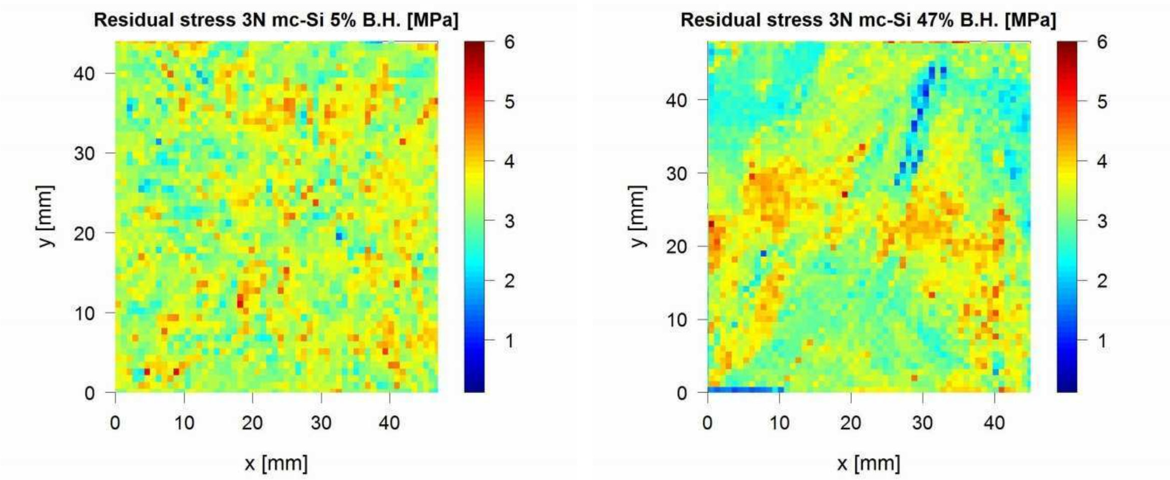

a) b)

Figure 74 Residual stress map at 5% of the relative block height (image a)) and at 47% of the relative block height (image b)) of the 3N mc-Si.

The inspection of mc-Si with transmitted light microscopy proved the presence of areas with high density of dark spots, which are most probably second phase particles. Polished mc-Si samples that broke during polishing usually present areas with a high density of dark spots near the fracture patterns (see Figure 75).

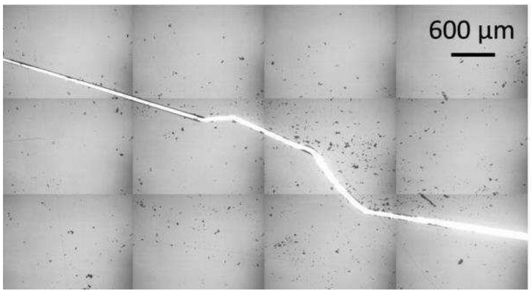

Figure 75 IR-light transmission microscopy picture of a fractured piece of a 3N mc-Si sample. The silicon chip broke during surface polishing in an area where a high concentration of particles was found.

4.3.3 Boron doped Multicrystalline Silicon (*B-doped* mc-Si)

Silicon oxide precipitation was observed within the *B-doped* mc-Si. However, these particles did not appear as the SiO_x spheres that gathered at grain boundaries like in the bottom of the *3N* mc-Si block. Instead, the SiO_x particles encountered in *B-doped* mc-Si appeared as small crystallites with approximately 1 µm diameter (see Figure 76 a)). Also larger SiO_x dendritic particles were sporadically observed (see Figure 76 b)).

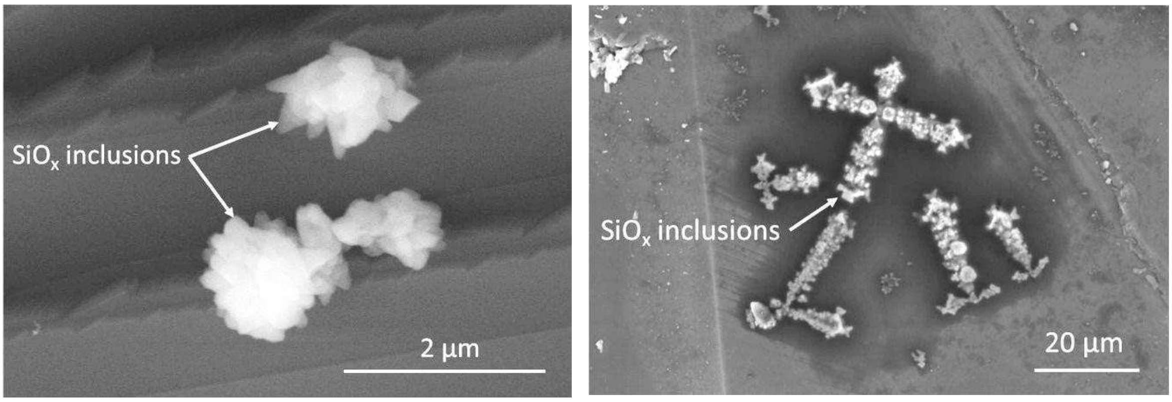

a) b)

Figure 76 Image a) depicts small SiO_x particles in B-doped mc-Si and image b) shows larger dendritic SiO_x particles.

Metallic clusters or particles were observed with the SEM at 42% and 89% of the relative block height (see Figure 77 and Figure 78). The presence of metallic particles could be linked to local micro-cracking and to the lower values of fracture toughness measured at these block heights.

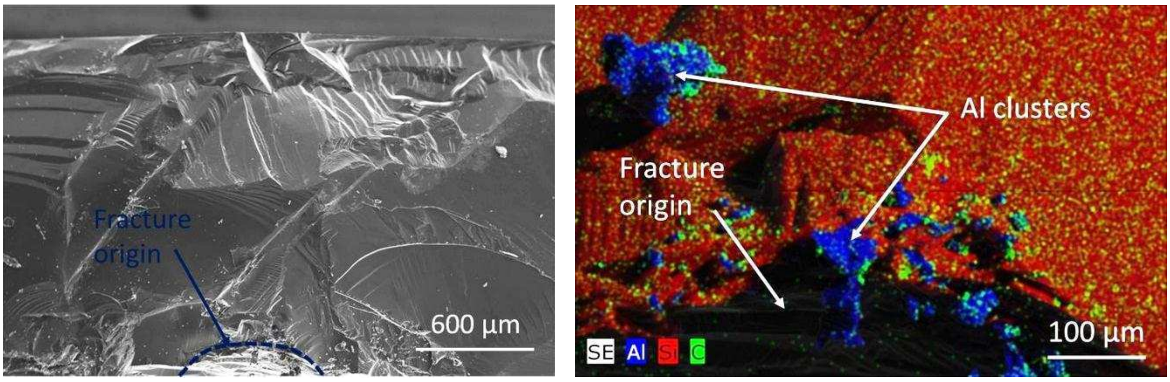

a) b)

Figure 77 Image a) shows a fracture surface of B-doped mc-Si at 42% of the block height where the elliptic fracture origin is marked by the dashed blue line and image b) shows Al particles in the fracture origin.

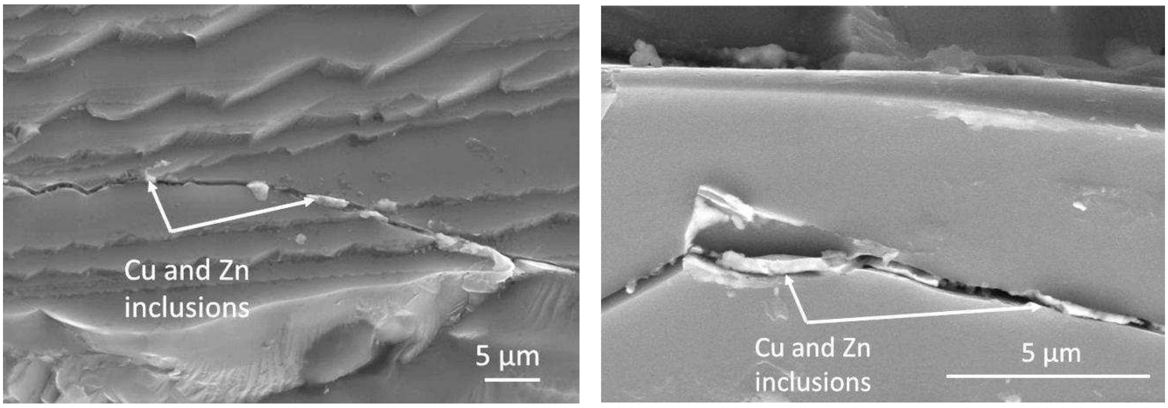

a) b)

Figure 78 Micro-cracking together with metallic particles (Cu and Zn) at 89% of the relative block height of the B-doped mc-Si block.

4.3.4 Up-graded Metallurgical Multicrystalline Silicon (*UMG* mc-Si)

The *UMG* mc-Si samples tested with the TPB test were taken from a cut ingot from a side wall of the mc-Si block. EDX analysis on impurity clusters like the one depicted in Figure 79 a) revealed the presence of O, N, C and Al and these impurity clusters do not show a clear crystalline structure. It could be that the mc-Si samples used for TPB testing and for fracture toughness and elastic modulus measurements contained a higher amount of impurities coming from the crucible which could be linked to the significantly low values of fracture toughness measured with these samples. Particles were not frequently found in the *UMG* mc-Si samples used for RoR tests which leads to conclude that the impurity clusters found in the samples for TPB tests were due to the proximity of these samples to the crucible wall. Figure 79 b) shows a small particle that could be SiC or Si_3N_4 due to its appearance.

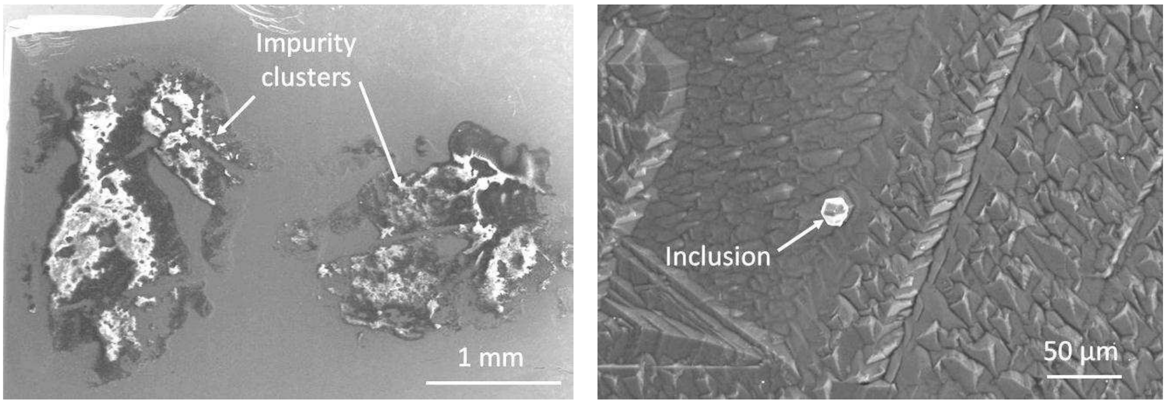

a) b)

Figure 79 Impurity cluster at 38% of the relative block height of the UMG mc-Si block (image a)) and particle at the 8% of the block height (image b)).

4.3.5 Solar Grade Multicrystalline Silicon (*SoG* mc-Si)

The peculiarity of the *SoG* mc-Si block was the presence of SiC particles and sporadic micro-cracking at the top parts of the block (see Figure 80).

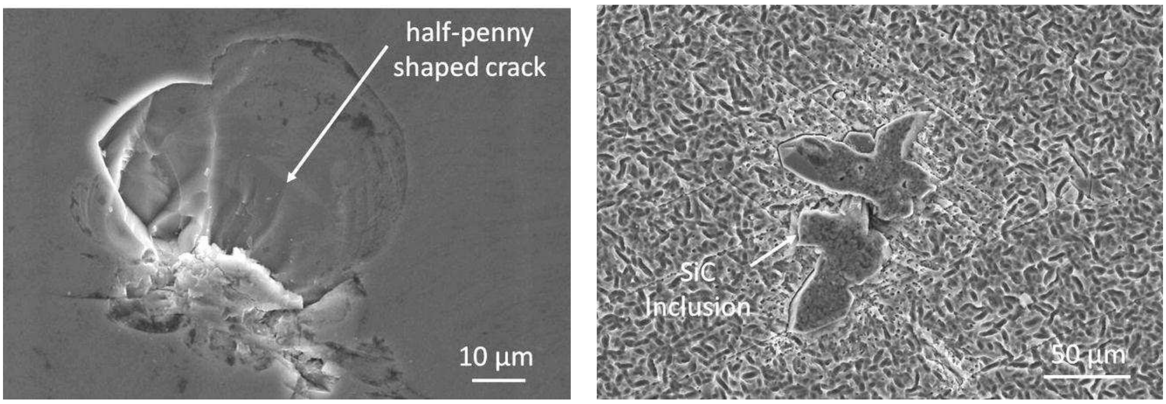

a) b)

Figure 80 Half-penny shaped micro-crack on the surface of a silicon sample at 93% of the relative block height of the SoG mc-Si block (image a)). Image b) shows a SiC particle at 86% of the relative block height of the SoG mc-Si block.

4.4 Discussion

The experimental results presented in the previous sections of this chapter are contrasted in this section with the theoretical models for the mechanical behavior of ceramics in order to evaluate the causes of breakage and to predict the fracture stresses of silicon containing different second phase particles. Table 4 summarizes the material parameters used for the calculation of thermal residual stresses, the critical particle radius, elastic stresses, change in local toughness, elastic modulus and fracture criteria.

The values of the thermal expansion coefficients of silicon, silicon carbide and silicon nitride are temperature dependent [69], [126], [127], [128], [129]. Thus, the values for these materials in Table 4 were determined at 775°C, which is the brittle-ductile temperature of silicon considered in this work [79]. The elastic modulus and Poisson´s ration of silicon carbide and silicon nitride at 775°C were published by Sakaguchi et al. [130]. The rest of the properties were acquired from [131]. Sinclair and Lawn [132] estimated the surface energies of different crack planes for diamond structure crystals. For silicon, the surface energies of the {111} and {110} planes are 1.41 $\mathrm{J/m^2}$ and 1.74 $\mathrm{J/m^2}$, respectively. Therefore, the mean value of 1.6 $\mathrm{J/m^2}$ was used for the calculations in this work.

Table 4 Material properties of silicon and the second phase particles found within mc-Si blocks at 775°C.

Material	$\alpha \times 10^{-6}[\mathrm{K^{-1}}]$	$\nu[-]$	E[GPa]	K_{Ic}[MPa]
Si	4.3	0.218	162.6	0.83-0.94
Al	23	0.334	69	22-30
Cu	16.9	0.34	117	-
SiO_x (am.)	0.5	0.165	73	0.6-0.8
SiO_x (cryst.)	12.3	0.17	70	-
Si_3N_4	2.35	0.27	310	4-6
SiC	4.8	0.15	380	2.5-5

4.4.1 Metals

The results in the previous section showed a decrease in the mechanical properties at the upper parts of the mc-Si blocks where metal impurities can segregate. Very remarkable is the decrease of all the mechanical properties at the top parts of the *4N+Al* mc-Si block. The *3N* mc-Si block also experienced a noticeable decrease of mechanical properties at the top of the block. The thermal mismatch between metals and silicon is critical due to the large difference in thermal expansion coefficients (see Figure 81). Al can build thermal stresses in the radial direction up to 1600 MPa and Cu up to 1500 MPa at the particle´s interface.

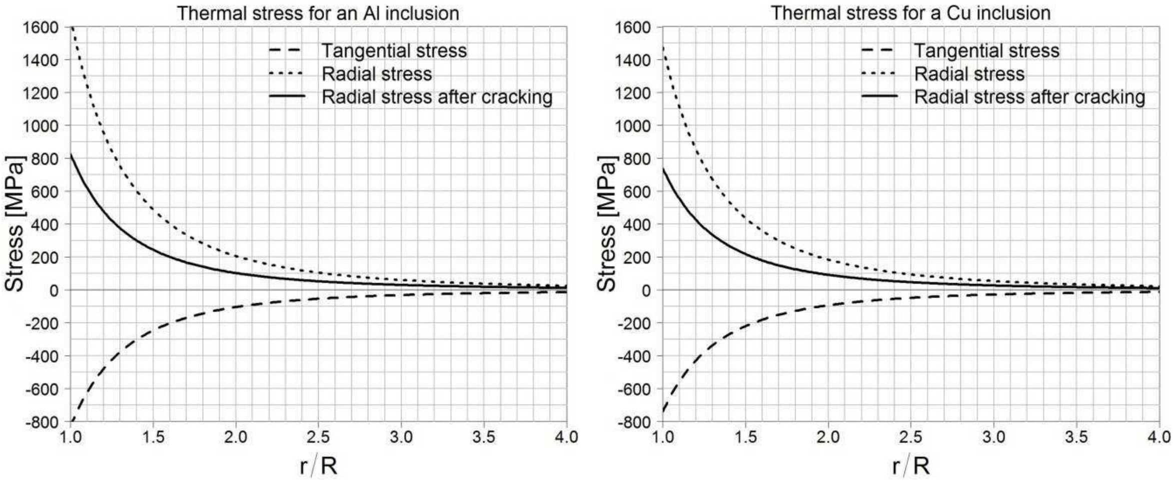

a) b)

Figure 81 Radial and tangential residual thermal stress profiles in the surroundings of an Al particle (image a)) and a Cu particle (image b)).

These large residual thermal stresses reveal that the critical particle size for circumferential micro-cracking in the case of metals is small. The model of Davidge [36] presents a conservative estimate for the critical particle radius. In the case of metals within the silicon matrix, this value is smaller than 1 µm (see Table 5). According to Ito et al. [37] the minimum critical particle radius is smaller than 1 µm for metallic particles with initial flaws at the particle´s interface that extend 60-120° (see Figure 82). If the impurity particle is considered to exhibit a circular form, the critical particle radius is according to Evans near 1 µm. This agreement on the critical particle radius by the application of different models assures the micro-cracking in the surroundings of metallic particles. Semi-spherical cracks around the particles are observed with the SEM (see Figure 67, Figure 68 and Figure 73 b)). This observation is in agreement with the literature [36] and the thermal residual stress reduces to the half of its initial value after micro-cracking.

Table 5 Minimum critical particle radius for Al and Cu particles within a silicon matrix.

Particle	*R* (Davidge) [µm]	*R* (Ito) [µm]	*R* (Evans) [µm]
Al	0.28	0.39	0.96
Cu	0.46	0.65	1.21

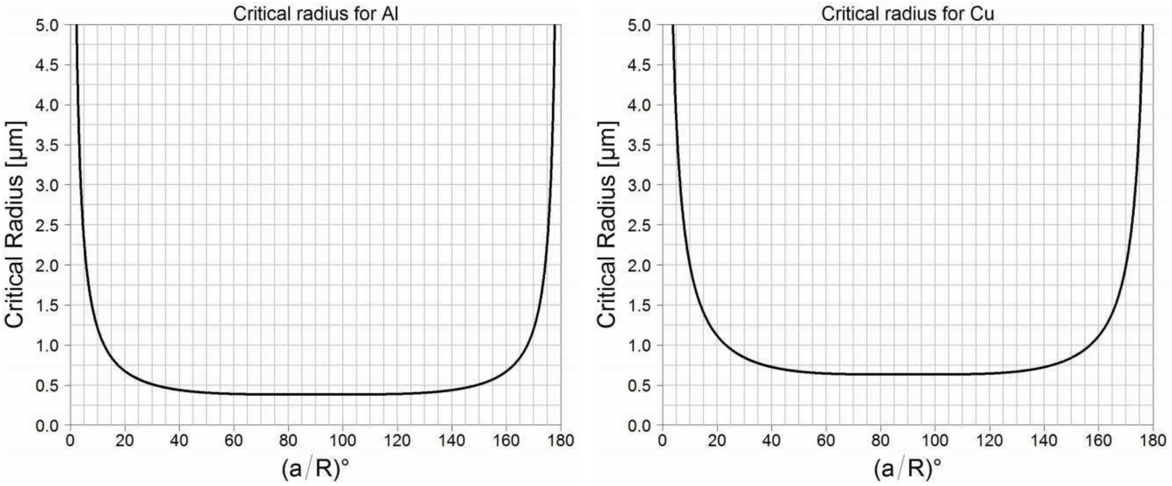

a) b)

Figure 82 Critical particle radius for spontaneous micro-cracking during the cooling step of the crystallization process against the angle that the initial flaw extends at the particle interface for Al and Cu according to Ito et al. [37]. The angle is defined as the division of the length of the arc of extension of the defect by the particle´s radius as indicated in Figure 8.

Figure 83 a) depicts the decrease in elastic modulus with increasing crack density in the silicon matrix. The value of elastic modulus without micro-cracking is considered to be ~170 GPa which is the mean value of elastic modulus measured for *4N+Al* and for *3N* mc-Si before micro-cracking occurred (see Figure 59 d) and Figure 61 d)).

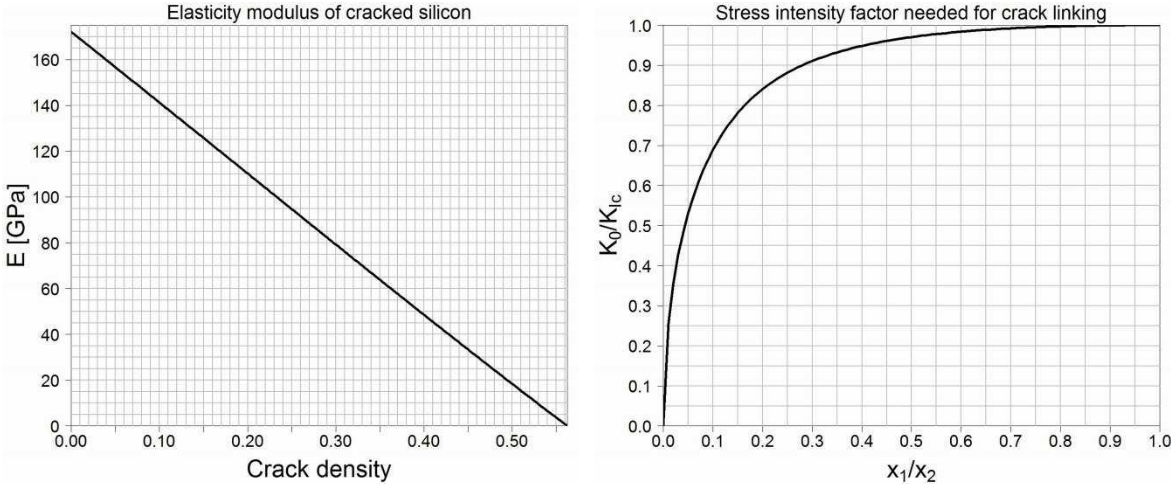

a) b)

Figure 83 Image a) depicts the decrease of elastic modulus with increasing density of cracks within the silicon matrix after Budiansky and O´Connell [64]. Image b) shows the decrease in stress intensity factor at the tip of a crack approaching a collinear crack [59]. The magnitudes x_1 *and* x_2 *are described in Figure 16.*

Given that the decrease in elastic modulus measured at 78% of the relative block height of the *4N+Al* mc-Si was due to micro-cracking, the crack density in silicon can be read in the graph of Figure 83 a). Thus, a measured elastic modulus of 126 GPa at 78% of the relative block height corresponds to a crack density value of 0.15. According to equation (2.110), the fracture toughness should decrease 14%. Before micro-cracking occurred, the fracture toughness measured at 58% of the relative block height is 1.61 MPa $\sqrt{\text{m}}$ and a decrease of 14% means a value of fracture toughness of 1.39 MPa $\sqrt{\text{m}}$. This value is near the measured value of 1.27 MPa $\sqrt{\text{m}}$ which is a good approximation but not totally accurate. The inaccuracy could be due to the fact that the real values of elastic modulus and toughness of the material without micro-cracking at that position are not known and therefore the values of elastic modulus and toughness of a lower position in the block are considered. The inaccuracy could be also due to the large error bars of the elastic modulus and the fracture toughness measurements, which indicates that the material has a relatively inhomogeneous microstructure. Another reason for the inaccuracy could be an underestimation of the decrease in the elastic modulus as Al particles cause a reduction of the elastic modulus of silicon, in addition to micro-cracking, according to Hashin and Shtrikman [62] (see Figure 84).

It has to be noticed that the error bars of the toughness measurements are large and therefore the observed trend of fracture toughness of the *4N+Al* mc-Si through the block height must be analyzed carefully. Large error bars mean that the material is significantly inhomogeneous within the same block height. The fracture toughness values measured at 78% of the relative block height range from 0.95 MPa $\sqrt{\text{m}}$ to 1.58 MPa $\sqrt{\text{m}}$. This means that the tested sample that showed the highest value of fracture toughness, 1.58 MPa $\sqrt{\text{m}}$, experienced non to very little crack linking while the samples with very low fracture toughness most probably experienced strong crack linking. The lengths of the notches introduced in the samples for the toughness measurements range from 0.2 to 0.9 mm.

According to Figure 83 b), the stress intensity factor needed for crack linking is lower than the toughness of the material when a propagating crack finds a collinear crack located at a distance smaller than the length of the propagating crack. Therefore, a 0.5 mm notch senses and links cracks that he may find within 0.5 mm ahead of its tip. If we consider that the toughness without micro-cracking at 78% of the block height is 1.61 MPa $\sqrt{m}$, the sample whose measured toughness was 0.95 MPa $\sqrt{m}$ represents a decrease of toughness down to 59% of the toughness without micro-cracking. If we read the abscissas value for 0.59 in Figure 83 b) we can interpret that the notch of this sample linked with a crack located at distance 7.5% of its length.

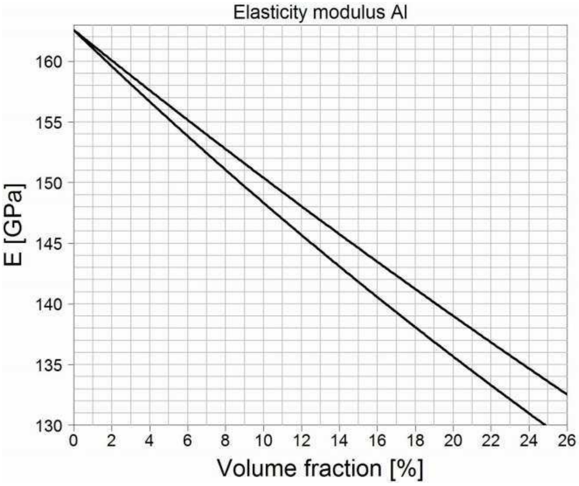

Figure 84 Decrease in elastic modulus against volume fraction of Al particles in the silicon matrix.

Given that the decrease in elastic modulus measured at 79% of the relative block height of the *3N* mc-Si was due to micro-cracking, a measured elastic modulus of 167 GPa corresponds to a low crack density value of ~0.04. This decrease in the elastic modulus of silicon should manifest in a decrease of the fracture toughness from 1.57 MPa $\sqrt{m}$ at 65% of the block height to 1.54 MPa $\sqrt{m}$ at 79% according to Rose [59]. However, the measured decrease in toughness showed a value of 1.33 MPa $\sqrt{m}$. In this case, there is a large inaccuracy in the prediction of the value of material fracture toughness. The inaccuracy could be again due to the fact that the real value of elasticity and toughness of the material without micro-cracking at that position are not known and therefore the values of elastic modulus and toughness of a lower position in the block are considered. Another reason could be the lengths of the notches introduced for measuring fracture toughness. Figure 73 b) shows micro-cracking of approximately 50 µm length. The notches are much larger than the micro-cracking already existing in the surroundings of the particles, so that crack linking is more probable to occur during fracture toughness measurement than during ordinary fracture caused by much smaller surface defects that would link cracks within the silicon bulk with a much lower probability. It can be concluded from these observations, that in the case that micro-cracking occurs, it is convenient to introduce notches with a length similar to the extent of the micro-cracking in the samples for fracture measurement.

Figure 85 shows the cross section of a *4N+Al* mc-Si silicon chip broken with the RoR bending test. The fracture origin was found in an area of material where extensive micro-cracking appears through the wafer thickness. The measured fracture stress of such damaged sample was 70 MPa, which is a very low value and could be due to crack linking from the surface of the wafer under tensile stress to the other side of the wafer under compressive stress.

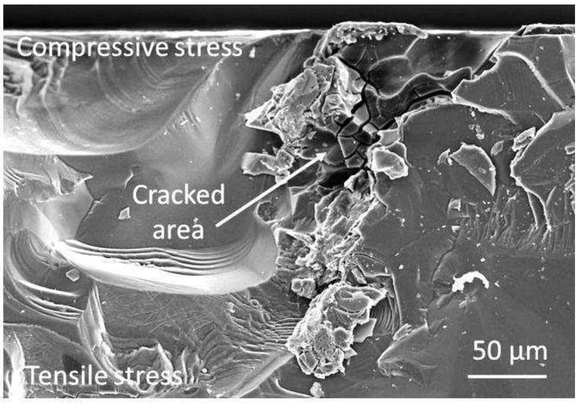

Figure 85 Cross section of fracture in the surroundings of Al particles in a cracked silicon matrix.

The fracture criterion when micro-cracking around particles occur is defined by equation (2.97). At 78% of the relative block height of the *4N+Al* mc-Si block the failure criterion for the TPB test stays:

$$\delta R \geq \left(\frac{1.26}{Y \times 43.1}\right)^2 \tag{4.1}$$

where 1.26 is the measured toughness of the material in MPa $\sqrt{\mathrm{m}}$ at 78% of the block height, 43.1 is the uniaxial calculated characteristic stress in MPa and δR is the crack length. The crack length is thus ∼633 µm if the cracks causing failure are considered half-penny-shaped surface cracks (see the values of geometry factors in section 2.1.1.2.3). By measuring particle radius and micro-crack lengths from Figure 67 a), the factor that relates the micro-crack length with the particle radius, δ, is approximately 3.6. A crack length of 633 µm would be caused then by a ∼176 µm Al particle.

In the case of the biaxial loading with the RoR bending test of a half-penny-shaped surface crack at 77% of the relative block height of the *4N+Al* mc-Si block, the failure criterion stays:

$$\delta R \geq \left(\frac{1.26}{Y \times 72.7}\right)^2 \tag{4.2}$$

where 72.7 is the biaxial calculated characteristic stress. The crack length is thus ∼188 µm for half-penny-shaped surface cracks which corresponds to particles with 52 µm radius. The thicknesses of the samples broken with the RoR are ~260 µm. Therefore, the critical crack length sensed by these bending tests is smaller than the critical crack length measured with the TPB test, i.e. the RoR bending test cannot sense crack lengths larger than the thickness of the samples.

At 79% of the relative block height of the *3N* mc-Si block the failure criteria for the TPB test stays:

$$\delta R \geq \left(\frac{1.33}{Y \times 182}\right)^2 \tag{4.3}$$

where 1.33 is the measured fracture toughness of the material in MPa $\sqrt{\text{m}}$ at 79% of the block height and 182 is the calculated characteristic stress in MPa. The length of a half-penny-shaped surface crack is thus ~33 µm, which is in good agreement with the crack lengths observed with the SEM images (see Figure 73 b)).

4.4.2 Amorphous Silicon Oxide

The presence of SiO_x at the bottom of the *3N* mc-Si block was revealed by the inspection of the samples with the SEM (see Figure 71 and Figure 72). The mechanical strength measured with the RoR bending test at 5% of the block height was significantly lower than the mechanical strength measured in the upper parts of the block. Fractography analysis showed fracture patterns that followed the location of the SiO_x particles at grain and twin boundaries (see Figure 92 a)). The low values of mechanical strength and toughness measured with the TPB test at 25% of the block height could be also due to the precipitation of SiO_x. However, it was not possible to reveal the presence of SiO_x by the fractography analysis of the samples broken with the TPB test. The samples broken with the RoR bending test where glued to a plastic tape on the side of the samples under compression so the broken pieces could be analyzed together in the microscope after fracture. This eased the observation of SiO_x within the fracture paths.

Figure 86 depicts the profiles of residual thermal stress in the vicinities of amorphous SiO_x particles. Tangential thermal stresses are tensile and reach values beyond 100 MPa at the particle´s interface.

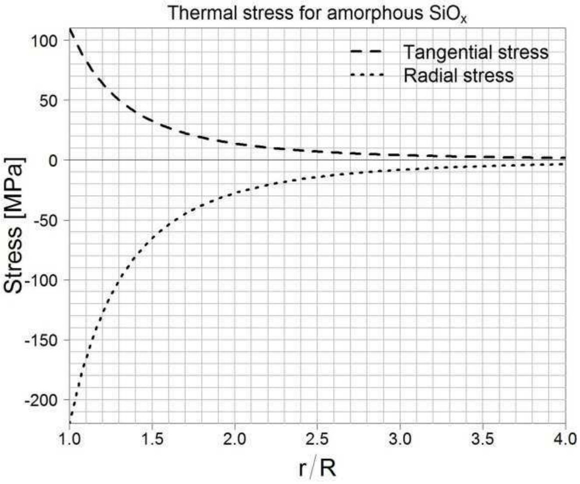

Figure 86 Radial and tangential residual thermal stress profiles in the surroundings of an amorphous silicon oxide particle.

If the particle is considered spherical with an annular initial flaw in its equator (see Figure 10), the minimum critical particle radius is 282 µm for an initial flaw length of ~$0.3R$ (see Table 6 and Figure 87). If the SiO_x particle is considered circular with an initial flaw size of $0.2R$ and perpendicular to the particle´s interface, the critical particle radius is 701 µm. The observed particle radii were smaller (see Figure 71) than these two hypothetical cases and therefore spontaneous radial micro-cracking of the silicon matrix does not occur in the surroundings of amorphous SiO_x.

The curve depicting the minimum particle radius in Figure 87 decreases until it reaches a minimum value at an initial flaw size of $0.3R$. That means that, as the size of the initial flaw increases, the intensification of tangential thermal stress of a SiO_x particle at the tip of the initial flaw also increases and thus smaller SiO_x particles will already cause spontaneous micro-cracking. If the initial flaw extends further than a length $0.3R$, the effect of the decrease in the magnitude of the thermal tangential stress (see Figure 86) counteracts the increase of stress intensification by a larger initial flaw and thus the minimum critical particle radius increases.

Table 6 Minimum critical particle radius for amorphous SiO_x particles within a silicon matrix.

Particle	R (Green) [µm]	R (Evans) [µm]
SiO_x	282	701

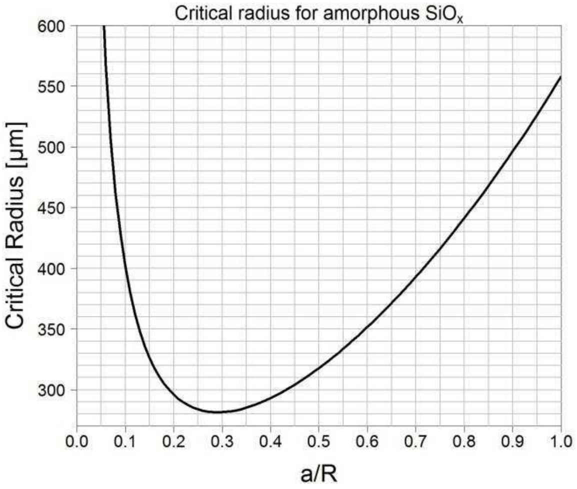

Figure 87 Critical particle radius for spontaneous micro-cracking during the cooling step of the crystallization process against the initial flaw size at the amorphous silicon oxide particle interface according to Green [41].

When a load is applied in the surroundings of a SiO_x particle, the stress field is disturbed by the presence of the particle, as it has lower elastic constants than silicon. Figure 88 depicts the stress profiles at the particle´s interface against the orientation with the applied load (see also Figure 11). When a uniaxial load of 150 MPa is applied radial elastic stresses are less intense than the applied load while tangential stresses oriented between 55° and 125° from the applied load are intensified (see Figure 88). The intensification of tangential elastic stress is maximum at 90° from the applied load where the elastic stress reaches a value of ~240 MPa.

It has to be mentioned that the requirements for applying the models for the calculation of residual thermal stresses and intensification of elastic stresses are not fully met. The silicon matrix is not isotropic and cannot be considered completely homogeneous either and the particles are not spherical and are not larger than the grains size to counteract taking these assumptions which are necessary for the application of the models. Thus, the calculated thermal and elastic stresses are approximate sufficient values for discussing the results and observations presented in the previous sections of this chapter.

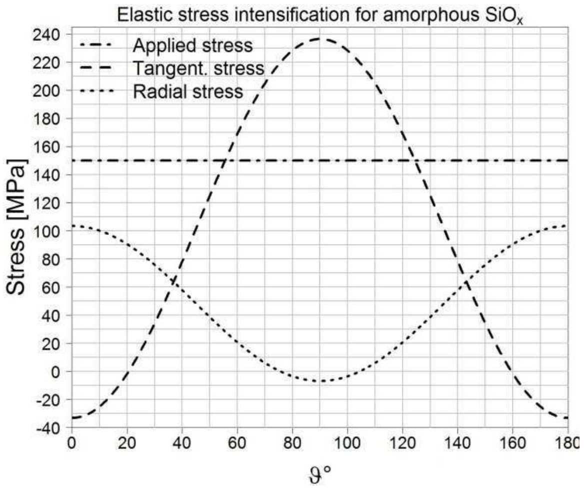

Figure 88 Radial and tangential elastic stress profiles in the surroundings of an amorphous SiO_x particle.

Both tangential thermal and elastic stresses are tensile in the case of SiO_x particles. The maximum overlap of tensile tangential thermal and elastic stresses occurs at an orientation of 90° from the applied load and is depicted in Figure 89. In the case that 150 MPa are applied in the vicinities of a SiO_x particle, the particle would be experiencing almost 350 MPa at its interface due to the overlap of tangential stresses.

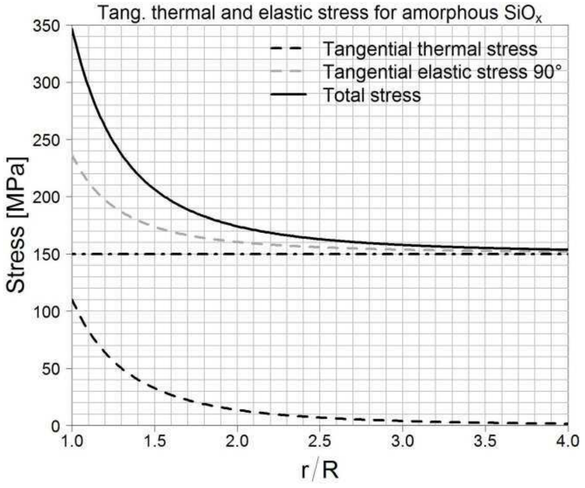

Figure 89 Overlap of tangential thermal and elastic stresses in the surroundings of an amorphous SiO_x particle.

Ranges for the failure criteria near amorphous SiO_x particles depending on the particle geometry are depicted in Figure 90. A conservative failure criterion can be used for fracture prediction if the overlap of tangential thermal and elastic stresses is considered to act on a particle sized crack when an external load is applied. This failure criterion described by equation (2.96) is depicted by the solid line in Figure 90.

The dotted line presents the failure criterion according to Green [41] and described by equation (2.104). This failure criterion considers that fracture is caused by radial crack extension when a load is applied in the surroundings of a spherical particle with an initial flaw size of length $0.2R$. Thermal stresses are considered for this fracture criteria but intensification of the applied load is not taken into account.

The dashed line depicts the fracture criterion when the SiO_x particle is considered to be circular with an initial flaw size of length $0.2R$. The appropriate expressions for the stress intensity factors proposed by Evans [26] are introduced in equation (2.105) which gives equation (2.106) and the critical radius of circular cracks is calculated with this expression. Thermal end elastic mismatch are considered in this failure criterion and the application of a uniaxial applied load.

The calculated characteristic stress at 25% of the block height of the *3N* mc-Si block, broken with the TPB test, is considered here for further analysis. The calculated characteristic stress is 144.2 MPa. If the abscissas value for the characteristic stress is read in Figure 90, the critical particle radius for silicon oxide can be obtained. The Green and Evans criteria are very similar and predict a critical amorphous SiO_x particle radius of 36 and 44 µm respectively. The conservative failure criterion predicts critical particle radius of approximately 2 µm if the amorphous SiO_x concentrates stress as a surface scratch-like crack. Even though SiO_x particles do not appear with the form of a crack but as spherical defects, the consideration of the particle as a particle sized surface scratch-like crack gives a better fracture criterion. This is caused by the oriented precipitation of amorphous SiO_x particles, i.e. amorphous SiO_x particles show a coplanar array following the paths of the grain boundaries and are much closed to each other (see Figure 71). This configuration allows the entanglement of the tensile tangential thermal stresses between the particles being most probably the flaw-linking stress intensity factor, K_{Ic}^{*} (in equation (3.21)), between two amorphous SiO_x particles very low. Therefore, the formation of a crack that links two or more amorphous SiO_x particles is possible at a very low applied load, σ_L, and this crack is the critical defect that is controlling the mechanical strength of the *3N* mc-Si at the bottom of the block.

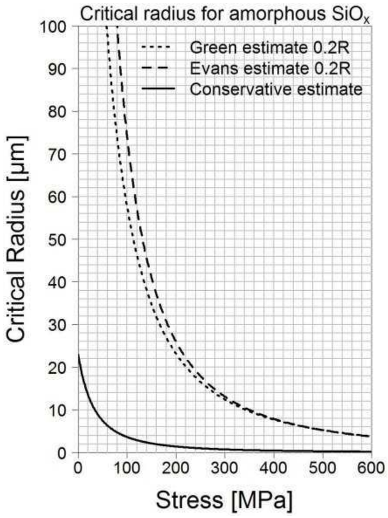

Figure 90 Critical particle radius of amorphous SiO_x when an external load is applied.

The relative low values of fracture toughness measured at the bottom of the *3N* mc-Si could be also due to the presence of SiO_x particles. Figure 91 a) shows the change of stress intensity factor at the tip of a crack as it approaches an amorphous SiO_x particle. The tip of the crack experiences an increase in stress intensity factor as it approaches the particle. The dotted line depicts the stress intensity factor at the tip of the crack due to the residual tangential thermal stress in the surroundings of a particle with 2 µm radius. The dashed line represents the stress intensity factor in the presence of the amorphous SiO_x particle that results when the crack approaches the particle and a biaxial load which induces a stress intensity factor of 0.65 MPa $\sqrt{\mathrm{m}}$ in the absence of the particle is applied. The overlap of both thermal and elastic stress intensity factors indicates that a crack at the particle´s interface experiences a stress intensity factor of 0.91 MPa $\sqrt{\mathrm{m}}$ when only a biaxial load exerting a stress intensity factor of 0.65 MPa $\sqrt{\mathrm{m}}$ is applied. Thus, the crack is accelerated to the SiO_x particle and the effective toughness of the material diminishes. For SiO_x particles with larger radius, the stress intensity factor due to thermal stresses would be also larger. Thus, larger amorphous SiO_x particles would decrease the effective fracture toughness of mc-Si in a larger extent.

The change in critical stress intensity factor that experiences a crack approaching an amorphous SiO_x particle when a uniaxial load is applied can be read from the dotted line of Figure 15. SiO_x is softer than silicon, and a propagating crack must release the half of the energy for its propagation when it reaches the particle´s interface. With the aid of equation (2.41), it can be calculated that the critical stress intensity factor of silicon reduces from 0.9 MPa $\sqrt{\mathrm{m}}$ to 0.64 MPa $\sqrt{\mathrm{m}}$ at the particle´s interface. Tangential thermal stresses at the interface of a particle with 2 µm radius provide already 0.14 MPa $\sqrt{\mathrm{m}}$ (see Figure 91 a)). Thus, the application of a small uniaxial load that adds 0.5 MPa $\sqrt{\mathrm{m}}$ would already cause radial cracking at the interface of the amorphous SiO_x particle.

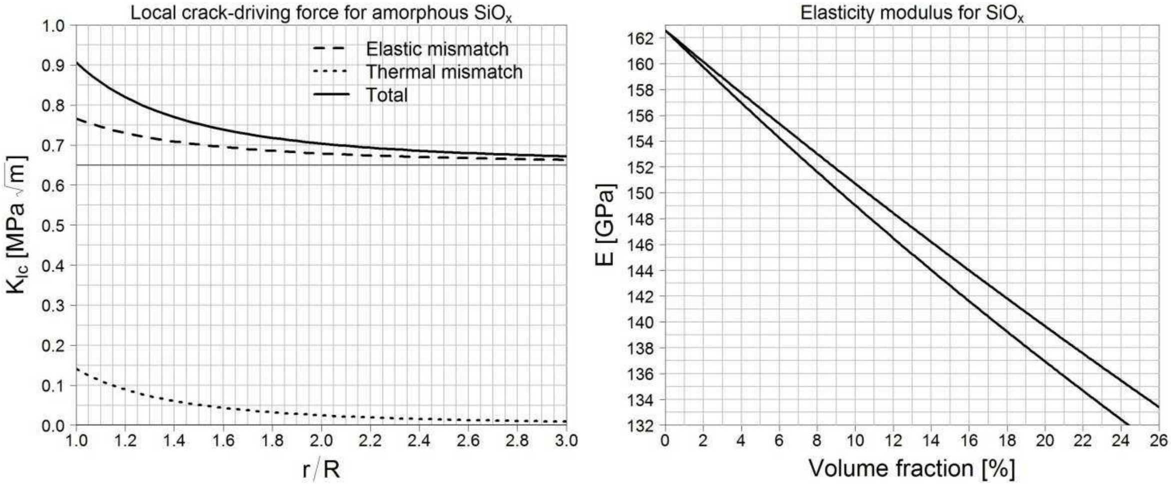

a) b)

Figure 91 Image a) depicts the overlap of stress intensity factors due to thermal and elastic mismatch at the tip of a crack approaching an amorphous SiO_x particle after Khaund et al. [53]. Image b) shows the decrease in elastic modulus against volume fraction of SiO_x particles in the silicon matrix according to Hashin and Shtrikman [62].

These analyses are not able to predict the total change in measured fracture toughness of silicon containing amorphous SiO_x particles because this is dependent on how many particles encounters the propagating crack in its path until total fracture. But it provides a good explanation and a quantitative approximation for the diminishment of the fracture toughness of silicon when it contains amorphous SiO_x particles.

According to Figure 91 b) the presence of amorphous SiO_x particles in the silicon matrix would decrease the elastic modulus of silicon. The results presented in Figure 61 d) does not show a significant decrease in the values of elastic modulus at 25% of the relative block height in comparison with the values of elastic modulus at other positions within the block where the precipitation of amorphous SiO_x particles was not observed. The reason for this could be that the volume fraction of the SiO_x particles may be too small to be sensed by the measurement of the dynamic elastic modulus.

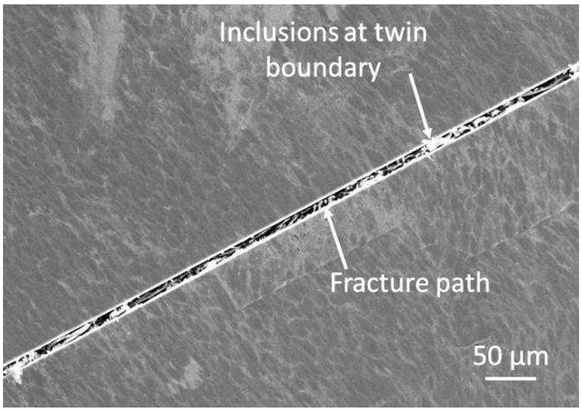

Figure 92 Front section of fracture in the surroundings of SiO_x particles.

Figure 93 shows the fracture surface of a *3N* mc-Si sample that broke under 159 MPa with the TPB test. The fracture pattern of silicon shows a great complexity and its interpretation is not a trivial issue. The area that seems to have cleaved and that therefore was the fracture origin is indicated by the dotted blue circle. A mirror area was not observed but hackle lines pointing clearly at the fracture origin were noticeable. River lines form nearer to the top surface of the silicon sample where the crack finally propagates through the whole thickness of the sample. Rib lines are perpendicular to the hackle lines which corroborates the location of the fracture origin. Wallner lines could be observed on the left edge of the sample, as the propagating crack most probably sensed edge defects.

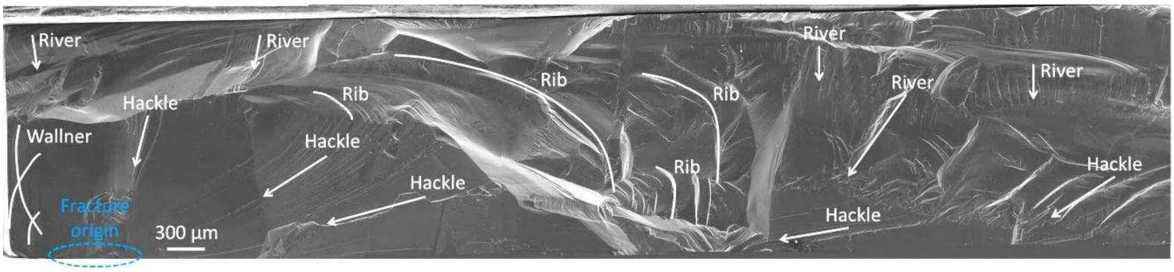

Figure 93 Fracture surface of a 3N mc-Si sample broken with the TPB test.

A closer look of the area in Figure 93 where the fracture origin should be found shows a semi-elliptical defect which is the fracture initiator (see Figure 94). The Bansal macroscopic failure criterion presented in section 3.3.1.3 with equation (3.18) predicts a fracture stress of 143.5 MPa for the measured defect dimensions in Figure 94 and for the fracture toughness at the top of the *3N* mc-Si block, 1.33 MPa $\sqrt{\text{m}}$. The measured fracture stress is 159 MPa, thus the Bansal criterion is a good approximation for correlating mechanical strength with defect size of mc-Si.

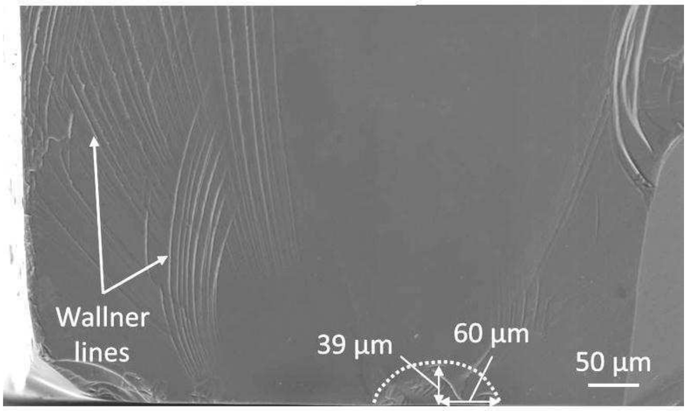

Figure 94 Area of the fracture surface depicted in Figure 93 where the fracture origin of the mc-Si sample is located.

Sometimes fracture initiation features cannot be found easily. It can be that the particle or group of particles loosened after fracture or it can be that a crack is first formed in a region with tensile residual stress. Once the crack is formed cleavage occurs. This could be the micro-mechanism of fracture at grain boundaries or twins. Thus, the risk of not locating the fracture origin and not measuring correctly its size can impede the proper application of macroscopic fracture criteria.

4.4.3 Silicon Oxide Crystallites

The presence of SiO_x particles with the form of crystallites was observed with the SEM (see Figure 76 a)) in the whole body of the *B-doped* mc-Si block. The impact of crystalline SiO_x particles on the mechanical properties of silicon must be also analyzed as amorphous and crystalline SiO_x particles have almost identical elastic constants but different thermal expansion coefficients (see Table 4).

The measured mechanical strength and the fracture toughness which showed high values could be due to the presence of these particles in *B-doped* mc-Si. Fracture hackle lines of the *B-doped* broken mc-Si samples with this type of particles showed a peculiar zig-zag shape (see Figure 76 a)) which is a manifestation of the resistance that this material exerts against fracture. Also the change of the plane of propagation of the crack can be observed in Figure 95 where the crack even braches into two planes of propagation as it reaches the position where small particles are located. The deflection of the planes of propagation of the crack in neighboring twin grains can also be observed in this image.

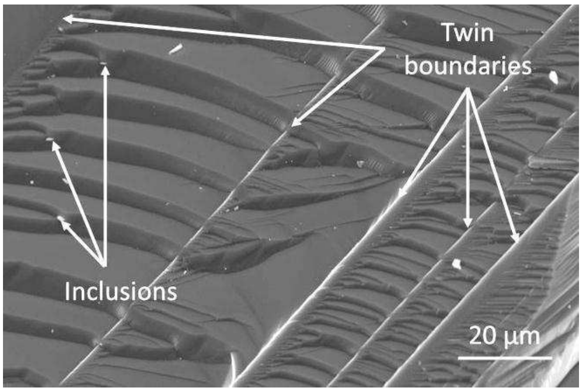

Figure 95 Deflection of the planes of crack propagation in neighboring twin boundaries and branching of the crack plane where small particles are located.

The lower measured fracture toughness in the middle and top positions the *B-doped* mc-Si block could be most probably a consequence of the presence of metallic clusters (see Figure 77 and Figure 78) as explained in section 4.4.1.

Figure 96 depicts the profiles of residual thermal stress in the vicinities of crystalline SiO_x particles. Tangential thermal stresses are compressive while radial thermal stresses are tensile and reach values beyond 450 MPa at the particle´s interface.

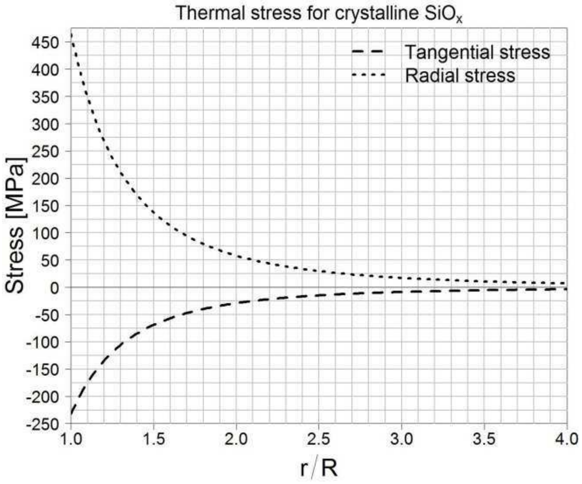

Figure 96 Radial and tangential residual thermal stress profiles in the surroundings of a crystalline SiO_x particle.

The large thermal radial stresses reveal that the critical particle size for circumferential micro-cracking in the case of crystalline SiO_x particles is small. The model of Davidge [36] predicts a value of critical crystalline SiO_x particle radius which is 2.34 µm (see Table 7). According to Ito et al. [37] the minimum critical particle radius is 3.26 µm for crystalline SiO_x particles with initial flaws at the particle´s interface that extend 60-120°. If the impurity particle is considered to exhibit a circular form, the critical particle radius is according to Evans 12.43 µm.

The most conservative critical particle radius calculated with the Davidge model assures that spontaneous micro-cracking in the surroundings of crystalline SiO_x particles does not occur for particles with radius smaller than ~2 µm. Cracks around the particles that have smaller radius than 1 µm are not observed with the SEM (see Figure 76 a)).

Table 7 Minimum critical particle radius for crystalline SiO_x particles within a silicon matrix

Particle	*R* (Davidge) [µm]	*R* (Ito) [µm]	*R* (Evans) [µm]
SiO_x	2.34	3.26	12.43

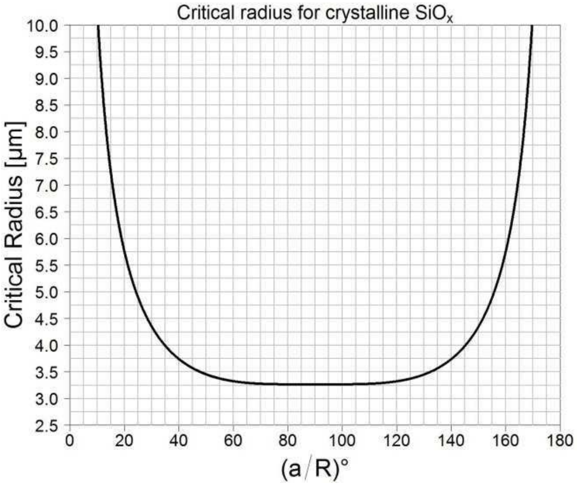

Figure 97 Critical radius for spontaneous micro-cracking during the cooling step of the crystallization of mc-Si against the initial flaw size at the crystalline SiO_x particle interface.

When a load is applied in the surroundings of a crystalline SiO_x particle, the stress field is disturbed by the presence of the particle, as it has lower elastic constants than silicon. Figure 98 depicts the stress profiles at the particle´s interface against the orientation with the applied load (see also Figure 11). When a uniaxial load of 150 MPa is applied radial elastic stresses are less intense than the applied load while tangential stresses oriented between 55° and 125° from the applied load are intensified (see Figure 98). The intensification of tangential elastic stress is maximum at 90° from the applied load where the elastic stress reaches a value of ~240 MPa.

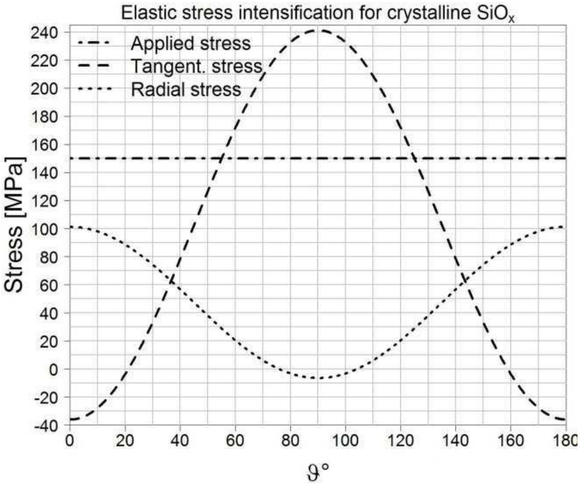

Figure 98 Radial and tangential elastic stress profiles in the surroundings of a crystalline SiO_x particle.

Radial thermal and elastic stresses are both tensile but the elastic stress is less intense than the applied stress while tangential thermal and elastic stresses are compressive and tensile respectively. The maximum overlap of both tangential and radial stresses must be analyzed to check which stress overlap is the most inconvenient for crystalline SiO_x particles.

The maximum overlap of radial thermal and elastic stresses occurs at an orientation of 0° from the applied load and is depicted in Figure 99 a). In the case that 150 MPa are applied in the vicinities of a crystalline SiO_x particle, the particle would be experiencing more than ~550 MPa at its interface due to the overlap of stresses.

The maximum overlap of tangential thermal and elastic stresses occurs at an orientation of 90° from the applied load and is depicted in Figure 99 b). In the case that 150 MPa are applied in the vicinities of a crystalline SiO_x particle, the particle would be experiencing ~10 MPa at its interface due to the overlap of stresses.

Therefore, the overlap of radial stresses is the configuration of stresses that causes fracture in the surroundings of crystalline SiO_x particles.

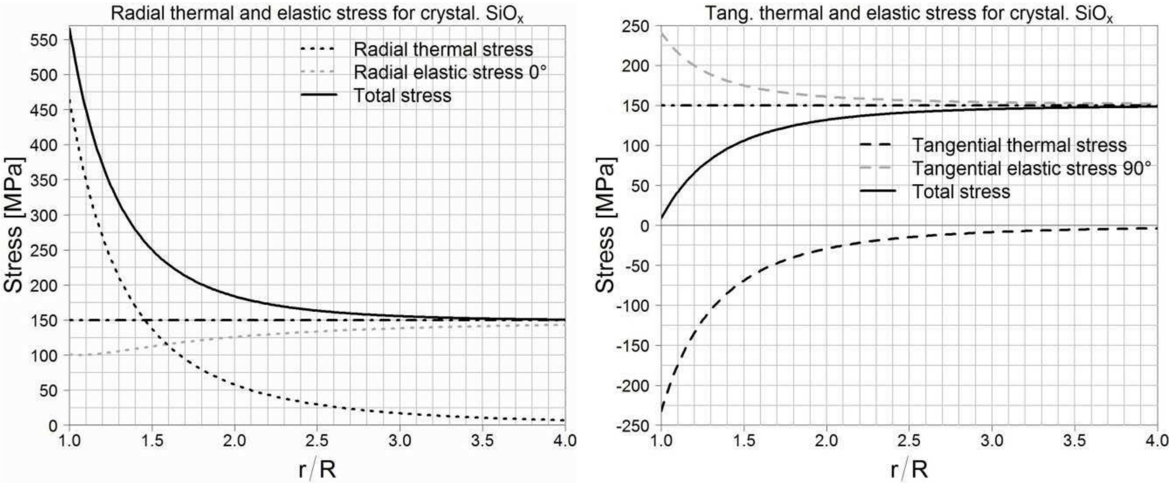

a) b)

Figure 99 Overlap of tangential thermal and elastic stress in the surroundings of a crystalline SiO_x *particle.*

Ranges for the failure criteria near crystalline SiO_x particles depending on the particle geometry are depicted in Figure 100. A conservative failure criterion can be used for fracture prediction if the overlap of radial thermal and elastic stresses is considered to act on a particle sized crack when an external load is applied. This failure criterion described by Equation (2.96) is depicted by the solid line in Figure 100. The dotted and dashed lines present the failure criterion according to Green [41] and described by equation (2.101) for two different sizes of initial flaws at the particle´s interface. This failure criterion considers that fracture is caused by circumferential crack extension when a load is applied in the surroundings of a spherical particle. Thermal stresses are considered for this fracture criteria but intensification of the applied load is not taken into account.

The calculated characteristic stress at 58% of the block height of the *B-doped* mc-Si block, broken with the TPB test, is considered here for further analysis. The calculated characteristic stress is 178.2 MPa. If the abscissas value for the characteristic stress is read in Figure 100, the critical particle radius for crystalline silicon oxide can be obtained. The Green criterion predicts critical crystalline SiO_x particle radii of 1.7 and 3.25 µm for initial flaws that extend 70° and 18° at the particle´s interface respectively. The conservative failure criterion predicts a critical particle radius of 0.75 µm if the crystalline SiO_x concentrates the stress as a surface scratch-like crack.

The consideration of the particle as a spherical particle with an interfacial initial flaw gives a better fracture criterion than the conservative failure criterion. SiO_x particles do not have spherical forms; instead, they have angular forms (see Figure 76 a)). The consideration of a spherical particle can underestimate stress concentration at the corners of the particle. A conservative solution for this issue is the consideration of stress intensification at initial flaws at the particle´s interface. Thus, critical radii in the range of 1.7 to 3.25 µm are expected to cause the fracture of *B-doped* mc-Si at 178.2 MPa depending on the sharpness of the particle.

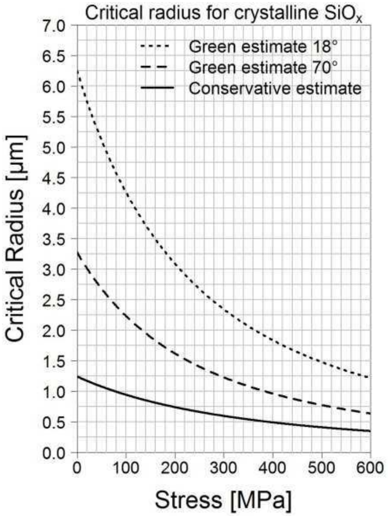

Figure 100 Critical particle radius of a crystalline SiO_x particle when an external load is applied.

The relative high values of fracture toughness measured with the *B-doped* mc-Si could be also due to the presence of crystalline SiO_x particles. Figure 101 shows the change of stress intensity factor at the tip of a crack as it approaches a crystalline SiO_x particle. The tip of the crack experiences a decrease in stress intensity factor as it approaches the particle. The dotted line depicts the stress intensity factor at the tip of the crack due to the residual tangential thermal stress in the surroundings of a particle with 1 µm radius. The dashed line represents the stress intensity factor in the presence of the crystalline SiO_x particle that results when the crack approaches the particle and a biaxial load which induces a stress intensity factor of 0.6 $\mathrm{MPa}\sqrt{\mathrm{m}}$ in the absence of the particle is applied. The overlap of both thermal and elastic stress intensity factors indicates that a crack at the particle´s interface experiences a stress intensity factor of 0.49 $\mathrm{MPa}\sqrt{\mathrm{m}}$ when a biaxial load exerting a stress intensity factor of 0.6 $\mathrm{MPa}\sqrt{\mathrm{m}}$ is applied. Thus, the crack is decelerated as it approaches the crystalline SiO_x particle and the effective toughness of the material raises. For larger SiO_x particles with larger radius, the stress intensity factor due to tangential thermal stresses would be lower. Thus, larger crystalline SiO_x particles would increase the effective fracture toughness of mc-Si in a larger extent. Nevertheless, this increase in fracture toughness may not be translated into an increase in mechanical strength as the same larger crystalline SiO_x

particles acting as fracture origins would lead to the measurement of lower mechanical strength of mc-Si. B is reported in the literature to suppress the growth of SiO_x precipitates [133], which in the case of crystalline SiO_x particles allows the transfer of the benefit of the increase in fracture toughness into an increase in mechanical strength.

The change in critical stress intensity factor that experiences a crack approaching a crystalline SiO_x particle when a uniaxial load is applied can be read from the dotted line of Figure 15. SiO_x is softer than silicon, and a propagating crack must release the half of the energy for its propagation when it reaches de particle´s interface. With the aid of equation (2.41), it can be calculated that the critical stress intensity factor of silicon reduces from $0.9\ \mathrm{MPa}\sqrt{\mathrm{m}}$ to $0.64\ \mathrm{MPa}\sqrt{\mathrm{m}}$ at the particle´s interface. Tangential thermal stresses at the interface of a particle with 1 µm radius lower the intensity factor in $0.22\ \mathrm{MPa}\sqrt{\mathrm{m}}$ (see Figure 101). Thus, a uniaxial load that exerts an intensity factor of $0.86\ \mathrm{MPa}\sqrt{\mathrm{m}}$ must be applied to cause fracture by circumferential cracking which is a value of stress intensity factor very near the value $0.9\ \mathrm{MPa}\sqrt{\mathrm{m}}$ that would cause fracture cracking in the absence of SiO_x particles. Thus, SiO_x particles almost do not influence the fracture toughness of mc-Si under uniaxial loading according to these theoretical calculations. However, the small size and high density of these particles in *B-doped* mc-Si most probably allows the toughening by other mechanisms like crack branching shown in Figure 95 or crack bowing at SiO_x particles.

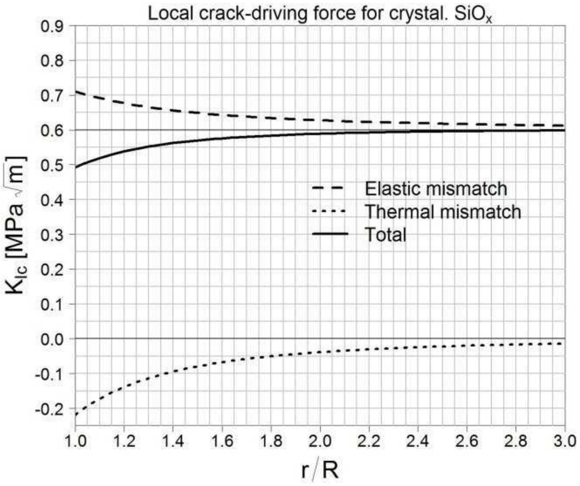

Figure 101 Overlap of stress intensity factors due to thermal and elastic mismatch at the tip of a crack approaching a crystalline SiO_x particle.

The Bansal [112] criterion (see equation (3.18)) is also applied for fractography analysis of the images in Figure 102. Taking the value of fracture toughness at 89% and 58% of the block height, $1.38\ \mathrm{MPa}\sqrt{\mathrm{m}}$ and $1.79\ \mathrm{MPa}\sqrt{\mathrm{m}}$ respectively, and the dimensions of the semi-elliptical flaw measured in the images, the calculated fracture stresses can be compared with the measured fracture stress. The calculated stresses were 128 MPa (image a) and 194 MPa (image b) and the measured stresses were 140 MPa and 201 MPa respectively. The comparison of both values of stresses shows that the Bansal failure criterion can predict fracture stresses with an acceptable accuracy when the fracture toughness of the material and the dimensions of the defect causing failure can be measured.

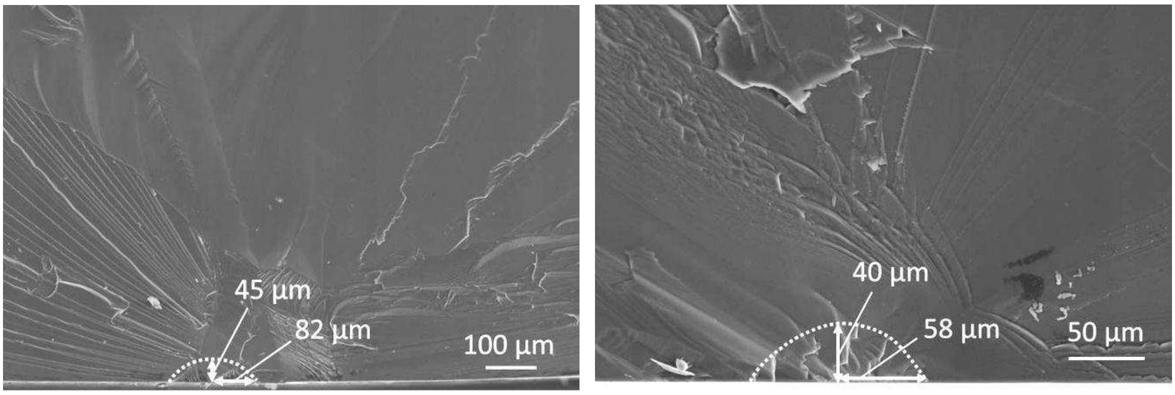

a) b)

Figure 102 Fracture origins of B-doped mc-Si samples that broke with 140 MPa (image a) and 201 MPa (image b) at 89% and 59% of the relative block height respectively.

4.4.4 Silicon Nitride

The precipitation of Si_3N_4 and SiC particles was observed by the inspection of the samples from the *4N+Al* mc-Si block with the SEM (see Figure 65 and Figure 66). The density of these precipitates increased from the bottom to the top of the block due to the segregation of nitrogen and carbon to the upper part of the block. A decrease in the mechanical strength measured with the three-point bending test was observed in the first half of the *4N+Al* mc-Si silicon block (see Figure 59) and fractography analysis showed radial cracking originated at Si_3N_4 silicon nitride particles (see Figure 109 a)).

Tangential thermal stresses are tensile and reach a value of 140 MPa at the particle´s interface, whereas radial stresses are compressive (see Figure 103). Calculations of thermal stresses for SiC and Si_3N_4 particles within a silicon matrix have been also performed in the literature [134], [135].

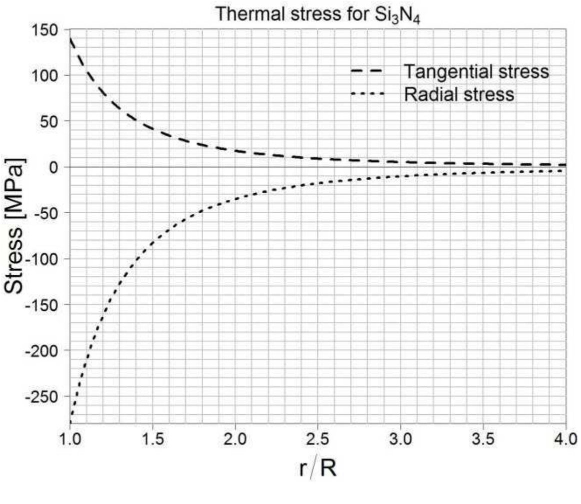

Figure 103 Radial and tangential residual thermal stress profiles in the surroundings of a Si_3N_4 particle.

If the Si_3N_4 particle is considered to be spherical with an annular initial flaw in its equator, the minimum critical particle radius is 175 µm (see Table 8 and Figure 104) for an initial flaw length of ~0.3R. If the Si_3N_4 particle is considered to be circular with an initial flaw size length of 0.2R and perpendicular to the particle´s interface, the critical particle radius is

436 µm. The observed particle sizes were smaller than these two hypothetical cases (see Figure 65); therefore, radial micro-cracking of the silicon matrix does not occur in the surroundings of the Si_3N_4 particles after the crystallization process.

Table 8 Minimum critical particle size for Si_3N_4 particles within a silicon matrix.

Particle	*R* (Green) [µm]	*R* (Evans) [µm]
Si_3N_4	175.03	435.95

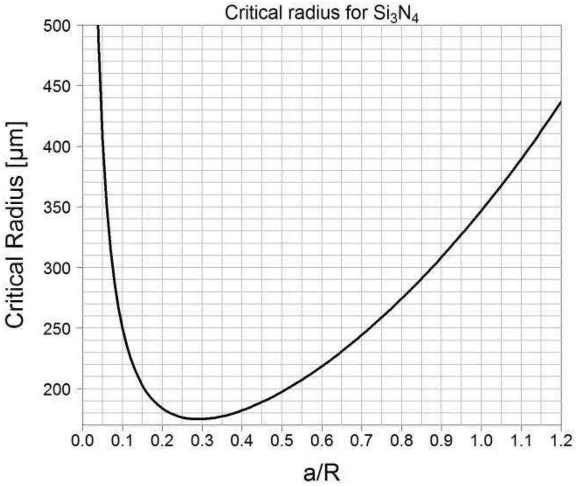

Figure 104 Critical radius for spontaneous micro-cracking during the cooling step of the crystallization of mc-Si against the initial flaw size at a Si_3N_4 particle interface.

When a load is applied in the surroundings of a Si_3N_4 particle, the stress field is disturbed by the presence of the particle because Si_3N_4 has greater elastic constants than silicon. Figure 105 depicts the stress profiles at the particle´s interface against the angle of orientation with the applied load.

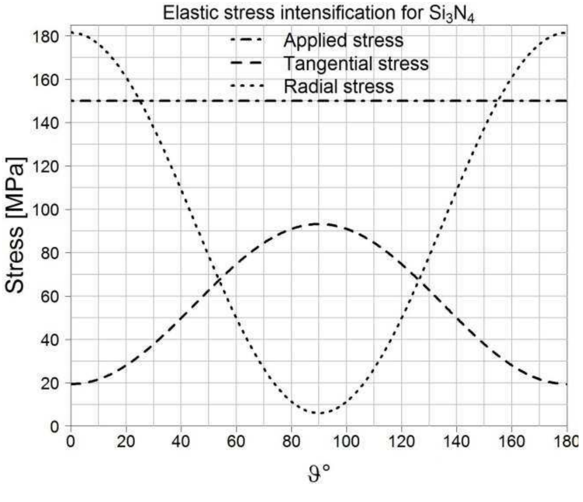

Figure 105 Radial and tangential elastic stress profiles in the surroundings of a Si_3N_4 particle.

Tangential elastic stresses are less intense than the applied load while radial stresses oriented 0-25° and 155-180° from the applied load are intensified. The intensification of radial elastic stress when a load of 150 MPa is applied is maximum at 0° and 180° from the applied load. The radial elastic stress reaches a value of ~180 MPa in these orientations.

The overlap of tangential and radial thermal and elastic stresses is depicted in Figure 106. The intensification of radial elastic stresses is maximum at an orientation 0° and 180° from the applied load, but as the magnitude of the radial compressive thermal stresses is larger, a Si_3N_4 particle remains under compression in its vicinities for the given orientations (see Figure 106 a)) when actually a tensile stress of 150 MPa is applied.

Tangential elastic stresses are lower than the applied stress but maximum at an orientation 90° from the applied load. The overlap of tangential elastic stresses with tensile tangential thermal stress reaches a value of ~230 MPa at the particle´s interface for the given orientation (see Figure 106 b)) when only 150 MPa are applied. The latter is the most critical configuration of overlap of thermal and elastic stresses that can cause failure in the surroundings of a Si_3N_4 particle.

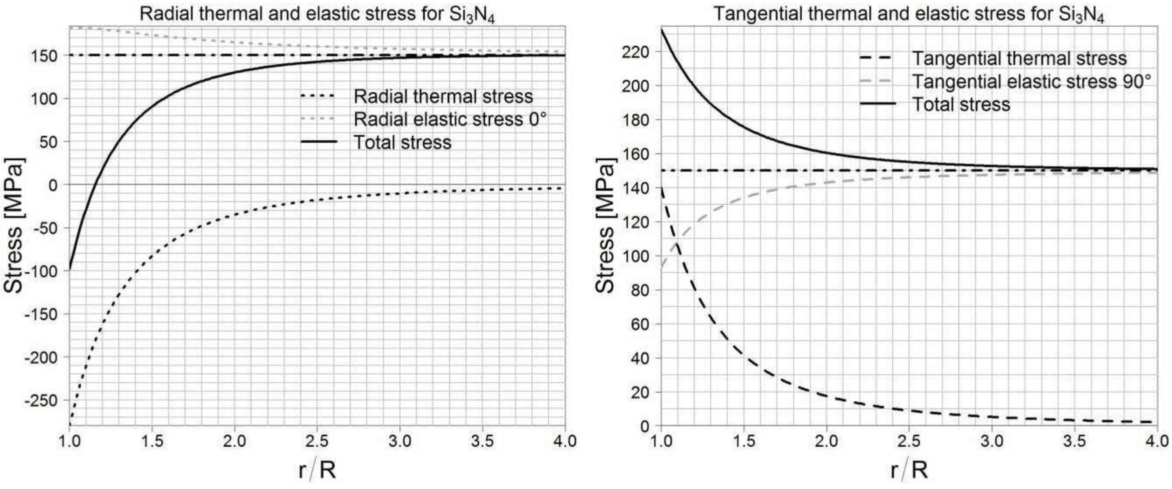

a) b)

Figure 106 Profiles of thermal stress and intensification of stress for an applied load of 150 MPa, in the case of a Si_3N_4 particle.

The calculated characteristic stress at 58% of the block height of the *4N+Al* mc-Si block, broken with the TPB test, is considered here for microscopic failure prediction as relevant amount of Si_3N_4 particles were found at this block height. The calculated characteristic stress is 136.8 MPa. If the abscissas value for the characteristic stress is read in Figure 107, the critical particle radius for Si_3N_4 can be obtained. The Green and Evans criteria for radial cracking predict a critical particle size of 32 and 74 µm respectively. The conservative failure criterion predicts a smaller critical particle size of 5 µm. Si_3N_4 particles do not appear with spherical forms, but they do appear with angular forms (see Figure 109 a)). The consideration of a spherical particle by Green´s model can underestimate stress concentration at the corners of the particle. A conservative solution for this issue is to consider stress intensification at initial flaws at the particle´s interface. Initial flaw sizes of $0.2R$ are considered for both the Green and the Evans criteria. These two failure criteria provide a better approximation than the conservative failure criterion for the critical particle size that causes radial cracking. The difficulty in deciding which failure criteria is most suitable for Si_3N_4 particles lies in the determination of the particle size by microscope observation and comparison with the particle sizes calculated by different models. For the purpose of this work, we choose the Green failure criterion, which is more conservative than the Evans criterion.

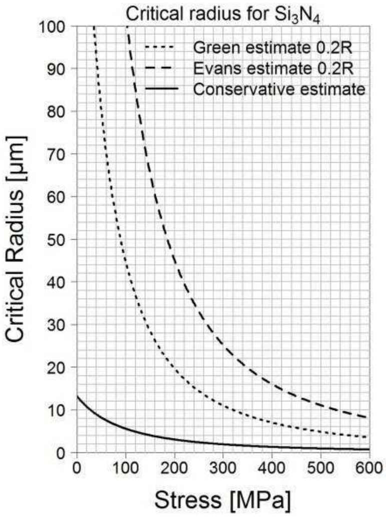

Figure 107 Critical particle radius of Si_3N_4 *particles when an external load is applied.*

Figure 108 a) shows the change of stress intensity factor at the tip of a crack as it approaches a Si_3N_4 particle. The tip of the crack experiences an increase in stress intensity factor as it approaches the particle. The dotted line depicts the stress intensity factor at the tip of the crack due to the residual tangential thermal stress in the surroundings of a Si_3N_4 particle with 30 µm radius. The dashed line represents the stress intensity factor that results when the crack approaches the particle and a biaxial load which induces a stress intensity factor of 0.6 MPa $\sqrt{\mathrm{m}}$ is applied. The overlap of both thermal and elastic stress intensity factors indicates that a crack at the particle´s interface experiences a stress intensity factor of almost 1.24 MPa $\sqrt{\mathrm{m}}$ when only a biaxial load of 0.6 MPa $\sqrt{\mathrm{m}}$ is applied. Thus, the crack is accelerated to the Si_3N_4 particle and the effective toughness of the material diminishes.

The change in critical stress intensity factor that a crack approaching a Si_3N_4 particle experiences when a uniaxial load is applied can be read from the dashed line of Figure 15. The propagating crack needs to release approximately twice the energy for its propagation when it reaches the interface of a Si_3N_4 particle because Si_3N_4 is stiffer than silicon. With the aid of equation (2.41), it can be calculated that the critical stress intensity factor of silicon increases from 0. 9 MPa $\sqrt{\mathrm{m}}$ to 1.27 MPa $\sqrt{\mathrm{m}}$. Thermal stresses at the interface of a particle with 30 µm provides already 0.72 MPa $\sqrt{\mathrm{m}}$ (see Figure 108 a)) according to Khaund et al. [53]. Thus, the application of a uniaxial load that adds 0.55 MPa $\sqrt{\mathrm{m}}$ would cause the cracking through the Si_3N_4 particle. This value is still lower than the 0.9 MPa $\sqrt{\mathrm{m}}$ needed for crack propagation in silicon without second phase particles; therefore, the toughness of silicon diminishes.

This analysis concludes that Si_3N_4 particles may not be responsible for the light increase in toughness within the first half of the *4N+Al* mc-Si block which will be further discussed in the next section. The low values of fracture toughness of the *UMG* mc-Si block (see Figure 63 c)) could be due to the presence of big sized clusters in mc-Si which contained O, N, C and Al. This clusters that apparently do not show any crystallographic structure (see Figure 79 a)) most probably introduce large tangential tensile thermal stresses similarly to the Si_3N_4 particles and thus the fracture toughness of the material diminishes.

According to Figure 108 b) the presence of Si_3N_4 in the silicon matrix would increase the elastic modulus of silicon. Results depicted in Figure 59 show higher values of elastic modulus within the first half of the *4N+Al* mc-Si block where Si_3N_4 and SiC particles are observed. The dynamic elastic modulus measured with the *UMG* mc-Si samples indicates that Si_3N_4 particles may be also encountered in the material. In the case that the high values of measured elasticity modulus, ~175 MPa, are due to the presence of Si_3N_4, the content of Si_3N_4 particles can be read in the graph of Figure 108 b) and is in the range between 11% and 12% of volume fraction.

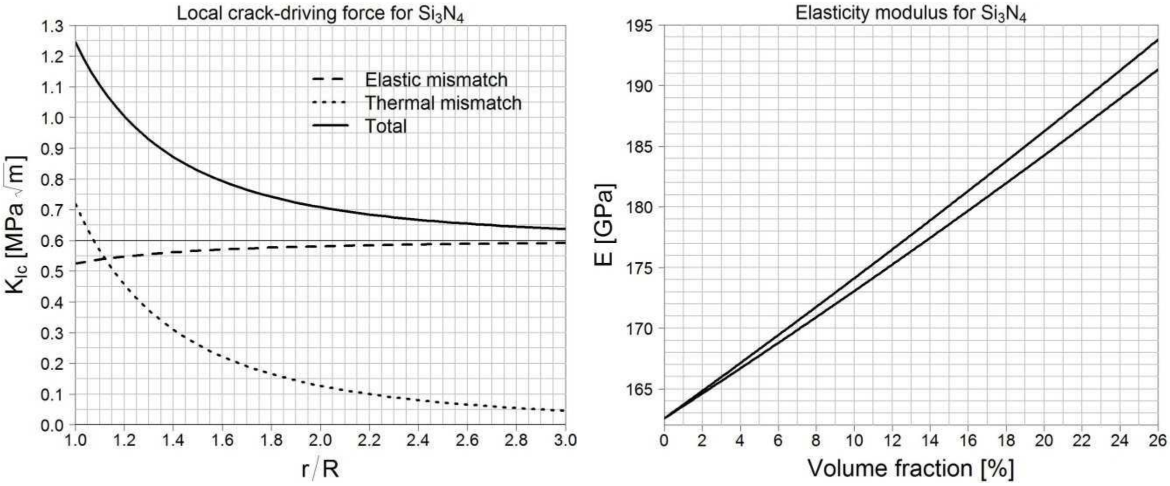

a) b)

Figure 108 Image a) depicts the overlap of stress intensity factors due to thermal and elastic mismatch at the tip of a crack approaching a Si_3N_4 particle. Image b) shows the increase in elastic modulus against volume fraction of Si_3N_4 particles in the silicon matrix.

The Bansal [112] criterion (see equation (3.18)) for fractography analysis can be applied in the fracture origin of a *4N+Al* mc-Si sample that broke under 158.8 MPa. Taking the value of fracture toughness at 58% of the block height, $K_{Ic} = 1.61\ \mathrm{MPa}\sqrt{\mathrm{m}}$, and the dimensions of the semi-elliptical flaw measured from Figure 109 b), $a = 46\ \mu\mathrm{m}$ and $c = 146\ \mu\mathrm{m}$, the calculated fracture stress is 134.2 MPa. The Bansal criterion is still inaccurate compared to the measured fracture stress value. The inaccuracy is 15% and the Bansal model gives a maximum error of 5%. In some cases, the fracture of mc-Si is almost too complicated for macroscopic fractography analysis. The inaccuracy could lie on the difficulty of measuring the dimensions of the fracture origin, as a clear mirror area with a semi-elliptical flaw is not easy to observe. Another reason could be also the inhomogeneity of mc-Si as the error bars of fracture toughness are large and therefore taking the mean value of fracture toughness can be inaccurate for single samples.

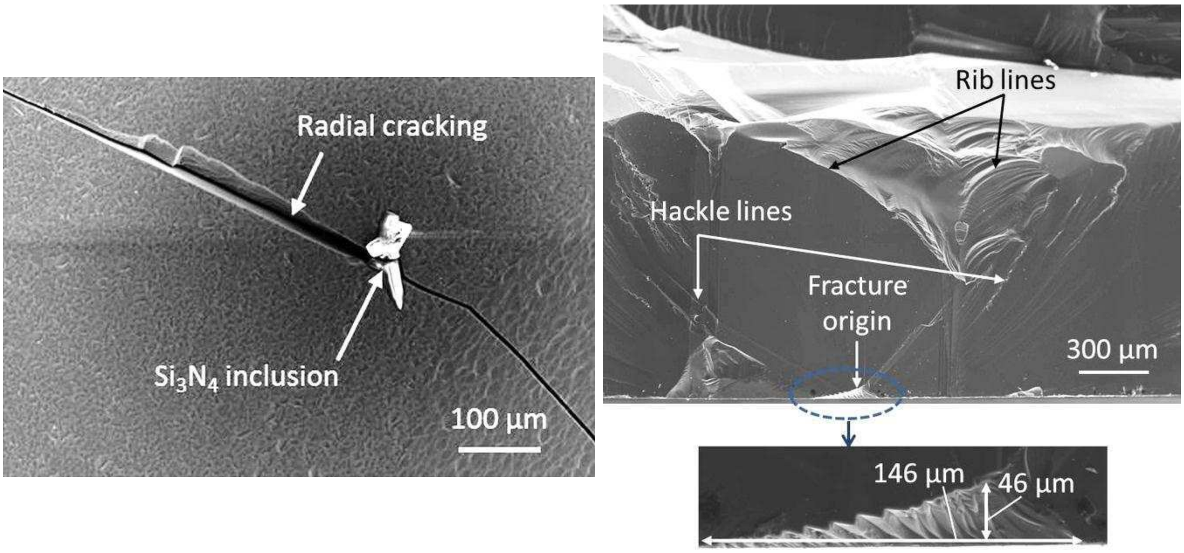

a) b)

Figure 109 Front and cross section of fracture of two different samples containing Si_3N_4 *particles.*

4.4.5 Silicon Carbide

SiC precipitation was observed within the *4N+Al* mc-Si block, within the upper half of the *3N* mc-Si and at the top part of the *B-doped* and *SoG* mc-Si blocks. The density of SiC particles usually increases in the direction bottom to top of the mc-Si blocks due to the segregation of carbon to the upper parts of the blocks. We proceed in this section with the analysis of the influence of SiC particles in all mechanical properties in order to evaluate its effect on the mechanical behavior of mc-Si wafers.

Figure 110 depicts the profiles of residual thermal stress in the vicinities of SiC particles. Radial thermal stresses are tensile and reach a value of almost 70 MPa at the particle´s interface while tangential stresses are compressive. Calculations of thermal stresses for silicon carbide and silicon nitride particles within a silicon matrix have been also performed in the literature [134], [135].

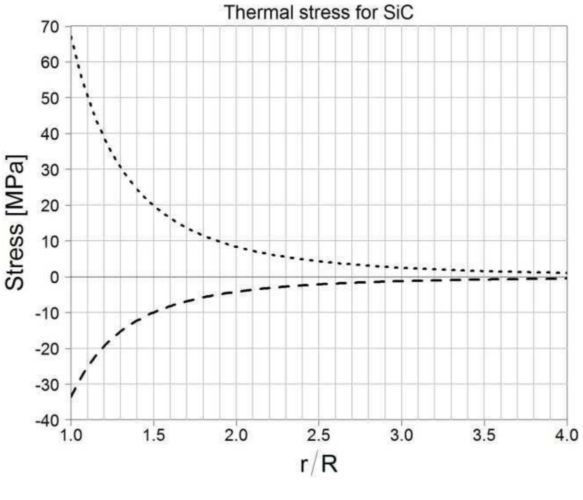

Figure 110 Radial and tangential residual thermal stress profiles in the surroundings of a SiC particle.

If the particle is considered to be spherical, the minimum critical particle radius for spontaneous micro-cracking is 252 µm for initial flaws that extend between 70° and 110° at the particle´s interface (see Figure 111 and Table 9) according to Ito et al [37]. The Davidge model [36] also considers a spherical particle and appears more conservative than the Ito et al. model. If the SiC particle is considered circular with an initial flaw size of 0.2*R*, the critical particle radius is 563 µm. The observed particle sizes were smaller (see Figure 65 a)) than the calculated critical radius and therefore radial micro-cracking of the silicon matrix does not occur in the surroundings of SiC particles.

Table 9 Minimum critical particle size for SiC particles within a silicon matrix.

Particle	*R* (Davidge) [µm]	*R* (Ito) [µm]	*R* (Evans) [µm]
SiC	252.16	351.38	562.87

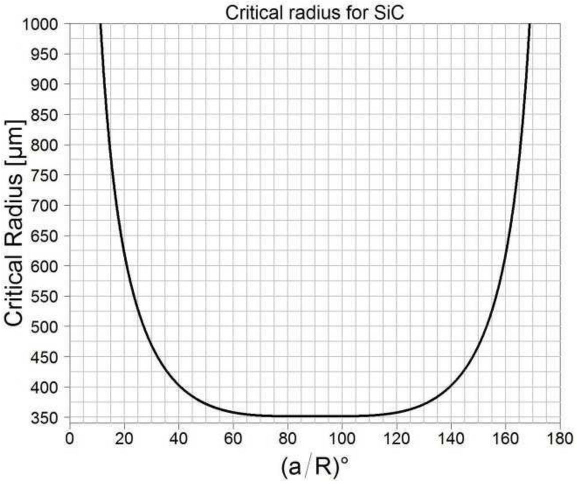

Figure 111 Critical radius for spontaneous micro-cracking during the cooling step of the crystallization of mc-Si against the initial flaw size at the SiC particle interface.

When a load is applied in the surroundings of a SiC particle, the stress field is disturbed by the presence of the particle, as SiC has higher elastic constants than silicon. Figure 112 depicts the stress profiles at the particle´s interface against the orientation with the applied load when a uniaxial load of 150 MPa is applied. Tangential elastic stresses are less intense than the applied load while radial stresses oriented 0-25° and 155-180° from the applied load are intensified (see Figure 112). The intensification of radial elastic stress is maximum at 0° and 180° from the applied load where the elastic stress reaches a value of ~180 MPa.

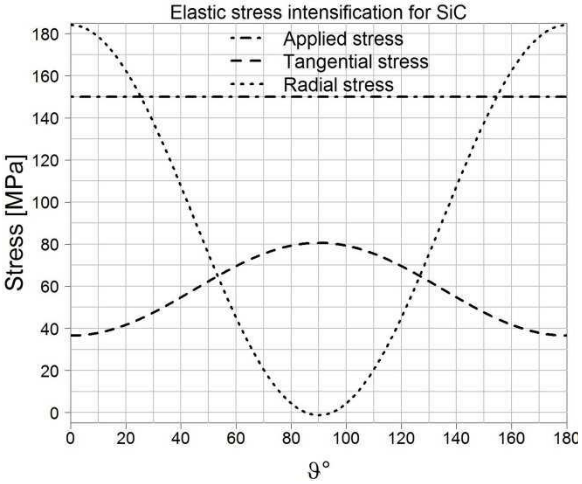

Figure 112 Radial and tangential elastic stress profiles in the surroundings of a SiC particle.

Both radial thermal and elastic stresses are tensile in the case of SiC particles. The maximum overlap of tensile radial thermal and elastic stresses occurs at an orientation of 0° and 180° from the applied load and is depicted in Figure 113. In the case that 150 MPa is applied in the vicinities of SiC, the particle would experience 250 MPa at its interface due to the overlap of radial stresses.

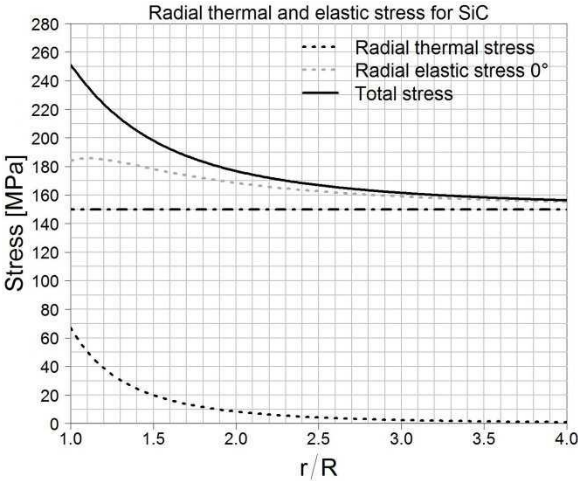

Figure 113 Overlap of radial thermal and elastic stress in the surroundings of a SiC particle.

The calculated characteristic stress at 86% of the block height of the *SoG* mc-Si block, broken with the TPB, is considered here for microscopic failure prediction as relevant amount of SiC particles were found at this block height. The calculated characteristic stress is 200.4 MPa. If the abscissas value for the characteristic stress is read in Figure 114, the critical particle radius for SiC can be obtained. The Green criterion for circumferential cracking predicts critical particle radius of 24 and 46 µm for initial interfacial flaws that extend 70° and 18° respectively. The conservative failure criterion predicts a critical particle radius of ~2 µm. SiC particles do not appear with spherical but angular or cylindrical forms (see Figure 65, Figure 73 and Figure 80 b)). The consideration of a spherical particle can underestimate stress concentration at the corners of the particle. A conservative solution for this issue is the consideration made in this work of stress intensification at initial flaws at the particle´s interface. The Green failure criterion provides a better approximation than the conservative failure criterion for the critical particle size that causes cracking. The difficulty in deciding which initial flaw describes best the particle irregular shape resides, like in the case of Si_3N_4 particles, in the determination of the size of the particles. The proper measurement of the mean radius size of angular and cylindrical silicon carbide particles could help in the deliberation of which initial flaw size fits the best. For the purpose of this work we choose the initial flaw size that extends 70° at the particle´s interface. In this case, the particle critical radius is 24 μm which is a magnitude in the range of the particles size observed in the images indicated above.

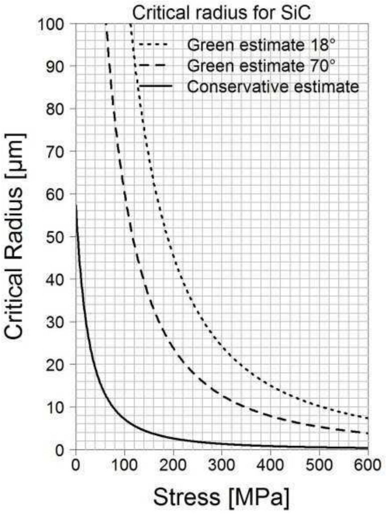

Figure 114 Critical particle radius of SiC when an external load is applied.

Figure 116 a) shows the change of stress intensity factor at the tip of a crack as it approaches a SiC particle. The tip of the crack experiences a decrease in stress intensity factor as it approaches the particle. The dotted line depicts the stress intensity factor at the tip of the crack due to compressive tangential residual thermal stress in the surroundings of a SiC particle with 30 μm radius. The dashed line represents the stress intensity factor that results when the crack approaches the particle and a biaxial load which induces a stress intensity factor of $0.6\ \mathrm{MPa}\sqrt{\mathrm{m}}$ is applied. The overlap of both thermal and elastic stress intensity factors indicates that a crack at the particle´s interface experiences a stress intensity factor of $0.36\ \mathrm{MPa}\sqrt{\mathrm{m}}$ when a biaxial load of $0.6\ \mathrm{MPa}\sqrt{\mathrm{m}}$ is applied. Thus, the propagating crack is restrained in the direction to the SiC particle and tries to deflect the particle. The effective toughness of the material increases then.

The change in critical stress intensity factor that a crack approaching a SiC particle experiences when a uniaxial load is applied can be read from the dotted line of Figure 15. The propagating crack needs to release approximately twice the energy for its propagation when it reaches the interface of a SiC particle. With the aid of equation (2.41), it can be calculated that the critical stress intensity factor of silicon increases from $0.9\ \mathrm{MPa}\sqrt{\mathrm{m}}$ to $1.27\ \mathrm{MPa}\sqrt{\mathrm{m}}$. Thermal stresses at the interface of a particle with 30 μm radius increases the toughness in $0.17\ \mathrm{MPa}\sqrt{\mathrm{m}}$ (see Figure 116 a)). Thus, the crack propagation needs the application of a uniaxial load that induces $1.44\ \mathrm{MPa}\sqrt{\mathrm{m}}$. This value is higher than the $0.9\ \mathrm{MPa}\sqrt{\mathrm{m}}$ needed for crack propagation in silicon without SiC particles; therefore, the toughness of silicon increases. This analysis concludes that SiC particles may be responsible for the increase in toughness at the upper parts of mc-Si blocks and at the lower parts of the *4N+Al* mc-Si block. The measured mechanical strength of mc-Si, containing SiC particles with radius sizes smaller than 10 µm, would be significantly high (see Figure 114). In that case, the SiC particles would not represent a critical defect causing fracture and the increase in fracture toughness due to the presence of SiC particles would be very noticeable. This is the case of a silicon sample from the *3N* mc-Si block at 54% of the relative block height that broke under 514 MPa (see Figure 115). Abrupt fracture lines indicate that this silicon sample needed a high energy to fracture and crack paths had to jump or be deflected when finding SiC particles.

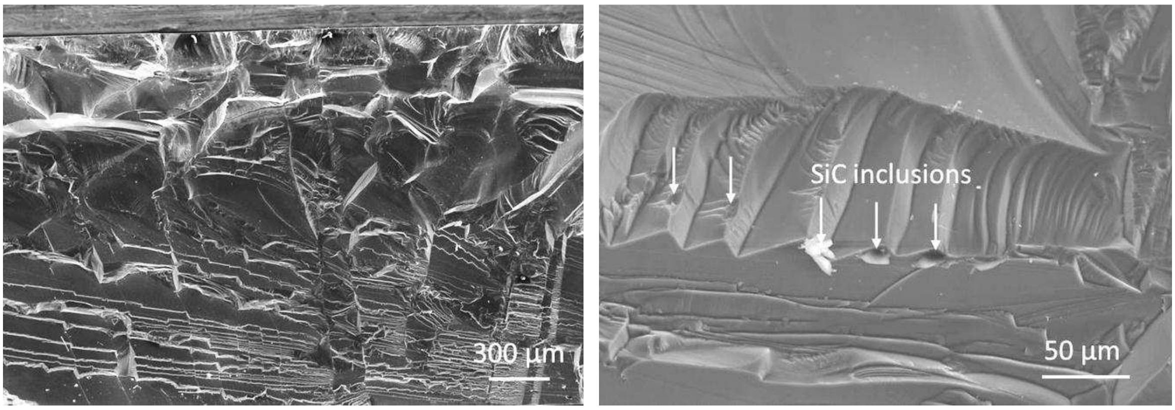

a) b)

Figure 115 Cross sections of fracture of mc-Si samples containing SiC particles. The white arrows in image b) point at possible locations of SiC particles that force the crack to change the propagation plane.

According to Figure 116 b) the presence of SiC in the silicon matrix would increase the elastic modulus of silicon.

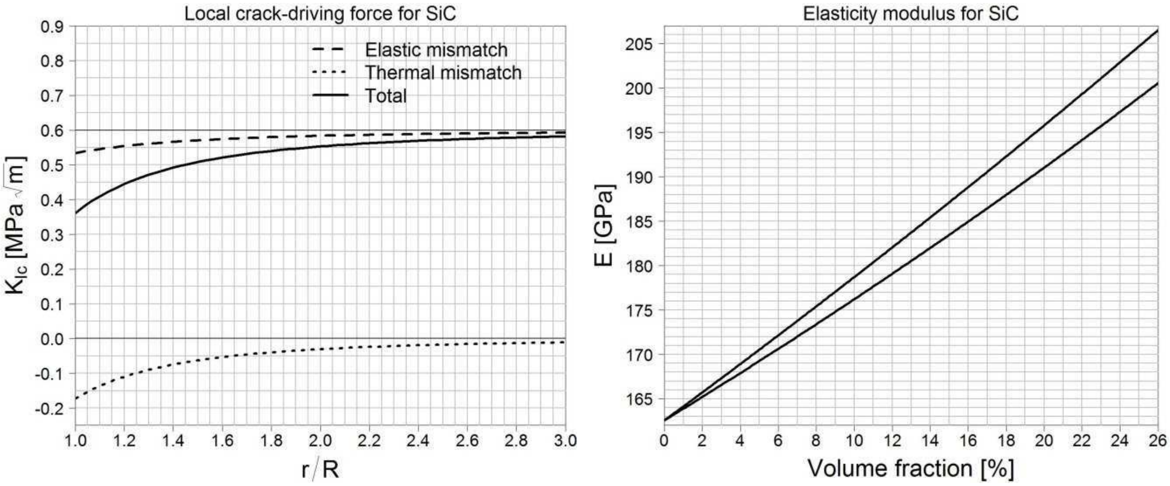

a) b)

Figure 116 Image a) depicts the overlap of stress intensity factors due to thermal and elastic mismatch at the tip of a crack approaching a SiC particle. Image b) shows the increase in elastic modulus against volume fraction of SiC particles in the silicon matrix.

The results of elastic modulus for both *B-doped* and *SoG* mc-Si blocks are above the value of the Hill elastic modulus of silicon and may most probably be caused by the presence of SiC particles within the silicon matrix. The volume fraction of SiC particles contained in the silicon matrix can be read in Figure 116 b). Mc-Si samples with elastic modulus as high as 180 GPa have SiC contents between 11% and 13%.

At the top part of the *4N+Al* mc-Si block, SiC particles appear to play a secondary role in breakage when the precipitation of the particles is not homogeneous (see Figure 117). The sample broke during polishing most probably due to cracks at the surroundings of Al particles (located by the letter "a" in Figure 117). However, initial fracture could have also occurred in the area located by the letter "b". SiC precipitation concentrated within a volume of the material, probably within one grain. This part of the material is very tough and will show high fracture toughness and elastic modulus. Thus, stresses find a resistance to propagate within this area and concentrate in the surroundings of this area which is free of silicon carbide particles. The area located by "b" would concentrate the stress almost like a notch in the material and therefore this area could have also been the fracture origin.

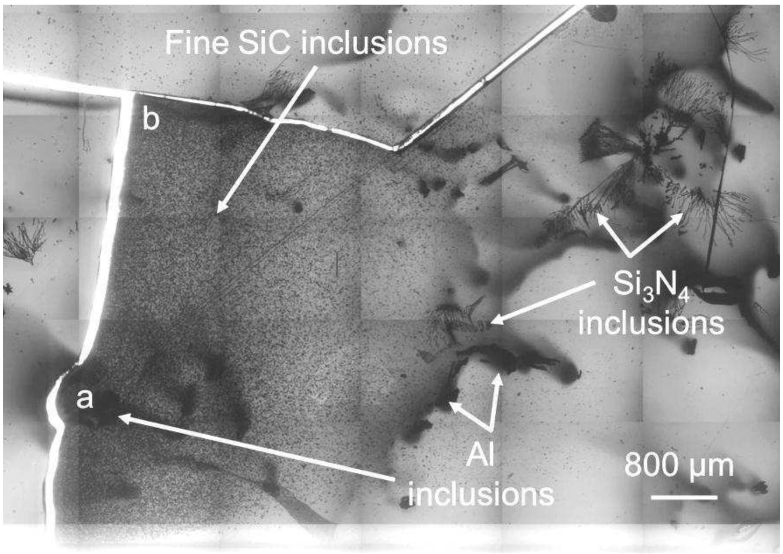

Figure 117 Infrared light microscopy of a polished silicon sample at the top part of the 4N+Al mc-Si block.

5. Experimental Results II

This chapter focuses on the influence of solar cell processes on the mechanical behavior of mc-Si wafers. The mechanical strength after every solar cell processing step from different qualities of mc-Si wafers is measured with the RoR bending test. Experimental values of characteristic stress and elastic modulus measured at different relative heights within the mc-Si blocks after every solar cell processing step are presented and discussed. 4N+Al, 3N and B-doped mc-Si is processed until the manufacture of an epitaxial wafer equivalent while UMG and SoG mc-Si is processed as conventional inert solar cells. High temperature processes can lower moderately the mechanical strength of mc-Si wafers but the most detrimental solar cell processes for the mechanical survival of the wafers are the multi-wire sawing and the metallization processes. The multi-wire sawing process introduces micro-cracks with lengths in the range of several microns which limit the mechanical strength of silicon wafers to a value of approximately 150 MPa. Damage removals by chemical etching or by texture can double the mechanical strength of the wafers while other solar cell processes have a minor impact on the mechanical performance of the wafers. Final solar cells after metallization show comparable mechanical strength to as-cut wafers due to large thermal stresses which eases the formation of cracks in the vicinities of the metallization contacts.

5.1 Influence of Solar Cell Processes on the Strength of Silicon Wafers

5.1.1 Wafer Manufacture

Multi-wire Sawing

The mean value of mechanical strength of as-cut *3N*, *B-doped* and *industry standard* mc-Si and Cz-Si wafers is in the range of 150 and 160 MPa approximately (see Figure 118). This indicates that the damage introduced during the sawing of the wafers with the same cutting parameters is the crucial type of defect limiting the mechanical strength of the wafers. However, in the case of the *4N+Al* mc-Si block the mechanical strength of the silicon wafers decreases in the direction bottom to top of the block which points that a defect already contained in the upper parts of the block has a major impact on the mechanical behavior of the wafers. A reverse tendency is observed in the case of *UMG* and *SoG* mc-Si where the mechanical strength increases in the direction bottom to top of the block. The silicon blocks are cut at once into thin wafers under the same cutting parameter; thus, higher values of mechanical strength at the top of the blocks may indicate that the material properties of silicon, as impurity atoms segregate to the top of the block, exert a resistance to the introduction of sawing damage.

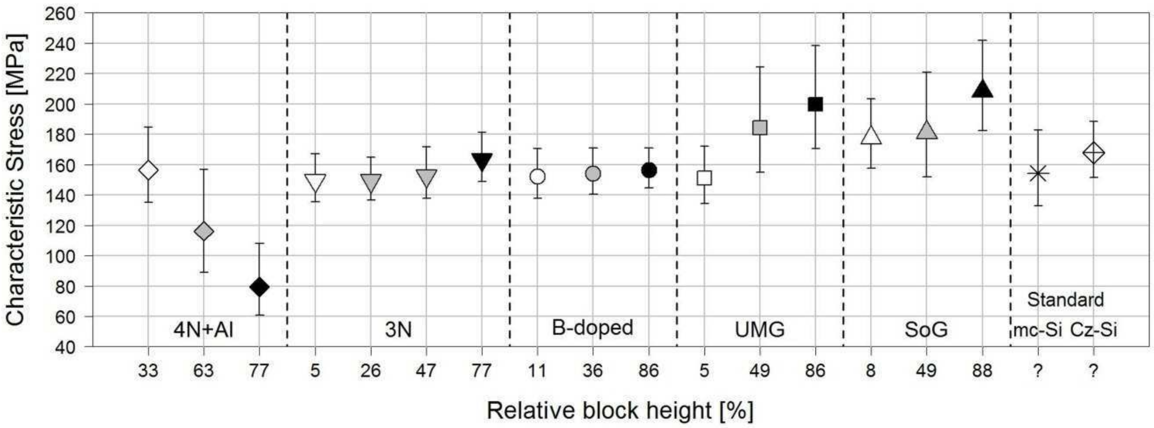

Figure 118 Characteristic stress of mc-Si wafers after multi-wire sawing.

The values of static elastic modulus obtained from the curves of force-displacement of the ROR bending test are depicted in Figure 119. *UMG* and *SoG* mc-Si show slightly higher elastic modulus than the rest of the mc-Si blocks.

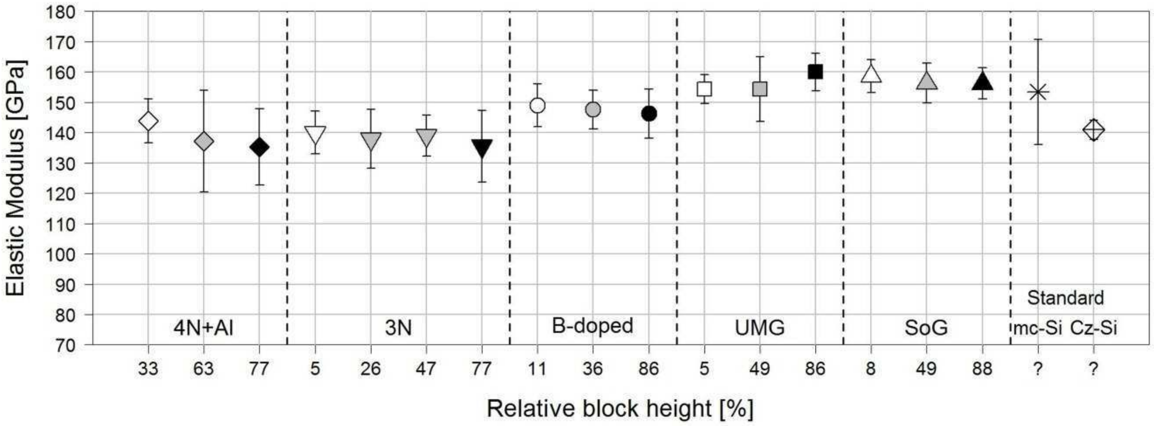

Figure 119 Static elastic modulus of mc-Si wafers after multi-wire sawing.

Damage etch

The comparison of the characteristic stresses depicted in Figure 118 and Figure 120 shows that the removal of the sawing damage approximately doubles the mechanical strength of the silicon wafers. After damage etch the difference in mechanical performance between silicon samples collected at different parts of a block is noticeable and is governed by the defects formed during the crystallization process as explain in Experimental Results I.

4N+Al mc-Si shows a clear deterioration of the mechanical strength and elastic modulus (see also Figure 121) in the direction bottom to top of the block. As already discussed in the previous chapter, *3N* mc-Si exhibits a considerably low mechanical behavior at the bottom of the block and *UMG* and *SoG* mc-Si at the very top of the block.

It must be noticed that *industry standard* Cz-Si shows a higher mechanical strength than *industry standard* mc-Si while having lower elastic modulus. The different orientations of the grains contained in mc-Si wafers can impede partially the bending of the wafers; therefore, the elastic modulus of mc-Si wafers is higher than the elastic modulus of Cz-Si wafers. Moreover, mc-Si has grain boundaries and SiC and Si_3N_4 particles where large residual stresses can be formed during the crystallization process [136]. SiO_x particles are the type of particles that mc-Si and Cz-Si share but still mc-Si contains a broader variety and density of defects and thus the mechanical strength of mc-Si is a little lower.

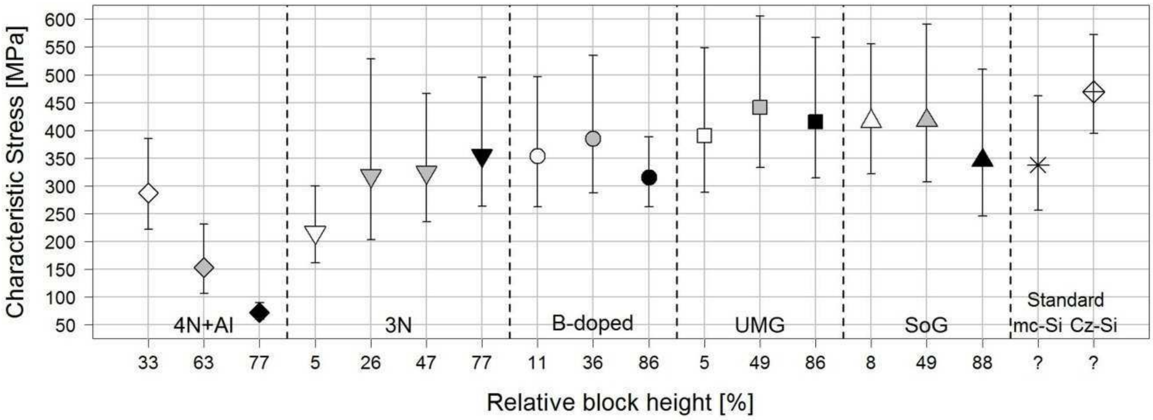

Figure 120 Characteristic stress of mc-Si wafers after damage etch.

The comparison of static elastic modulus between mc-Si blocks of different qualities is more homogeneous than after multi-wire sawing and is approximate to the value of 145 GPa with exception of the *4N+Al* mc-Si block.

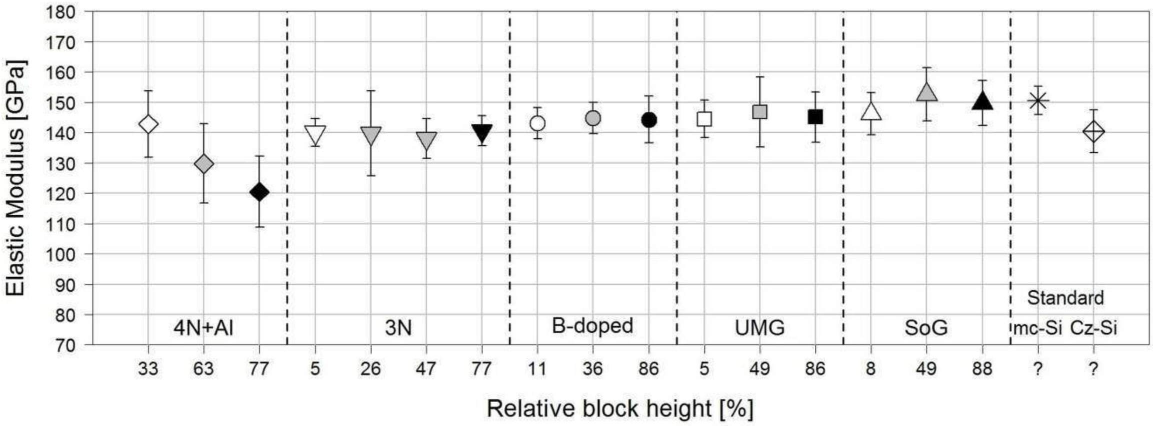

Figure 121 Static elastic modulus of mc-Si wafers after damage etch.

5.1.2 Epitaxial Wafer Equivalent Processes

Substrate Annealing

The comparison of the characteristic stresses of damage etched and annealed wafers (see Figure 120 and Figure 122) shows that the difference in mechanical strength of silicon wafers at different positions within the block becomes smaller with the exception of *4N+Al* mc-Si. The mechanical strength of the wafers tends to approximate to the value of 300 MPa; wafers with high mechanical strength after damage etch experienced a diminishment of the characteristic stress after annealing and vice versa. This indicates that the heating of the samples influences the microstructure of the material and therefore its mechanical strength.

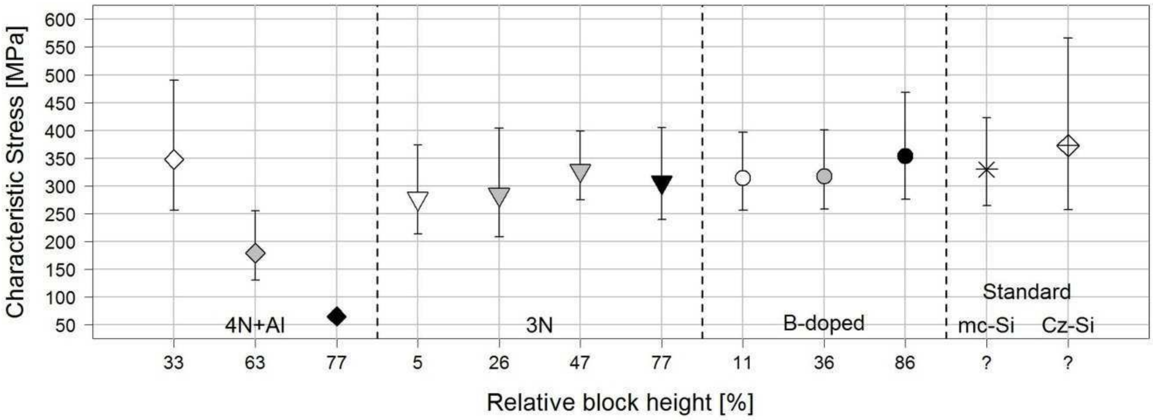

Figure 122 Characteristic stress of silicon wafers after annealing.

Generally, the static elastic modulus of silicon wafers decreased approximately 10 GPa in all cases (see Figure 123) with exception of Cz-Si where the decrease in elastic modulus is 30 GPa.

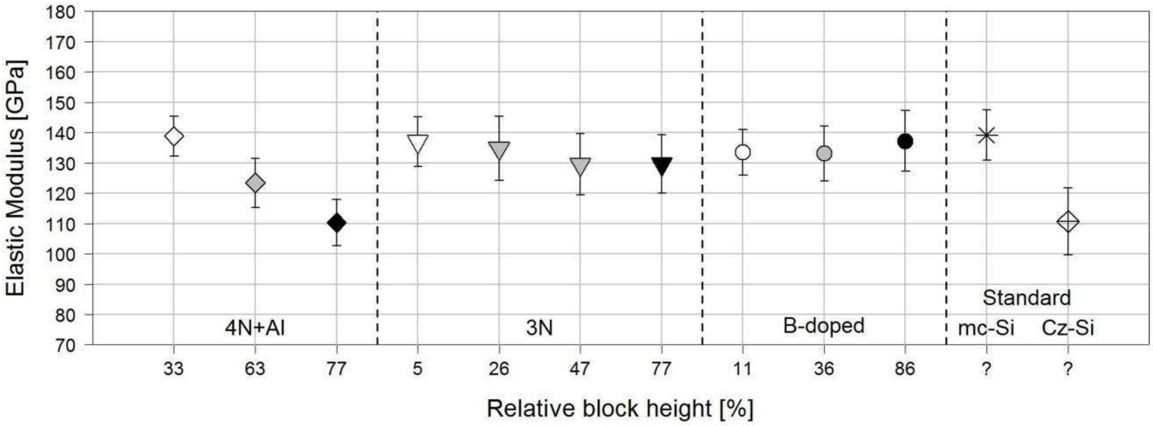

Figure 123 Static elastic modulus of silicon wafers after annealing.

Epitaxial Film Growth

The difference in characteristic stresses of the wafers after epitaxial growth is even narrower than after annealing (see Figure 122 and Figure 124). Only samples at 33% of the relative block height were tested for the *4N+Al* mc-Si block. Samples at higher positions within this block presented small halls and therefore it was considered that these samples are not to be further used as they do not have a complete structural integrity. The wafers were broken with the epitaxial silicon thin film under tensile stress and the deposition of this film approximates even more the mechanical strength of all the wafers to the value of 300 MPa.

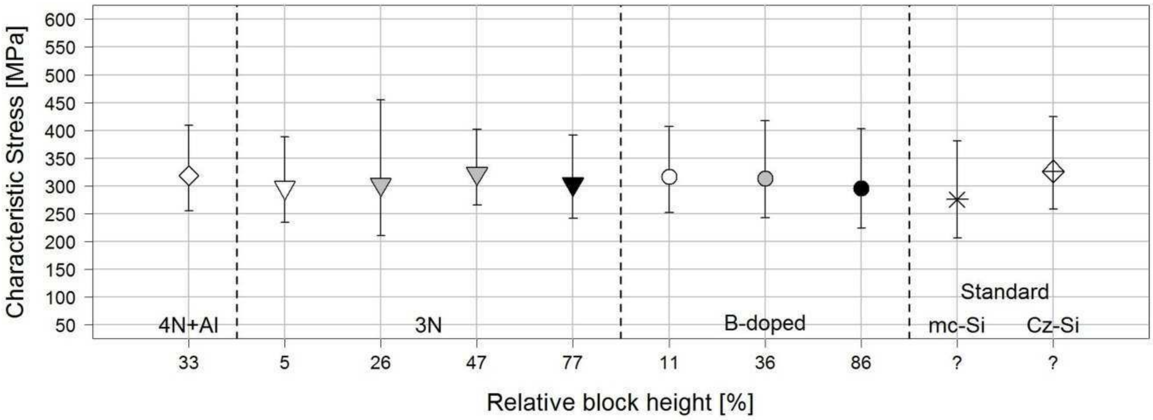

Figure 124 Characteristic stress of silicon wafers after epitaxial film growth.

After epitaxial film growth the static elastic modulus of all mc-Si wafers converges even more to the value of 130 GPa while Cz-Si reduces its elastic modulus down to 100 GPa.

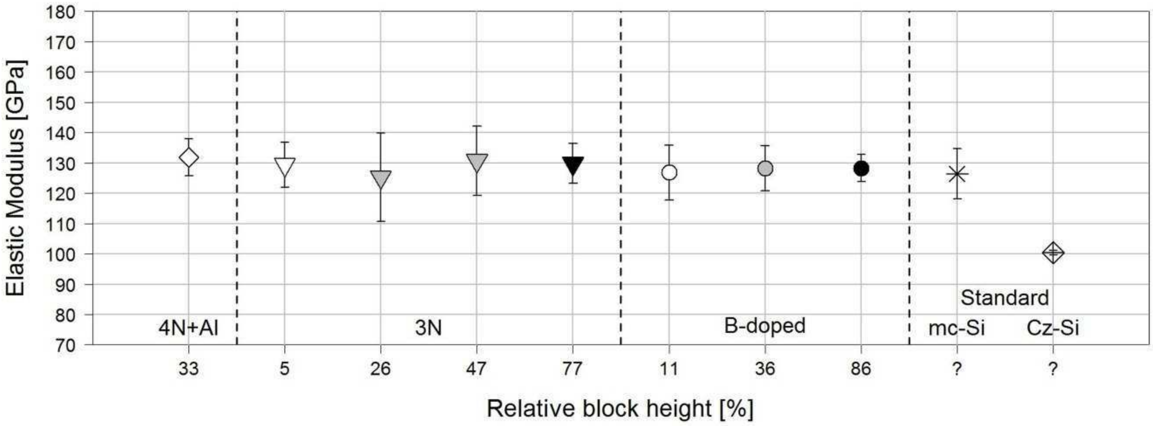

Figure 125 Static elastic modulus of silicon wafers after epitaxial film growth.

5.1.3 Inert Cell Processes

Texture

The mechanical strength of *UMG* and *SoG* mc-Si wafers increases a factor of ~1.5 (see Figure 126) after texture in comparison with sawn wafers (see Figure 118). This increase in mechanical strength is lower than in the case of damage etched wafers which experienced an increase in mechanical strength by a factor of ~2 (see section 5.1.1). 20 µm were removed from the surface of the silicon wafers after damage etch while only approximately 4 µm were removed after texture. Thus, a partial removal of the saw damage can lead to a lower increase in mechanical strength.

The values of static elastic modulus of silicon wafers after texture (see Figure 127) are very similar to the values of elastic modulus after damage etching.

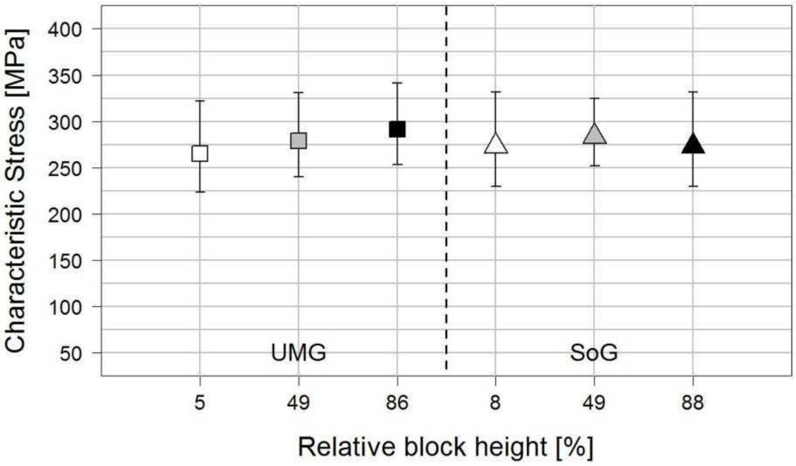

Figure 126 Characteristic stress of silicon wafers after texture.

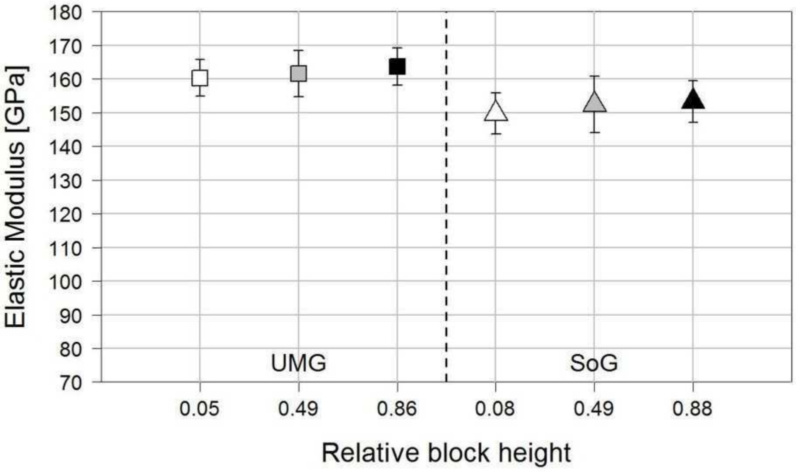

Figure 127 Static elastic modulus of silicon wafers after texture.

Phosphorous Emitter Diffusion

Figure 128 depicts the characteristic stress of *UMG* and *SoG* mc-Si wafers after phosphorus emitter diffusion, which increases a factor of ~1.2 in comparison with the mechanical strength of the previous textured wafers. However, the increase in mechanical strength is in the range of the maximum difference in characteristic stress between neighboring wafers which is approximately 30 MPa (see section 4.1). Thus, the slight increase in mechanical strength after phosphorus emitter diffusion must be interpreted carefully.

The statistic elastic modulus of all the silicon wafers after phosphorus emitter diffusion remains in approximately 150 GPa (see Figure 129) like for textured wafers.

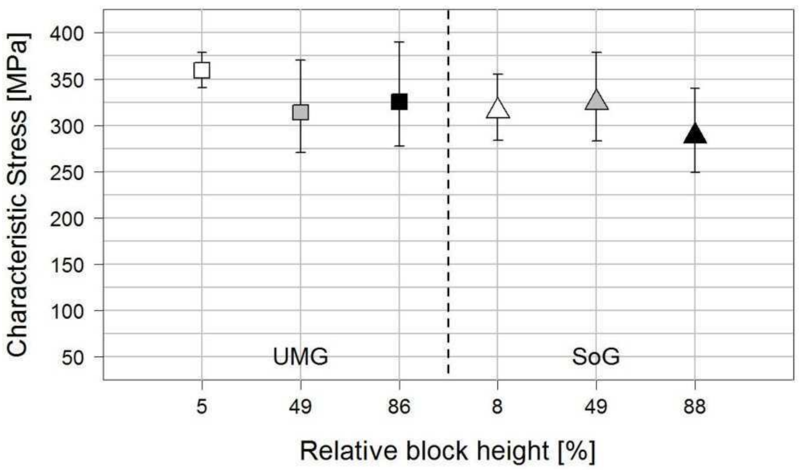

Figure 128 Characteristic stress of silicon wafers after phosphorus emitter diffusion.

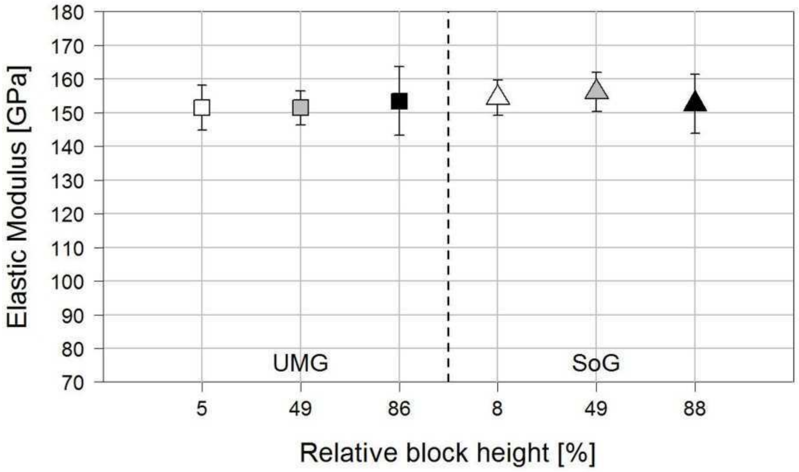

Figure 129 Static elastic modulus of silicon wafers after phosphorus emitter diffusion.

Phosphosilicate Glass Etch

When the phosphosilicate glass layer deposited on the wafers after phosphorus emitter diffusion is removed, the mechanical strength of *UMG* and *SoG* mc-Si wafers is comparable to the mechanical strength after texture and is approximately ~275 MPa (see Figure 130). This indicates that the increase in characteristic stress after phosphorus emitter diffusion is due to the properties and thus to the residual stress of the phosphosilicate glass layer.

Figure 131 depicts that the statistic elastic modulus of silicon wafers after phosphosilicate glass etch is approximately 15 GPa lower than the elastic modulus of the wafers processed until texture and phosphorus emitter diffusion.

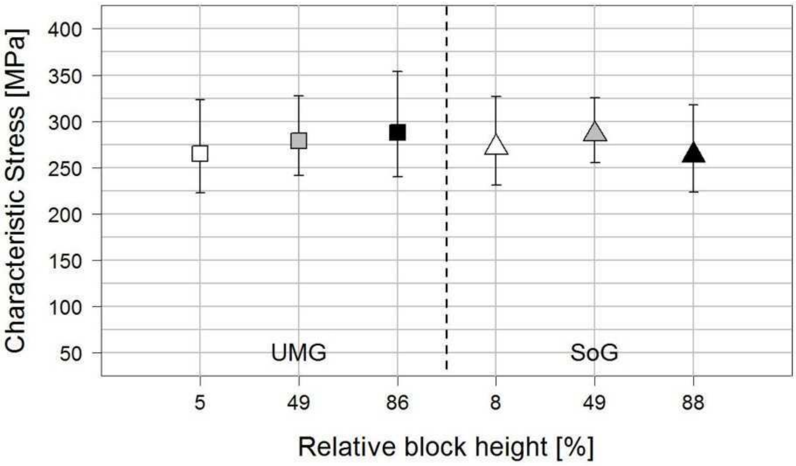

Figure 130 Characteristic stress of silicon wafers after phosphosilicate glass etch.

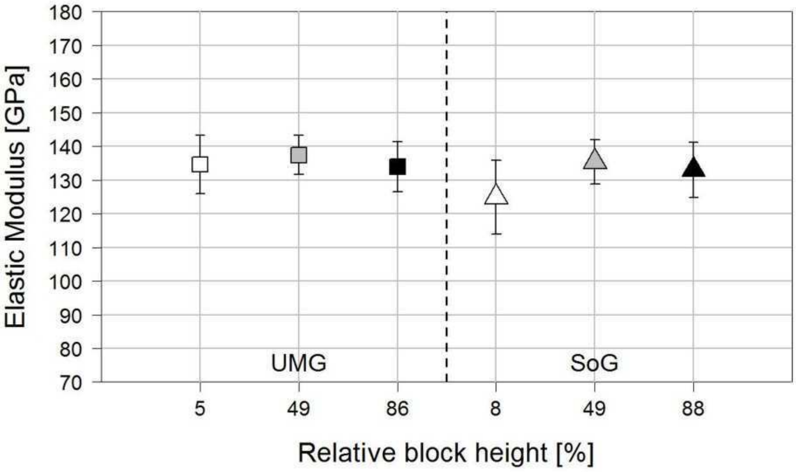

Figure 131 Static elastic modulus of silicon wafers after phosphosilicate glass etch.

Antireflection Coating

The characteristic stress of silicon wafers after the deposition of the thin silicon nitride antireflection coating decreases in ~25 MPa (see Figure 132) in comparison with the previous processing step.

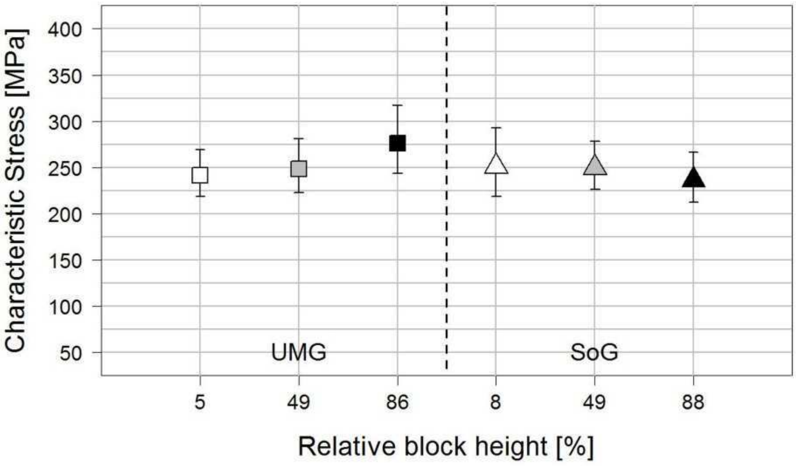

Figure 132 Characteristic stress of silicon wafers after silicon nitride antireflection coating.

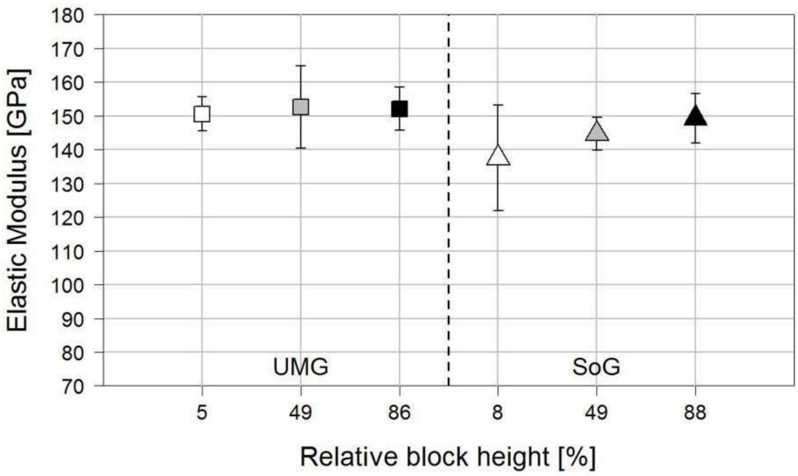

Figure 133 Static elastic modulus of silicon wafers after silicon nitride antireflection coating.

However, the statistic elastic modulus of these passivated wafers is approximate to 150 GPa, either the wafers undergo previously phosphorus emitter diffusion or not (see Figure 133 and Figure 135).

Skipping the steps of phosphorus emitter diffusion and phosphosilicate glass etch, i.e. textured wafers are further processed to the deposition of the silicon nitride antireflection coating, does not influence considerably the mechanical strength of the silicon wafers and their characteristic stress is ~225 MPa (see Figure 134). However, the decrease in mechanical strength, which is approximately 25 MPa, is in the range of the difference in characteristic stress between neighboring wafers. Therefore, this decrease in mechanical strength must be interpreted carefully.

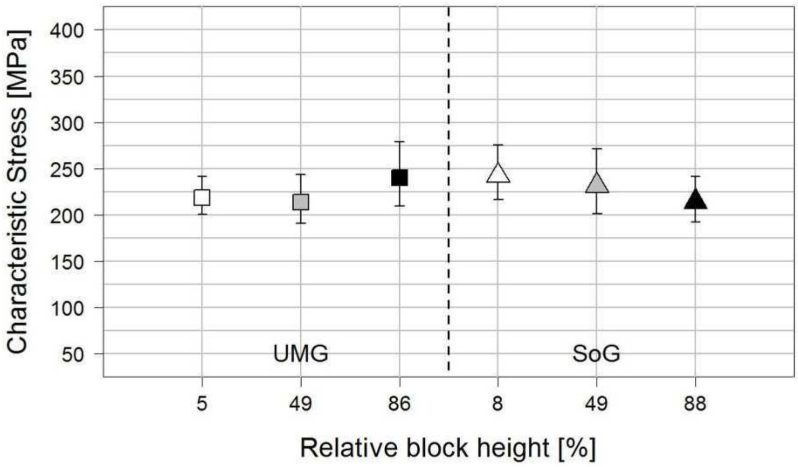

Figure 134 Characteristic stress of silicon wafers after silicon nitride antireflection coating (skipping phosphorus emitter diffusion).

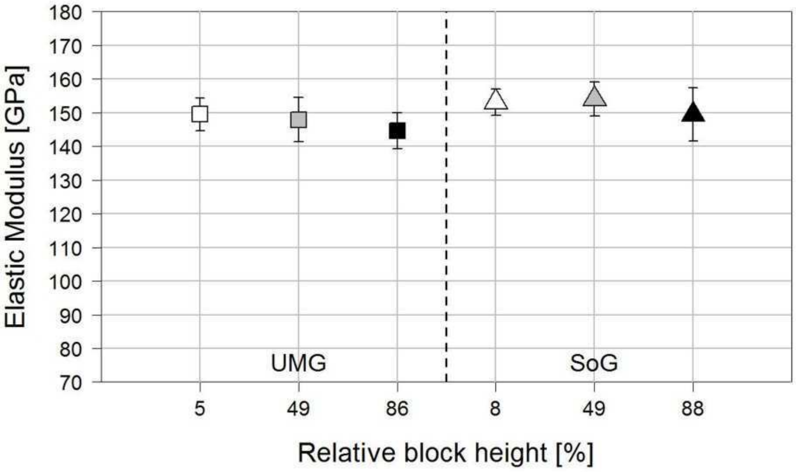

Figure 135 Static elastic modulus of silicon wafers after silicon nitride antireflection coating (skipping phosphorus emitter diffusion).

Metallization

Figure 136 and Figure 137 depict the fitting of fracture stresses to the Weibull distribution of *UMG* and *SoG* mc-Si wafers at the top part of the blocks after metallization. The fracture stresses of the samples broken with the front contact under tensile stress (Figure 136 a)) show a good fit to the Weibull distribution while the fitting of the fracture stresses of the samples broken with the back contact under tensile stress (Figure 136 b)) is poor.

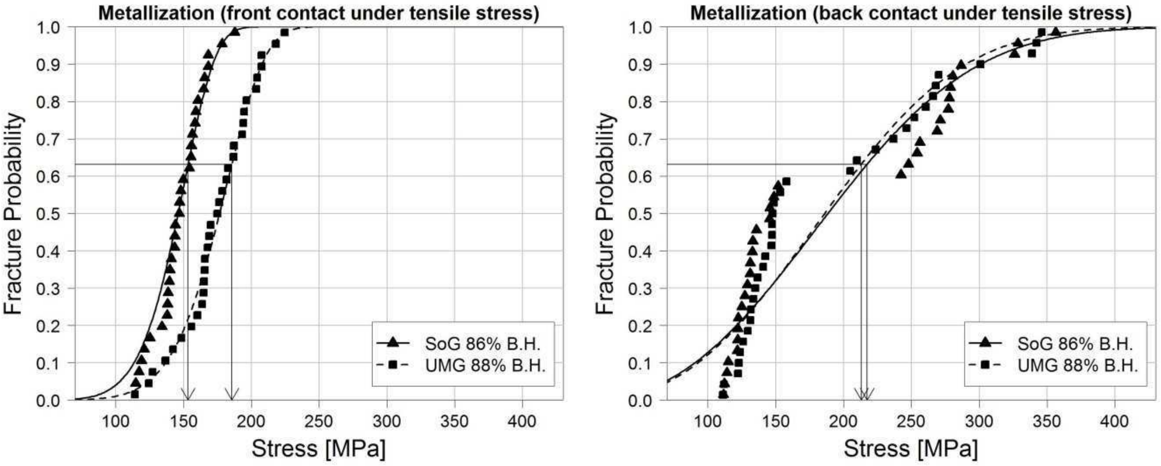

a) b)

Figure 136 Weibull plots of UMG and SoG mc-Si after metallization, front contact under tensile stress (image a)) and back contact under tensile stress (image b)).

When the Weibull graph of Figure 136 b) is split into two separate graphs; one for back contact samples without bus bar (Figure 137 a)) and the other for back contact samples with bus bar (Figure 137 b)), the experimental values of fracture stresses fit well the Weibull distribution.

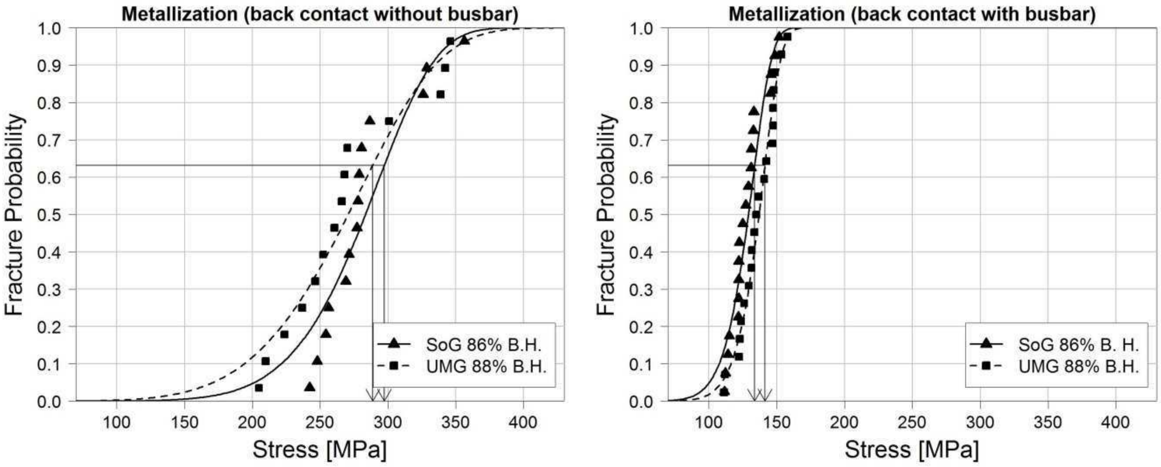

a) b)

Figure 137 Weibull plots of UMG and SoG mc-Si after metallization, areas from the back contact under tensile stress without bus bar (image a)) and areas from the back contact under tensile stress with bus bar (image b)).

The characteristic stress of *UMG* and *SoG* mc-Si wafers after metallization at different relative block heights is shown in Figure 138. The mechanical strength of samples broken with the front contact under tensile stress is comparable to the mechanical strength of as-cut wafers and is in the range of 150-180 MPa.

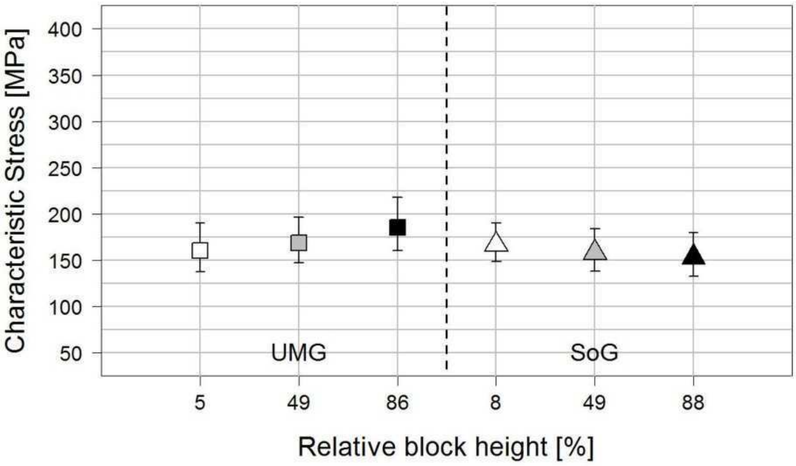

Figure 138 Characteristic stress of silicon wafers after metallization (front contact under tensile stress).

The statistic elastic moduli of *UMG* and *SoG* mc-Si wafers after metallization with the front contact under tensile stress (see Figure 139) are in the range 90-105 GPa and are much lower than the elastic moduli measured at previous processing steps. Thus, the decrease in mechanical strength may most probably be linked to the decrease in elastic modulus.

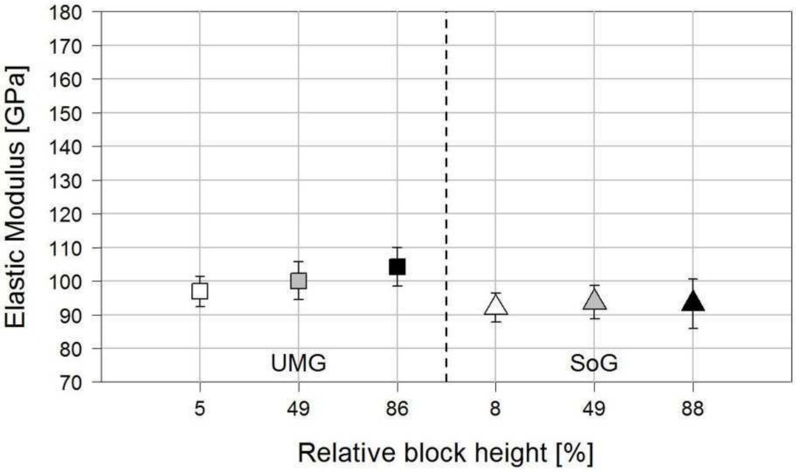

Figure 139 Static elastic modulus of silicon wafers after metallization (front contact under tensile stress).

The mechanical strength of the samples broken with the back contact without bus bar under tensile stress is almost double (see Figure 140) than the mechanical strength of the samples broken with the front contact under tensile stress and comparable to the mechanical strength of the wafers measured at previous processing steps.

However, the elastic modulus of the samples broken with the back contact without bus bar under tensile stress (see Figure 141) is approximately 100 GPa as the elastic modulus of the samples with the front contact under tensile stress. In this case the mechanical strength of the samples broken with the back contact without bus bar under tensile stress seems not be linked with the decrease in elastic modulus. These issues will be further discussed in section 5.2.3.

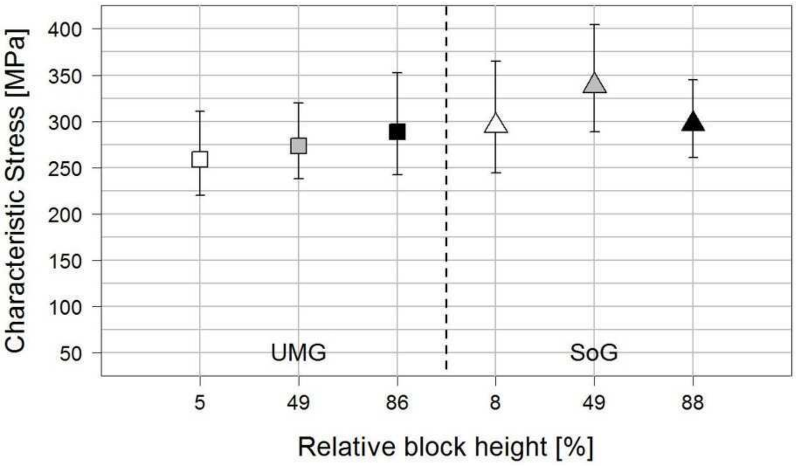

Figure 140 Characteristic stress of silicon wafers after metallization (areas from the back contact under tensile stress without bus bars).

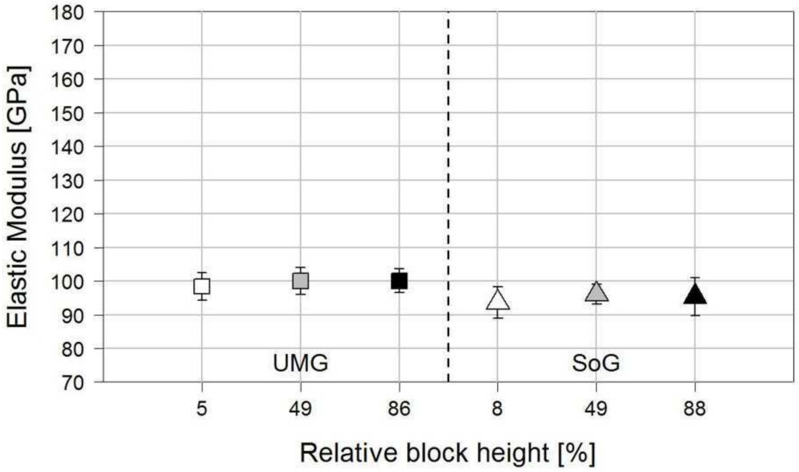

Figure 141 Static elastic modulus of silicon wafers after metallization (areas from the back contact under tensile stress without bus bars).

The mechanical strength of the samples broken with the back contact with bus bar under tensile stress is slightly lower, ~145 MPa, (see Figure 142) than the mechanical strength of the samples with the front contact under tensile stress and as-cut wafers.

The elastic modulus of the samples broken with the back contact with bus bars under tensile stress (see Figure 143) is below 90 GPa and comparable to the elastic modulus of the samples with the front contact under tensile stress. The decrease in mechanical strength may most probably be linked again to the decrease in elastic modulus.

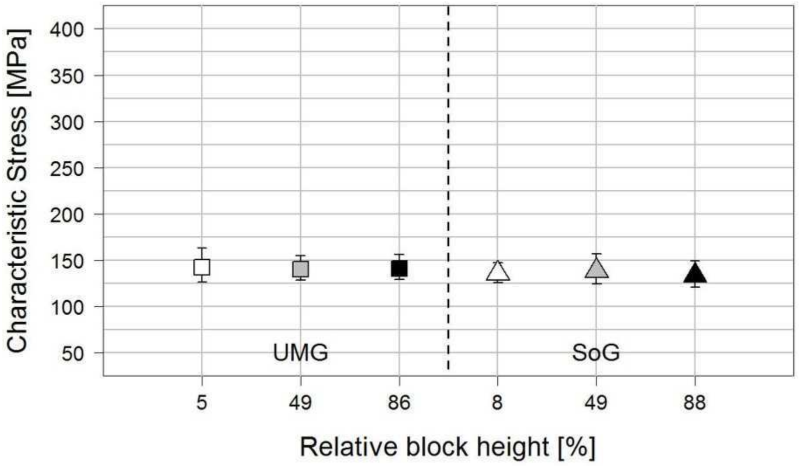

Figure 142 Characteristic stress of silicon wafers after (bus bars from the back contact under tensile stress).

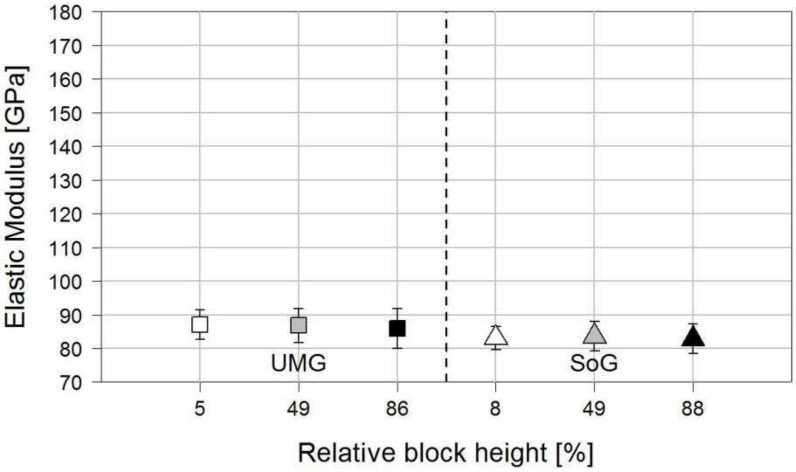

Figure 143 Static elastic modulus of silicon wafers after metallization (bus bars from the back contact under tensile stress).

5.2 Influence of Solar Cell Processes on the Microstructure of Silicon Wafers

5.2.1 Wafer Manufacture

Multi-wire Sawing

Defects on the surface of the wafers are introduced during the multi-wire sawing process and determine the mechanical strength of the silicon wafers. During the slicing of the wafers, the loading produced by the abrasive SiC particles when they indent the silicon surface form a sub-surface damage layer [137]. The subsurface damage layer (see Figure 144) is constituted of an upper few hundred nanometers to few micrometers thick polycrystalline silicon layer, a fracture zone where micro-cracks show a dominant presence in the material, a transition zone with high concentration of dislocations and reached by some micro-cracks from the layer above and an elastically strained zone due to the difference of density between the damaged material at the top surface and the bulk silicon.

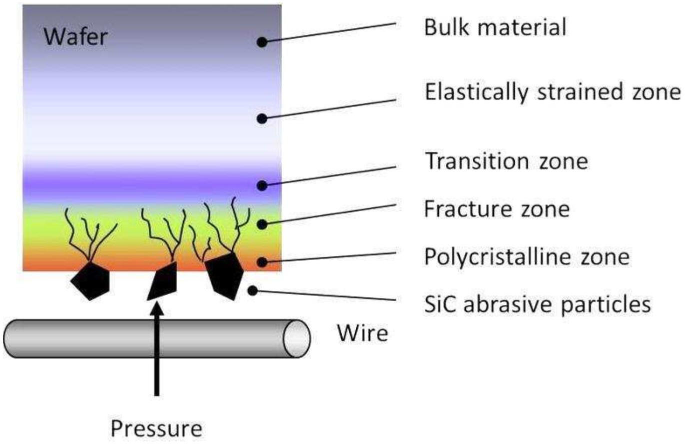

Figure 144 Sub-surface damage structure layer of a crystalline silicon wafer resulting from the multi-wire saw cutting process after [137].

Figure 145 shows cross sections with different morphologies of micro-cracks introduced in the silicon surface during multi-wire sawing. The lengths of the observed cracks vary from less than 1 µm to 7-8 µm. The cracks that are perpendicular to the silicon surface are the most detrimental for the mechanical strength of the wafers.

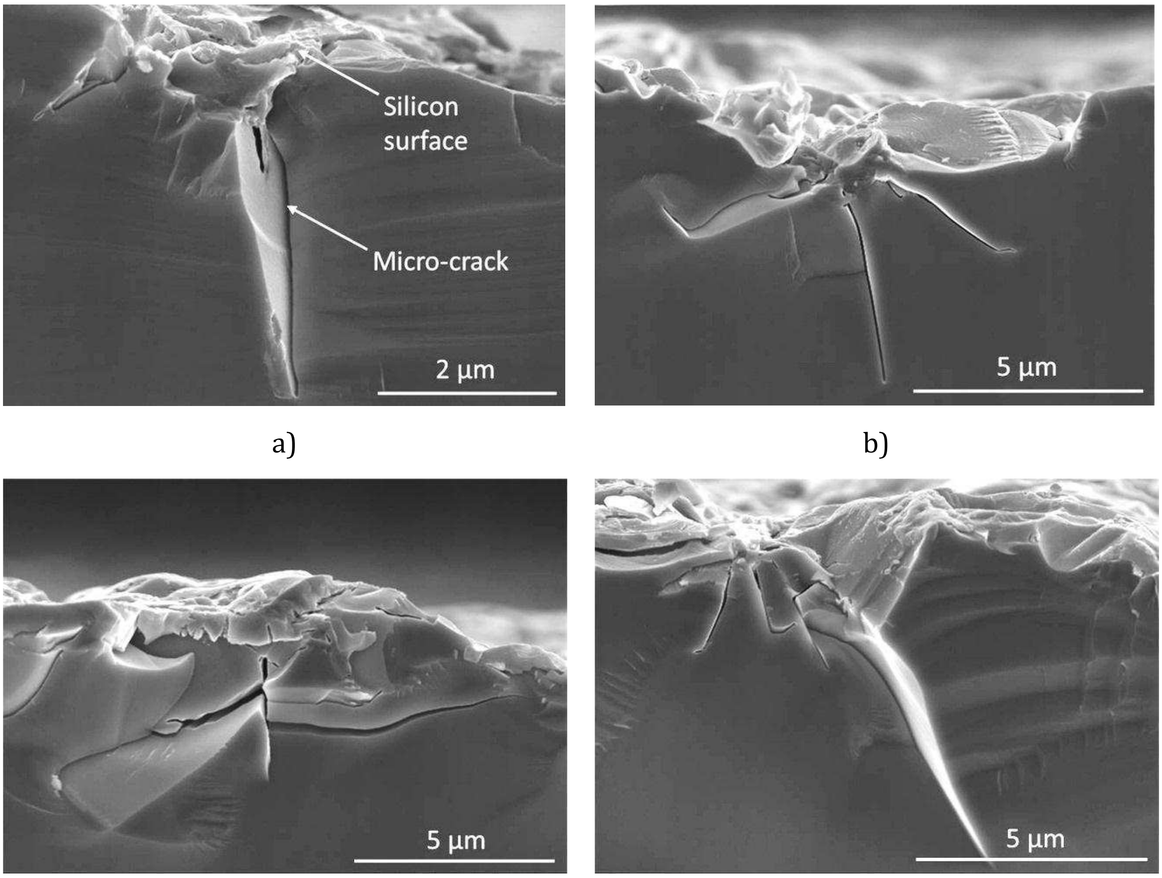

a) b)

c) d)

Figure 145 Micro-cracks in the surface of as-cut silicon wafers.

Top views of the silicon surfaces can be seen in Figure 146 and Figure 147. The silicon surface depicted in Figure 146 a) shows a typical rough silicon surface dominated by the polycrystalline silicon layer. Al phase between grains and large cracks can be distinguished on the surface of the *4N + Al* mc-Si at 77% of the relative block height. These cracks are much larger than the cracks introduced during multi-wire sawing and therefore they control the mechanical strength of these wafers. This is the reason why the mechanical strength of these wafers is the lowest measured mechanical strength from all wafers tested in Figure 118.

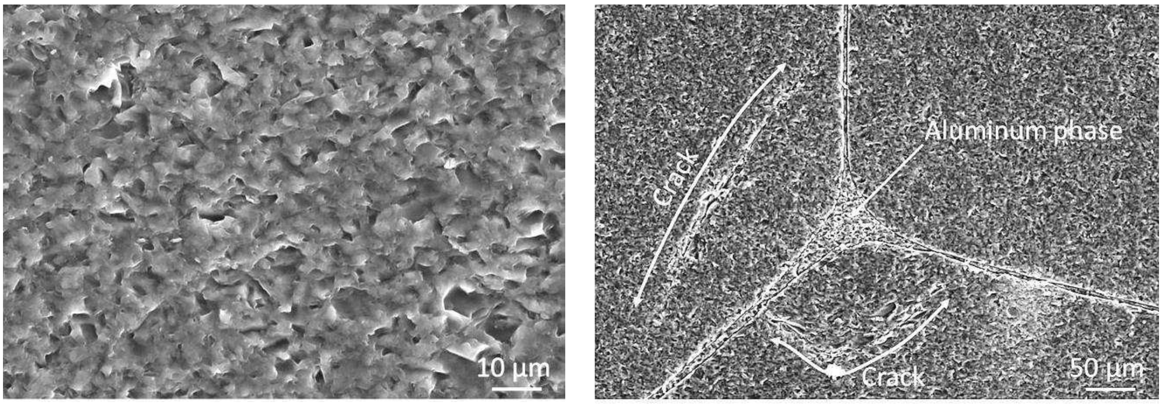

a) b)

Figure 146 The image on the left depicts a typical top view of the surface of an as-cut silicon wafer. The image on the right depicts the as-cut surface of 4N + Al mc-Si at 77% of the relative block height.

Figure 118 also shows that the mechanical strength of silicon samples from the bottom parts of the *UMG* and *SoG* mc-Si blocks were lower than the mechanical strength at the top parts of the blocks. SEM images in Figure 147 a) and b) illustrate that the silicon surface at the bottom of the blocks is rough, dominated by the polycrystalline silicon layer and micro-cracks were not visible. SEM images in Figure 147 c) and d) illustrate that the silicon surface at the top of the blocks is also rough but it is not dominated by the polycrystalline silicon layer and micro-cracks were very well visible from the top views of the silicon surfaces.

The observation of the cross sections depicted in Figure 148 shows that the micro-cracks at the bottom of the blocks emanate from below the polycrystalline silicon layer and have a tendency to dispose perpendicular and parallel to the silicon surface while the cracks at the top of the blocks are more superficial and have a tendency to dispose mostly parallel to the silicon surface. The configuration of micro-cracks parallel to the silicon surface is less detrimental for the mechanical strength of silicon wafers than perpendicular cracks. This could explain the higher mechanical strengths measured at the top of the blocks.

The reason for the resultant different configurations of micro-cracks of as-cut wafers from a same block which are cut at the same time with the same cutting parameters could be due to second phase particles like B, P, C, N and metals segregate to the top of the block. Solute impurity atoms can increase the elastic modulus and the hardness of silicon [138] and therefore mc-Si at the top of the block may exert more resistance to the indentation of the SiC particles during multi-wire sawing.

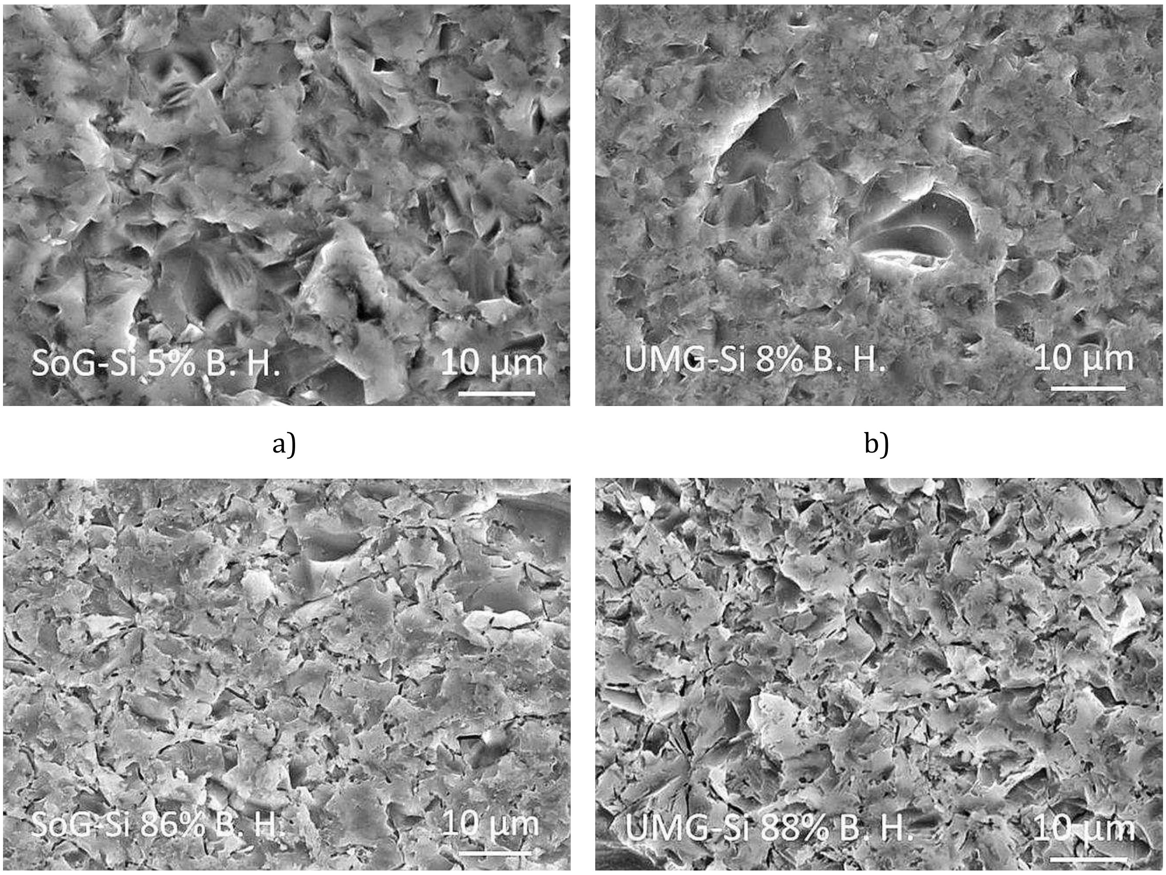

a) b)

c) d)

Figure 147 The images on the left and on the right show top views of the surfaces from the middle area of as-cut SoG and UMG mc-Si wafers respectively.

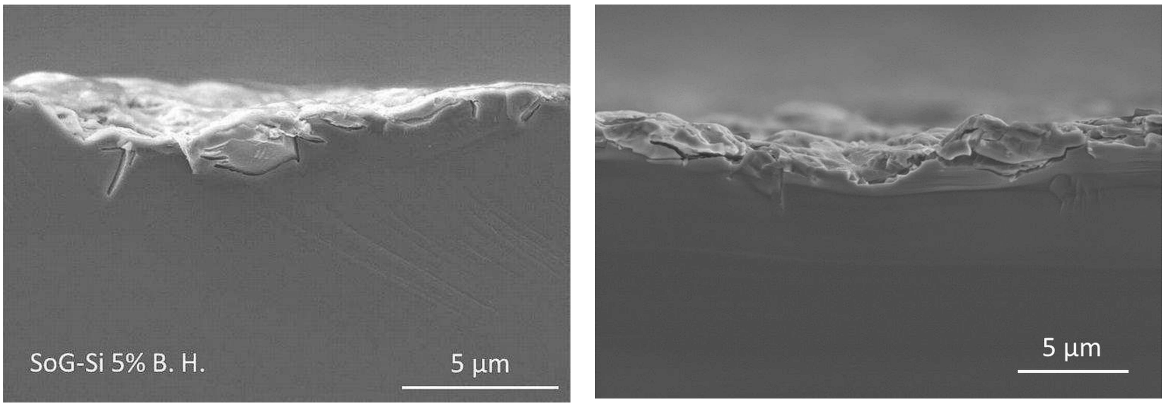

a) b)

Figure 148 The images depict the cross section from the middle area of SoG mc-Si wafers where the morphology of the micro-cracks introduced during wire-sawing can be observed.

The fracture stress map of an as-cut mc-Si wafer in Figure 149 shows a slight tendency of fracture stresses, where they are lower at the wire entrance than at the wire exit. Larger SiC particles cut mostly at the wire inlet while smaller particles cut at the wire outlet. Larger SiC particles cause rougher silicon surfaces and deeper micro-cracks [139] and therefore the mechanical strength of the silicon samples at the areas nearer to the wire inlet is lower than at the wire outlet.

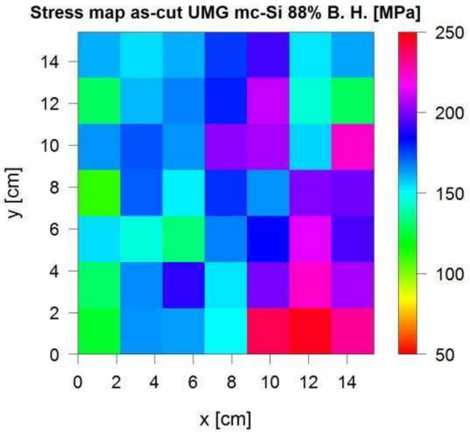

Figure 149 Map of fracture stresses of as-cut wafers measured with the RoR bending test that indicates lower fracture stresses at the wire inlet than at the wire outlet.

Damage etch

After etching the silicon wafers for the removal of the sub-surface damage, the mechanical strength of the wafers double (see section 5.1.1). This is due to the removal of a 10-15 µm silicon layer per side of the wafers and no sub-surface damage remains in the silicon surfaces after damage etch. Surface finish and defects formed during the crystallization process control then the mechanical strength of the wafers.

Figure 150 a) shows the top view of a damage etched silicon sample where two grains have different surface patterns because the etching occurs differently at different crystalline orientations. The cross section in Figure 150 b) presents a smooth top silicon surface free of micro-cracks.

4N+Al mc-Si at 77% of the relative block height was the only quality of material that decreased its mechanical strength and static elastic modulus after damage etching. This is due to the fact that the cracks in the surroundings of the Al phase were so large that they were not removed by the etching process but became even sharper as the polycrystalline silicon layer at the surface of the wafers was removed.

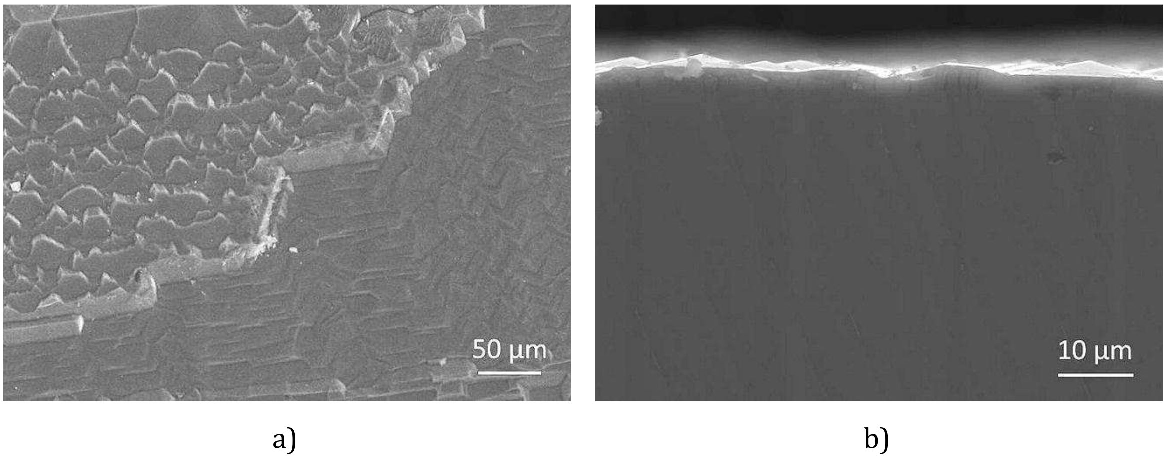

Figure 150 Top view and cross section of a damage etched mc-Si wafer.

5.2.2 Epitaxial Wafer Equivalent Processes

Substrate Annealing

After annealing, the SiO_x particles found at the bottom of the *3N* mc-Si block are no longer visible (see Figure 151). These particles precipitate at temperatures between 700-1100°C [91], and as the annealing of the sample occurs rapid and at 1150°C, most probably all SiO_x particles dissolved in the silicon matrix. The literature [140] also reported the dissolution of SiO_x precipitates after annealing at 1050°C and the introduction of tensile strain in the silicon matrix which can be released by mechanisms like vacancy injection and dislocation loops. SiO_x particles can precipitate again after cooling but they were not observed in the SEM inspections of the wafers.

The presence of small crystalline SiO_x particles is responsible for the high measured fracture toughness and mechanical strength of *B-doped* mc-Si. Therefore, the dissolution of crystalline SiO_x particles could be the cause of the lower mechanical characteristic stresses of annealed *B-doped* mc-Si wafers in comparison with etched wafers.

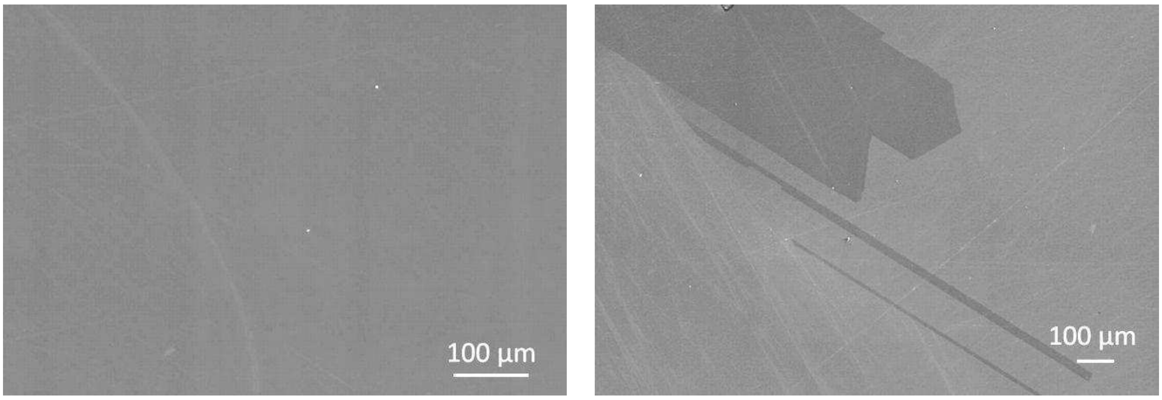

a) b)

Figure 151 The images show the polished surface of a 3N mc-Si wafer at 5% of the relative block height after annealing. The silicon surface and the grain boundaries are free from SiO_x particles.

Figure 152 a) depicts particle free grain boundaries but particles or impurity clusters were observed in the silicon matrix. Areas with this type of impurity clusters, which do not present a crystalline or organized structure, were rarely found, i.e. the silicon matrix appeared mostly free of particles like in Figure 151. A closer look on an impurity cluster in Figure 152 b) showed that the cluster was cracked in its inside. EDX analysis revealed that the composition of the impurity cluster consisted of Si, O and C. This type of defects could be the defects that define the lowest values of fracture stresses measured with annealed wafers.

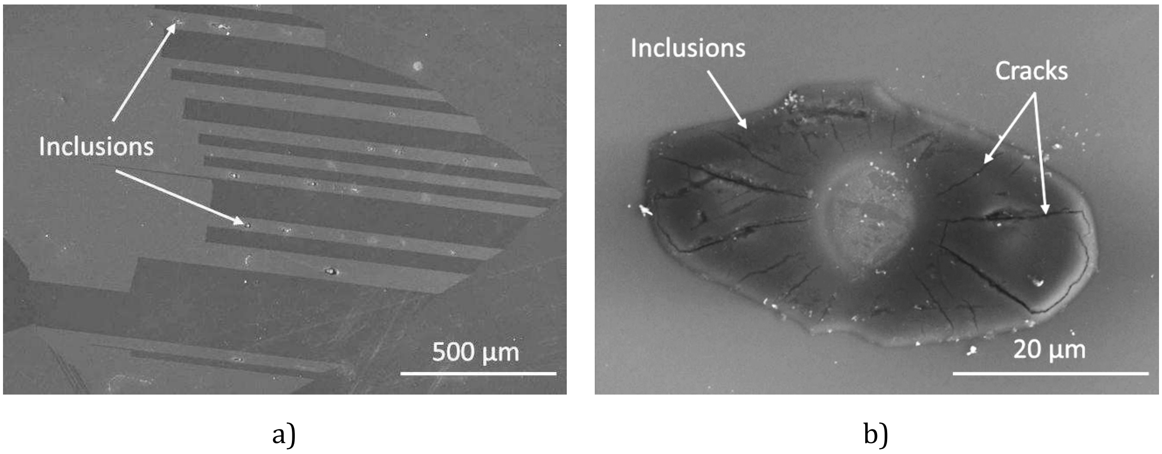

Figure 152 The images show the polished surface of a 3N mc-Si wafer at 5% of the relative block height after annealing. The grain boundaries are free from SiO_x particles but impurity clusters or particles are observed in the silicon matrix.

SiC and Si_3N_4 are formed in the liquid phase at high temperature [91]. The annealing temperature, 1150°C, is still a lower temperature than the SiC and Si_3N_4 precipitation temperature in the melt and therefore SiC and Si_3N_4 are still visible after the annealing step (see Figure 153 a)). The phase diagrams of SiC and Si_3N_4 can be found in the literature [141] and [142] respectively. The residual thermal stress in the surroundings of these particles can be relieved as the annealing temperature is above the silicon brittle-ductile temperature but it can build again as the wafers are rapidly cooled down. Moreover, other types of defects can be introduced in the silicon matrix which can explain the slight decrease in mechanical strength of annealed wafers. This will be discussed in the next section.

Al showed a much different behavior as its melting temperature is 660°C. After the annealing of *4N+Al* mc-Si wafers from the top of the block, holes were observed in the places where the Al/Si eutectic phase were spotted (see Figure 153 b)) as Al melted away. This explains the decrease in mechanical strength and static elastic modulus of annealed wafers in comparison with damage etched wafers.

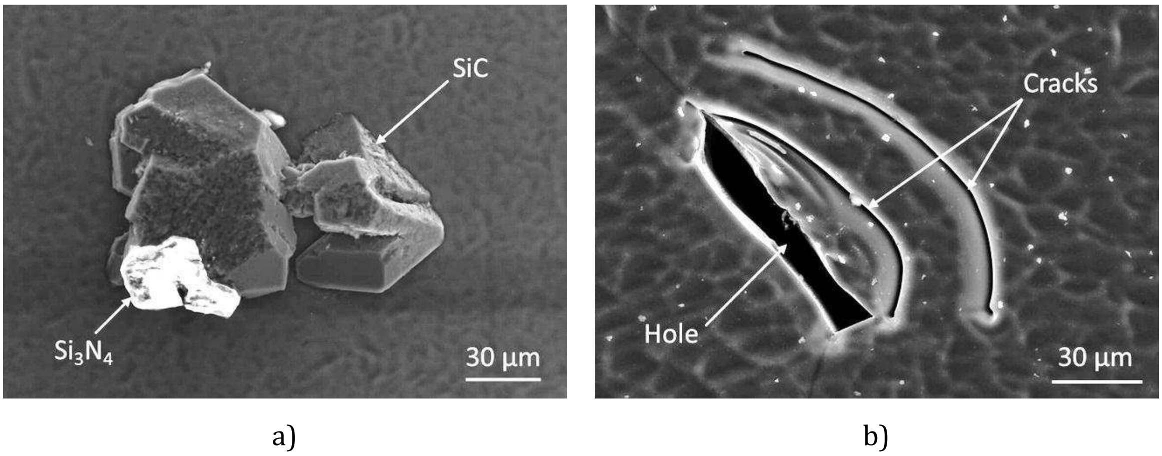

Figure 153 Image a) shows the presence of SiC and Si_3N_4 particles in 4N+Al mc-Si after annealing at 63% of the relative block height. Image b) reveals the hole that an Al/Si eutectic phase left after melting away during the annealing process at the same relative block height than image a) and cracks in its surroundings.

Figure 154 shows residual stress maps of annealed *industry standard* Cz- and mc-Si. The residual stress level measured with damage etched silicon wafers, with exception of the *4N+Al* mc-Si, ranged between 3 and 6 MPa while annealed wafers reached residual stresses up to 12 MPa. The wafers are placed vertically in the oven for annealing and the wafer carriages are made out of silica which has a much lower thermal expansion coefficient, $0.5 \times 10^{-6} [K^{-1}]$, than silicon. When the wafers are heated up, the silica carriages do not expand as much as silicon and they represent a constraint for the volume expansion of the silicon wafer resulting in the introduction of residual thermal stresses that are depicted in Figure 154. Image b) schemes the cracking that *industry standard* mc-Si suffered during annealing due to residual thermal stress caused by constraint for its expansion that the silica carriages exerted.

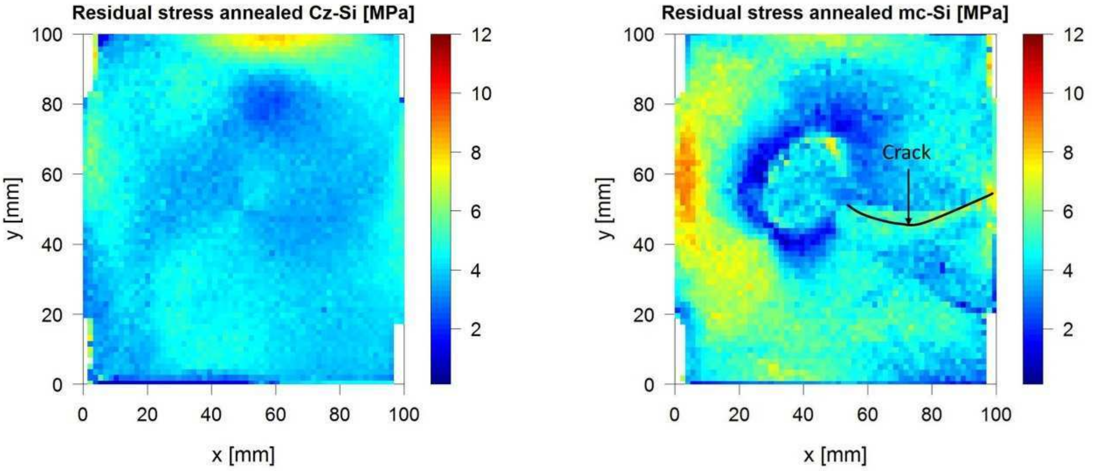

a) b)

Figure 154 Residual stress map of industry standard Cz-Si (image a)) and mc-Si (image b)).

Epitaxial Film Growth

The mechanical strength of silicon wafers converged strongly to the value of 300 MPa after the deposition of the epitaxial silicon film, which points to the fact that the mechanical strength of the wafers is strongly influenced by the deposited layer. The stress level of the film could be a limiting factor for the mechanical strength as well as the surface structures of the wafer equivalents. Figure 155 a) shows the surface structure of a wafer equivalent broken sample. Triangular inverted pyramidal structures which seem to be grain and twin boundaries. Figure 155 b) give a closer look of the cross section of these structures. This surface morphology could also intensify slightly applied stresses at the tips of the pyramids, thus lowering the mechanical strength of wafer equivalents in comparison with damage etched and annealed wafers.

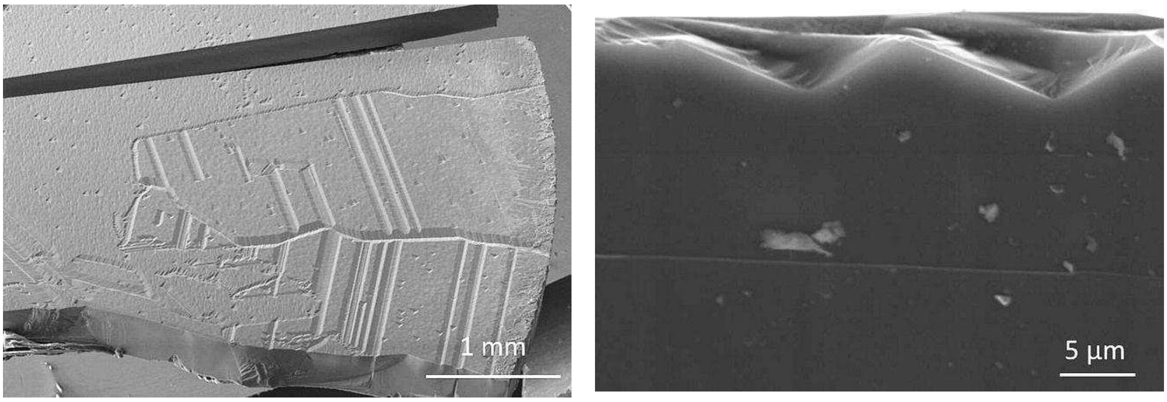

a) b)

Figure 155 Image a) depicts a broken piece of a silicon wafer equivalent. The top view of the broken sample corresponds to the surface where the silicon thin film was deposited and that was subjected to tensile stress during bending. Image b) gives a closer look to the cross section of a mc-Si wafer equivalent.

5.2.3 Inert Cell Processes

Texture

During standard solar cell processing, as-cut wafers skip damage etching and proceed with the texturing step for the treatment of the surface of the silicon wafers (see Figure 156 a)) to reduce light reflection. This treatment removes cracks partially and blunts the tips of the cracks [143], [144] (see Figure 156 b)). Hence, the mechanical strength of the wafers was increased but this increase in mechanical strength is lower than in the case of damage etched wafers as indicated in section 5.1.1 and 5.1.3. 20 µm were removed from the surface of the silicon wafers after damage etching while only approximately 4 µm were removed after texture. Thus, a partial removal of the saw damage can lead to a lower increase in mechanical strength.

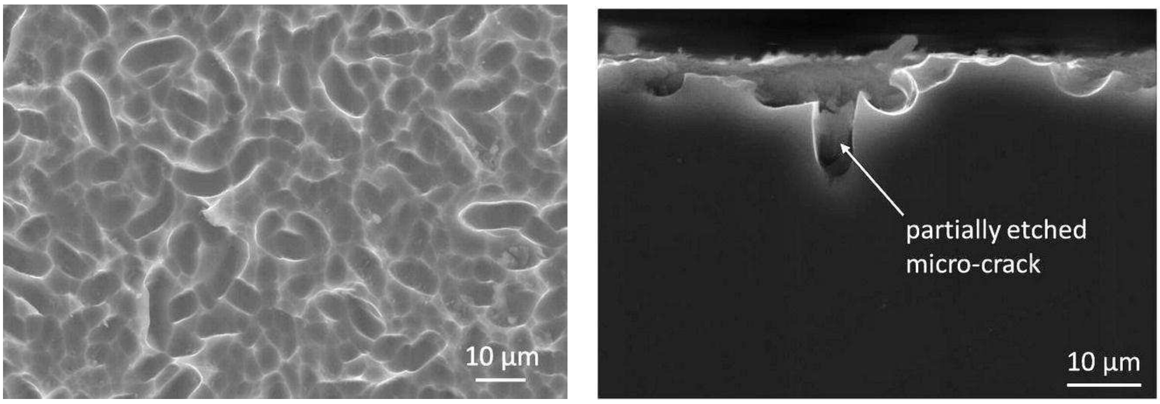

a) b)

Figure 156 Image a) shows the surface morphology of a textured mc-Si wafer. The cross section of image b) points to a partially etched micro-crack as the texturing process did not remove entirely the cracks introduced in the silicon surface during multi wire-sawing.

Phosphorous Emitter Diffusion

Silicon wafers experienced an increase in mechanical strength of 20% after phosphorus emitter diffusion (see section 5.1.3). The surface and the cross section of these wafers (see Figure 157) are comparable to the surface and cross section of textured wafers. Therefore, the cause for the increase in mechanical strength of silicon wafers after phosphorus emitter diffusion lies in the properties and thus on the residual stress of the deposited phosphosilicate glass layer and will be discussed in the next section.

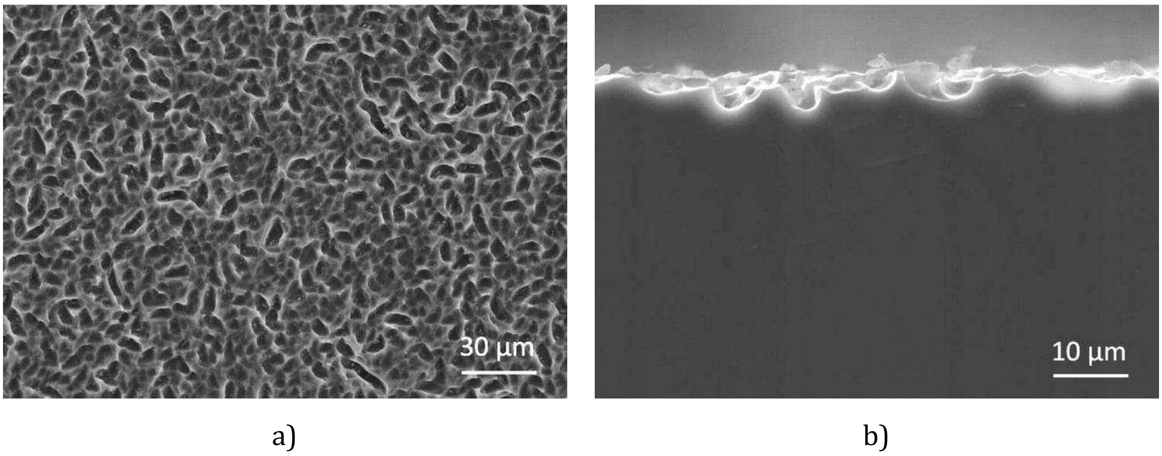

a) b)

Figure 157 The mc-Si surface depicted in image a) shows that the surface morphology of mc-Si wafers is maintained after emitter diffusion. Image b) shows surface grooves in a cross section view.

Phosphosilicate Glass Etch

When the phosphosilicate glass layer deposited after the phosphorus emitter diffusion layer is removed after subsequent etching the mechanical strength of the wafers decreases to the level of stress of textured wafers. The etching for the removal of the phosphosilicate glass layer etches more deeply defects as grain boundaries (see Figure 158 a)). However, the etching which reveals defects is very slight as the cross section of the wafers shows a surface morphology comparable to the surface morphology resulting from previous processing steps.

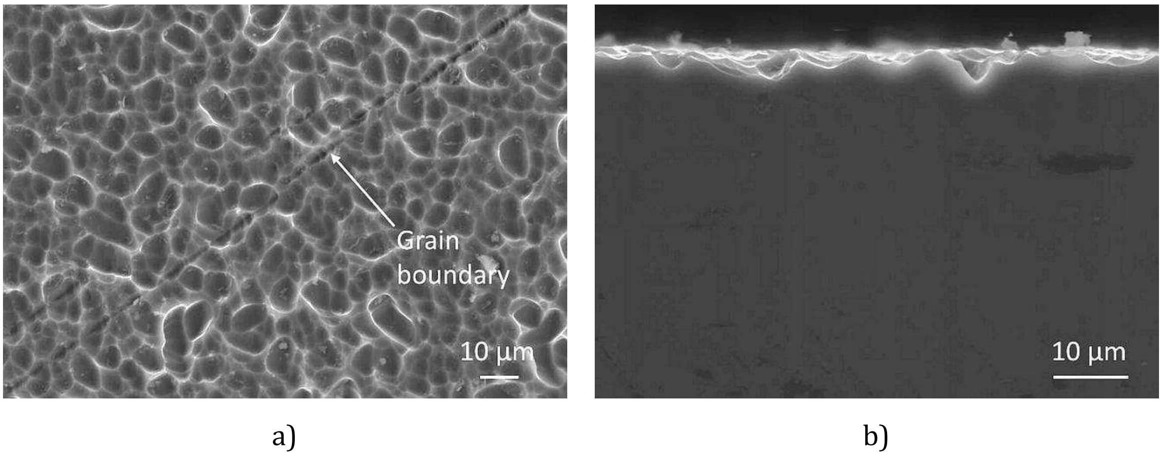

a) b)

Figure 158 Image a) shows that after the etching process for the removal of the phosphosilicate glass layer, grain boundaries are revealed in the microscope as they are slightly deeper etched than defects free areas. The cross section view in image b) shows the morphology of the grooved surface.

Antireflection Coating

Prior to the deposition of the antireflection coating, the surface of the silicon wafers must be cleaned with an aqueous solution containing HF in order to achieve a high quality antireflection coating. This solution etches selectively defects in silicon; areas free of defects preserve the surface morphology of textured wafers (see Figure 159 a)) while areas with high density of dislocations and grain boundaries show high density of etch pits (see Figure 159 b)).

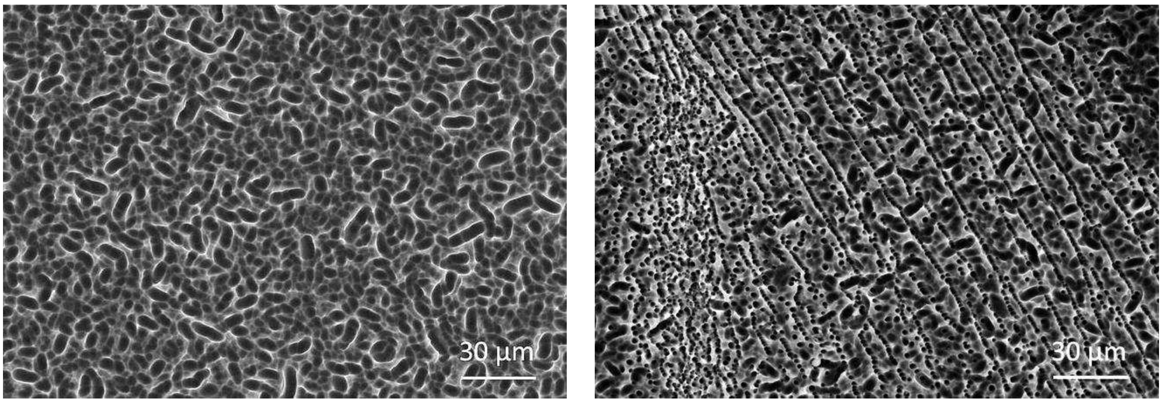

a) b)

Figure 159 Image a) shows that the morphology of the silicon surface is also maintained after the deposition of the antireflection coating. The dark points in image b) reveals the presence of dislocations as they are deeply etched during the cleaning step before the deposition of the antireflection coating.

The cross section view in Figure 160 shows the morphology of etch pits. Etch pits end in the shape of sharp notches [145]. Therefore they are more effective in diminishing the mechanical strength of silicon wafers than the surface grooves resulting from the texturing processes but they are much less effective than sharp micro-cracks introduced during the multi-wire sawing process. Round silicon samples tested with the RoR bending test presenting high density of etch pits broke at lower stress levels than samples that were free of etch pits.

Residual stress on the wafer surface resulting from the properties of the silicon nitride antireflection coating will be discussed in the next section.

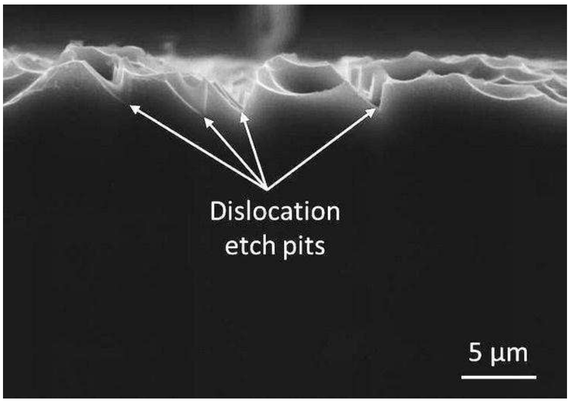

Figure 160 Cross section view that shows sharp ending grooves in the surface of a silicon wafer as dislocations are selectively etched during the cleaning step before the deposition of the antireflection coating.

Metallization

Figure 161 a) shows the configuration of fracture stresses of the front contact of a *SoG* mc-Si solar cell at 49% of the relative block height (see Figure 45) for checking the scheme of the positions where the bending tests were performed. Fracture stresses of the front contact range between 150 and 200 MPa approximately (see also Figure 138). The mechanical strength of the front contact of the solar cell is almost half the value of the mechanical strength of the wafers after texture and is comparable to mechanical strength of as-cut wafers. The silicon samples broken with the front contact under tensile stress containing fingers and fingers and bus bar (see Figure 45) induce the same level of damage in the solar cell. Thus, all measured fracture stresses from the front contact fit properly the Weibull distribution (see Figure 136 a) and Figure 161 a)).

The map of fracture stresses measured with the back contact subjected to tensile stress shows a less homogeneous pattern. The back contact samples containing only the Al back layer and the samples with Al layer and bus bar showed two different fracture stress levels (see Figure 161 b)). The mechanical strength of the samples with Al layer and bus bar are comparable to the mechanical strength of as-cut wafers while the mechanical strength of the samples containing only the Al layer is higher and comparable to the mechanical strength of textured or phosphorus emitter diffused wafers. Obviously, the severity of the damage induced by the Al back layer and the back bus bars is completely different. Therefore, the fracture stresses measured with the two different types of back contact samples do not fit well the Weibull distribution (see Figure 136 b)). The solution adopted in this work for this issue is fitting the fracture stresses from the two different types of samples to separate Weibull distributions (see Figure 137 a) and b)). The mechanical strength for both types of samples will be defined then by the characteristic stress calculated from each of the Weibull distributions (see Figure 140 and Figure 142).

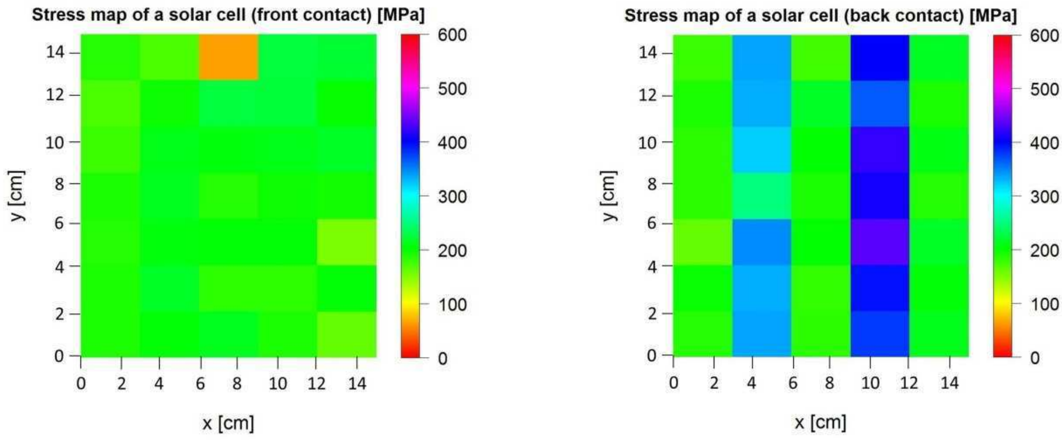

a) b)

Figure 161 Map of fracture stresses of a silicon solar cell measured with the RoR bending test. Image a) depicts the stress map obtained from the fracture stresses measured with the front contact subjected to tensile stress and image b) the fracture stress map with the back contact under tensile stress.

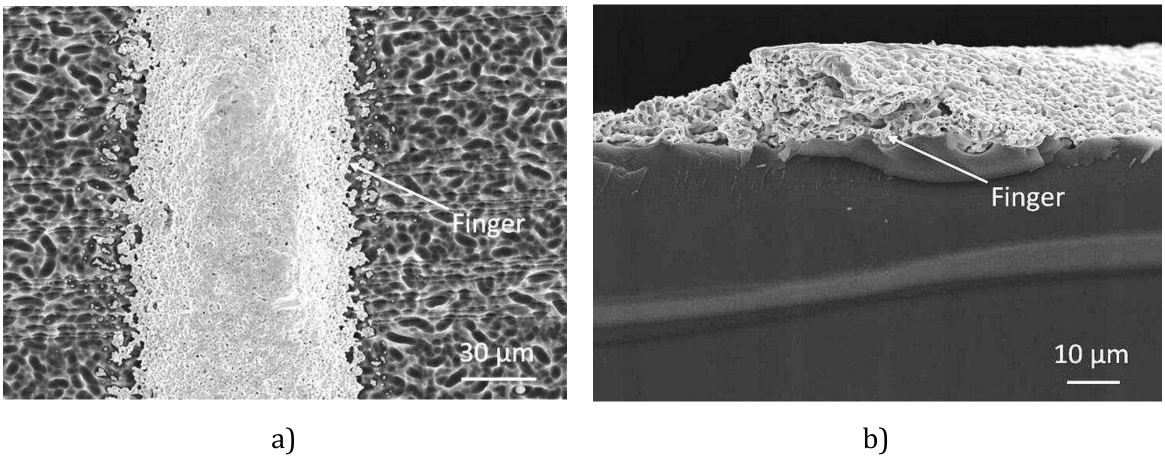

a) b)

Figure 162 The top view of a front contact finger is shown in image a). Image b) depicts a cross section at a front contact finger.

Figure 162 shows the front view and the cross section of a front contact finger and micro-cracks were not observed in the vicinities of finger contacts.

The cross section in Figure 163 a) shows a front contact bus bar with a clean interface with silicon free of cracks. Almost all cross sections observed were free of cracks but some areas were found where sharp cracks emanate in the silicon below the bus bars (see Figure 163 b)).

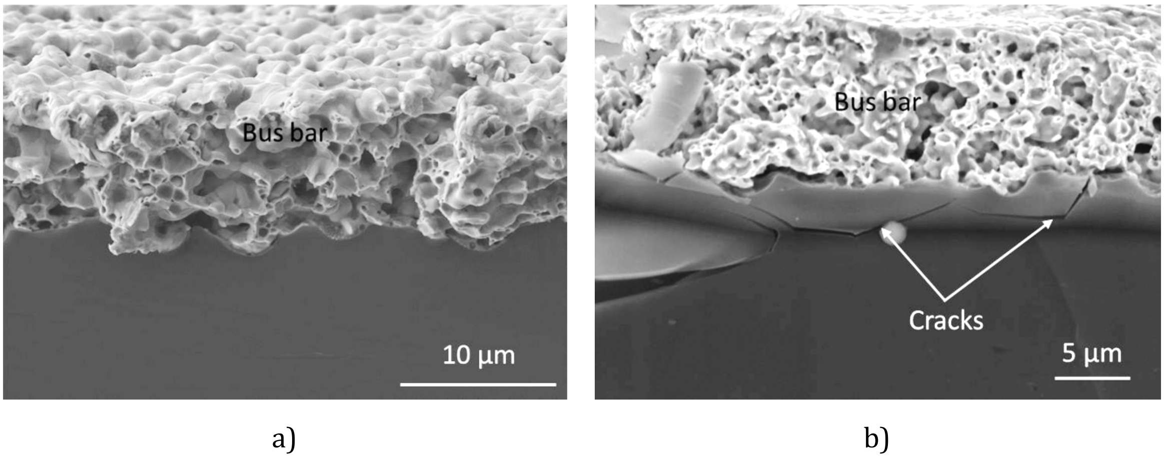

a) b)

Figure 163 The cross section of a front contact bus bar shown in image a) is free of cracks at its interface with the silicon wafer. Image b) depicts a cross section at a front contact bus bar where sharp cracks emanate from the interface between the finger and the silicon surface.

The interface between the Al layer and back bus bars appears also free of cracks (see Figure 164 a). However, some damage can be observed below back contact bus bars in the shape of rib marks as indicated in Figure 164 b).

Figure 165 a) illustrates the morphology of the Al back layer consisting of Al spheres and a eutectic Al/Si layer in direct contact with the silicon surface. The eutectic layer shows most commonly a good attachment to the silicon surface but some areas showed the presence of interfacial defects which can be due to spontaneous delamination or just to the absence of the eutectic layer like in Figure 165 b).

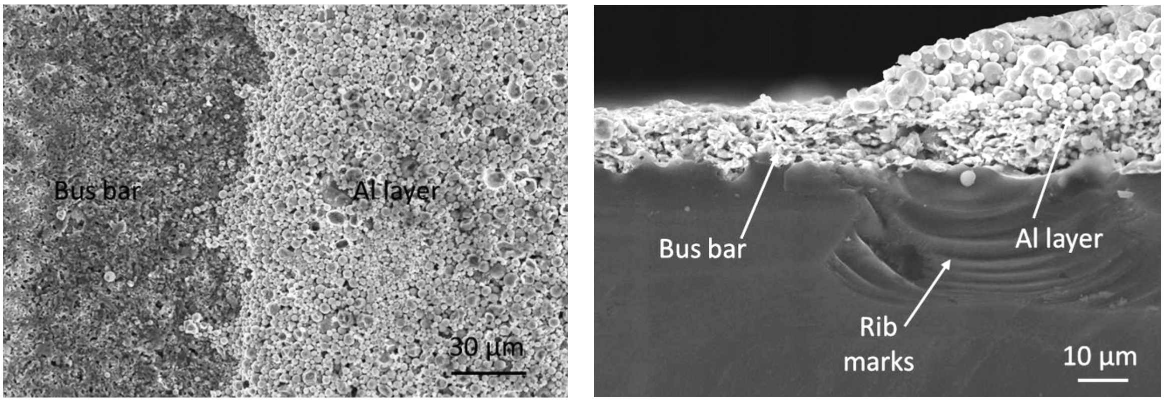

a) b)

Figure 164 Image a) shows a top view of the back contact of a solar cell where the interface between a bus bar and the back Al layer can be observed. Image b) is the cross section view of the interface between a back contact bus bar and the back Al layer.

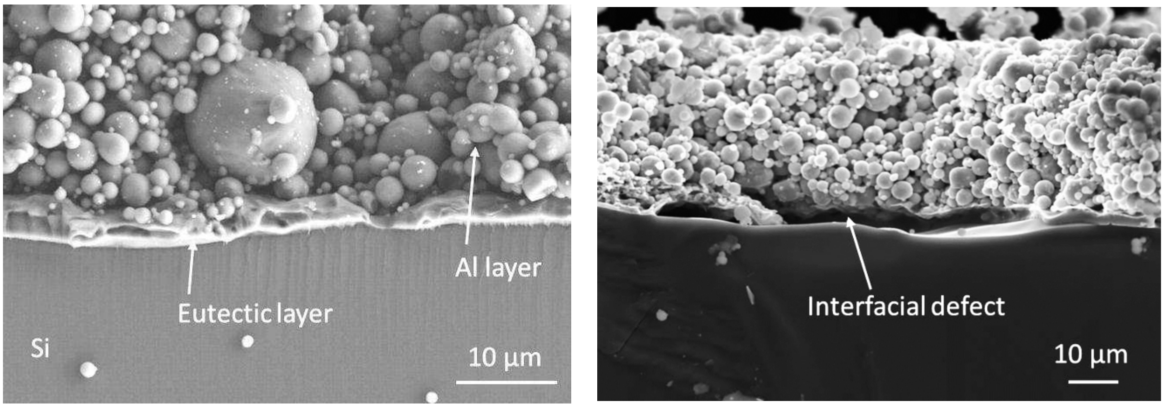

a) b)

Figure 165 Image a) shows a cross section of the back Al contact layer. Delamination of several tens of microns or just not formation of the eutectic layer can occur between the back contact Al layer and the silicon surface as indicated in image b).

5.3 Discussion

5.3.1 Epitaxial Wafer Equivalent

The development of the mechanical strength of the silicon wafers explained in the previous sections from multi-wire sawing until the deposition of the epitaxial film for producing wafer equivalents is analyzed and presented in this section (see the graphs in Figure 166). The evolutions of the characteristic stress of different qualities of mc-Si from comparable block heights are depicted together. Results obtained with *industry standard* mc- and Cz-Si are also illustrated in Figure 166 e) in order to have a reference for comparing the results of other qualities of mc-Si.

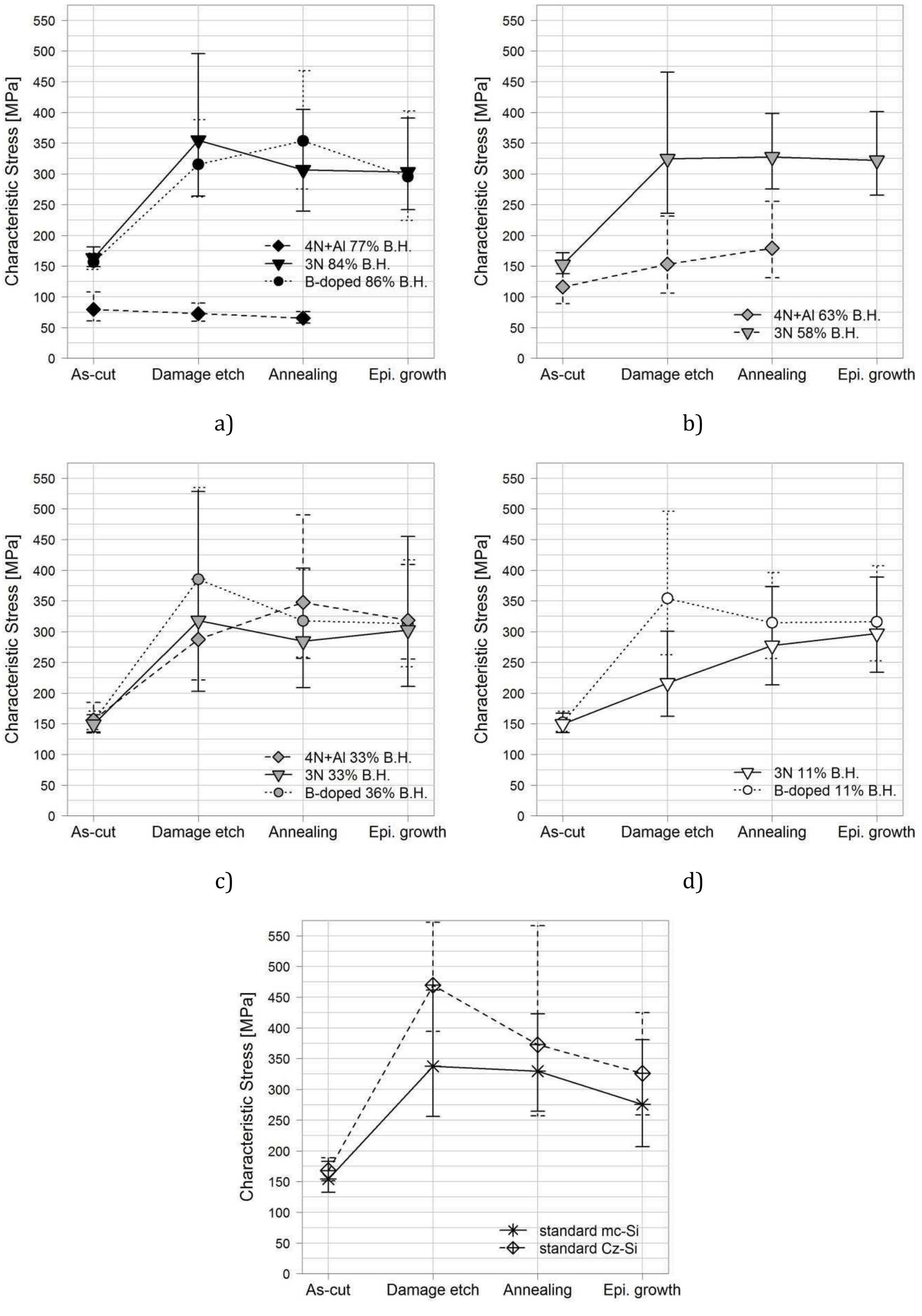

a) b)

c) d)

e)

Figure 166 Evolution of the mechanical strength of mc-Si substrates through the processing steps for the manufacture of epitaxial wafer equivalents.

Multi-wire Sawing

As already explained in the previous sections, the multi-wire sawing process is one of the solar cell processes that more strongly lowers the mechanical strength of silicon wafers. The failure criterion described by equation (2.97) for scratch-like cracks ($Y = 1.12\sqrt{\pi}$) and considering the theoretical value of fracture toughness of silicon ($K_{Ic} = 0.9\ \mathrm{MPa}\sqrt{\mathrm{m}}$) predicts a crack length of ~9 µm. This value agrees quite well with the lengths of the cracks observed with the SEM.

The static elastic modulus of as-cut wafers is relatively high and ranged approximately between 140 and 160 GPa. The cracks introduced during wire-sawing are very superficial and therefore they do not change the properties of the silicon bulk of the wafers, being the value of the elastic modulus preserved.

Damage etching

When the micro-cracks introduced during multi-wire sawing are removed, the mechanical strength of as-cut wafers is doubled and the defects formed in the silicon bulk during the crystallization process dominate the mechanical properties of mc-Si wafers. This issue has been thoroughly analyzed and described in this chapter and in the literature [98].

The mechanical strength of mc-Si wafers crystallized with alternative silicon feedstock present comparable mechanical strength to the mechanical strength of *industry standard* Cz- and mc-Si, being Cz-Si the material with the highest mechanical strength. Only wafers from the middle and the top part of the *4N+Al* mc-Si block and from the bottom part of the *3N* mc-Si block have significant lower mechanical strength than *industry standard* mc-Si.

The static elastic modulus of damage etched wafers is relatively high and ranged between 140 and 150 GPa with exception of the wafers from the middle and the top part of the *4N+Al* mc-Si block whose static elastic moduli are 130 and 120 GPa respectively. These last two materials showed a proven strong influence of their mechanical properties with the content of silicon bulk defects. Therefore in the following, values of static elastic modulus which are lower than 140 GPa will be interpreted to be due to the deterioration of the mechanical properties of the silicon bulk of the wafers.

Substrate Annealing

The first to consider for the analysis of the mechanical strength of annealed wafers is the formation of residual stresses during cooling as the outer and inside parts of the wafers will not have the same temperature and the thermal expansion coefficient of silicon depends on the temperature. Equation (2.139) allows the calculation of thermal stresses during rapid processing. During annealing the wafers are heated up to 1150°C, but above 800°C silicon can relax stresses by plastic flow. Thus the temperature range will be considered to range from 800°C to 25°C. The values of the thermal expansion coefficient of silicon at these temperatures are taken from Table 14 of Appendix A and its engineering elastic constants, E and ν, from the average values in Table 12 and Table 13 of Appendix A. According to equation (2.139) silicon wafers would remain under a tensile residual thermal stress of ~743 MPa after rapid cooling. Obviously this is a very large value of residual stress that would cause severe damage or breakage of silicon wafers. Equation (2.160) predicts that silicon wafers can stand a maximum temperature difference of 368°C until fracture due to thermal shock. Therefore, a temperature range of 775°C causing ~743 MPa would cause catastrophic failure of the wafers and is therefore very unlikely as the wafers survived the annealing process. Moreover, measured residual stresses of silicon wafers after annealing reached up a value of 12 MPa, which is a quite lower value. This measured value could be underestimated due to the small resolution of the measurement; but considering that actual local stresses are 10 times larger than the measured value, the actual hypothetical residual stress is still very far from the calculated ~743 MPa. Residual stresses may not be so large because the cooling of the wafers may not be so rapid as most of the times the wafers are cooled inside the oven which takes longer to cool down than outside the oven. The temperature gradient inside the RTCVD reactor was 100°C/min and if we consider this temperature gradient as the temperature range for thermal shock, then the calculated residuals stress is ~96 MPa which is a more reasonable value. Anyways, the presence of tensile residual thermal stresses of small magnitude in silicon wafers after annealing agrees with the moderate decrease in mechanical strength of annealed silicon wafers.

A less detrimental thermal shock can lower the mechanical strength of the wafers by the activation via thermal shock of cracks which are already in the material but that stop their propagation when the thermal stress stops increasing or disappears. This was the case of the *industry standard* mc-Si wafer depicted in Figure 154 b). According to equation (2.161), the crack that propagated from one edge to the center of the wafer may most probably have been 29 µm long before activation by thermal shock, which is the length that corresponds to a temperature gradient of 100°C/min.

The presence of SiC and Si_3N_4 particles, like for example in the middle parts of the *3N* and *4N+Al* mc-Si blocks, does not influence significantly the mechanical strength of the annealed wafers (see Figure 166 b)). The increment of temperature during heating up heals residual thermal stresses in the vicinities of SiC and Si_3N_4 particles but they will form again when the wafers are cooled down. SiC and Si_3N_4 particles appear unbroken and well bonded to the silicon matrix after annealing; hence the failure type at temperatures beyond the ductile-brittle temperature in the surroundings of these particles is most probably the yielding of the silicon matrix. Void nucleation by plastic flow most probably occurs near particle clusters. If the dimension of the voids could be measured, the intensification of an applied stress could be calculated with equation (2.162). Also a failure criterion for the voids with an annular crack could be applied for failure prediction with equation (2.165).

SiO_x particles dilute and the residual thermal stresses in their surroundings relax during heating up. Thus, the mechanical strength of annealed wafers at the bottom of the *3N* mc-Si increases as amorphous SiO_x particles are dissolved (see Figure 166 d)) and the dissolution of crystalline SiO_x particles reduces slightly the mechanical strength of *B-doped* mc-Si (see Figure 166 d)).

After annealing of the silicon wafers from the top of the *4N+Al* mc-Si block, the Al phase melted away leaving holes and the cracks in its surroundings did not heal. Therefore, the mechanical strength of these wafers slightly lowers after annealing (see Figure 166 a)).

The level of residual stress or the magnitude of other defects caused by thermal shock or by the yielding of the silicon matrix would be approximately the same for all processed wafers independently on their previous mechanical strength, and therefore the mechanical strength of almost all annealed wafers tend to converge to the value of 300 MPa.

The decrease of static elastic modulus of annealed wafers in approximately 10 GPa corroborates the negative effect of tensile residual thermal stresses and defects introduced during annealing on the mechanical behavior of the silicon wafers. Cz-Si experiences a lowering in elastic modulus of 30 GPa. Monocrystalline silicon cannot benefit from the barrier effect of grain boundaries to the movement of dislocations. Therefore, the yielding of the Cz-Si matrix could cause larger defects in Cz-Si wafers and hence a larger decrease in elastic modulus and mechanical strength than in the case of mc-Si wafers.

Epitaxial Film Growth

When the wafer equivalents are tested with the RoR bending test with the epitaxial deposited silicon film under tensile stress, the characteristic stress of the wafers converge even stronger than only annealed wafers to the value of 300 MPa. This is due most probably to the residual stress state and defects in the silicon thin film as they are supporting the largest tensile stress during bending.

Residual stresses within films are, as already explained in section 2.1.4.1.1, mostly due to the difference in thermal expansion coefficient between the film and the substrate (thermal stress), to the difference in lattice parameter between the film and the substrate (intrinsic stress) and to the temperature gradient. As the film and the substrate are both silicon the difference in thermal expansion coefficient and lattice parameter in equation (2.138) is zero; and thus, residual stresses are not expected within silicon epitaxial films deposited on silicon substrates. However, recent literature [146] states that the silicon epitaxial film is subjected to tensile residual stresses of small magnitude. This is due most probably to the building of intrinsic stresses by some processes that raise the density of the material of the film like annihilation of vacancies, dislocations and grain boundaries. This issue is far beyond the scope of this work. However, it can be concluded that the stress state of the film and thermal stresses that arise due to the difference in thermal expansion coefficient between areas of the wafers which are at different temperature during cooling, as it has been explained for annealed wafers, are controlling the mechanical strength of wafer equivalents. Thus, the failure analysis that can be applied on wafer equivalents is the same than the failure analysis for annealed wafers.

5.3.2 Inert Solar Cell

The development of the mechanical strength of the silicon wafers explained in the previous section from multi-wire sawing until the metallization process for producing conventional inert solar cells is analyzed and presented in this section (see the graphs in Figure 167). The evolution of the characteristic stress of the two different qualities of mc-Si from comparable block heights are depicted together to ease their comparison. The top of the *SoG* mc-Si block where SiC were observed and the bottom of the *UMG* mc-Si block show less mechanical strength than the other parts of the blocks. However, the defects introduced during multi-wire sawing and metallization seem to be more detrimental to the mechanical behavior of the wafers than the presence of the particles.

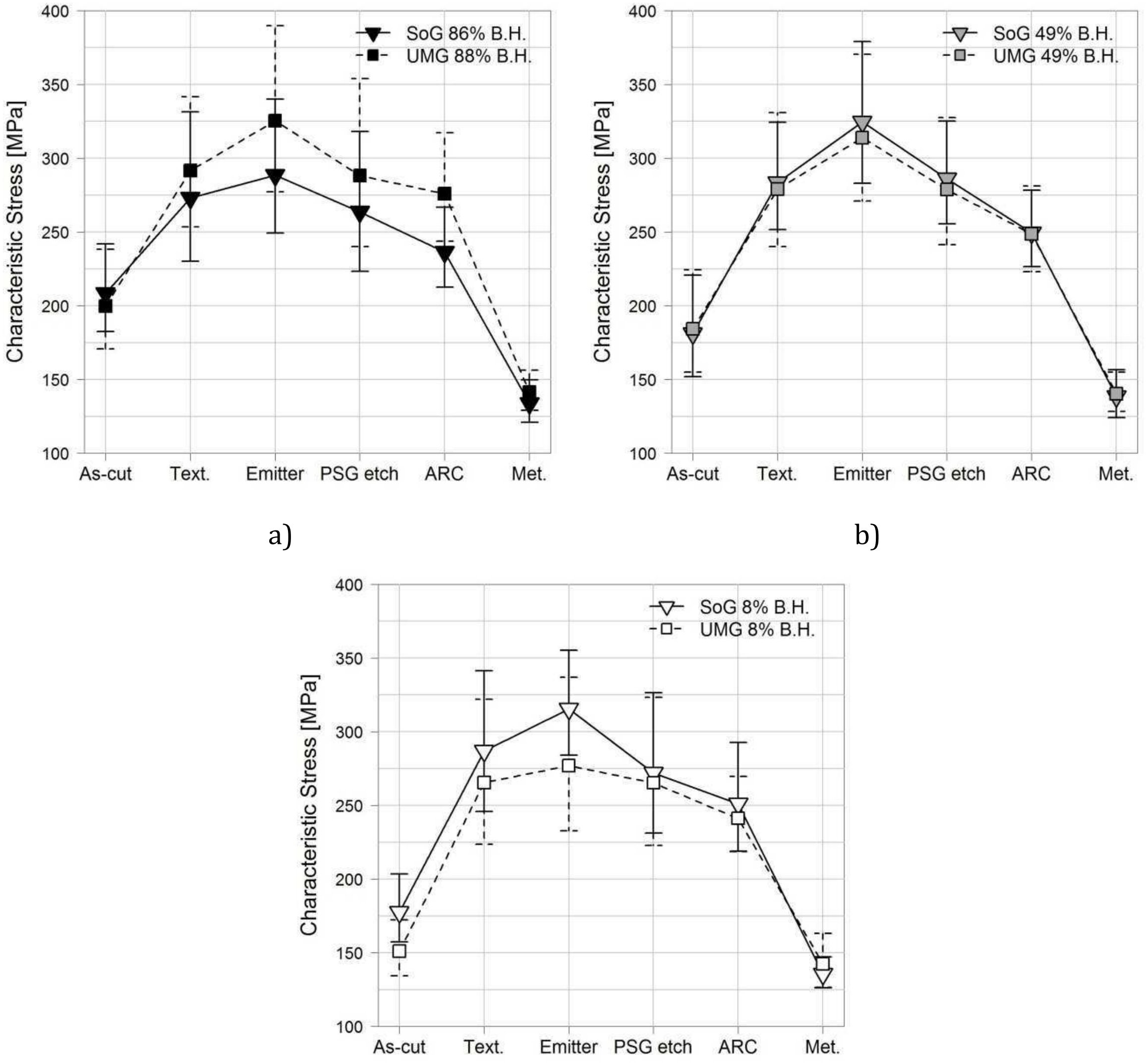

a)

b)

c)

Figure 167 Evolution of the mechanical strength of mc-Si wafers through the processing steps for the manufacture of conventional inert solar cells.

Multi-wire sawing

As-cut wafers from the top parts of the *UMG* and *SoG* mc-Si blocks showed higher mechanical strength than as-cut wafers from the lower parts of the blocks. It was observed that the density of micro-cracks which are perpendicular to the silicon surface is lower at the top of the blocks. Hence, the probability of loading micro-cracks under loading-mode *I* may be lower at the top of the blocks and thus the mechanical strength of these wafers increases.

Texture

The increase in mechanical strength of textured wafers is lower than the increase in mechanical strength after damage etching as the texture process did not remove the micro-cracks in the silicon surface completely. Similar increases in mechanical strength of silicon wafers are reported in the literature [98] where a mathematical model is proposed for modeling the increase in mechanical strength as a function of numeric parameters associated to the blunting of the crack tips and the removal of the cracks.

The comparison of textured *UMG* and *SoG* mc-Si wafers shows that wafers from the middle part of the block have exactly the same mechanical behavior while the top part of the *SoG* mc-Si block has lower mechanical strength than the top part of the *UMG* mc-Si block and the bottom part of the *UMG* mc-Si block has lower mechanical strength than the top part of the *UMG* mc-Si block. This is due most probably to the presence of observed SiC particles at the top of the *SoG* mc-Si block and to the possible presence of amorphous SiO_x and Si_3N_4 particles at the bottom of the *UMG* mc-Si block. However, these differences in mechanical strength are smaller than 30 MPa and may not be significant but they are sustained and even become larger by further solar cell processing.

Emitter Diffusion

Thermal stress is reported in the literature [147] to be the major contributor to the residual stress level in amorphous films. Thermal expansion coefficient of phosphosilicate glass is a value difficult to find in the literature. Sunami et al. [148] reported that the thermal expansion coefficient of SiO_2 layers is equal to that of fused silica, $\alpha_{SiO_2} = 0.55 \times 10^{-6}\ °\mathrm{K}^{-1}$, and a thermal expansion coefficient for a PSG layer deposited on a silicon substrate with a composition $\mathrm{P_2O_5/SiO_2} = 0.04$, is $\alpha_{SiO_2} = 0.87 \times 10^{-6}\ °\mathrm{K}^{-1}$. The PSG layer which is approximately 100 nm is deposited at 900°C and the cooling of PSG layers from 900°C to room temperature is reported to introduce a compressive stress of 200 MPa [147], [148].

Assuming that the elastic properties of the PSG layer are the same like those for amorphous silica (see Table 15 of Appendix A) and considering intrinsic stresses in equation (2.138) negligible, i.e. residual stress is approached to be constituted only by thermal stress, the calculated compressive residual stress within the PSG layer is 252 MPa which is in relative good agreement with the measured values found in the literature.

The layer could fail spontaneously by buckling driven delamination if the compressive residual stress exceeds the value of critical stress for buckling described by equation (2.159). A residual compressive stress of 200 MPa as indicated in the literature could cause the buckling of blisters with relation between film thickness and blister diameter $t_f/b = 0.057$. Therefore, if the PSG layer is 100 nm thick the residual stress can only cause blisters with a maximum radius of 1.75 µm.

If the whole length of the surface defects found in silicon wafers were subjected to the compressive residual stress, then the increase in mechanical strength would be the magnitude of the compressive residual stress, 200 MPa. Unfortunately, the thickness of the PSG layer is much smaller than the size of surface defects and therefore the strengthening effect is softer. If a relatively short crack on the silicon surface which is 0.5 µm long is considered, i.e. the compressive stress covers 20% of the surface crack ($t/a_0 = 0.2$). Figure 26 shows that the application of a tensile stress, which is approximately 52% of the residual compressive stress (104 MPa), cancels the closing effect of the compressive stress of the PSG layer, i.e. the crack closure length is zero ($c/a_0 = 0$). Results for smaller ratios t/a_0 are not depicted in Figure 26 but can be calculated with equation (2.154). If we consider a 2 µm surface crack ($t/a_0 = 0.05$) then an applied tensile stress, which is 16% of the residual compressive stress (32 MPa), cancels the closing effect of the compressive stress of the PSG layer, i.e. the crack closure length is zero ($c/a_0 = 0$). Thus, larger defects require lower applied tensile stress to cancel the strengthening effect of the PSG layer.

The level of strengthening obtained by a compressive residual stress that does not cover entirely a surface crack can be obtained with the aid of Figure 27. If we consider the mechanical strength of textured wafers, 275 MPa, as the fracture strength of the wafers without the strengthening effect (σ_{fr}^0) in comparison with the mechanical strength of emitter diffused wafers, 325 MPa, which shows the strengthening effect (σ_{fr}) and a surface crack length of 0.5 µm ($t/a_0 = 0.2$), then the corresponding ordinate value in Figure 27 for $-\sigma_{fr}^0/\sigma_c = 275/200 = 1.375$ is ~1.2. That means that the strengthening prediction of Figure 27 with the just described conditions is $\sigma_{fr}/\sigma_{fr}^0 \approx 1.2$, which fits with the experimental observation $\sigma_{fr}/\sigma_{fr}^0 = 325/275 \approx 1.2$. Thus, the consideration of the compressive residual stress acting on 0.5 µm long cracks seems to approximate appropriately the mechanical behavior of emitter diffused wafers.

Phosphorous Glass Etch

The strengthening effect of the PSG layer disappears after its removal and the mechanical strength of the wafers is governed by the same factors explained in the case of damage etched and textured wafers.

Antireflection coating

The calculation of the residual stress of SiN_x passivation layers is not straightforward as the thermal expansion coefficient and elastic constants of the layer and therefore, its residual stress depend on the deposition conditions [149], [150]. The residual stress of SiN_x antireflection layers deposited at low temperatures is reported to range between ±250 MPa [149]. Without exact knowledge of the residual stress and film properties is extremely speculative to predict spontaneous micro-cracking of the SiN_x passivation layers.

The decrease in mechanical strength of passivated wafers could be due to tensile residual stresses acting on the 75 nm of the layer thickness. Similar to the case of the strengthening effect of emitter diffused wafers, the decrease in mechanical strength may not reach the amount of the entire tensile residual stress as surface defects are larger than the thickness of the layer.

If the residual stress is compressive a strengthening effect of passivated wafers should be measured. However, the mechanical strength of passivated wafers is 10% lower than the mechanical strength of wafers after PSG etch. In the case that the residual stress is compressive but the mechanical strength of the wafers decrease, another issues influencing the mechanical strength of the wafers should be taken into account. Dislocation etch pits were observed after the deposition of the antireflection coating. The sharp shapes of the dislocation etch pits could be intensifying the applied stress in their tips and hence lowering the mechanical strength of passivated wafers. Another issue to take into account is the diffusion of hydrogen into the silicon bulk of the wafers which passivates the defects and impurities in the bulk silicon. Clusters of hydrogen atoms can be seen as voids or hydrogen bubbles that can intensify the applied stress in their surroundings. This is known as hydrogen embrittlement [151]. The stress intensification could be calculated with the aid of equation (2.165).

Processes that influence the mechanical strength of the wafers by influencing the state of surface defects, like multi-wire sawing and emitter diffusion, do not decrease the elastic modulus of the wafers which is kept near 150 GPa. On the other hand, processes that influence the mechanical strength of the wafers by influencing the state of bulk defects, like for example spontaneous micro-cracking during crystallization in the surroundings of metallic particles or defects formed in the silicon bulk during annealing, indeed lowers the elastic modulus of silicon. The elastic modulus of passivated wafers does not decrease and is approximately 150 GPa. Therefore, the decrease in mechanical strength of passivated wafers is more likely to be due to tensile residual stress within the SiN_x passivation layers and/or stress intensification at dislocation etch pits rather than to hydrogen embrittlement.

Metallization

The analysis of the mechanical strength of the metallic contacts has to distinguish between the front and the back contacts and between samples with and without bus bars. The mechanical strength of the samples broken with the front contact under tensile stress is comparable to the mechanical strength of as-cut wafers 150-160 MPa (see Figure 167).

The fracture stresses of the samples that contain only thin contact fingers and samples with small contact fingers and bus bar follow a single Weibull distribution. The composition of the metallic paste of both the fingers and the bus bars is the same, Ag. Therefore, they exert the same influence on the mechanical strength of the solar cell. The thermal expansion coefficient of silver is $18 \times 10^{-6}\ ^{\circ}\mathrm{K}^{-1}$; thus, like in the case of the cooling of metallic particles after the crystallization of the silicon block, the cooling after contact firing from 900°C to room temperature must introduce large residual thermal stresses in the silicon bulk. As the fingers and bus bars have elongated shapes, the estimation of the thermal residual stress is out of the scope of this work where approximations for the calculation of thermal stresses are provided for spherical particles and thin films or plates. However, common sense and experience leads to conclude that Ag fingers and bus bars introduce large amount of most probably radial thermal residual stresses.

Another issue to consider in the case of fingers and front or rear bus bars is the local formation of a glass frit phase at the interface between Ag and Si (see Figure 168) which adheres the metallic contact to the silicon surface. Similarly to silicon oxide particles, this glass frit phase with lower thermal expansion coefficient than silicon could be introducing locally tangential thermal residual stresses. Both residual stresses either introduced in silicon by the Ag contacts or by the glass frit phase would ease the formation of cracks near the silicon surface (see Figure 163 b)) already at low applied stresses. The fracture criterion is then the same than the one explained for as-cut wafers, where stress intensification at the tips of these cracks controls the mechanical strength.

The decrease in static elastic modulus is very significant, being 90-100 GPa for solar cell samples broken with the front contact subjected to tensile stress. The decrease in elastic modulus could be due to the large residual stresses introduced by the metallic contacts which ease the cracking of the silicon bulk. The elastic modulus of the back Al contact layer is 43 GPa [152] and therefore also lowers the elastic modulus of the whole layered structure (solar cell).

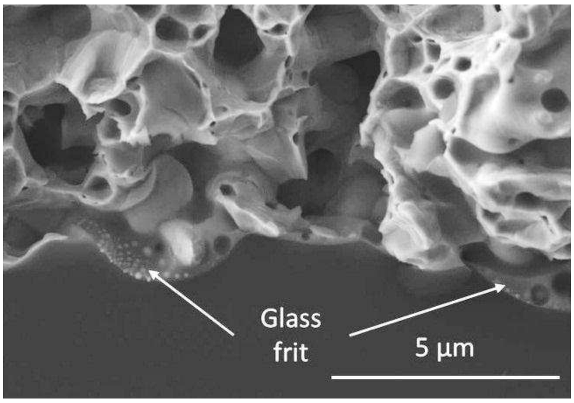

Figure 168 Glass frit phase at the interface between Ag and Si observed in the cross section of a solar cell at a front bus bar.

The fracture stresses of the solar cell samples containing bus bars where the back contact is subjected to tensile stress are much lower than the solar cell samples containing only back Al layer. The mechanical strength of these samples is comparable and a bit lower, 145 MPa, than the mechanical strength of the front fingers and bus bars. The same states for the elastic modulus of these samples which is approximately 85 GPa. The literature reports [153] that metallic contacts where there is an AgAl/Al overlap like in the case of the rear bus bars show the lowest mechanical strength. The ternary Ag-Al-Si phase diagram indicates that, depending on the composition of the system in the locations of the AgAl/Al overlap, the most probable phases that are present are Si accompanied by two of the following phases; Al, Ag_2Al and Ag_3Al [154].

The mechanical strength of the solar cell samples without bus bars broken with the back contact subjected to tensile stress is much higher, 250-325 MPa, sometimes higher than the mechanical strength of textured wafers. This value is not depicted in Figure 167. The mechanical strength of the samples with bus bars is shown in Figure 167 as they can control the mechanical strength of the solar cell if the solar cell is broken entirely.

The 3-4 µm eutectic layer adhered to the silicon surface is where significant thermal stresses are built. Thermal residual stresses can be calculated with equation (2.140) if the bow of the wafers is measured. The Al-Si eutectic temperature, 577°C, is the considered processing temperature and stress is formed when the wafer is cooled from this temperature to room temperature. Under this condition, equation (2.140) predicts 800 MPa tensile thermal stresses within the eutectic layer. However, the literature [155] reports that the calculated values of bows are overestimated when compared with measured bows and that the residual thermal tensile stress is actually 200 MPa. The reason for this is stress relaxation by plastic flow of the Al-Si eutectic layer.

Considering that the residual stress of the 3-4 µm thick Al-Si eutectic layer is 200 MPa, spontaneous cracking criteria can be analyzed. Spontaneous film cracking under tensile residual stress can occur either by channel cracking or by delamination cracking. The Dundurs parameter of Al according to equation (2.142) is -0.34 and the parameter $g(\alpha_D, \beta_D) = 1$ can be read in the graph of Figure 22 b).

The toughness of Al in Table 15 converted to fracture energy release rate with equation (2.41) for plane stress is introduced in the failure criterion for channel cracking (see equation (2.156)). The left term of equation (2.156) is smaller than the right term, $1.58 \times 10^{-4} < 0.64$. Thus, channel cracking of Al-Si eutectic layer is far from occurring due to its ductile behavior.

The left term of equation (2.157) is also smaller than the right term, $0.155 < 2$, hence the delamination of the interface between the Al-Si eutectic layer and the silicon bulk does not occur. For this failure criterion an interface fracture energy release rate of $10\,\mathrm{J/m^2}$ between Al and Si is considered.

The conditions for substrate delamination according to equation (2.158) are not met either, $1.03 < 2.93$. These predictions agree with the experimental observations as no micro-cracking or delamination was observed in the back Al layer. The only observed features were zones similar to delamination where the eutectic layer did not form.

The reasons for the high mechanical strength of the solar cell samples where the back Al layer was subjected to tensile stress are the good integrity of the Al layer which does not crack spontaneously, which even though being under tensile residual stress can profit from its ductility for crack initiation. Moreover, the silicon just below the Al layer is under a small compressive stress. The approximate amount of compressive stress is 8 MPa according to equation (2.134).

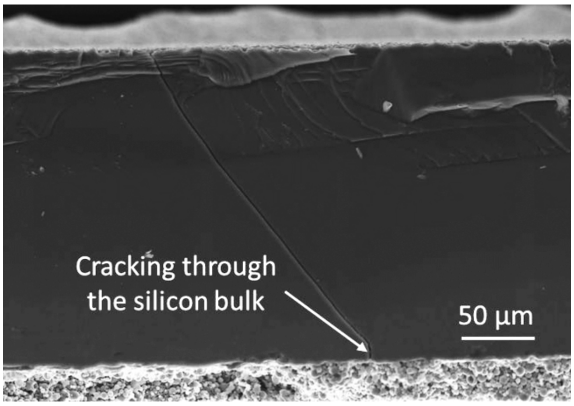

Figure 169 The image shows crack propagation through the thickness of a solar cells where the back contact is subjected to tensile stress. The crack propagates into the silicon bulk rather than through the Al-Si interface.

When the solar cell samples break with the back Al layer under tensile stress cracks propagating from interface defects extend into the silicon bulk rather than through the Al-Si interface like shown in Figure 169. The criterion expressed with equation (2.149) to know whether a crack kinks or continues its propagation through an interface predicts the same behavior. Reading $\psi = \omega(\alpha_D) = 50°$ from Figure 20 and $G/(G_{tip})_{max} = 0.75$ from Figure 21, and being 10 $\mathrm{J/m^2}$ the interface toughness and 1.6 $\mathrm{J/m^2}$ the toughness or energy release rate of silicon, the criterion remains as $0.75 = 1.2/1.6 < 10/1.6$. That means that the energy release rate at the tip of the kinked crack reaches the value of critical energy release rate of the substrate before the energy release rate for interface crack propagation reaches the interface toughness. Thus, the crack prefers to propagate through the silicon bulk rather than through the interface.

When the solar cell samples break with the front contact under tensile stress propagating cracks will deflect to the Al-Si interface or will penetrate into the back Al layer. Figure 24 predicts the ratio of energy release rates at the tips of the deflected crack and the penetrating crack; and for $\alpha_D = -0.34$, $(G_{tip})_d/(G_{tip})_p = 0.25$ can be read in Figure 24. The deflection-penetration criterion remains then as $0.25 = 10/40 < 10/9797$. The toughness of Al, 26 $\mathrm{MPa}\sqrt{\mathrm{m}}$, converted to fracture energy release rate with equation (2.41) for plane stress is 9797 $\mathrm{J/m^2}$. As the estimated toughness of the film is much larger than the estimated toughness of the interface $9797 \gg 10$, the energy release rate of the tip of the deflected crack reaches the value of the interface toughness before the energy release rate of the penetrating crack reaches the toughness of the Al layer. Thus, the crack prefers to propagate through the interface rather than through the Al layer. This prediction agrees with the observation of the fracture surfaces depicted in Figure 170.

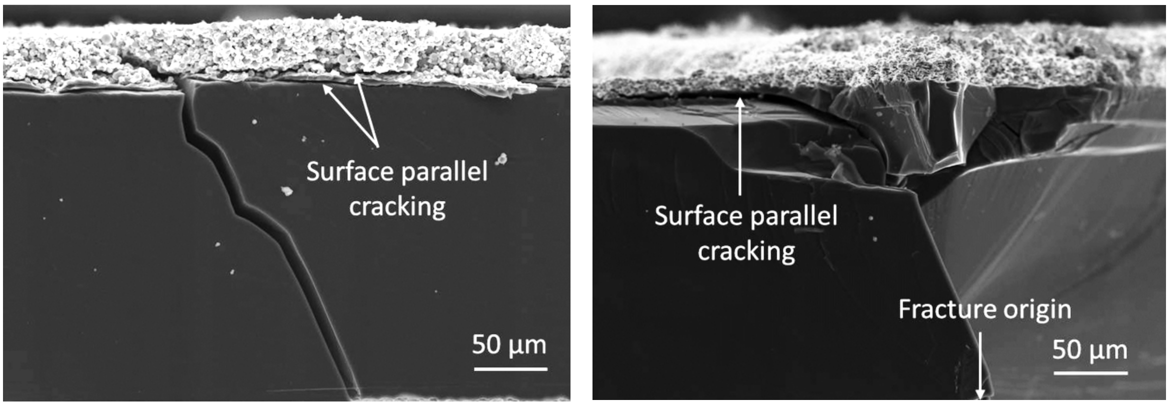

Figure 170 The images show crack propagation through the thickness of solar cells where the front contact is subjected to tensile stress. The crack deviates 90° and propagates parallel to the Al/Si interface when it reaches the back Al contact layer.

6. Conclusions

This chapter presents the relevant conclusions extracted from the evaluation and analysis of the experimental results carried out in this work. The influence of second phase particles on the mechanical behavior of different qualities of mc-Si samples is summarized and the type of particles that result most deleterious for the survival of silicon wafers is identified. Moreover, the influence of every solar cell processing step on the mechanical strength of silicon wafers is reviewed. The most critical processing steps for the mechanical performance of mc-Si wafers are detected and the causes for low mechanical performance are discussed.

The analysis of the experimental results presented in this work from the mechanical characterization of mc-Si blocks crystallized with different qualities of silicon feedstock allows concluding that second phase particles with much larger thermal expansion coefficient than silicon, metals like Al and Cu, are the most detrimental type of defects for multicrystalline silicon for photovoltaic applications. Circumferential micro-cracking occurs in the surroundings of metallic impurities where small metal clusters precipitate. Cracks represent the most severe type of defect controlling the mechanical strength of multicrystalline silicon and should be avoided. Therefore, silicon feedstock with very high amount of metals, especially Al, is not recommended for manufacturing mc-Si with acceptable mechanical strength. The wafers manufactured from the *4N+Al* silicon feedstock showed the worst mechanical behavior.

The second most detrimental type of impurity is amorphous silicon oxide. Amorphous silicon oxide has lower thermal expansion coefficient and elastic modulus than silicon. These two material properties induce the overlap of tensile tangential thermal and elastic stresses which enhances fracture by radial cracking. Additionally, the oriented precipitation of amorphous silicon oxide at grain and twin boundaries eases the link of radial cracks between particles and decreases the mechanical strength of multicrystalline silicon. The content of metal impurities within the *3N* silicon feedstock was not critical as to cause extensive micro-cracking like in the case of the *4N+Al* silicon feedstock but it may have enhanced the precipitation of amorphous silicon oxide at the bottom of the multicrystalline silicon block.

Silicon nitride particles have lower thermal expansion coefficient but higher elastic modulus than silicon. The effect of the lower thermal expansion coefficient is more dominant than the higher elastic modulus. Thus, silicon nitride particles with tensile tangential thermal stresses in their surroundings, decreases the local fracture toughness and cause failure by radial cracking. Silicon nitride increases the elastic modulus of multicrystalline silicon; but as it decreases local toughness, silicon nitride particles do not contribute to raising the mechanical strength of silicon. Silicon nitride and other rich N clusters may be responsible of the low fracture toughness measured with the *UMG* mc-Si block.

Silicon carbide is a type of particle with a moderate influence on the mechanical strength of multicrystalline silicon. It has higher thermal expansion coefficient and elastic modulus than silicon. These two properties increase both the fracture toughness and elastic modulus of multicrystalline silicon. If the radius of the silicon carbide particles stays lower than ~10 µm, the increase in fracture toughness and elastic modulus would allow a higher mechanical strength of the silicon wafers. However, if the precipitation of silicon carbide particles is not homogeneous within the material failure can occur at the interface between areas with high and low density of silicon carbide particles. The presence of silicon carbide particles slightly reduced the mechanical strength of the samples at the top of the *SoG* mc-Si block.

Crystalline silicon oxide is the least deleterious type of impurity particle. Crystalline silicon oxide particles have higher thermal expansion coefficient but lower elastic modulus than silicon. The effect of the higher thermal expansion coefficient is more dominant than the lower elastic modulus. Thus, the toughening effect of the compressive tangential thermal stresses is dominant in the surroundings of the crystalline silicon oxide particles. B suppresses the growth of silicon oxide precipitates which allows the increase in toughness to be translated into an increase in the mechanical strength of *B-doped* mc-Si.

The mechanical strength of as-cut silicon substrates for the manufacture of wafer equivalents is comparable to the mechanical strength of industry standard silicon wafers. Micro-cracks introduced in the silicon surface during multi-wire sawing are the dominant type of defect controlling the mechanical strength of the wafers. Only wafers from the top of the *4N+Al* silicon block with extensive micro-cracking that formed during the cooling phase of the crystallization process in the surrounding of Al particles and that are larger than micro-cracks formed during the multi-wire sawing process, show very low mechanical strength.

After the removal of a 10-15 µm silicon layer per side of the wafers after damage etching, the mechanical strength of the wafers can double the mechanical strength of as-cut wafers. The difference in mechanical strength between different qualities of damage etched mc-Si wafers is due to the presence of cracks and second phase particles formed during the crystallization process. The influence of every single type of second phase particles on the mechanical behavior of the silicon wafers has been just summarized in this chapter.

The deposition of the epitaxial silicon layer decreases the mechanical strength of the silicon substrate. The cooling of the wafers can introduce thermal residual stress; thermal shock caused defects or flaws formed by the yielding of the silicon matrix. As these are process induced defects, the difference in mechanical strength between different qualities of mc-Si wafers becomes smaller and the wafers converge to a certain level of mechanical strength. The presence of the epitaxial silicon layer intensifies the convergence in mechanical strength of wafer equivalents. The level of stress of the epitaxial silicon layer and its surface morphology as well as thermal stresses in the substrate control the mechanical strength of wafer equivalents.

Lastly, it can be concluded that epitaxial wafer equivalents manufactured from low cost silicon substrates show sufficient mechanical strength for further solar cell processing.

The mechanical characterization of mc-Si wafers through the solar cell processing chain revealed that texture and phosphorus emitter diffusion are the solar cell processing steps that increase the mechanical strength of silicon wafers.

The texture process removes micro-cracks partially and blunts the tips of remaining cracks. The amount of silicon removed during texture was insufficient to remove micro-cracks completely. Thus, the increase in mechanical strength of the wafers after texture was lower than the increase in mechanical strength after damage etching which removed deeper silicon layers. Therefore, longer texture processes that remove a deeper silicon layer would be recommended in order to improve the mechanical strength of textured wafers.

The mechanical strength of silicon wafers reached a maximum value after phosphorus emitter diffusion. The deposition of a phosphosilicate glass layer on the surface caused compressive thermal stresses which exerts a strengthening effect that increased 20% the mechanical strength of the silicon wafers.

The solar cell processes that decrease the mechanical behavior of silicon wafers, in an increasing order of impact were block crystallization, the removal of the phosphosilicate glass layer, silicon nitride antireflection coating, multi-wire sawing and metallization.

As it has been already mentioned, the influence of particles formed during crystallization on the mechanical behavior of the silicon wafers has been summarized in this chapter. Therefore, the control of the crystallization process is of most importance in order to provide silicon wafers with acceptable mechanical behavior for further solar cell processing.

The removal of the phosphosilicate glass layer also removes the compressive stress in the silicon surface. Therefore, the mechanical strength of the wafers is comparable to the mechanical strength of textured wafers before phosphorus emitter diffusion.

The 10% reduction in mechanical strength of silicon wafers after silicon nitride antireflection coating in comparison with textured wafers is presumably due to stress intensification at sharp etch pits observed on the surface of passivated wafers.

As it has been already discussed, micro-cracks introduced in the wafer’s surface during multi-wire sawing were responsible for the very low strength of as-cut wafers.

Finally, Al/Ag and Ag bus bars from the back and the front contacts of the solar cell reduced the mechanical strength of the final solar cells to the level of as-cut wafers. High thermal stresses introduced in silicon by the firing of the bus bars makes silicon prone to crack easily at these areas, being these cracks the flaw type controlling the mechanical strength of final solar cells. The Al layer from the back contact even increases the mechanical strength of the solar cell as a layered structure but the negative effect of the bus bars makes this effect not noticeable for the solar cell as a whole structure.

As a final summary, the main contributions of this work are the analysis of the mechanical behavior of silicon wafers as particle composites where impurity particles play a major role in the fracture of silicon and as laminate composites as layers of different materials are deposited on the silicon wafers through solar cell processing. Failure criteria for silicon wafers containing different types of second phase particles and with layers of different materials on them are researched in the literature and applied in order to evaluate the experimental results and predict the mechanical behavior of the silicon wafers. Finally, the influence of impurity particles on the fracture toughness and the elastic modulus of silicon have been also theoretically and experimentally analyzed in this work. All these contributions applied to silicon wafers were not found in the literature and therefore they represent new knowledge. Some measurement techniques performed on silicon, like the ROR bending test on small round pieces from the same wafer which offers a spatial distribution of the fracture stresses of the wafer, fracture toughness measurements with wire and laser introduced notches and dynamic elastic modulus measurements, are not found in actual literature and therefore they also represent a new contribution to the mechanical characterization of silicon.

During the life performance of solar cells, which are assembled into solar panels and exposed to the environment, they will be subjected to cyclic loadings like temperature changes, rainfalls, wind, etc. Therefore, the study of the fatigue behavior of silicon containing different types of impurity particles or layered structures is a very interesting field of research for future works.

Appendices

Appendix A: Material Properties

Table 10 Elastic constants of silicon. Stiffness values are given in GPa and compliance values are given in GPa^{-1} [156], [157], [158].

c_{11}	c_{12}	c_{44}	s_{11}	s_{12}	s_{44}
165.64	63.94	79.51	7.68×10^{-3}	-2.14×10^{-3}	12.6×10^{-3}

Table 11 Engineering elastic constants of silicon. VR states for Voigt and Reuss and HS states for Hashin and Shtrikman. B and μ, an are given in [GPa].

	B	μ_{lower}	$\mu_{av.}$	μ_{upper}
VR	97,84	64,87	66.46	68,04
HS	97,84	66.36	66.50	66.64

Table 12 Engineering elastic modulus of silicon in [GPa]. VR states for Voigt and Reuss and HS states for Hashin and Shtrikman.

	E_{lower}	$E_{av.}$	E_{upper}
VR	159.44	162.57	165.66
HS	162.37	162.67	162.94

Table 13 Engineering Poisson´s ratio of silicon [-]. VR states for Voigt and Reuss and HS states for Hashin and Shtrikman.

	ν_{lower}	$\nu_{av.}$	ν_{upper}
VR	0.217	0.223	0.229
HS	0.223	0.223	0.223

Table 14 Values of the thermal expansion coefficient of silicon at different temperatures [69].

$T[\mathrm{K}]$	$\alpha(T)\times 10^{-6}[\mathrm{K}^{-1}]$	$T[\mathrm{K}]$	$\alpha(T)\times 10^{-6}[\mathrm{K}^{-1}]$
100	-0.51	380	3.11
120	-0.02	400	3.21
140	0.41	500	3.59
160	0.80	600	3.83
180	1.14	700	3.99
200	1.45	800	4.10
220	1.73	900	4.19
240	1.97	1000	4.26
260	2.19	1100	4.32
280	2.39	1200	4.38
300	2.57	1300	4.44
320	2.73	1400	4.50
340	2.87	1500	4.56
360	2.99		

Table 15 Material properties of silicon and the second phase particles found within the crystallized mc-Si blocks at 775°C.

Material	$\alpha\times 10^{-6}[\mathrm{K}^{-1}]$	$\nu[-]$	$E[\mathrm{GPa}]$	$K_{Ic}[\mathrm{MPa}]$
Si	4.3	0.223	162.6	0.83-0.94
Al	23	0.334	69	22-30
Cu	16.9	0.34	117	-
SiO_x (am.)	0.5	0.165	73	0.6-0.8
SiO_x (cryst.)	12.3	0.17	70	-
Si_3N_4	2.35	0.27	310	4-6
SiC	4.8	0.15	380	2.5-5

Appendix B: Tables for the Calculation of the Maximum-Likelihood Estimates

Table 16 Unbiaxing factors for the maximum likelihood estimate of the Weibull modulus.

Number of Specimens, *n*	**Unbiasing Factor, *UF***	**Number of Specimens, *n***	**Unbiasing Factor, *UF***
5	0.700	42	0.968
6	0.752	44	0.970
7	0.792	46	0.971
8	0.820	48	0.972
9	0.842	50	0.973
10	0.859	52	0.974
11	0.872	54	0.975
12	0.883	56	0.976
13	0.893	58	0.977
14	0.901	60	0.978
15	0.908	62	0.979
16	0.914	64	0.980
18	0.923	66	0.980
20	0.931	68	0.981
22	0.938	70	0.981
24	0.943	72	0.982
26	0.947	74	0.982
28	0.951	76	0.983
30	0.955	78	0.983
32	0.958	80	0.984
34	0.960	85	0.985
36	0.962	90	0.986
38	0.964	100	0.987
40	0.966	120	0.990

Table 17 Normalized upper and lower bounds on the maximum likelihood estimate of the Weibull modulus - 90% confidence ranges.

Number of Specimens, n	$q_{0.05}$	$q_{0.95}$	**Number of Specimens, n**	$q_{0.05}$	$q_{0.95}$
5	0.683	2.779	42	0.842	1.265
6	0.697	2.436	44	0.845	1.256
7	0.709	2.183	46	0.847	1.249
8	0.720	2.015	48	0.850	1.242
9	0.729	1.896	50	0.852	1.235
10	0.738	1.807	52	0.854	1.229
11	0.745	1.738	54	0.857	1.224
12	0.752	1.682	56	0.859	1.218
13	0.759	1.636	58	0.861	1.213
14	0.764	1.597	60	0.863	1.208
15	0.770	1.564	62	0.864	1.204
16	0.775	1.535	64	0.866	1.200
17	0.779	1.510	66	0.868	1.196
18	0.784	1.487	68	0.869	1.192
19	0.788	1.467	70	0.871	1.188
20	0.791	1.449	72	0.872	1.185
22	0.798	1.418	74	0.874	1.182
24	0.805	1.392	76	0.875	1.179
26	0.810	1.370	78	0.876	1.176
28	0.815	1.351	80	0.878	1.173
30	0.820	1.334	85	0.881	1.166
32	0.824	1.319	90	0.883	1.160
34	0.828	1.306	95	0.886	1.155
36	0.832	1.294	100	0.888	1.150
38	0.835	1.283	110	0.893	1.141
40	0.839	1.273	120	0.897	1.133

Table 18 Normalized upper and lower bounds on the function t - 90% confidence ranges.

Number of Specimens, *n*	$t_{0.05}$	$t_{0.95}$	**Number of Specimens, *n***	$t_{0.05}$	$t_{0.95}$
5	-1.247	1.107	42	-0.280	0.278
6	-1.007	0.939	44	-0.273	0.271
7	-0.874	0.829	46	-0.266	0.264
8	-0.784	0.751	48	-0.260	0.258
9	-0.717	0.691	50	-0.254	0.253
10	-0.665	0.644	52	-0.249	0.247
11	-0.622	0.605	54	-0.244	0.243
12	-0.587	0.572	56	-0.239	0.238
13	-0.557	0.544	58	-0.234	0.233
14	-0.532	0.520	60	-0.230	0.229
15	-0.509	0.499	62	-0.266	0.225
16	-0.489	0.480	64	-0.222	0.221
17	-0.471	0.463	66	-0.218	0.218
18	-0.455	0.447	68	-0.215	0.214
19	-0.441	0.433	70	-0.211	0.211
20	-0.428	0.421	72	-0.208	0.208
22	-0.404	0.398	74	-0.205	0.205
24	-0.384	0.379	76	-0.202	0.202
26	-0.367	0.362	78	-0.199	0.199
28	-0.352	0.347	80	-0.197	0.197
30	-0.338	0.334	85	-0.190	0.190
32	-0.326	0.323	90	-0.184	0.185
34	-0.315	0.312	95	-0.179	0.179
36	-0.305	0.302	100	-0.174	0.175
38	-0.296	0.293	110	-0.165	0.166
40	-0/288	0.235	120	-0.158	0.169

Appendix C: R Routine for the Calculation of the Maximum-Likelihood Estimates

###Programming the "*ln*" function###

```
ln<-function(x, ...)

{

log(x, base=exp(1))

}
```

###Importing fracture stresses and sorting them in increasing order###

```
S_biaxial<-read.table("samplename.txt")

S_biaxial_a<-c(S_biaxial[,1])

S_biaxial_ordered<-sort(S_biaxial_a)
```

###Calculation of $\widehat{m}$ and $\widehat{\sigma_\theta}$ by the maximum-likelihood method###

```
m_init<-1.00

m_end<-50.00

step<-0.01

N<-length(S_biaxial_ordered)

r<-N

a<-c()

b<-c()

c<-c()

fun<-c()

diff<-c()

res<-c()

m<-seq(m_init,m_end,by=step)

for(i in 1:length(m))

{

a<-sum((S_biaxial_ordered)^(m[i])*ln(S_biaxial_ordered))

b<-sum((S_biaxial_ordered)^m[i])

c<-sum(ln(S_biaxial_ordered))

fun[i]<-1/((a/b)-((1/r)*c))

diff[i]<-fun[i]-m[i]
```

```
fun[i]

if( -0.009 < diff[i] & diff[i] < 0.009 ) {

res_m<-data.frame(fun[i],m[i],diff[i])

}

}

S_m<-S_biaxial_ordered^res_m[,2]

S_biaxial_characteristic<-(sum(S_m)/r)^(1/res_m[,2])
```

###Unbiasing $\hat{m}$ and calculation of the confidence ranges for m###

```
UF_m<-read.table("UF_m.txt",col.names=c("UF_m"))

u_m<-res_m[,2]*UF_m[length(S_biaxial_ordered),]

q_m<-read.table("q_m.txt",col.names=c("q_0.05","q_0.95"))

u_m_u_b<-res_m[,2]/q_m[length(S_biaxial_ordered),1]

u_m_l_b<-res_m[,2]/q_m[length(S_biaxial_ordered),2]

Weibull_module<-data.frame(u_m,u_m_u_b,u_m_l_b)
```

###Exporting m with confidence bounds###

```
write.table(Weibull_module,"m_samplename.txt",row.names=FALSE,col.names=
FALSE)
```

###Calculation of the confidence ranges for $\hat{\sigma}_\theta$###

```
t_S_characteristic<-
read.table("t_S_characteristic.txt",col.names=c("t_0.05","t_0.95"))

t_S_u_b<-S_biaxial_characteristic*exp(-
t_S_characteristic[length(S_biaxial),1]/res_m[,2])

t_S_l_b<-S_biaxial_characteristic*exp(-
t_S_characteristic[length(S_biaxial),2]/res_m[,2])

S_characteristic<-data.frame(S_biaxial_characteristic,t_S_u_b,t_S_l_b)
```

###Exporting σ_θ with confidence bounds###

```
write.table(S_characteristic,"Charact_stress_samplename.txt",row.names=F
ALSE,col.names=FALSE)
```

###Calculation and exporting of data files necessary in the routine of Appendix D for depicting the graph of the cumulative Weibull density function###

###Calculation and exporting of the experimental values (fracture probability and stresses)###

```
p<-seq(1,length(S_biaxial_ordered),1)

P_f<-(p-0.5)/length(S_biaxial_ordered)

P_f_S_biaxial<-data.frame(P_f,S_biaxial_ordered)

write.table(P_f_S_biaxial,"P_f_S_biaxial_samplename.txt",row.names=FALSE
,col.names=FALSE)
```

###Calculation and exporting of the cumulative Weibull density function###

```
s<-seq(0,1725,1)

Prob_failure<-1-exp(-(s/S_biaxial_characteristic)^u_m)

write.table(Prob_failure,"Prob_failure_samplename.txt",row.names=FALSE,c
ol.names=FALSE)
```

###Exporting data for depicting arrows pointing at the σ_θ in the cumulative Weibull density function graph###

```
l_o_a<-0.632

c_o_a<-0

l_f_a<-0.632

c_f_a<-S_biaxial_characteristic

l_o_b<-0.632

c_o_b<-S_biaxial_characteristic

l_f_b<-0

c_f_b<-S_biaxial_characteristic

arrows_wcdf<-data.frame(l_o_a, c_o_a, l_f_a, c_f_a, l_o_b, c_o_b, l_f_b,
c_f_b)

write.table(arrows_wcdf,"arrows_wcdf_samplename.txt",row.names=FALSE,col
.names=FALSE)
```

Appendix D: R Routine for the Representation of the Cumulative Weibull Density Function

Importing the data which was calculated and exported with the routine of Appendix C for depicting the cumulative Weibull density function###

```
P_f_S_biaxial_samplename<-
read.table("P_f_S_biaxial_samplename.txt",col.names=c("P_f",
"S_biaxial"))

P_f_samplename<-c(P_f_S_biaxial_samplename[,"P_f"])

S_biaxial_samplename<-c(P_f_S_biaxial_samplename[,"S_biaxial"])

Prob_failure_samplename<-
read.table("Prob_failure_samplename.txt",col.names=c("Prob_failure"))

Prob_failure_samplename<-c(Prob_failure_samplename[,"Prob_failure"])

arrows_wcdf_samplename<-
read.table("arrows_wcdf_samplename.txt",col.names=c("l_o_a","c_o_a","l_f
_a","c_f_a","l_o_b","c_o_b","l_f_b","c_f_b"))

l_o_a_samplename<-c(arrows_wcdf_samplename[,"l_o_a"])

c_o_a_samplename<-c(arrows_wcdf_samplename[,"c_o_a"])

l_f_a_samplename<-c(arrows_wcdf_samplename[,"l_f_a"])

c_f_a_samplename<-c(arrows_wcdf_samplename[,"c_f_a"])

l_o_b_samplename<-c(arrows_wcdf_samplename[,"l_o_b"])

c_o_b_samplename<-c(arrows_wcdf_samplename[,"c_o_b"])

l_f_b_samplename<-c(arrows_wcdf_samplename[,"l_f_b"])

c_f_b_samplename<-c(arrows_wcdf_samplename[,"c_f_b"])
```

###Representation of the cumulative Weibull density function###

```
gridy<-seq(50,650,50)

gridx<-seq(0.1,0.9,0.1)

s<-seq(0,1725,1)

yrange<-c(0,1)

xrange<-c(0,675)

jpeg("samplename.jpg", width=1440, height=1300, pointsize=32)

par(mai=c(0,0,0,0),mar=c(5, 5, 2, 1))

plot(S_biaxial_samplename, P_f_samplename, type="p", pch=8,
col="black", cex=1.3, lwd=2.0, bg="white", ylab="", xlab="",
cex.axis=1.35,  font.lab=2, cex.lab=1.8, lab=c(10,10,20), ylim=yrange,
xlim=xrange, main=(""), cex.main=1.6, xaxs="i", yaxs="i", las=1)
```

```
mtext(side=2, text="Fracture Probability", line=3.5, cex= 1.75)

mtext(side=1, text="Stress [MPa]", line=3, cex= 1.75)

abline(h=gridx, v=0, col="grey", lty=1, lwd=2.5)

abline(h=0, v=gridy, col="grey", lty=1, lwd=2.5)

points(S_biaxial_samplename,P_f_samplename, pch=8, col="black",
bg="white", cex=1.3, lwd=2.5)

lines(s, Prob_failure_samplename,col="black", lty=1, lwd=3.0)

arrows(c_o_a_samplename, l_o_a_samplename, c_f_a_samplename,
l_f_a_samplename, length=0, code=2, col="black", lty=1, lwd=2)

arrows(c_o_b_samplename, l_o_b_samplename, c_f_b_samplename,
l_f_b_samplename, length=0.50, code=2, col="black", lty=1, lwd=2)

x<-410

y<-0.22

legend(x, y, c("samplename"), text.col = "black", pch=c(8), col =
c("black"), pt.bg=c("white"), pt.lwd=2.0, lty = c(1), lwd=c(2.5),
bty="o", bg="white", cex=1.35)

dev.off()
```

Appendix E: Weibull Graphs and Weibull Parameters for the Three-point Bending Test

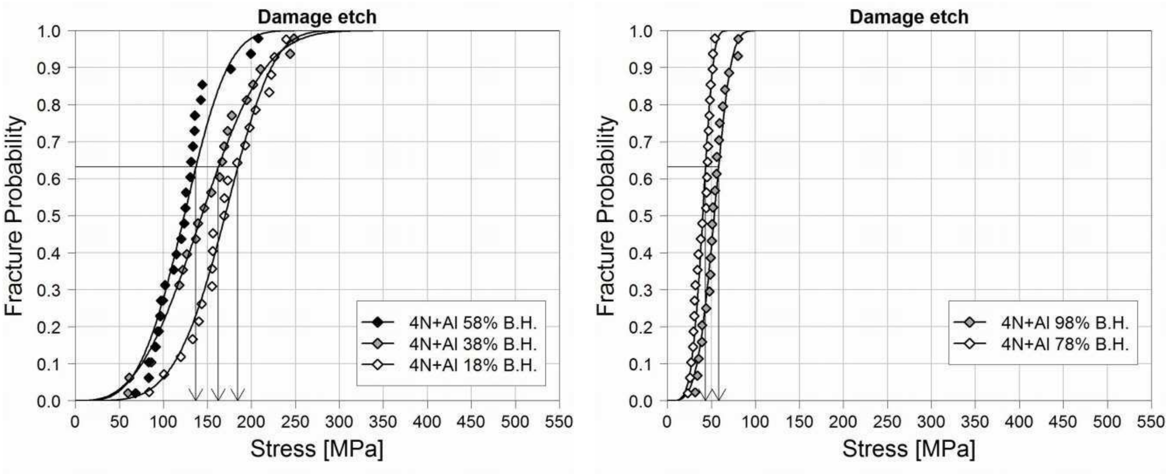

a) b)

Figure 171 Weibull graphs plotting fracture probability against applied uniaxial stress for 4N+Al mc-Si after damage etching.

Table 19 Characteristic stress, σ_θ [MPa], and Weibull modulus, m [-], for damage etched 4N+Al mc-Si.

B. H.	$\sigma_{\theta_{lower}}$	σ_θ	$\sigma_{\theta_{upper}}$	m_{lower}	m	m_{upper}
TPB						
98%	44.9	58.1	77.6	3.0	4.0	5.4
78%	34.7	43.1	55.1	3.7	4.8	6.3
58%	102.2	136.8	190.1	2.7	3.6	4.7
38%	113.7	162.4	242.9	2.2	2.9	3.9
18%	146.3	184.5	239.6	3.3	4.5	6.0

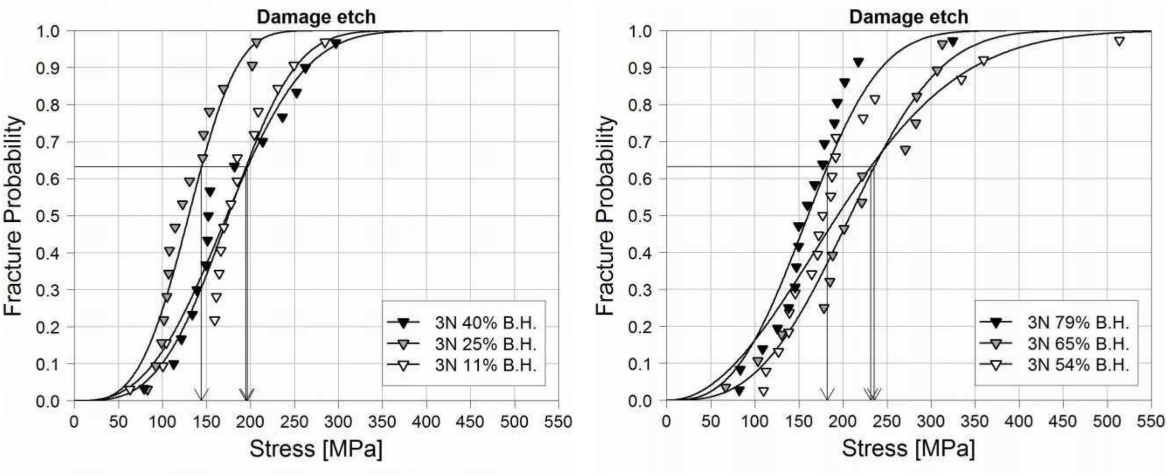

a) b)

Figure 172 Weibull graphs plotting fracture probability against applied uniaxial stress for 3N mc-Si after damage etching.

Table 20 Characteristic stress, σ_θ [MPa], and Weibull modulus, m [-], for damage etched 3N mc-Si.

B. H.	$\sigma_{\theta_{lower}}$	σ_{θ}	$\sigma_{\theta_{upper}}$	m_{lower}	m	m_{upper}
79%	127.4	182.0	272.2	2.1	2.9	4.0
65%	168.5	235.5	343.2	2.1	3.0	4.3
54%	140.6	231.6	406.1	1.5	2.1	2.8
40%	138.2	196.7	292.5	2.0	2.9	4.1
25%	107.2	144.2	201.2	2.4	3.4	4.8
11%	143.9	194.9	274.2	2.4	3.3	4.7

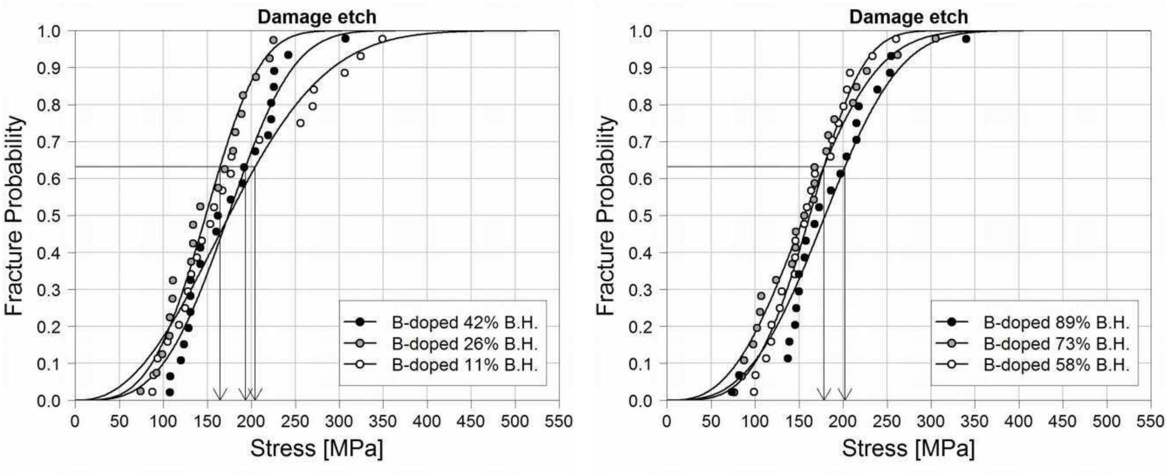

a) b)

Figure 173 Weibull graphs plotting fracture probability against applied uniaxial stress for B-doped mc-Si after damage etching.

Table 21 Characteristic stress, σ_θ [MPa], and Weibull modulus, m [-], for damage etched B-doped mc-Si.

B. H.	$\sigma_{\theta_{lower}}$	σ_θ	$\sigma_{\theta_{upper}}$	m_{lower}	m	m_{upper}
89%	144.4	202.1	295.3	2.3	3.1	4.1
73%	122.2	178.1	272.2	2.1	2.8	3.7
58%	135.9	178.2	241.7	2.9	3.8	5.1
42%	142.4	193.5	273.3	2.6	3.4	4.5
26%	122.6	164.4	228.9	2.6	3.5	4.8
11%	130.8	204.5	338.1	1.7	2.3	3.1

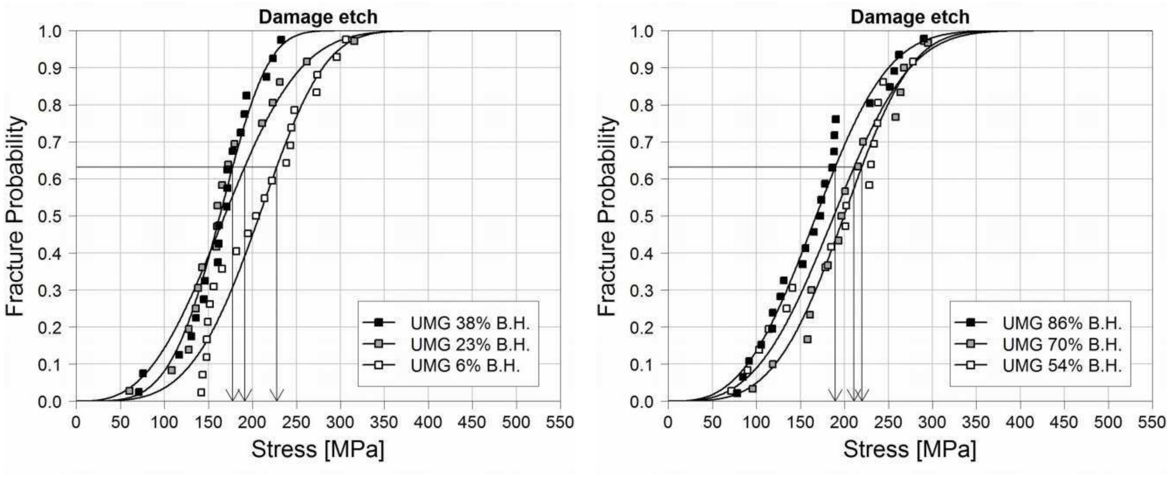

a) b)

Figure 174 Weibull graphs plotting fracture probability against applied uniaxial stress for UMG mc-Si after damage etching.

Table 22 Characteristic stress, σ_θ [MPa], and Weibull modulus, m [-], for damage etched UMG mc-Si.

B. H.	$\sigma_{\theta_{lower}}$	σ_{θ}	$\sigma_{\theta_{upper}}$	m_{lower}	m	m_{upper}
86%	133.9	189.5	280.1	2.3	3.0	4.0
70%	168.4	219.7	296.5	2.7	3.8	5.4
54%	152.7	210.9	303.4	2.3	3.2	4.4
38%	139.4	177.4	232.6	3.2	4.3	5.8
23%	133.9	191.1	285.4	2.1	2.9	4.0
6%	175.9	227.5	304.0	3.0	4.0	5.4

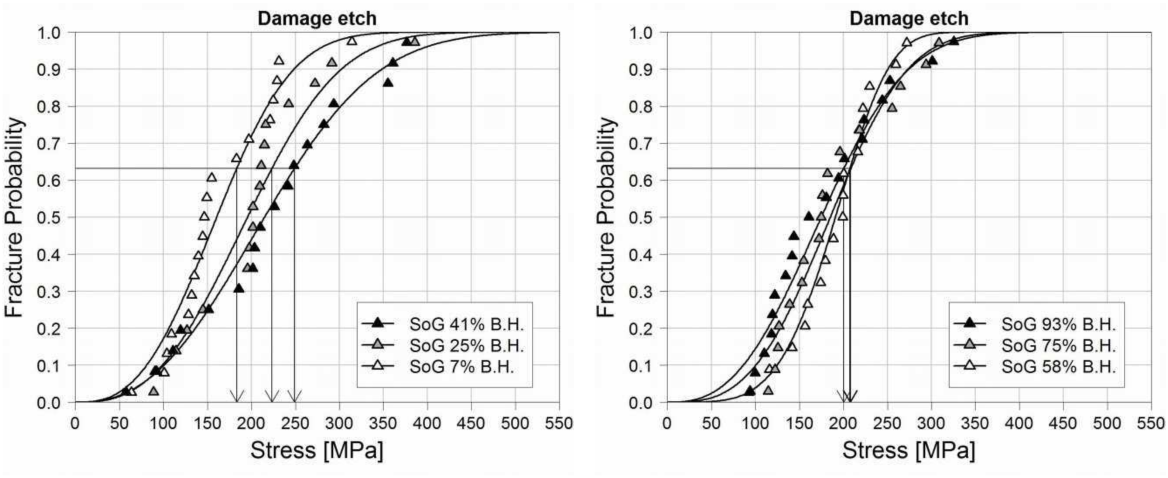

a) b)

Figure 175 Weibull graphs plotting fracture probability against applied uniaxial stress for SoG mc-Si after damage etching.

Table 23 Characteristic stress, σ_θ [MPa], and Weibull modulus, m [-], for damage etched SoG mc-Si.

B. H.	$\boldsymbol{\sigma_{\theta_{lower}}}$	$\boldsymbol{\sigma_\theta}$	$\boldsymbol{\sigma_{\theta_{upper}}}$	$\boldsymbol{m_{lower}}$	$\boldsymbol{m}$	$\boldsymbol{m_{upper}}$
93%	136.3	200.4	309.5	2.0	2.7	3.6
75%	149.7	208.4	302.3	2.2	3.1	4.3
58%	164.6	207.3	268.8	3.2	4.4	6.2
41%	165.0	249.0	395.8	1.8	2.5	3.4
25%	154.0	223.3	339.3	2.0	2.8	3.8
7%	126.1	183.3	279.3	2.0	2.7	3.8

Appendix F: Weibull Graphs and Weibull Parameters for the Ring-on-ring Bending Test

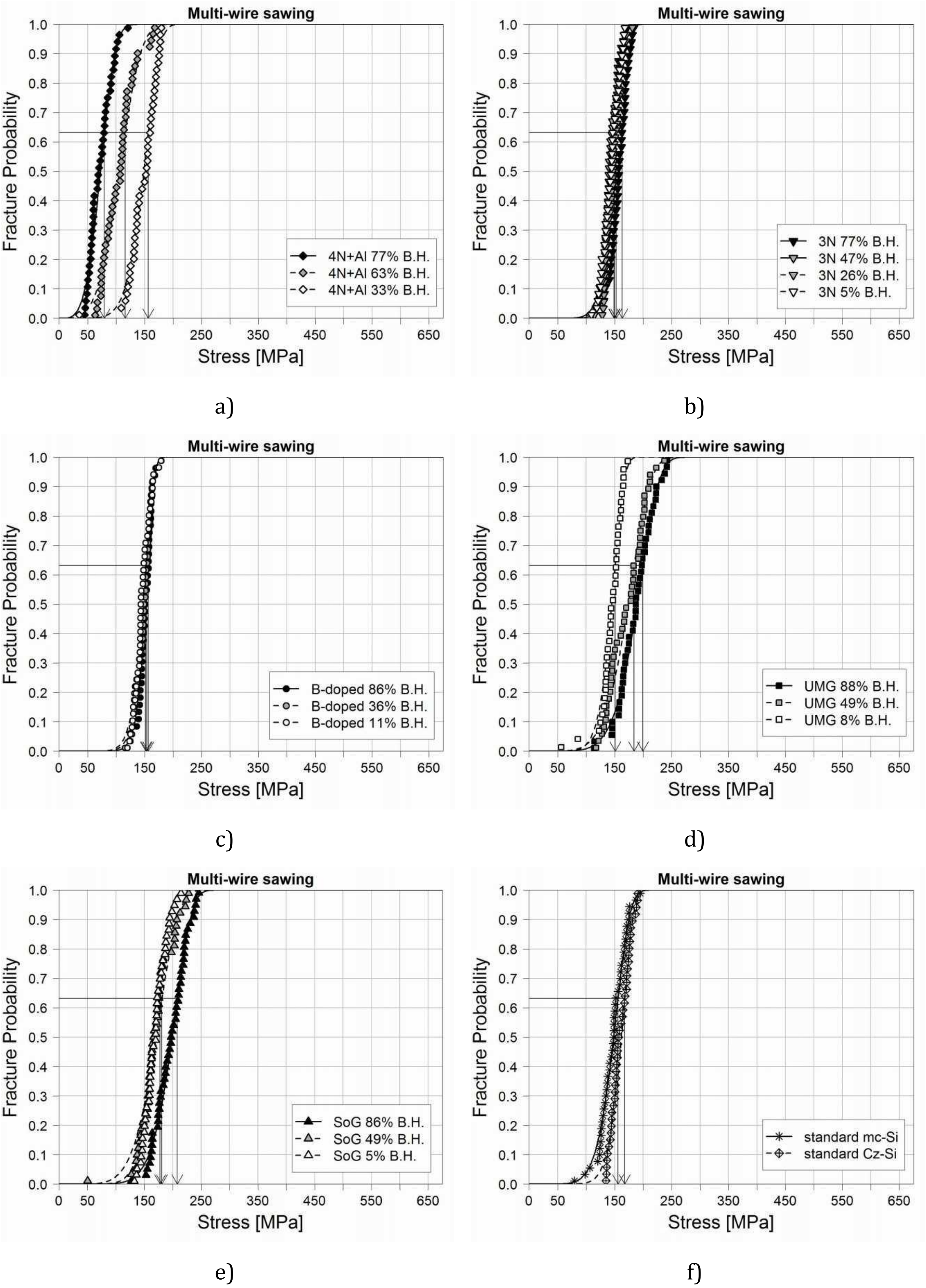

a) b) c) d) e) f)

Figure 176 Weibull graphs plotting fracture probability against applied equibiaxial stress after multi-wire sawing.

Table 24 Characteristic stress, σ_θ [MPa], and Weibull modulus, m [-], for sawn wafers.

B. H.	$\sigma_{\theta_{lower}}$	σ_θ	$\sigma_{\theta_{upper}}$	m_{lower}	m	m_{upper}
4N+Al mc-Si						
77%	60.8	79.6	107.9	3.2	4.0	4.9
63%	89.1	116.2	156.7	3.3	4.0	4.9
33%	135.0	156.4	184.7	5.9	7.3	8.9
3N mc-Si						
77%	149.0	163.3	181.1	9.5	11.7	14.3
47%	137.6	152.6	171.6	8.4	10.3	12.6
26%	136.7	149.3	164.8	10.0	12.2	14.9
5%	135.4	149.5	167.1	8.8	10.8	13.3
B-doped mc-Si						
86%	144.8	156.5	171.0	11.1	13.7	16.8
36%	140.6	154.1	170.9	9.6	11.7	14.3
11%	137.7	152.2	170.4	8.8	10.7	13.1
UMG mc-Si						
88%	170.7	199.7	238.3	5.8	7.0	8.4
49%	155.0	184.4	224.3	5.0	6.2	7.6
8%	134.4	151.0	172.2	7.3	9.1	11.4
SoG mc-Si						
86%	182.5	208.3	241.8	6.8	8.1	9.8
49%	152.0	181.2	220.8	5.0	6.1	7.5
5%	157.4	177.6	203.5	7.4	8.9	10.8
Standard mc-Si						
?	134.3	155.9	184.5	5.9	7.2	8.8
Standard Cz-Si						
?	151.3	167.8	188.5	8.5	10.4	12.7

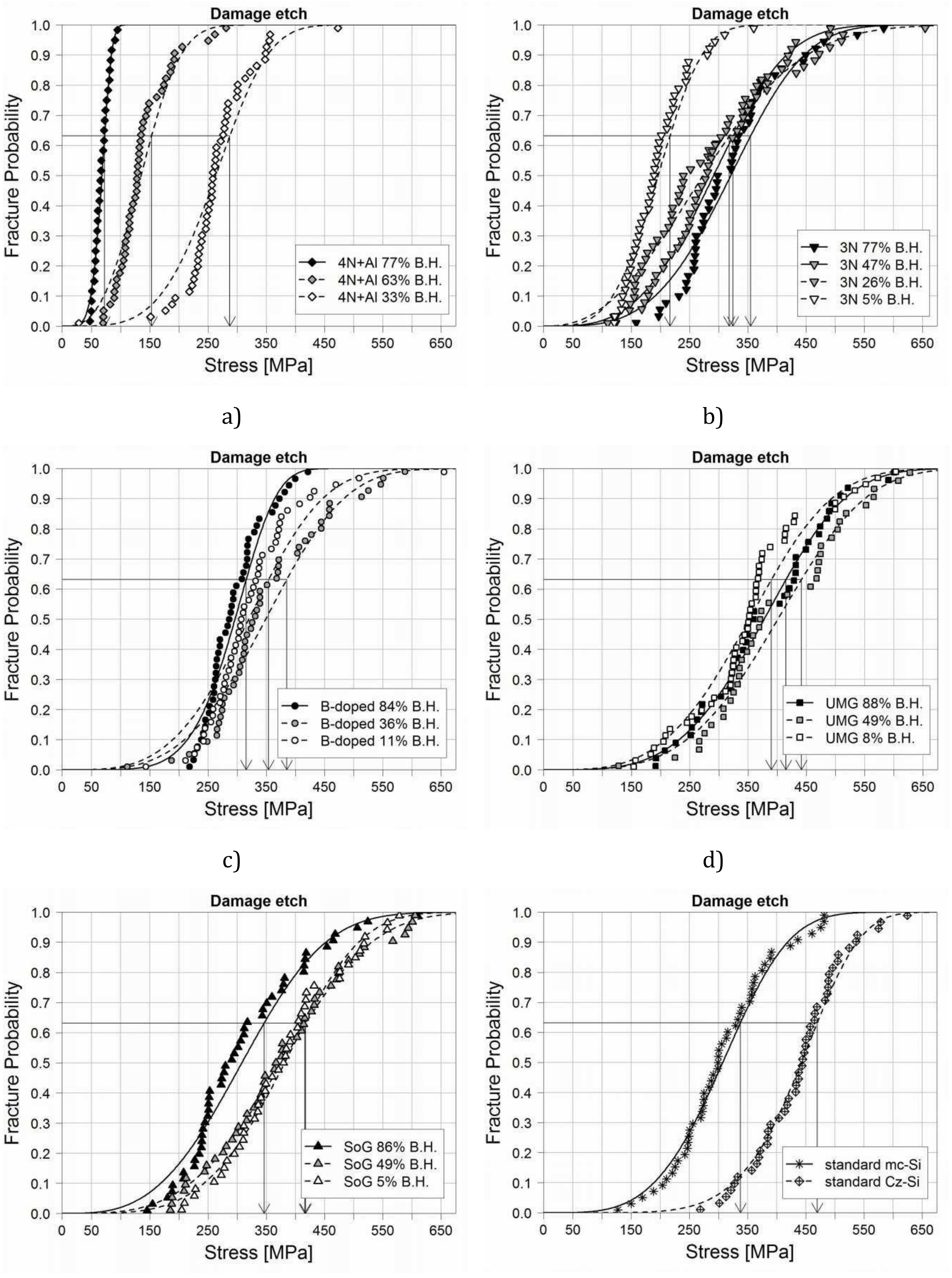

a) b)

c) d)

e) f)

Figure 177 Weibull graphs plotting fracture probability against applied equibiaxial stress after damage etching.

Table 25 Characteristic stress, σ_θ [MPa], and Weibull modulus, m [-], for damage etched wafers.

B. H.	$\sigma_{\theta_{lower}}$	σ_{θ}	$\sigma_{\theta_{upper}}$	m_{lower}	m	m_{upper}
4N+Al mc-Si						
77%	60.1	72.7	90.0	4.4	5.6	7.1
63%	106.2	153.2	231.5	2.4	2.9	3.6
33%	221.6	287.5	385.6	3.4	4.1	5.0
3N mc-Si						
77%	263.7	354.9	495.7	3.0	3.6	4.4
47%	235.9	324.8	465.8	2.8	3.4	4.1
26%	203.0	318.3	528.5	2.0	2.4	2.9
5%	161.9	216.5	300.4	3.0	3.7	4.5
B-doped mc-Si						
84%	262.3	315.6	388.6	4.8	5.8	7.1
36%	287.9	385.2	534.8	3.1	3.7	4.5
11%	262.5	354.1	496.0	3.0	3.6	4.4
UMG mc-Si						
88%	314.8	415.1	567.0	3.1	3.9	4.8
49%	333.7	441.6	605.6	3.1	3.8	4.7
8%	288.6	390.2	548.1	3.0	3.6	4.3
SoG mc-Si						
86%	245.5	346.2	510.0	2.6	3.1	3.8
49%	307.0	417.8	591.4	2.9	3.5	4.2
5%	322.0	416.3	555.9	3.4	4.2	5.1
Standard mc-Si						
?	255.9	337.7	461.7	3.2	3.9	4.7
Standard Cz-Si						
?	394.2	469.6	572.0	5.1	6.1	7.5

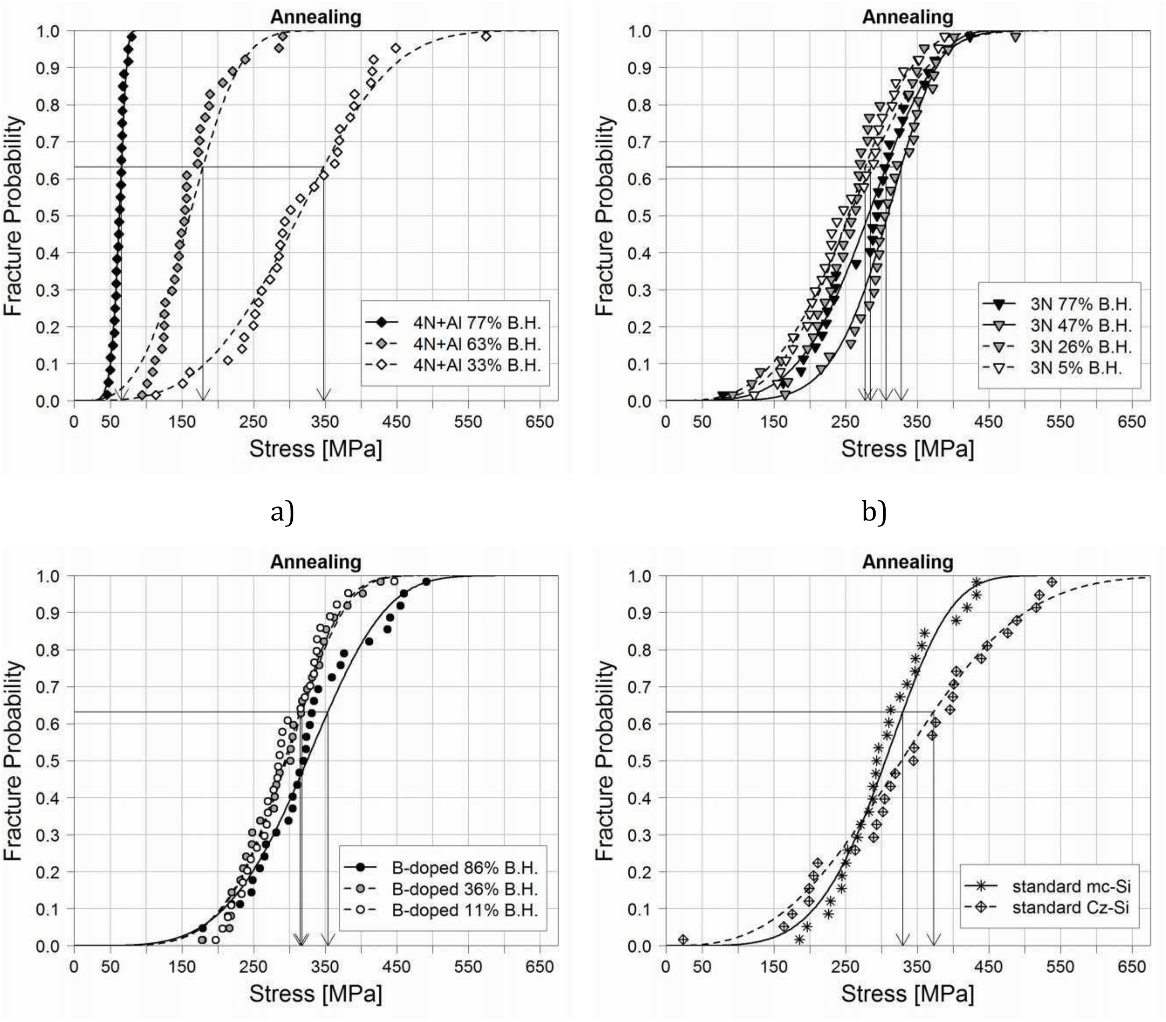

a) b)

d) d)

Figure 178 Weibull graphs plotting fracture probability against applied equibiaxial stress after annealing.

Table 26 Characteristic stress, σ_θ [MPa], and Weibull modulus, m [-], for annealed wafers.

B. H.	$\sigma_{\theta_{lower}}$	σ_θ	$\sigma_{\theta_{upper}}$	m_{lower}	m	m_{upper}
4N+Al mc-Si						
77%	57.6	65.5	75.8	6.4	8.2	10.4
63%	130.8	179.2	255.4	2.7	3.4	4.3
33%	256.4	347.8	490.3	2.8	3.5	4.4
3N mc-Si						
77%	239.5	306.6	405.0	3.4	4.3	5.5
47%	275.3	327.7	398.6	4.7	6.1	7.8
26%	208.7	284.6	403.6	2.7	3.4	4.3
5%	213.2	277.5	373.4	3.2	4.0	5.1
B-doped mc-Si						
86%	275.6	353.6	468.3	3.3	4.2	5.4
36%	258.7	317.8	400.7	4.1	5.1	6.5
11%	256.6	314.8	396.4	4.1	5.2	6.6
Standard mc-Si						
?	264.5	329.8	423.0	3.7	4.8	6.1
Standard Cz-Si						
?	257.1	372.8	566.5	2.2	2.8	3.6

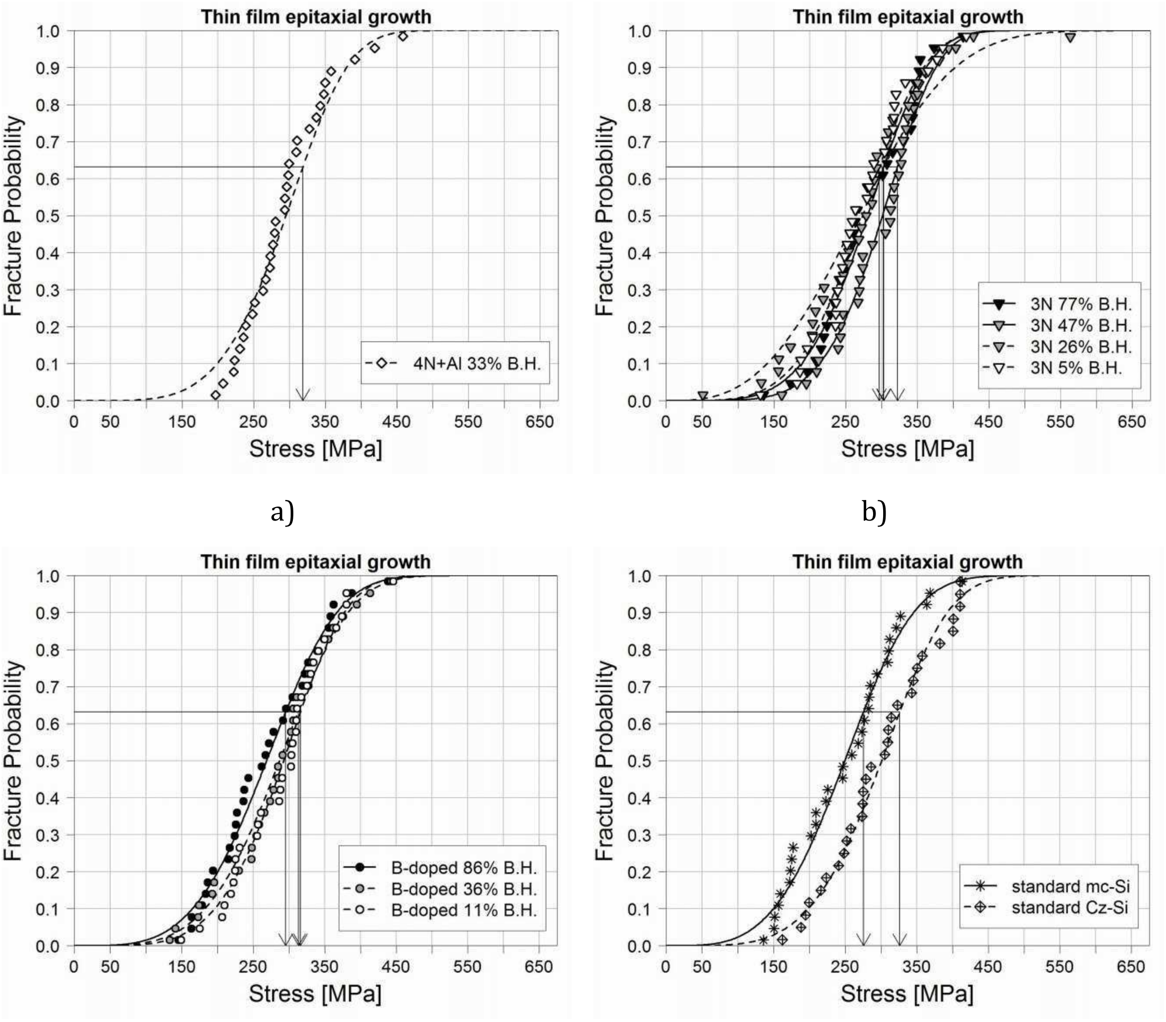

a) b)

c) d)

Figure 179 Weibull graphs plotting fracture probability against applied equibiaxial stress after thin film deposition.

Table 27 Characteristic stress, σ_θ [MPa], and Weibull modulus, m [-], for wafer equivalents.

B. H.	$\sigma_{\theta_{lower}}$	σ_θ	$\sigma_{\theta_{upper}}$	m_{lower}	m	m_{upper}
4N+Al mc-Si						
77%	-	-	-	-	-	-
63%	-	-	-	-	-	-
33%	255.2	318.8	409.5	3.8	4.8	6.0
3N mc-Si						
77%	241.9	303.2	391.1	3.7	4.7	5.9
47%	265.2	322.3	401.5	4.3	5.4	6.9
26%	210.8	302.7	455.0	2.3	2.9	3.7
5%	234.1	297.2	388.8	3.5	4.4	5.6
B-doped mc-Si						
84%	224.5	295.5	402.7	3.1	3.9	4.9
36%	242.8	313.2	417.1	3.3	4.2	5.3
11%	252.5	316.2	407.4	3.7	4.7	6.0
Standard mc-Si						
?	206.7	275.6	381.0	2.9	3.7	4.7
Standard Cz-Si						
?	258.3	326.4	424.8	3.5	4.5	5.8

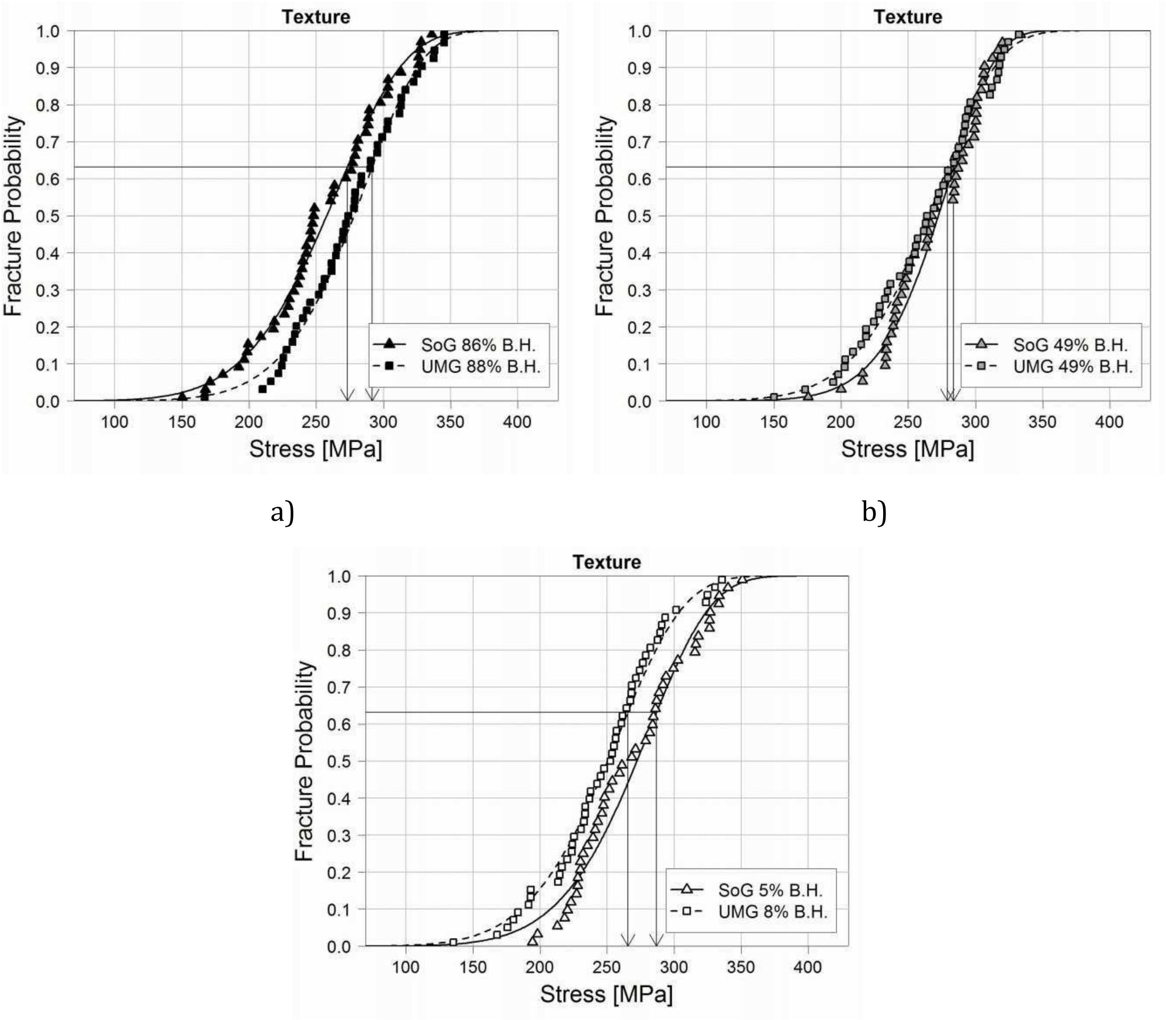

a)

b)

c)

Figure 180 Weibull graphs plotting fracture probability against applied equibiaxial stress after texture.

Table 28 Characteristic stress, σ_θ [MPa], and Weibull modulus, m [-], for textured wafers.

B. H.	$\sigma_{\theta_{lower}}$	σ_θ	$\sigma_{\theta_{upper}}$	m_{lower}	m	m_{upper}
UMG mc-Si						
88%	253.4	291.6	341.6	6.3	7.7	9.3
49%	240.0	279.1	330.8	5.9	7.1	8.6
8%	223.6	265.4	322.0	5.2	6.3	7.6
SoG mc-Si						
86%	230.0	273.1	331.4	5.2	6.3	7.6
49%	251.7	283.6	324.4	7.5	9.0	10.9
5%	230.1	273.2	331.4	5.7	7.0	8.5

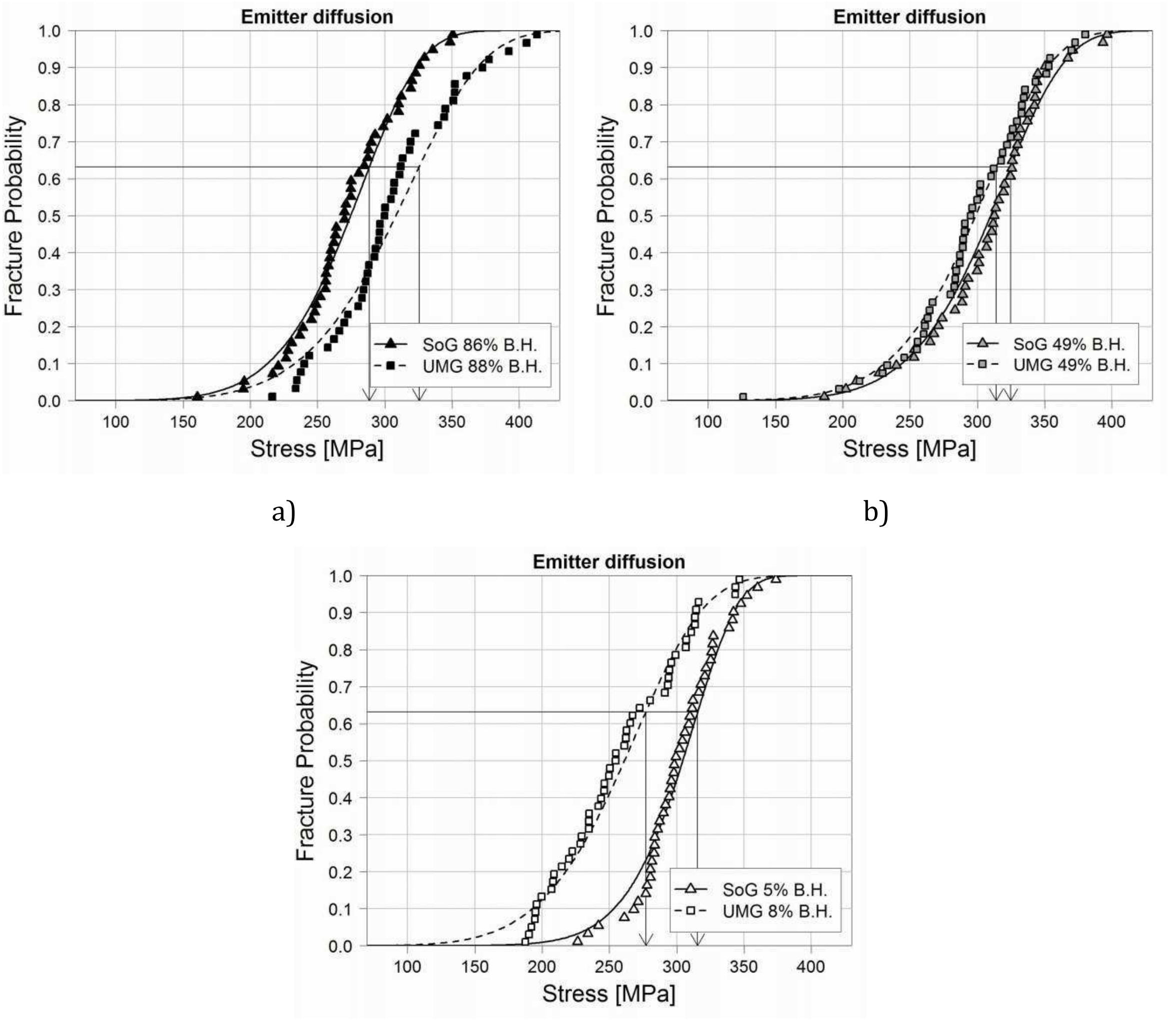

a)

b)

c)

Figure 181 Weibull graphs plotting fracture probability against applied equibiaxial stress after emitter diffusion.

Table 29 Characteristic stress, σ_θ [MPa], and Weibull modulus, m [-], for wafers after emitter diffusion.

B. H.	$\sigma_{\theta_{lower}}$	σ_θ	$\sigma_{\theta_{upper}}$	m_{lower}	m	m_{upper}
UMG mc-Si						
88%	277.3	325.5	389.9	5.5	6.7	8.2
49%	271.0	314.0	370.4	6.0	7.3	8.9
8%	340.8	359.2	378.7	5.1	6.2	7.5
SoG mc-Si						
86%	249.3	288.5	340.1	6.1	7.4	8.9
49%	283.0	324.7	379.1	6.5	7.8	9.5
5%	284.0	315.5	355.2	8.4	10.2	12.4

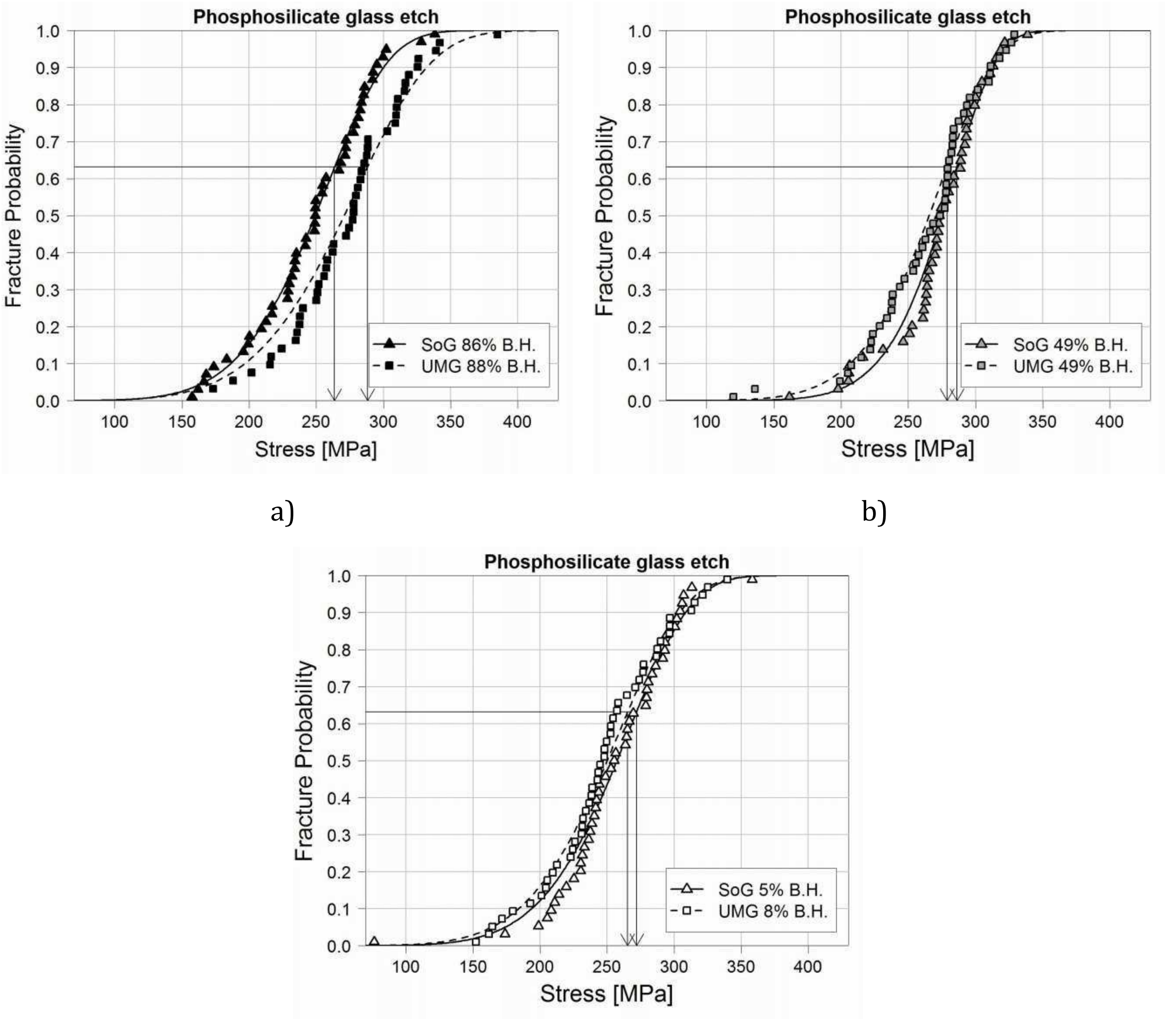

a) b)

c)

Figure 182 Weibull graphs plotting fracture probability against applied equibiaxial stress after phosphosilicate glass etching.

Table 30 Characteristic stress, σ_θ [MPa], and Weibull modulus, m [-], after phosphosilicate glass etching.

B. H.	$\sigma_{\theta_{lower}}$	σ_θ	$\sigma_{\theta_{upper}}$	m_{lower}	m	m_{upper}
UMG mc-Si						
88%	240.0	288.1	354.0	4.9	5.9	7.2
49%	241.5	278.7	327.6	6.2	7.5	9.1
8%	222.7	265.3	323.2	5.1	6.1	7.4
SoG mc-Si						
86%	223.2	263.6	318.0	5.4	6.5	7.8
49%	255.4	286.2	325.2	7.8	9.5	11.5
5%	231.2	271.9	326.5	5.5	6.6	8.0

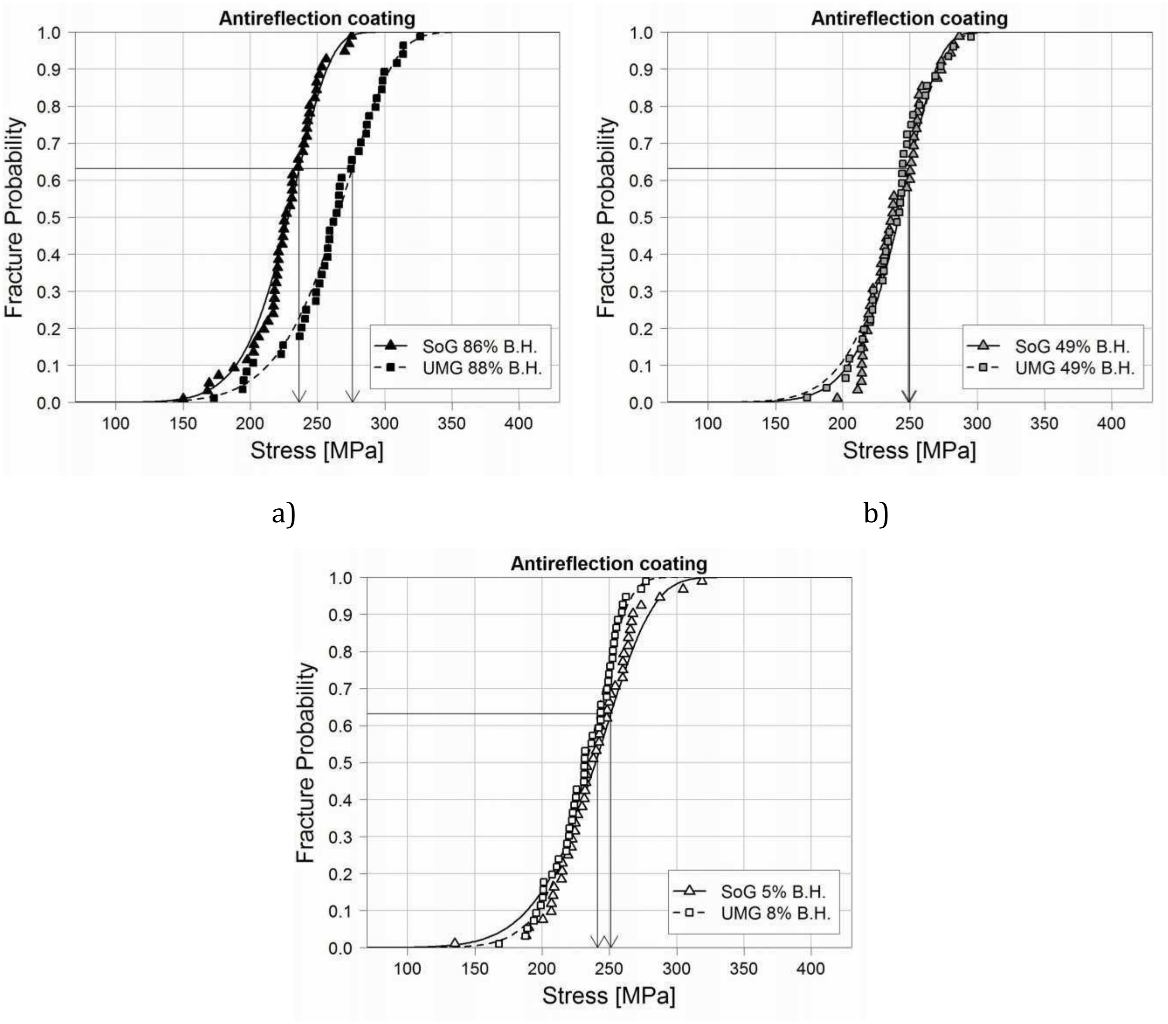

a) b)

c)

Figure 183 Weibull graphs plotting fracture probability against applied equibiaxial stress after antireflection coating.

Table 31 Characteristic stress, σ_θ [MPa], and Weibull modulus, m [-], after antireflection coating.

B. H.	$\boldsymbol{\sigma_{\theta_{lower}}}$	$\boldsymbol{\sigma_\theta}$	$\boldsymbol{\sigma_{\theta_{upper}}}$	$\boldsymbol{m_{lower}}$	$\boldsymbol{m}$	$\boldsymbol{m_{upper}}$
UMG mc-Si						
88%	243.9	275.9	317.2	7.1	8.7	10.6
49%	223.0	248.7	281.2	7.9	9.8	12.1
8%	218.6	241.3	269.6	9.0	10.9	13.2
SoG mc-Si						
86%	212.5	236.4	266.6	8.3	10.1	12.2
49%	226.6	249.6	278.4	9.1	11.1	13.5
5%	218.9	251.0	292.7	6.5	7.9	9.6

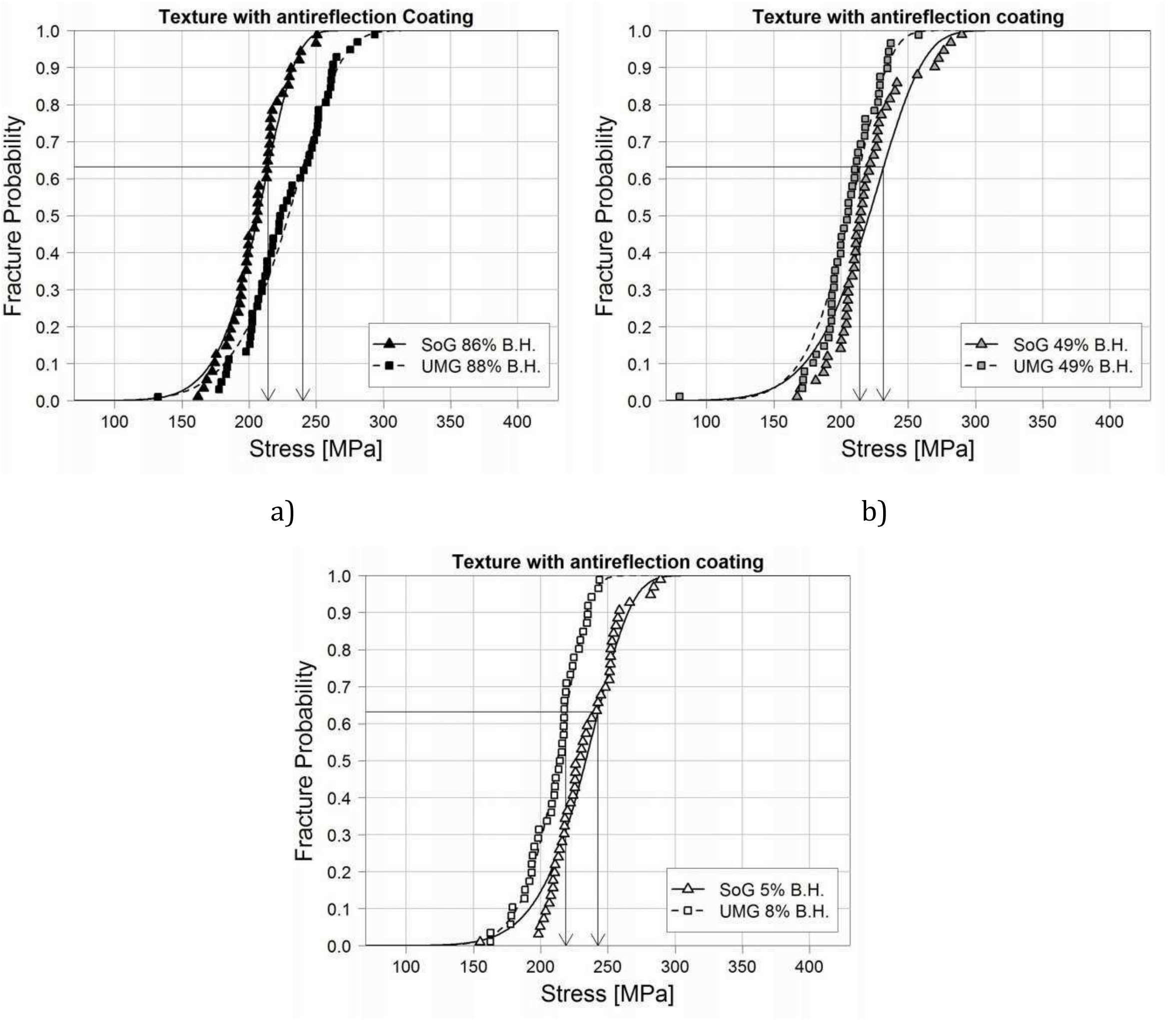

a) b)

c)

Figure 184 Weibull graphs after antireflection coating (skipping emitter diffusion).

Table 32 Characteristic stress, σ_θ [MPa], and Weibull modulus, m [-], after antireflection coating (skipping emitter diffusion).

B. H.	$\sigma_{\theta_{lower}}$	σ_θ	$\sigma_{\theta_{upper}}$	m_{lower}	m	m_{upper}
UMG mc-Si						
88%	209.9	239.9	278.8	6.7	8.1	9.7
49%	190.9	213.9	243.3	7.7	9.4	11.5
8%	200.4	218.7	241.4	10.0	12.3	15.0
SoG mc-Si						
86%	192.6	214.2	241.6	8.3	10.1	12.3
49%	201.1	231.6	271.4	6.3	7.6	9.3
5%	216.7	242.6	275.6	7.9	9.5	11.5

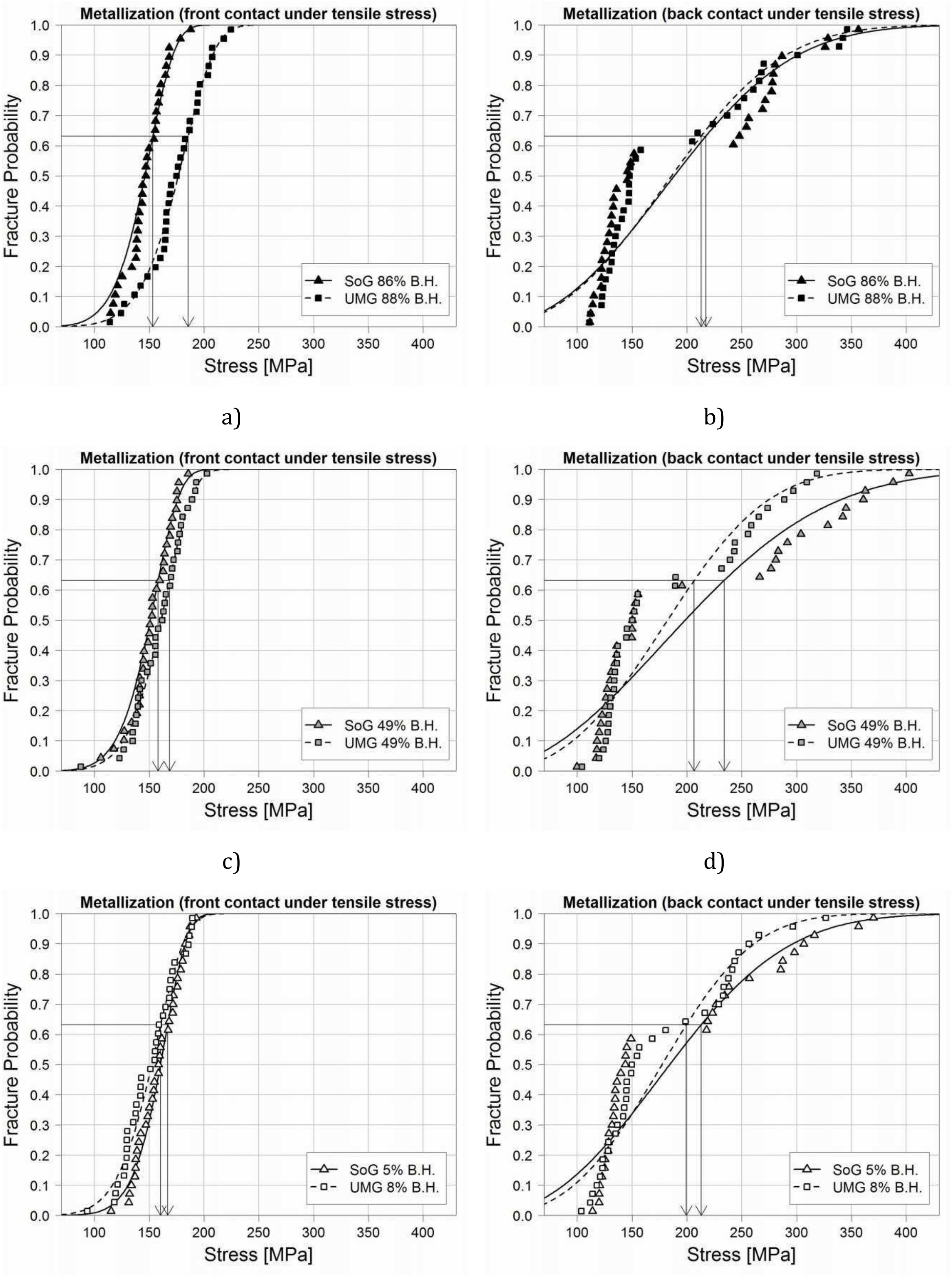

a) b)

c) d)

e) f)

Figure 185 Weibull graphs plotting fracture probability against applied equibiaxial stress after metallization.

Table 33 Characteristic stress, σ_θ [*MPa*], *and Weibull modulus, m* [-], *for wafers after metallization (front contact under tensile stress).*

B. H.	$\sigma_{\theta_{lower}}$	σ_θ	$\sigma_{\theta_{upper}}$	m_{lower}	m	m_{upper}
UMG mc-Si						
88%	160.5	185.5	218.2	5.8	7.4	9.3
49%	147.0	168.6	196.7	6.2	7.8	9.7
8%	137.8	160.4	190.3	5.6	7.0	8.8
SoG mc-Si						
86%	132.9	153.3	180.0	5.9	7.5	9.4
49%	138.0	158.1	184.3	6.2	7.8	9.8
5%	148.5	166.8	190.1	7.3	9.1	11.5

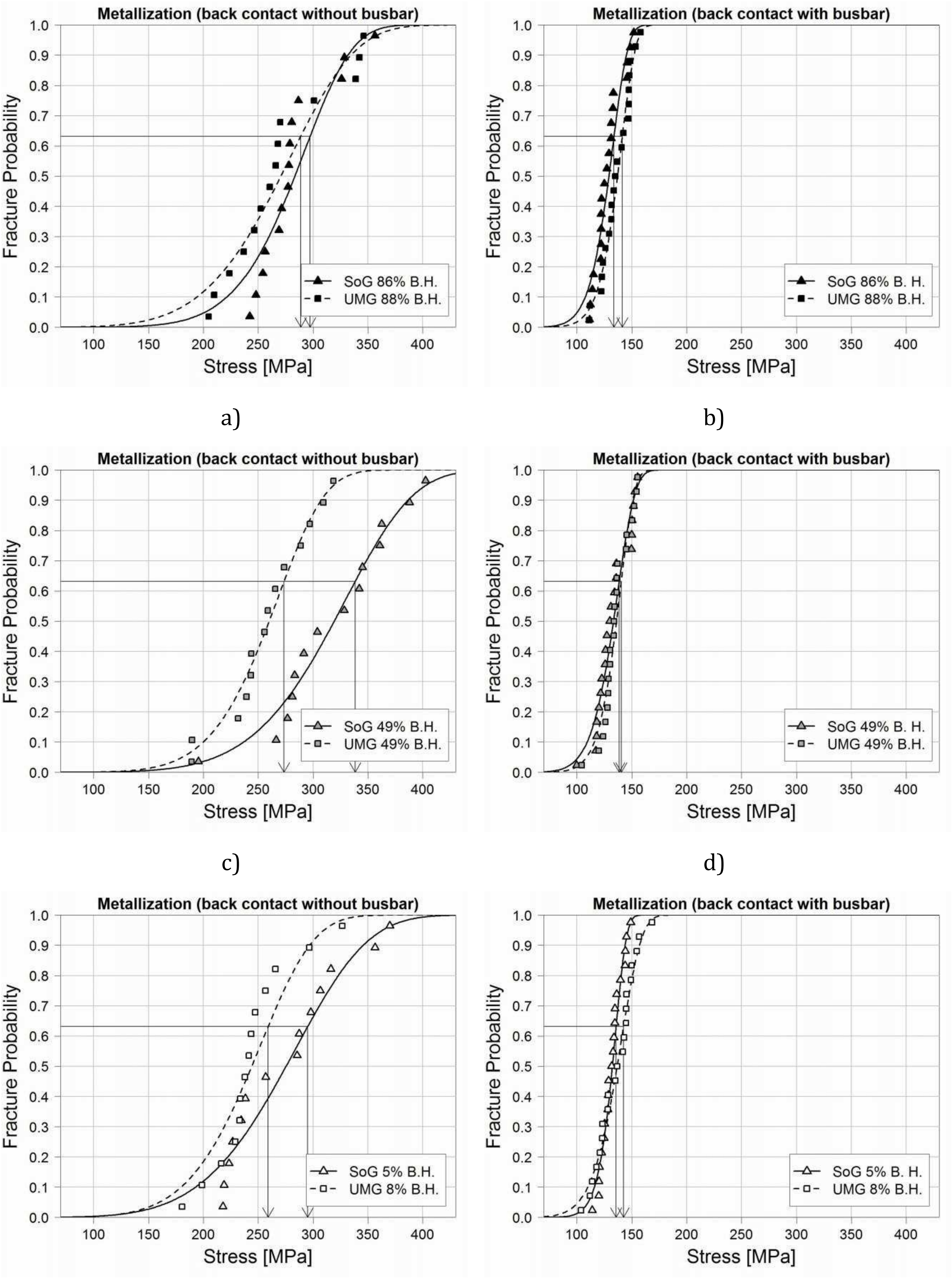

a) b)

c) d)

e) f)

Figure 186 Weibull graphs plotting fracture probability against applied equibiaxial stress after metallization (back contact under tensile stress).

Table 34 Characteristic stress, σ_θ [MPa], and Weibull modulus, m [-], for wafers after metallization (areas from the back contact under tensile stress without bus bars).

B. H.	$\sigma_{\theta_{lower}}$	σ_θ	$\sigma_{\theta_{upper}}$	m_{lower}	m	m_{upper}
UMG mc-Si						
88%	242.0	288.7	352.1	3.9	5.7	8.2
49%	238.0	273.5	320.0	5.0	7.2	10.4
8%	220.2	259.1	311.1	4.3	6.1	8.9
SoG mc-Si						
86%	260.8	297.3	344.5	5.3	7.6	11.1
49%	288.7	338.4	404.7	4.4	6.3	9.1
5%	244.3	295.1	365.1	3.7	5.3	7.7

Table 35 Characteristic stress, σ_θ [MPa], and Weibull modulus, m [-], for wafers after metallization (bus bars from the back contact under tensile stress).

B. H.	$\sigma_{\theta_{lower}}$	σ_θ	$\sigma_{\theta_{upper}}$	m_{lower}	m	m_{upper}
UMG mc-Si						
88%	129.2	141.3	156.4	8.6	11.5	15.5
49%	128.4	140.4	155.2	8.7	11.6	15.7
8%	126.4	142.5	163.1	6.4	8.6	11.6
SoG mc-Si						
86%	121.0	133.7	149.7	7.6	10.3	14.0
49%	124.2	138.5	156.7	7.1	9.5	12.7
5%	126.1	135.7	147.3	10.6	14.2	19.1

Appendix G: Fracture Toughness Measurements for Wire Introduced Single Notch

Table 36 Sample dimensions, notch lengths, measured fracture forces and calculated fracture toughness values for 4N+Al mc-Si.

B. H.	**Thickness [mm]**	**Notch length [mm]**	**Width [mm]**	**Force [N]**	K_{Ic} [MPa $\sqrt{\text{m}}$]	**Average** K_{Ic} **and MSE** [MPa $\sqrt{\text{m}}$]
98%	1.83	0.686	9.82	49.22	1.30	1.34±0.19
	1.89	0.444	9.79	45.38	1.49	
	1.87	0.789	9.86	45.31	1.17	
	1,87	0.917	9.77	74.34	1.71	
	1.80	0.666	9.82	51.89	1.53	
	1.84	0.754	9.86	45.05	1.18	
	1.90	0.722	9.82	42.29	1.21	
	1.89	0.805	9.82	50.76	1.32	
	1.83	0.686	9.86	45.24	1.19	
78%	1.79	0.681	9.76	31.79	0.82	1.27±0.32
	1.74	0.765	9.73	32.41	1.04	
	1.87	0.701	9.60	40.98	0.99	
	1.81	0.620	9.80	61.09	1.40	
	1.77	0.659	9.84	34.63	0.88	
	1.82	0.809	9.89	50.79	1.51	
	1.79	0.770	9.91	41.73	1.22	
	1.83	0.810	9.74	58.69	1.75	
	1.77	0.579	9.71	58.49	1.35	
	1.77	0.711	9.74	62.02	1.73	
58%	1.83	0.686	9.70	70.41	1.75	1.61±0.20
	1.89	0.444	9.88	97.64	1.58	
	1.87	0.789	9.86	50.19	1.34	
	1.87	0.917	9.76	44.57	1.48	
	1.80	0.666	9.97	82.64	2.02	
	1.84	0.754	9.98	53.33	1.39	
	1.90	0.722	9.84	72.95	1.70	
	1.89	0.805	9.93	61.61	1.62	

38%	1.93	0.756	9.87	65.15	1.52	1.43±0.15
	1.91	0.594	9.82	80.03	1.56	
	1.86	0.703	9.77	64.07	1.55	
	1.86	0.739	9.81	55.46	1.40	
	1.92	0.812	9.90	41.21	1.06	
	1.90	0.736	9.89	63.21	1.51	
	1.78	0.824	9.95	46.63	1.51	
	1.75	0.881	9.84	38.88	1.46	
	1.79	0.749	9.91	47.07	1.33	
18%	189	0.426	985	85.28	1.34	1.38±0.21
	1.86	0.280	9.77	135.98	1.78	
	1.90	0.218	1.00	105.44	1.14	
	1.92	0.505	9.91	80.96	1.36	
	1.56	0.443	9.52	50.69	1.29	

Table 37 Sample dimensions, notch lengths, measured fracture forces and calculated fracture toughness values for 3N mc-Si.

B. H.	**Thickness [mm]**	**Notch length [mm]**	**Width [mm]**	**Force [N]**	K_{Ic} **[MPa $\sqrt{\mathrm{m}}$]**	**Average K_{Ic} and MSE [MPa $\sqrt{\mathrm{m}}$]**
79%	1.80	0.789	8.66	96.93	1.58	1.33±0.18
	1.92	0.910	4.33	30.3	0.99	
	1.81	0.100	5.77	36.07	1.26	
	1.87	0.697	9.42	123.36	1.45	
	1.79	0.525	8.10	113.71	1.36	
	1.72	0.980	7.30	68.23	2.17	
	1.78-	0.580	9.49	121.2	1.35	
	1.9	0.520	6.20	115.18	1.55	
65%	1.81	0.465	9.53	84.48	1.60	1.57±0.17
	1.83	0.502	9.44	91.94	1.81	
	1.83	0.501	9.41	70.94	1.39	
	1.90	0.487	9.56	95.95	1.67	
	1.84	0.939	6.51	25.06	1.36	
54%	1.75	0.385	9.39	77.15	1.41	1.55±0.14
	1.88	0.306	9.56	123.28	1.68	
40%	1.90	0.577	9.63	68.12	1.33	1.29±0.05
	1.88	0.370	9.62	82.22	1.24	
25%	1.91	0.523	6.17	46.23	1.30	1.25±0.05
	1.95	0.213	9.56	113.11	1.20	
11%	1.84	0.265	9.52	112.84	1.52	1.46±0.07
	1.78	0.957	9.50	155.69	1.39	

Table 38 Sample dimensions, notch lengths, measured fracture forces and calculated fracture toughness values for B-doped mc-Si.

B. H.	**Thickness [mm]**	**Notch length [mm]**	**Width [mm]**	**Force [N]**	K_{Ic} [MPa $\sqrt{\text{m}}$]	**Average** K_{Ic} **and MSE** [MPa $\sqrt{\text{m}}$]
89%	1.93	0.620	9.64	77.22	1.54	1.38±0.26
	1.92	0.386	9.50	59.77	0.89	
	1.93	0.370	9.60	55.93	0.80	
	1.91	0.416	9.51	83.83	1.32	
	1.83	0.491	9.47	78.66	1.51	
	1.83	0.850	1.31	42.5	1.00	
	1.85	0.790	1.31	56.14	1.17	
	1.79	0.756	1.29	75.6	1.65	
	1.84	0.745	9.64	62.37	1.66	
	1.78	0.730	9.60	49.44	1.42	
73%	1.82	0.779	9.40	65.6	1.95	1.77±0.22
	1.86	0.100	1.30	52.53	1.53	
	1.80	0.883	1.33	68.51	1.76	
	1.84	0.630	9.55	66.78	1.53	
	1.63	0.530	6.30	80.6	3.22	
	1.79	0.757	9.35	68.04	2.06	
58%	1.88	0.789	9.49	62.43	1.71	1.79±0.27
	1.81	0.634	9.45	73.92	1.79	
	1.86	0.614	1.33	125.14	1.97	
	1.91	0.564	9.53	78.89	1.51	
	1.87	0.840	6.44	50.55	2.25	
	1.91	0.608	9.56	68.13	1.38	
	1.86	0.639	9.50	86.61	1.95	
42%	1.91	0.457	9.56	85.88	1.42	1.63±0.21
	1.90	0.101	9.51	34.93	1.32	
	1.93	0.510	9.59	51.56	0.89	
	1.93	0.772	9.64	49.67	1.22	
	1.90	0.406	9.59	93.99	1.46	
	1.86	0.687	9.57	56.63	1.37	

	1.88	0.510	9.54	86.61	1.60	
	1.82	0.600	9.56	88.35	1.99	
	1.86	0.657	9.54	65.15	1.51	
	1.84	0.672	9.48	74.31	1.82	
	1.84	0.520	1.32	104.39	1.48	
26%	1.88	0.630	9.57	80.25	1.74	1.82±0.15
	1.89	0.620	9.54	87.41	1.85	
	1.88	0.820	9.51	67.84	1.94	
	1.85	0.777	9.55	58.24	1.63	
	1.90	0.680	6.51	50.07	1.67	
	1.85	0.740	9.57	78.05	2.06	
11%	1.87	0.670	9.51	79.72	1.86	1.71±0.11
	1.95	0.700	9.50	74.92	1.65	
	1.89	0.101	9.60	49.6	1.88	
	1.97	0.590	9.60	88.59	1.63	
	1.83	0.100	9.70	39.52	1.64	
	1.91	0.630	9.68	78.19	1.61	

Table 39 Sample dimensions, notch lengths, measured fracture forces and calculated fracture toughness values for UMG mc-Si.

B. H.	Thickness [mm]	Notch length [mm]	Width [mm]	Force [N]	K_{Ic} [MPa $\sqrt{m}$]	Average K_{Ic} and MSE [MPa $\sqrt{m}$]
86%	1.99	0.446	9.96	58.63	0.84	0.86±0.12
	1.95	0.466	9.52	59.46	0.95	
	1.98	0.512	9.95	39.79	0.63	
	1.87	0.485	9.50	47.33	0.86	
	1.95	0.447	9.60	56.5	0.88	
	1.96	0.311	9.48	66.17	0.84	
	1.97	0.393	9.42	72.61	1.05	
70%	1.90	0.486	9.71	51.95	0.89	0.87±0.11
	1.84	0.328	9.49	65.72	0.99	
	1.97	0.356	9.64	54.23	0.73	
54%	1.89	0.496	9.91	51.49	0.89	0.85±0.06
	1.84	0.477	9.74	43.59	0.80	
	1.90	0.379	9.89	53.62	0.77	
	1.94	0.656	9.93	46.18	0.93	
38%	1.82	0.830	9.87	16.88	0.52	0.78±0.17
	1.83	0.646	9.76	37.03	0.86	
	1.89	0.399	9.90	43.41	0.65	
	1.88	0.665	9.91	44.69	0.98	
	1.91	0.503	1.26	66.56	0.89	
23%	1.82	0.391	9.87	69.94	1.13	1.37±0.33
	1.96	0.413	9.95	88.11	1.25	
	1.84	0.559	9.81	85.39	1.73	
	1.84	0.344	9.88	100.64	1.49	
	1.82	0.554	9.84	87.6	1.80	
	1.81	0.598	1.28	50.77	0.87	
6%	1.67	0.350	9.87	49.36	0.90	1.05±0.17
	1.71	0.344	9.91	56.02	0.96	
	1.76	0.181	9.91	109.34	1.28	

Table 40 Sample dimensions, notch lengths, measured fracture forces and calculated fracture toughness values for SoG mc-Si.

B. H.	**Thickness [mm]**	**Notch length [mm]**	**Width [mm]**	**Force [N]**	K_{Ic} $[\mathrm{MPa}\sqrt{\mathrm{m}}]$	**Average** K_{Ic} **and MSE** $[\mathrm{MPa}\sqrt{\mathrm{m}}]$
93%	1.97	0.631	9.60	60.79	1.18	1.49±0.36
	1.92	0.611	9.58	64.53	1.29	
	1.88	0.728	9.55	83.89	2.09	
	1.90	0.753	9.61	55.98	1.39	
75%	1.84	0.884	9.59	73.49	2.47	1.83±0.44
	1.87	0.439	9.58	98.95	1.68	
	1.88	0.413	9.62	128.34	2.06	
	1.89	0.414	9.61	72.33	1.14	
	1.95	0.866	9.52	64.24	1.79	
58%	1.83	0.397	9.57	107.64	1.79	1.65±0.38
	1.80	0.373	9.44	132.13	2.22	
	1.87	0.480	9.55	108.34	1.94	
	1.81	0.719	9.50	53.39	1.45	
	1.84	0.716	9.53	79.79	2.06	
	1.82	0.709	9.52	47.42	1.25	
	1.88	0.670	9.60	50.89	1.17	
	1.81	0.910	9.50	34.85	1.31	
41%	1.81	0.290	9.46	86.52	1.26	1.58±0.39
	1.82	0.762	9.40	62.18	1.80	
	1.86	0.547	9.70	75.07	1.48	
	1.91	0.560	9.54	107.79	2.05	
	1.80	0.447	9.54	50.49	0.95	
	1.84	0.680	9.43	77.43	1.93	
25%	1.81	0.750	9.51	60.42	1.72	1.44±0.14
	1.83	0.740	9.56	52.77	1.44	
	1.81	0.378	9.52	89.41	1.49	
	1.80	0.907	9.57	38.6	1.45	
	1.81	0.347	9.53	88.88	1.42	
	1.83	0.380	9.45	74.32	1.22	

	1.83	0.400	9.54	77.77	1.31	
7%	1.81	0.523	9.57	48.48	0.99	1.41±0.26
	1.80	0.577	9.58	81.83	1.82	
	1.82	0.599	9.55	65.9	1.49	
	1.87	0.609	9.51	57.09	1.22	
	1.84	0.340	9.53	96.9	1.47	
	1.90	0.694	9.51	63.28	1.46	

Appendix H: Fracture Toughness Measurements for Laser Introduced Single Notch

Table 41 Sample dimensions, notch lengths, measured fracture forces and calculated fracture toughness values for 4N+Al mc-Si.

B. H.	Thickness [mm]	Notch length [mm]	Width [mm]	Force [N]	K_{Ic} [MPa $\sqrt{\text{m}}$]	Average K_{Ic} and MSE [MPa $\sqrt{\text{m}}$]
98%	1.74	0.262	2.47	21.8	1.25	1.10±0.13
	1.75	0.204	2.63	25.93	1.23	
	1.75	0.202	2.66	19.99	0.93	
	1.76	0.205	2.70	21.87	1	
58%	1.78	0.258	2.65	25,12	1.27	1.33±0.07
	1.77	0.209	3.33	34,71	1.28	
	1.76	0.276	2.68	27,13	1.44	

Table 42 Sample dimensions, notch lengths, measured fracture forces and calculated fracture toughness values for 3N mc-Si.

B. H.	Thickness [mm]	Notch length [mm]	Width [mm]	Force [N]	K_{Ic} [MPa $\sqrt{\text{m}}$]	Average K_{Ic} and MSE [MPa $\sqrt{\text{m}}$]
54%	1.81	0.264	2.62	27.14	1.36	1.41±0.13
	1.78	0.226	2.74	27.24	1.25	
	1.78	0.326	3.01	31.95	1.61	
11%	1.81	0.210	2.63	28.39	1.27	1.45±0.14
	1.82	0.267	2.69	30.15	1.46	
	1.80	0.344	2.65	27.93	1.61	

Table 43 Sample dimensions, notch lengths, measured fracture forces and calculated fracture toughness values for B-doped silicon.

B. H.	**Thickness [mm]**	**Notch length [mm]**	**Width [mm]**	**Force [N]**	K_{Ic} $[\mathrm{MPa}\sqrt{\mathrm{m}}]$	**Average** K_{Ic} **and MSE** $[\mathrm{MPa}\sqrt{\mathrm{m}}]$
89%	1.79	0.201	2.22	25.06	1.33	1.33±0.18
	1.81	0.324	2.44	24.91	1.49	
	1.79	0.173	2.89	26.12	1.00	
	1.81	0.290	2.63	25.23	1.32	
	1.80	0.319	2.41	25.09	1.52	
42%	1.82	0.281	2.36	28.66	1.62	1.53±0.06
	1.82	0.305	2.68	28.24	1.47	
	1.83	0.233	2.61	32.58	1.51	

Appendix I: Dynamic Elastic Modulus Measurements

Table 44 Sample density, mechanical resonance frequency and calculated dynamic elastic modulus for 4N+Al mc-Si.

B. H.	**Density [g/cm^3]**	**Frequency [kHz]**	**Elastic Modulus [GPa]**	**Average Elastic Modulus and MSE [GPa]**
98%	2.1956	2.8	149.92	149.28±9.34
	2.2326	2.63	144.92	
	2.284	2.71	155.66	
	2.305	2.69	161.59	
	2.2307	2.56	134.3	
78%	2.2542	2.47	133.24	126.28±5.84
	2.3095	2.47	125.42	
	2.3271	2.53	132.45	
	2.2781	2.35	122.07	
	2.231	2.39	118.2	
58%	2.3427	2.83	168.33	169.56±2.60
	2.3095	2.86	168.15	
	2.3271	2.86	169.25	
	2.327	2.89	174.64	
	2.2626	2.9	167.45	
38%	2.3248	2.89	175.4	170.83±3.79
	2.3329	2.89	172.89	
	2.3073	2.886	166.5	
	2.3106	2.88	166.13	
	2.2464	2.88	173.22	
18%	2.2778	2.47	157.16	168.33±10.53
	2.2504	2.89	158	
	2.3084	2.86	167.37	
	2.3148	2.94	173.62	
	2.3195	2.97	185.49	

Table 45 Sample density, mechanical resonance frequency and calculated dynamic elastic modulus for 3N mc-Si.

B. H.	**Density [g/cm^3]**	**Frequency [kHz]**	**Elastic Modulus [GPa]**	**Average Elastic Modulus and MSE [GPa]**
79%	2.2389	6.4	175.76	165.85±7.21
	2.2389	6.02	155.51	
	2.3251	5.93	164.96	
	2.279	5.8	167.18	
65%	2.3183	6.01	169.08	171.71±4.50
	2.2872	5.9	167.04	
	2.2907	6	178.93	
	2.286	6.03	171.78	
54%	2.3074	6.15	177.26	172.66±3.10
	2.2976	5.84	171.66	
	2.3325	6	168.66	
	2.273	6.04	173.07	
40%	2.3077	6.2	184.18	174.64±7.32
	2.2908	5.95	177.25	
	2.3336	5.89	163.94	
	2.2863	6.05	173.2	
25%	2.2988	6.06	174.06	172.16±4.60
	2.3215	6.2	178.82	
	2.3296	6	167.81	
	2.2887	5.83	167.93	
11%	2.2095	5.92	161.25	173.49±8.81
	2.3504	5.8	169.01	
	2.3292	6.07	182.3	
	2.2523	6.55	181.41	

Table 46 Sample density, mechanical resonance frequency and calculated dynamic elastic modulus for B-doped mc-Si.

B. H.	**Density [g/cm^3]**	**Frequency [kHz]**	**Elastic Modulus [GPa]**	**Average Elastic Modulus and MSE [GPa]**
89%	2.3089	2.97	187.02	180.91±4.25
	2.3431	2.78	183.63	
	2.3431	2.72	175.79	
	2.3337	2.81	181.57	
	2.3237	2.74	176.54	
73%	2.3278	2.81	176.74	173.06±3.85
	2.3322	2.74	169.58	
	2.3214	2.76	170.21	
	2.325	2.77	170.09	
	2.3132	2.75	178.69	
58%	2.3177	2.7	160.68	166.30±5.26
	2.3083	2.78	171.67	
	2.3205	2.81	173.59	
	2.3205	2.72	162.64	
	2.2731	2.78	162.91	
42%	2.2936	2.79	169.75	172.27±5.20
	2.3098	2.77	169.15	
	2.2983	2.78	166.01	
	2.3288	2.8	176.1	
	2.3348	2.83	180.36	
26%	2.3124	2.89	181.93	168.91±15.39
	2.2976	2.8	168.18	
	2.3099	2.88	182.11	
	2.2078	2.71	140.12	
	2.3086	2.82	172.21	

11%	2.2191	2.91	163.06	171.12±6.09
	2.359	2.9	177.47	
	2.3303	2.9	178.94	
	2.2998	2.79	167.57	
	2.3081	2.82	168.55	

Table 47 Sample density, mechanical resonance frequency and calculated dynamic elastic modulus for UMG mc-Si.

B. H.	Density $[\mathrm{g/cm^3}]$	Frequency [kHz]	Elastic Modulus [GPa]	Average Elastic Modulus and MSE [GPa]
86%	2,3295	3,764	171,49	174.71±4.01
	2,3078	3,84	180,45	
	2,2954	3,84	177,77	
	2,3024	3,62	169,45	
	2,3182	3,78	174,37	
70%	2,3325	3,75	178,04	175.71±2.09
	2,2933	3,78	173,02	
	2,326	3,68	177,42	
	2,3135	3,67	174,36	
54%	2,305	3,82	179,41	179.15±3.79
	2,2763	3,86	186,09	
	2,3222	3,66	174,71	
	2,3065	3,79	178,06	
	2,3026	3,8	177,46	
38%	2,3138	3,74	182	186.23±5.77
	2,3848	3,82	195,7	
	2,313	3,87	183,42	
	2,337	3,79	189,93	
	2,3216	3,82	180,1	
23%	2,3013	3,66	169,03	171.45±4.60
	2,2988	3,67	169,37	
	2,3066	3,62	168,76	
	2,3159	3,76	180,63	
	2,3082	3,67	169,45	
6%	2,3341	3,56	178,15	177.64±4.07
	2,3177	3,56	177,33	
	2,3228	3,59	179,01	
	2,3154	3,57	183,15	
	2,3008	3,67	170,54	

Table 48 Sample density, mechanical resonance frequency and calculated dynamic elastic modulus for SoG mc-Si.

B. H.	**Density [g/cm^3]**	**Frequency [kHz]**	**Elastic Modulus [GPa]**	**Average Elastic Modulus and MSE [GPa]**
93%	2,3042	3,823	168,01	174.15±4.10
	2,3105	3,86	173,52	
	2,3264	3,91	179,28	
	2,3296	3,826	175,8	
75%	2,2485	3,89	163,68	165.65±1.50
	2,2835	3,84	165,69	
	2,2355	3,9	165,34	
	2,308	3,83	167,9	
58%	2,2874	3,86	173,41	171.84±7.56
	2,3061	3,81	180,86	
	2,2875	3,75	173,19	
	2,1764	3,74	159,88	
41%	2,2474	3,67	155,98	163.27±8.00
	2,2198	3,78	158,51	
	2,3165	3,73	176,63	
	2,2866	3,656	161,96	
25%	2,2824	3,66	166,32	163.46±5.56
	2,2598	3,74	163,5	
	2,2377	3,67	154,55	
	2,2884	3,73	169,46	
7%	2,2643	3,55	159,68	164.75±9.48
	2,2342	3,62	151,83	
	2,364	3,625	172,2	
	2,4415	3,48	175,3	

Appendix J: Static Elastic Modulus

Table 49 Static elastic modulus measured with the RoR bending test and thickness of sawn wafers.

B. H.	**E and MSE [GPa]**	**Thickness and MSE [µm]**	***B. H.***	**E and MSE [GPa]**	**Thickness and MSE [µm]**
4N+Al mc-Si			***3N mc-Si***		
77%	135.2±12.6	278±7	77%	135.5±11.8	283±5
63%	137.2±16.8	272±14	47%	139.0±6.7	281±5
33%	143.9±7.2	281±4	26%	137.9±9.7	282±5
			5%	140.0±7.0	281±5
B-doped mc-Si			***UMG mc-Si***		
86%	146.3±8.1	280±6	88%	160.0±6.2	222±6
36%	147.6±6.4	283±5	49%	154.3±10.7	221±7
11%	149.0±7.0	279±5	8%	154.3±4.7	223±5
SoG mc-Si			***Standard mc-Si***		
86%	156.2±5.2	230±4	?	153.4±17.4	263±6
49%	156.3±6.6	227±3	***Standard Cz-Si***		
5%	158.6±5.4	228±3	?	140.9±3.1	265±5

Table 50 Static elastic modulus measured with the RoR bending test and thickness of damage etched wafers.

B. H.	**E and MSE [GPa]**	**Thickness and MSE [μm]**	***B. H.***	**E and MSE [GPa]**	**Thickness and MSE [μm]**
4N+Al mc-Si			***3N mc-Si***		
77%	120.5±11.8	252±6	77%	140.6±5.0	258±7
63%	129.8±13.1	261±14	47%	138.1±6.6	259±7
33%	142.8±10.9	267±6	26%	139.7±14.0	256±9
			5%	140.1±4.6	256±8
B-doped mc-Si			***UMG mc-Si***		
86%	144.3±7.7	265±7	88%	145.1±8.3	200±9
36%	144.8±5.1	258±5	49%	146.8±11.6	201±7
11%	143.1±5.1	261±8	8%	144.5±6.2	201±7
SoG mc-Si			***Standard mc-Si***		
86%	149.7±7.4	206±5	?	150.6±4.7	243±7
49%	152.6±8.7	203±4	***Standard Cz-Si***		
5%	146.2±6.9	209±4	?	140.4±7.1	234±9

Table 51 Static elastic modulus measured with the RoR bending test and thickness of annealed wafers.

B. H.	E and MSE [GPa]	Thickness and MSE [μm]	*B. H.*	E and MSE [GPa]	Thickness and MSE [μm]
4N+Al mc-Si			***3N mc-Si***		
77%	110.3±7.7	277±9	77%	129.6±9.6	279±10
63%	123.4±8.1	276±7	47%	129.5±10.1	279±11
33%	138.8±6.6	280±7	26%	134.8±10.6	280±11
			5%	137.0±8.2	271±8
B-doped mc-Si			***Standard mc-Si***		
86%	137.2±10.0	276±9	?	139.1±8.3	261±10
36%	133.1±9.1	277±8	***Standard Cz-Si***		
11%	133.5±7.5	277±6	?	110.7±11.1	245±10

Table 52 Static elastic modulus measured with the RoR bending test and thickness of wafer equivalents.

B. H.	E and MSE [GPa]	Thickness and MSE [μm]	*B. H.*	E and MSE [GPa]	Thickness and MSE [μm]
4N+Al mc-Si			***3N mc-Si***		
77%	-	-	77%	129.8±6.6	300±11
63%	-	-	47%	130.7±11.4	295±12
33%	131.9±6.1	298±9	26%	125.3±14.6	304±10
			5%	129.4±7.4	297±11
B-doped mc-Si			***Standard mc-Si***		
86%	128.3±4.5	307±9	?	126.4±8.3	290±13
36%	128.2±7.5	301±11	***Standard Cz-Si***		
11%	126.8±9.0	300±13	?	100.4±0.7	293±12

Table 53 Static elastic modulus measured with the RoR bending test and thickness of textured wafers.

B. H.	E and MSE [GPa]	Thickness and MSE [µm]	*B. H.*	E and MSE [GPa]	Thickness and MSE [µm]
UMG mc-Si			***SoG mc-Si***		
88%	163.7±5.5	215±7	86%	153.3±6.2	223±3
49%	161.6±6.9	215±7	49%	152.4±8.4	225±5
8%	160.3±5.4	217±6	5%	149.7±6.1	224±4

Table 54 Static elastic modulus measured with the RoR bending test and thickness after emitter diffusion.

B. H.	E and MSE [GPa]	Thickness and MSE [µm]	*B. H.*	E and MSE [GPa]	Thickness and MSE [µm]
UMG mc-Si			***SoG mc-Si***		
88%	153.4±10.2	216±7	86%	152.6±8.7	223±5
49%	151.4±5.0	217±7	49%	156.1±5.8	221±3
8%	151.5±6.7	217±6	5%	154.4±5.2	224±4

Table 55 Static elastic modulus measured with the RoR bending test and thickness after phosphosilicate glass etch.

B. H.	E and MSE [GPa]	Thickness and MSE [µm]	*B. H.*	E and MSE [GPa]	Thickness and MSE [µm]
UMG mc-Si			***SoG mc-Si***		
88%	133.9±7.4	228±9	86%	133.0±8.2	237±6
49%	137.4±5.8	223±7	49%	135.4±6.6	231±5
8%	134.6±8.7	226±9	5%	124.9±10.9	239±11

Table 56 Static elastic modulus measured with the RoR bending test and thickness after antireflection coating.

B. H.	E and MSE [GPa]	Thickness and MSE [µm]	*B. H.*	E and MSE [GPa]	Thickness and MSE [µm]
UMG mc-Si			***SoG mc-Si***		
88%	152.1±6.4	217±6	86%	149.3±7.4	218±3
49%	152.6±12.2	213±7	49%	144.7±4.8	220±3
8%	150.6±5.1	215±7	5%	137.5±15.6	222±3

Table 57 Static elastic modulus measured with the RoR bending test and thickness after antireflection coating (skipping emitter diffusion).

B. H.	**E and MSE [GPa]**	**Thickness and MSE [µm]**	***B. H.***	**E and MSE [GPa]**	**Thickness and MSE [µm]**
UMG mc-Si			***SoG mc-Si***		
88%	144.6±5.3	218±6	86%	149.4±7.9	225±3
49%	147.9±6.6	216±7	49%	154.0±5.1	221±2
8%	149.5±4.8	218±5	5%	153.1±3.9	222±3

Table 58 Static elastic modulus measured with the RoR bending test and thickness after metallization (front contact under tensile stress).

B. H.	**E and MSE [GPa]**	**Thickness and MSE [µm]**	***B. H.***	**E and MSE [GPa]**	**Thickness and MSE [µm]**
UMG mc-Si			***SoG mc-Si***		
88%	104.2±5.7	257±7	86%	93.3±7.3	273±6
49%	100.1±5.7	260±8	49%	93.7±5.0	271±5
8%	96.9±4.5	263±6	5%	92.1±4.2	275±4

Table 59 Static elastic modulus measured with the RoR bending test and thickness after metallization (areas from the back contact without bus bars under tensile stress).

B. H.	**E and MSE [GPa]**	**Thickness and MSE [µm]**	***B. H.***	**E and MSE [GPa]**	**Thickness and MSE [µm]**
UMG mc-Si			***SoG mc-Si***		
88%	100.1±3.6	254±8	86%	95.4±5.6	268±8
49%	100.0±4.0	253±5	49%	96.1±3.0	264±3
8%	98.4±4.1	256±5	5%	93.6±4.7	265±4

Table 60 Static elastic modulus measured with the RoR bending test and thickness after metallization (bus bars from the back contact under tensile stress).

B. H.	**E and MSE [GPa]**	**Thickness and MSE [µm]**	***B. H.***	**E and MSE [GPa]**	**Thickness and MSE [µm]**
UMG mc-Si			***SoG mc-Si***		
88%	86.0±5.9	257±6	86%	82.8±4.4	271±8
49%	86.8±5.0	257±6	49%	83.6±4.4	268±3
8%	87.0±4.4	258±5	5%	83.1±3.4	268±4

Abbreviations

Si	Silicon
UMG-Si	Up-graded metallurgical silicon
PV	Photovoltaics
mc-Si	Multicrystalline silicon
Cz-Si	Czochralski silicon
CO	Carbon monoxide
CO_2	Carbon dioxide
MG-Si	Metallurgical grade silicon
SoG-Si	Solar grade silicon
5N	99.99999% purity
TCS	Trichlorosilane
$SiHCl_3$	Trichlorosilane
H_2	Hydrogen gas
€	Euro
[ppmw]	Concentration in parts per million by weight
B	Boron
P	Phosphorous
O	Oxygen
C	Carbon
Al	Aluminum
Ag	Silver
Ga	Gallium
N	Nitrogen
As	Arsenic
Ti	Titanium
Cr	Chromium
Mn	Manganese
Fe	Iron
Co	Cobalt
Ni	Nickel
Cu	Copper
Zn	Zinc

Ca	Calcium
Mg	Magnesium
Mo	Molybdenum
Ti	Titanium
V	Vanadium
et al.	Et aliae (“and allies”)
i.e.	Id est (“that is”)
VGF	Vertical Gradient Freeze
e.g.	Exempli gratia (“for example”)
Epi WE	Epitaxial wafer equivalent
RTCVD	Rapid thermal chemical vapor deposition process
$HFCH_3COOH$	Hydrofluoric acid
HNO_3	Nitric acid
CH_3COOH	Acetic acid
$POCl_3$	Phosphorus oxychloride
O_2	Oxygen gas
P_2O_5	Phosphorus oxide
PSG	Phosphosilicate glass
SiN_x:H	Hydrogenated silicon nitride
PECVD	Plasma enhanced chemical vapor deposition
IR	Infrared
Nd	Neodymium
YAG	Yttrium aluminum garnet
ICP-OES	Inductively Coupled Plasma/Optical Emission Spectrometry
(RF)	Radiofrequency
Ar	Argon
SEM	Scanning electron microscope
EDX	Energy Dispersive *X*-Ray Spectroscopy
IR	Infrared
TPB	Three-point bending
ROR	Ring-on-ring
SENB	Single edge notch beam
MSE	Mean squared error

Symbols

Quantity	**Formula Symbol**	**Units**
Electric power (watt) per hour		W h
Mass		kg
Temperature	T	°C
Temperature	T	K
Concentration of impurity in the silicon solid	C_s	[ppmw]
Concentration of impurity in the silicon melt	C_l	[ppmw]
Equilibrium segregation coefficient	k_0	-
Area	A	m^2
Normal or tensile stress	σ	MPa
Normal force	F	N
Shear stress	τ	MPa
Shear force	T	N
Normal or extensional strain	ε_{ii}	-
Shear strain	γ_{ij}	-
Elastic or Young´s modulus	E	GPa
Poisson´s ratio	ν	-
Shear modulus	μ	GPa
Bulk modulus	B	GPa
Crack length	a	m
Stress intensity factor	K	$\mathrm{MPa}\sqrt{\mathrm{m}}$
Geometry factor	Y	-
Critical stress intensity factor or toughness	K_{IC}	$\mathrm{MPa}\sqrt{\mathrm{m}}$
Strain energy release rate	G	$\mathrm{J/m}^2$
Critical strain energy release rate	G_c	$\mathrm{J/m}^2$
Stored elastic strain energy	U	J
Stored elastic strain energy density	U_e	$\mathrm{J/m}^3$
Energy necessary to create a new fracture surface	U_S	$\mathrm{J/m}^3$
Displacement	u	m
Radial stress	σ_{rr}	MPa
Tangential stress	$\sigma_{\theta\theta}$	MPa
Thermal expansion coefficient	α	K^{-1}

Silicon ductile-brittle transition temperature	T_f	°C
Ambient temperature	T_{amb}	°C
Particle radius	R	m
Critical particle radius	R_c	m
Distance from the center of the particle	r	m
Stress inside the particle	P	MPa
Fracture surface energy	γ	$\mathrm{J/m^2}$
Distance between the center of a particle and the tip of a crack approaching the particle	t_d	m
Stress intensity factor at the tip of propagating crack that links with a collinear crack	K_0	$\mathrm{MPa}\sqrt{\mathrm{m}}$
Intrinsic fracture toughness of a cracked body	$\bar{K}_c$	$\mathrm{MPa}\sqrt{\mathrm{m}}$
Elastic modulus of a cracked body	$\bar{E}$	GPa
Volume fraction	V	-
Bulk modulus of a cracked body	$\bar{B}$	GPa
Crack density parameter	ϵ	-
Poisson´s ratio of a cracked body	$\bar{\nu}$	-
Number of cracks per unit volume	N	-
Dilatational strain	e_T	-
Biaxial strain in a film	ε_f	-
Biaxial stress in a film	σ_f	MPa
Biaxial elastic modulus of a film	Y_f	GPa
Biaxial elastic modulus of a substrate	Y_s	GPa
Bending moment in the film	M_f	N m
Bending moment in the substrate	M_s	N m
Thickness of the film	t_f	m
Thickness of the substrate	t_s	m
Length of the edge of a thin film laminate	l	m
Radius of curvature	r_k	m
Distance from the neutral plane	z	m
Curvature	k	$\mathrm{m^{-1}}$
Deflection	δ	m
Solar cell processing temperature	T_0	°C
Lattice parameter of the thin film	a_f	m

Lattice parameter of the substrate	a_s	m
First Dundurs mismatch parameter (in extensional stiffness)	α_D	-
Second Dundurs mismatch parameter (in volumetric stiffness)	β_D	-
Phase angle (proportion of failure *mode* I and II of the interface of a bilayer)	ψ	°
Interface toughness	Γ_c	$\mathrm{J/m^2}$
Steady-state energy release rate	G_{SS}	$\mathrm{J/m^2}$
Cracking number	Z	-
Crack closure length	c	m
Yield stress	τ_y	MPa
Fracture stress	σ_{fr}	MPa
Maximum difference in refractive indexes	Δn	-
Wavelength	λ	m
Photo-elastic constant	C	$\mathrm{m^2/N}$
Applied load	F	N
Span (distance between supports)	L	m
Sample width	b	m
Sample thickness	t	m
Volume		L
Sample diameter	D	m
Supporting ring diameter	D_S	m
Loading ring diameter	D_L	m
Fracture probability	P_f	%
Weibull modulus	m	-
Characteristic stress	σ_θ	MPa
Maximum-likelihood Weibull modulus estimate	$\widehat{m}$	-
Maximum-likelihood characteristic stress estimate	$\hat{\sigma}_\theta$	MPa
Unbiasing factor	UF	-
Residual stress constant	X	-
Interacting parameter between linking flaws	I	-
crack-to-depth ratio	Λ	-
span-to-depth ratio	Ω	-

Mass of a bar	m_b	kg
Length of a bar	L_b	m
Fundamental resonant frequency	f_f	Hz
Correction factor for the flexure vibration mode	T_v	-

List of Figures

List of Tables

List of Publications

T. Orellana Pérez, C. Funke, W. Fütterer, S. Riepe, H. J. Möller, E. M. Tejado Garrido, J. Y. Pastor Caño, "Impact of Impurities on the Mechanical Strength of Multicrystalline Silicon," in *26th European PV Solar Energy Conference and Exhibition* , Hamburg, 2011, pp. 1864-1870.

T. Orellana Pérez, C. Funke, W. Fütterer, T. Wagner, S. Riepe, S. Reber, H. J. Möller, "Mechanical Characterization of Epitaxial Wafer Equivalents from Block Casting to Thin Film Deposition," in *25th European PV Solar Energy Conference and Exhibition* , Valencia, 2010, pp. 3619-3625.

T. Orellana Pérez, C. Schmid, S. Riepe, H. J. Möller, S. Reber, "Mechanical Characterization of Wafer Equivalent Substrate Materials from Alternative Silicon Feedstock," in *24th European PV Solar Energy Conference and Exhibition* , Hamburg, 2009, pp. 1228-1233.

T. Orellana, E. M. Tejado, C. Funke, W. Fütterer, S. Riepe, H. J. Möller, J. Y. Pastor, "Influence of Impurities on the Mechanical Properties of Directionally Solidified Multicrystalline Silicon," (to be published)

T. Orellana, E. M. Tejado, C. Funke, W. Fütterer, S. Riepe, J. Y. Pastor, H. J. Möller ,"Influence of High Aluminum Content on the Mechanical Properties of Directionally Solidified Multicrystalline Silicon," (to be published)

List of Presentations

T. Orellana, S. Riepe, C. Funke, W. Fütterer, H. J. Möller, E. M. Tejado Garrido, J. Y. Pastor Caño, "Impact of Impurities on the Mechanical Properties of Block Cast Multicrystalline Silicon," *Freiberger Silicon Days: semiconductor materials, process technologies and diagnostics*, Freiberg, 17.06.2011

T. Orellana, "Multicrystalline Silicon for Fotovoltaic Applications," *Seminarios de Fronteras de la Ciencia de Materiales, Universidad Politécnica de Madrid*, 14.02.2011

Acknowledgements

I would like to thank Prof. Hans Joachim Möller for accepting this thesis in the TU Bergakademie Freiberg and for his kind receptions and fruitful meetings and discussions in Freiberg. His guidance, advices and corrections have been a very important support for this work.

My special thanks to Prof. Jose Ygnacio Pastor Caño from the Polytechnic University of Madrid, for the so friendly and productive co-working during the last two years during which I could profit from his experience in materials characterization. I would also like to thank his corrections and his encouragement during my stay in Madrid and afterwards.

Elena María Tejado Garrido has been my working partner for carrying the experiments in the Polytechnic University of Madrid and I would like to thank her for her efficiency, accuracy, patience and motivation carrying the experiments. She has been a great and very professional co-worker.

Also my special thanks to Dr. Claudia Funke from the TU Bergakademie Freiberg for her guidance both in content and experimental work at the TU Bergakademie as well as for her help with the stress calculations and corrections. I will never forget her support during my days of stay in the TU Bergakademie Freiberg where I could work with her, get to know a good friend and enjoy her company.

Wolfgang Fütterer and Thomas Wagner contributed to this work with their experience in finite element analysis of stresses.

I thank Dr. Stephan Riepe, Dr. Stefan Reber and Dr. Andreas Bett for the financial support of this work during my years working in the Fraunhofer Institute for Solar Energy Systems and for sharing discussions and advices. I would also like to thank them for their professional corrections of publications, posters and presentations.

I want to remember the valuable help of Shahida Binti Rahamad with performing a big amount of bending tests and for the pleasant working with her.

I must not forget my former colleagues at the Fraunhofer Institute for Solar Energy Systems. Without their help, efficient work and good mood at work this research would not have been possible. I would like to give special thanks to Miroslawa Kwiatkowska, Michaela Winterhalder, Elke Gust, Jutta Zielonka, Thomas Rachow, Frank Boldt, Isolde Reis, Karin Krauss, Fridolin Haas, Matthias Singh, Yaniss Wencel, Mark Schumann, Phillipp Häuber, David Sabo, Claudia Schmid, Thilo Haas and Alberto Soria Moya.

To the so many good friends that I have met in Freiburg goes my appreciation with love. It has been a time where we have shared and enjoyed our time together and have learned to live and work in Germany. I would like to remember Alberto, Laura, Juan Pablo, Lucía, Jara, Chabela, Jose, Guadalupe, María, Laura V., Micha, Mirjam, Juan, Eduardo, Eva, Víctor, Marja, Eka, Matthias, Sabine, Daniel and my sister Maribel.

I would like to thank my parents in law, Inge and Stephan, and my grandparents in law, Christa and Siegfried, for being my warm german family and for their support and care during these years since we met.

My husband, Mark Schumann, has been my working colleague, my friend, my love and my soul mate since we have met. We shared twenty-four hours per day and I never felt tired of it. I would like to thank him for his impeccable attitude as a working colleague and as my partner and for being my companion the rest of my life.

My deepest gratitude goes to my parents, Esteban and María Isabel, and to my grandparents, Teresa, Esteban and Presentación. It is a whole life of love, care and dedication to raise and educate me and give me the best chances in life. You have been my biggest support always and this work is dedicated, with my earnest affection, to you.

Bibliography

[1] European Photovoltaic Industry Association (EPIA). (2012) www.epia.org. [Online]. http://www.epia.org/publications/epiapublications/global-market-outlook-for-photovoltaics-until-2015.html

[2] B. Ceccaroli and Lohne O., "Solar Grade Silicon Feedstock," in *Handbook of Photovoltaic Science and Engineering*, A. Luque and S. Hegedus, Eds.: John Wiley & Sons, 2003, ch. 5, pp. 153-204.

[3] European Photovoltaic Industry Association (EPIA). (2011) www.epia.org. [Online]. http://www.epia.org/solar-pv/pv-technologies-cells-and-modules.html

[4] (2012, April) Photon DAS SOLARSTROM-MAGAZIN. [Online]. http://www.photon.de/presse/grafiken.htm

[5] A. F. B. Braga, S. P. Moreira, P. R. Zampieri, J. M.G. Bacchin, and P. R. Mei, "New Processes for the Production of Solar-grade Pollycrystalline Silicon: A Review," *Solar Energy Materials & Solar Cells*, vol. 92, pp. 418-424, 2008.

[6] S. Pizzini, "Towards Solar Grade Silicon: Challenges and Benefits for Low Cost Photovoltaics," *Solar Energy Materials and Solar Cells*, vol. 94, pp. 1528-1533, 2010.

[7] G. del Coso, C del Canizo, and W. C. Sinke, "The Impact of Silicon Feedstock on the PV Module Cost," *Solar Energy Materials & Solar Cells*, vol. 94, pp. 345-349, 2010.

[8] M. A. Martorano, J. B. Ferreira Neto, T. S. Oliveira, and T. O. Tsubaki, "Refining of Metallurgical Silicon by Directional Solidification," *Materials and Engineering B*, vol. 176, pp. 217-226, 2011.

[9] F. A. Trumbore, "Solid Solubilities of Impurity Elements in Germanium and Silicon," *The Bell System Technical Journal*, vol. 39, pp. 205-233, January 1960.

[10] N. Yuge et al., "Purification of Metallurgical Grade Silicon up to Solar Grade," *Progress in Photovoltaics: Research and Applications*, vol. 9, pp. 203-209, 2001.

[11] D. Sarti and R. Einhaus, "Silicon Feedstock for the Multi-crystalline Photovoltaic Industry," *Solar Energy Materials & Solar Cells*, vol. 72, pp. 27-40, 2002.

[12] S. Binneti et al., "Study of Defects and Impurities in Multicrystalline Silicon Grown from Metallurgical Silicon Feedstock," *Materials Science and Engineering B*, vol. 159-160, pp. 274-277, 2009.

[13] T. Orellana Pérez et al., "Impact of Impurities on the Mechanical Strength of Multicrystalline Silicon," *26th European Photovoltaic Solar Energy Conference*, pp. 1864-1870, September 2011.

[14] J. B. Wachtman, W. Roger Cannon, and M. J. Matthewson, *Mechanical Properties of Ceramics*.: John Wiley and Sons, 2009.

[15] D. J. Green, *An Introduction to the Mechanical Properties of Cermiacs.*: Cambridge University Press, 1998.

[16] W. Voigt, "Über die Beziehung zwieschen den beiden Elastizitätskonstanten isotroper Körper," *Annalen der Physik*, vol. 38, pp. 573-587, 1889.

[17] A. Reuss, "Berechnung der Fließgrenze von Mischkristallen auf Grund der Plastizitätsbedingung für Einkristallen," *Zeitschrift für Angewandte Mathematik und Mechanik*, vol. 9, no. 1, pp. 49-58, 1929.

[18] Z. Hashin and S. Shtrikman, "A Variational Approach to the Theory of The Elastic Behavior of Polycrystals," *Journal of the Mechanics and Physics of Solids*, vol. 10, no. 4, pp. 343-352, 1962.

[19] E. Orowan, "Fracture and Strength of Solids," *Reports on Progress in Physics*, vol. 12, pp. 185-233, 1949.

[20] R. W. Davidge, *Mechanical Behavior of Ceramics*. New York: Cambridge University Press, 1979.

[21] A. Kelly and N. H. MacMillan, *Strong Solids*, 3rd ed. Oxford: Oxford University Press, 1986.

[22] J. Frenkel, "Zur Theorie der Elastizitätsgrenze und der Festigkeit kristallinischer Körper," *Zeitschrift für Physik*, vol. 37, no. 7-8, pp. 572-609, 1926.

[23] A. A. Griffith, "The Phenomena of Rupture and Flaw in Solids," *Philosophical Transactions of the Royal Society of London*, vol. 221, no. A, pp. 163-198, 1920.

[24] G. R. Irwin, "Analysis of Stresses and Strains Near the End of a Crack Traversing a Plate," *Journal of Applied Mechanics*, vol. 24, pp. 361-364, 1957.

[25] Y Murakami, *Stress Intensity Factors Handbook*. New York: Pergamon, 1987.

[26] A. G. Evans, "The Role of Inclusions in the Fracture of Ceramic Materials," *Journal of Materials Science*, vol. 9, pp. 1145-1152, 1974.

[27] P. Lipetzky and S. Schmauder, "Crack-particle Interaction in Two Phase Composites. Part I: Particle Shape Effects," *International Journal of Fracture*, vol. 65, pp. 345-358, 1994.

[28] D. B. Binns, "Some Physical Properties of Two-Phase Crystal-Glass Solids," *Science of Ceramics*, pp. 315-334, 1962.

[29] W. J. Frey and J. D. Mackenzie, "Mechanical Properties of Selected Glass-Crystal Composites," *Journal of Materials Science*, vol. 2, pp. 124-130, 1967.

[30] D. P H. Hasselman and R. M. Fulrath, "Micromechanical Stress Concentrations in Two-Phase Brittle-Matrix Ceramic Composites," *Journal of the American Ceramic Society*, vol. 50, no. 8, pp. 399-404, 1967.

[31] D. P. Hasselman and R. M. Fulrath, "Proposed Fracture Theory of a Dispersion-Strengthened Glass Matrix," *Journal of the American Society*, vol. 49, no. 2, pp. 68-72, 1966.

[32] R. L. Bertolotti and R. M. Fulrath, "Effect of Micromechanical Stress Concentrations on Strength of Porous Glass," *Journal of the Americal Ceramic Society*, vol. 50, no. 11, pp. 558-562, 1967.

[33] J. Selsing, "Internal Stresses in Ceramics," *Journal of the American Ceramic Society*, vol. 44, no. 8, p. 419, August 1961.

[34] D. Weyl, "Über den Einfluß innerer Spannungen auf das Gefüge und die mechanische Festigkeit des Porzellans," *Berichte der Deutschen Keramischen Gesellschaft*, vol. 36, pp. 319-324, 1959.

[35] V. D. Krstic and A. K. Khaund, "Particle-size Dependence of Thermoelastic Stress Intensity Factor in Two Phase Materials," *Journal of Materials Science*, vol. 16, pp. 3319-3323, 1981.

[36] R. W. Davidge and T. J. Green, "The Strength of Two Phase Ceramic/Glass Materials," *Journal of Materials Science*, vol. 3, pp. 629-634, May 1968.

[37] Y. M. Ito, M. Rosenblatt, L. Y. Cheng, F. F. Lange, and A. G. Evans, "Cracking in Particulate Composites due to Thermalmechanical stress," *International Journal of Fracture*, vol. 17, no. 5, pp. 483-491, October 1981.

[38] P. C. Paris and G. C. Sih, "Stress Analysis of Cracks," *ASTM STP*, vol. 381, pp. 30-81, 1964.

[39] S. Vaidyanathan and I. Finnie, "Determination of Residual Stresses from Stress Intensity Factor Measurements," *Journal of Basic Engineering*, vol. 93, pp. 242-246, 1971.

[40] D. J. Green, "Stress Intensity Factor Estimates for Annular Cracks at Spherical Voids," *Journal of the American Ceramic Society*, vol. 63, no. 5-6, pp. 342-344, 1980.

[41] D. J. Green, "Stress-Induced Microcracking at Second-Phase Inclusions," *Journal of the American Ceramic Society*, vol. 64, no. 3, pp. 138-141, 1981.

[42] G. I. Barenblatt, "The Mathematical Theory of Equilibrium Cracks in Brittle Fracture," *Advances in Applied Mechanics*, vol. 7, pp. 55-126, 1962.

[43] J. N. Goodier, "Concentration of Stress Around Spherical and Cylindrical Inclusions and Flaws," *Journal of Applied Mechanics*, vol. 55, no. 7, pp. 39-44, 1933.

[44] B. R. Lawn, *Fracture of Brittle Solids (Cambridge Solid State Science Series)*, 2nd ed.: Cambridge University Press, 1993.

[45] I. N. Sneddom, "The Distribution of Stress in the Neighborhood of a Crack in an Elastic Solid," *Poceedings of the Royal Society of London. Series A, Mathematical and Physical*

Sciences, vol. 1009, pp. 229-260, 1946.

[46] A. F. Bower and M. Ortiz, "A Three-Dimensional Analysis of Crack Trapping and Bridging by Tough Particles," *Journal of the Mechanics and Physics of Solids*, vol. 39, no. 6, pp. 815-858, 1991.

[47] B-N. Kim, M. Watanabe, M. Enoki, and T. Kishi, "Simulation of Fracture Behavior in Particle-Dispersed Ceramic Composites," *Engineering Fracture Mechanics*, vol. 59, no. 3, pp. 289-303, 1998.

[48] J. Tirosh and A. S. Tetelman, "Fracture Conditions of a Crack Approaching a Disturbance," *International Journal of Fracture*, vol. 12, no. 2, pp. 187-199, 1976.

[49] D. J. Green, "Fracture Toughness Predictions for Crack Bowing in Brittle Particulate Composites," *Journal of The American Ceramic Society*, vol. 63, no. 5-6, pp. 340-342, January 1983.

[50] B. R. Lawn, N. P. Padture, L. M. Braun, and S. J. Bennison, "Model for Toughness Curves in Two-Phase Ceramics: I, Basic Fracture Mechanics," *Journal of the American Ceramic Society*, vol. 76, no. 9, pp. 2235-2240, September 1993.

[51] J. C. Swearengen, E. K. Beauchamp, and R. J. Eagan, "Fracture toughness of reinforced glasses," *Fracture Mechanics of Ceramics*, vol. 4, pp. 973-987, 1978.

[52] G. C. Wei and P. F. Becher, "Improvements in Mechanical Properties in SiC by the Addition of TiC Particles," *Journal of the American Ceramic Society*, vol. 67, no. 8, pp. 571-574, August 1984.

[53] A. K. Khaund, V. D. Krstic, and P. S. Nicholson, "Influence of Elastic and Thermal Mismatch on the Local Crack-driving Force in Brittle Composites," *Journal of Materials Science*, vol. 12, pp. 2269-2273, 1977.

[54] R Li and A. Chudnovsky, "Variation of the Energy Release Rate as a Crack Approches and Passes Through an Elastic Inclusion," *International Journal of Fracture*, vol. 59, no. 4, pp. R69-R74, 1993.

[55] A. A. Mammoli and M. B. Bush, "Effects of Reinforcement Geometry on the Elastic and Plastic Behaviour of Metal Matrix Composites," *Acta Metallurgica et Materialia*, vol. 43, no. 10, pp. 3743-3754, October 1995.

[56] L. P. Zhang, C. L. Davis, and M. Strangwood, "Dependency of Fracture Toughness on the Inhomogeinity of Coarse TiN Particle Distribution in a Low Alloy Steel," *Metallurgical and Materials Transactions A*, vol. 32, no. 5, pp. 1147-1155, May 2001.

[57] M. B. Bush, "The Interaction Between a Crack and a Particle Cluster," *International Journal of Fracture*, vol. 88, pp. 215-232, 1997.

[58] R. W. Rice, "Microstructural Dependence of Fracture Energy and Toughness of Ceramics and ceramic Composites Versus that of their Tensile Strength at 22°C," *Journal of the Materials Science*, vol. 31, pp. 4503-4519, 1996.

[59] L. R. F. Rose, "Effective Fracture Toughness of Microcracked Materials," *Journal of the American Ceramic Society*, vol. 69, no. 3, pp. 212-214, 1986.

[60] H. T. Davis, *Introduction to Non-linear Differential and Integral Equations.*: Dover Publications Inc., 1960.

[61] C. C. Yang, R. Huang, W. Yeih, and I. C. Sue, "Aggregate Effect on Elastic Moduli of Cement-based Composite Materials," *Journal of Marine Acience and Technology*, vol. 3, no. 1, pp. 5-10, 1995.

[62] Z. Hashin and S. Shtrikman, "A Variational Approach to the Theory of the Elastic Behavior of Multiphase Materials," *Journal of the Mechanics and Physics of Solids*, vol. 11, pp. 127-140, 1963.

[63] D. J. Green, P. Nicholson, and J. D. Embury, "Fracture of a Brittle Particulate Composite," *Journal of Materials Science*, vol. 14, pp. 1413-1420, 1979.

[64] B. Budiansky and R. J. O'Connoell, "Elastic Moduli of a Cracked Solid," *International Journal of Solids and Structures*, vol. 12, pp. 81-97, 1976.

[65] W. D. Nix, "Mechanical Properties of Thin Films," *Metallurgical Transactions A*, vol. 20A, pp. 1989-2217, November 1989.

[66] D. M. Mattox, "Atomistic Film Growth and Resulting Film Properties: Residual Film Stress," *Vacuum Technology and Coating*, pp. 22-23, November 2001.

[67] G. G. Stoney, "The Tension of Metallic Films Deposited by Electrolysis," *Proceedings of the Royal Society of London A*, vol. 82, pp. 172-175, 1909.

[68] M. F. Doerner and W. D. Nix, "Stresses and Deformation Processes in Thin Films on Substrates," *Critical Reviews in Solid State and Materials Sciences*, vol. 14, pp. 225-268, 1988.

[69] Y. Okada and Y. Tokumaru, "Precise Determination of Lattice Parameter and Thermal Expansion Coefficient of Silicon between 300 and 1500 K," *Journal of Applied Physics*, vol. 56, no. 2, pp. 314-320, 1984.

[70] S Timoshenko, "Analysis of Bi-Metal Thermostats," *Journal of the Optical Society of America*, vol. 11, pp. 233-255, 1925.

[71] A. Schneider, "Charakterisierungsverfahren und Industriekompatible Herstellungsprozesse für Dünne Multikristalline Siliziumsolarzellen," University of Konstanz, Germany, Ph.D. Thesis 2004.

[72] A. G. Evans and J. W. Hutchinson, "The Thermomechanical Integrity of Thin Films and Multilayers," *Acta Metallurgica et Materialia*, vol. 43, no. 7, pp. 2507-2530, 1995.

[73] J. W. Hutchinson and Z. Suo, "Mixed Mode Cracking in Layered Materials," *Advances in Applied Mechanics*, vol. 29, pp. 63-191, 1992.

[74] J. W. Hutchinson, "Stresses and Failure Modes in Thin Films and Multilayers," Division

of Engineering and Applied Sciences (Harvard University), Technical University of Denmark, NOTES FOR A DCAMM COURSE 1996.

[75] J. Dundurs, "Edge-bonded Dissimilar Orthogonal Elastic Wedges," *Journal of Applied Mechanics*, vol. 36, pp. 650-652, 1969.

[76] J. L. Beuth, "Cracking of Thin Bonded Films in Residual Tension," *International Journal of Solids and Structures*, vol. 29, no. 13, pp. 1657-1675, 1992.

[77] M. Y. He and J. W. Hutchinson, "Crack Deflection at an Interface Between Dissimilar Elastic Materials," *International Journal of Solids and Structures*, vol. 25, no. 9, pp. 1053-1067, 1989.

[78] D. J. Green, "Compressive Surface Strengthening of Brittle Materials," *Journal of Materials Science*, vol. 19, pp. 2165-2171, 1984.

[79] R. Hull, Ed., *Properties of Crystalline Silicon*. London, United Kingdom: INSPEC, The Institution of Electrical Engineers, 1999.

[80] A. S. Argon, *Strengthening Mechanisms in Crystal Plasticity*.: Oxford University Press, 2007.

[81] J Rabier and J. L. Demenet, "Low Temperature, High Stress Plastic Deformation of Semiconductors: The Silicon Case," *Physica Status Solidi*, vol. 222, no. 1, pp. 63-74, 2000.

[82] Hasselman, "Unified Theory of Thermal Shock Fracture Initiation and Crack Propagation in Brittle Ceramics," *Journal of the American Ceramic Society*, vol. 52, no. 11, pp. 600-604, 1969.

[83] M. I. Yasutake, M. Iwata, K. Yoshii, M. Umeno, and H. Kawabe, "Crack Healing and Fracture Strength of Silicon Crystals," *Journal of Materials Science*, vol. 21, pp. 2185-2192, 1986.

[84] J. Llorca, "An Analysis of the Influence of Reinforcement Fracture on the Strength of Discontinuously-Reinforced Metal-Matrix Composites," *Acta Metallurgica et Materialia*, vol. 43, no. 1, pp. 181-192, January 1995.

[85] S. Balasivanandha Prabu and L. Karunamoorthy, "Microstructure-based Finite Element Analysis of Failure Prediction in Particle-reinforced Metal-matrix Composite," *Journal of Materials Processing Technology*, vol. 207, pp. 53-62, 2008.

[86] F. I. Baratta, "Stress Intensity Factor Estimates for a Peripherally Cracked Spherical Void and a Hemispherical Surface Pit," *Journal of the American Ceramic Society*, vol. 61, no. 11-12, pp. 490–493, 1978.

[87] F. M. Boldt et al., "Effect of Segregation During Crystallization of Highly Impure Upgraded Metallurgical Silicon," in *25th EU PVSEC*, Valencia, 2010, pp. 1499-1502.

[88] R. Kvande et al., "Investigation of New Ready to Use Solar Crucible for Crystallisation of Multicrystalline Silicon Ingots," *Proceedings 22nd European Photovoltaic Solar*

Energy Conference , vol. 1103, p. 1099, 2007.

[89] S. Riepe et al., "Silicon Material and Technology Evaluation Center (SIMTEC) at Fraunhofer ISE - Achievements and Visions," *23rd European Photovoltaic Solar Energy Conference*, pp. 1264-1269, September 2008.

[90] H. J. Möller, C. Funke, M. Rinio, and S. Scholz, "Multicrystalline Silicon for Solar Cells," *Thin Solid Films*, vol. 487, pp. 179-187, 2005.

[91] H. J. Möller, T. Kaden, S. Scholz, and S. Würzner, "Improving Solar Grade Silicon by Controlling Extended Defect Generation and Foreign Atom Defect Interactions," *Applied Physics A Materials Sciencie & Processing*, vol. 96, pp. 207-220, 2009.

[92] R. Zeidler et al., "Tomographic Defect Reconstruction of Multicrystalline Silicon Ingots Using Photoluminescence Images of As-Cut Wafers and Solar Cells," in *27th EU PVSEC*, Frankfurt, 2012.

[93] H. J. Möller, "Basic Mechanisms and Models of Multi-Wire Sawing," *Advanced Engineering Materials*, vol. 6, no. 7, pp. 501-513, 2004.

[94] T. Orellana, "Optimization of Chemical Treatment of Monocrystalline Silicon Wafers after Wire-Sawing," Universidad Politécnica de Madrid, Final Project 2007.

[95] E. Schmich, N. Schillinger, and S. Reber, "Silicon CVD Deposition for Low-Cost Applications in Photovoltaics," *Surface and Coatings Technology*, vol. 201, no. 22-23, pp. 9325-9329, May 2007.

[96] S. Reber, C. Haase, N. Schillinger, S. Bau, and A. Hurrle, "The RTCVD160 - A New Lab-type Silicon CVD Processor for Silicon Deposition on Large Area Substrates," in *3rd World Conference on Photovoltaic Energy Conversion*, Osaka, 2003, pp. 1368-1371.

[97] D. H. Neuhaus and A. Münzer, "Industrial Silicon Wafer Solar Cells," *Advances in OptoElectronics*, vol. 2007, 2007.

[98] C. Funke, S. Wolf, and D. Stoyan, "Modeling the Tensile Strength and Crack Length of Wire-Sawn Silicon Wafers," *Journal of Solar Energy Engineering* , vol. 131, no. 1, February 2009.

[99] X. Hou and B. T. Jones, "Iduced Couple Plasma/Optical Emission Spectrometry," in *Encyclopedia of Analitical Chemistry*, John Wiley Sons Ltd., Ed. Chichester: R. A. Meyers, 2000, pp. 9468-9485.

[100] D. Brandon and W. D. Kaplan, *Microstructural Characterization of Materials*, 2nd ed. Chichester: Wiley & Sons Ltd., 2008.

[101] E. M. Gamarts et al., "Characterization of Stress in Semiconductor Wafers Using Birefringence Measurement," *Journal de Physique III*, vol. 3, pp. 1033-1049, May 1993.

[102] "Fine Ceramics (Advanced Ceramics, Advanced Technical Ceramics) - Test Method for Flexural Strength of Monolithic Ceramics at Room Temperature," Standard ISO 14704,

2008.

[103] "Standard Test Method for Flexural Strength of Advanced Ceramics at Ambient Temperature," American Society for Testing and Materials (ASTM) International, Standard ASTM C 1161-02, January 2003.

[104] "Standard Test Method for Monotonic Equibiaxial Flexural Strength of Advanced Ceramics at Ambient Temperature," American Society for Testing and Materials (ASTM) International, Standard ASTM C1499 - 08, 2008.

[105] W. Weibull, "A Statistical Theory of the Strength of Materials," *Proc. The Royal-Swedish Institutefor Engineering Research*, vol. 151, pp. 1-45, 1939.

[106] "Standard Practice for Reporting Uniaxial Strength Data and Estimating Weibull Distribution Parameters for Advanced Ceramics," American Society for Testing and Materials (ASTM) International, Standard ASTM C1239-07 , February 2007.

[107] "Standard Practice for Reporting Uniaxial Strength Data and Estimating Weibull Distribution Parameters for Advanced Ceramics," American Society for Testing and Materials (ASTM) International, Standard ASTM C1239-07, 2007.

[108] "Standard Practicefor Size Scaling of Tensile Strengths Using Weibull Statistics for Advanced Ceramics," American Society for Testing and Materials (ASTM) International, Standard ASTM C 1683-08, 2008.

[109] The R Projeckt for Statistical Computing. www.r-project.org. [Online]. http://www.r-project.org/

[110] "Standard Practice for Fractography and Characterization of Fracture Origins in Advanced Ceramics," American Society for Testing and Materials (ASTM) International, Standard ASTM C 1322-05b, 2005.

[111] L. D. Dyer, "Fracture Tracing in Semiconductor Wafers," in *Semiconductor Processing: A Symposium; 850*, D. C. Gupta, Ed. Baltimore: American Society for Testing and Materials, 1984, pp. 297-308.

[112] G. K. Bansal, "Effect of Flaw Shape on Strength of Ceramics," *Journal of the American Ceramic Society-Discussions and Notes*, vol. 59, no. 1-2, pp. 87-88, 1976.

[113] G. R. Irwin, "Crack Extension Force for a Part-Through Crack in a Plate," *Journal of Applied Mechanics*, vol. 29, no. 4, pp. 651-654, 1962.

[114] J. E. Ritter and R. W. Davidge, "Strength and Its Variability in Ceramics with Particular Reference to Alumina," *Journal of the American Ceramic Society*, vol. 67, no. 6, pp. 432-437, June 1984.

[115] B. R. Marshall and B. R. Lawn, "Residual Stress Effects in Sharp Contact Cracking. Part I: Indentation Fracture Mechanics," *Journal of Materials Science*, vol. 14, pp. 2001-2012, 1979.

[116] D. B. Marshall, B. R. Lawn, and P. Chantikul, "Residual Stress Effects in Sharp Contact Cracking," *Journal of Materiasl Science*, vol. 14, pp. 2225-2235, 1979.

[117] A. G. Evans and G. Tappin, "Effects of Microstructure on the Stress to Propagate Inherent Flaws," *Proceedings of the British Ceramic Society*, vol. 20, pp. 275-297, 1972.

[118] G. V. Guinea, J. Y. Pastor, J. Planas, and M. Elices, "Stress Intensity Factor, Compliance and CMOD for a General Three-Point-Bend Beam," *International Journal of Fracture*, vol. 89, pp. 103-116, 1998.

[119] "Standard Test Method for Dynamic Young´s Modulus, Shear Modulus, and Poisson´s Ratio by Impulse Excitation of Vibration," American Society for Testing and Materials (ASTM) International, Standard ASTM E 1876-09 ,.

[120] S. Spinner, T. W. Reichard, and W. E. Tefft, "A Comparison of Experimental and Theoretical Relations Between Young´s Modulus and the Flexural and Longitudinal Resonance Frequencies of Uniform Bars," *Journal of Research of the National Bureau of Standards-A. Physics and Chemistry*, vol. 64, no. 2, pp. 147-155, 1960.

[121] A. V. Popovich, A. Yunus, M. Janssen, M. I. Richardson, and J. I. Benetti, "Effect of Silicon Solar Cell Processing Parameters and Crystallinity on Mechanical Strength," *Solar Energy Materials and Solar Cells*, vol. 95, no. 1, pp. 97-100, 2011.

[122] I. Ansara, A. Dinsdale, and M. Rand, *Thermochemical Database for Light Metal Alloys*., 1998, vol. 2.

[123] H. J. Möller, L. Long, M. Werner, and D. Yang, "Oxygen and Carbon Precipitation in Multicrystalline Solar Silicon," *Physica Status Solidi (A)*, vol. 171, no. 1, pp. 175-189, 1999.

[124] A. Shigeru, "Morphology of oxide precipitates in silicon crystals," *Materials Transactions*, vol. 34, no. 9, pp. 746-752, 1993.

[125] Z. Xi et al., "Influence of Copper Precipitation on Oxygen Precipitation in Czochralski Silicon," *Semiconductor Science and Technology*, vol. 19, pp. 299-305, 2004.

[126] Z. Li and R. C. Bradt, "Thermal Expansion of the Cubic (3C) Polytype of SiC," *Journal of Materials Science*, vol. 21, pp. 4366-4368, 1986.

[127] D. N. Talwar and J. C. Sherbondy, "Thermal Expansion Coefficient of 3C-SiC," *Applied Physics Letters*, vol. 67, no. 22, pp. 3301-3303, 1995.

[128] S. Iwai and A. Yasunaga, "Über die Thermische Ausdehnung des Si_3N_4," *Die Naturwissenschaften*, vol. 46, no. 15, pp. 473-474, 1959.

[129] R. M. Williams, "Linear Thermal Expansion of Hot-Pressed Si_3N_4," *Journal of the American Ceramic Society-Discussions and Notes*, vol. 63, no. 1-2, pp. 108-109, 1980.

[130] S Sakaguchi, N. Murayama, Y. Kodama, and F. Wakai, "The Poisson´s Ratio of Engineering Ceramics at Elevated Temperature," *Journal of Materials Science Letters*,

vol. 10, pp. 282-284, 1991.

[131] M. F. Ashby, *Materials Selection in Mechanical Design*, 3rd ed.: Butterworth Heinemann, 2004.

[132] J. E. Sinclair and B. R. Lawn, "An Atomistic Study of Cracks in Diamond-Structure Crystals," *Proceedings of the Royal Society of London, A: Mathematical, Physical and Engineering Sciences*, vol. 329, pp. 83-103, 1972.

[133] S. Matsumoto, I. Ishihara, and H. Kaneko, "Growth Characteristics of Oxide Precipitates in Heavily Doped Silicon Crystals," *Applied Physics Letters*, vol. 46, no. 10, pp. 957-959, 1985.

[134] S. Schönfelder et al., "Quantitative Stress Measurements of Bulk Microdefects in Multicrystalline Silicon," in *24th EUPVSEC*, 2009, pp. 977-980.

[135] M. M´Hamdi and S. Gouttebroze, "Analysis of the Residual Stress Field Associated with Particles in Multi-crystalline Silicon," in *24th EUPVSEC*, 2009, pp. 1265-1268.

[136] V. Ganapati et al., "Infrared Birefringence Imaging of Residual Stress and Bulk Defects in Multicrystalline Silicon," *Journal of Applied Physics*, vol. 108, no. 6, 2010.

[137] H. -F. Hadamovsky, *Werkstoffe der Halbleitertechnik*. Leipzig: Deutscher Verlag, 1990.

[138] H. Liu, S. Gao, S. Niu, and L. Jin, "Measurements on Mechanical Properties of Boron-doped Silicon Materials for Micro Inertia Sensor," in *9th International Conference on Electronic Measurement & Instruments*, Beijing, 2009, pp. 2-174 - 2-179.

[139] T. Wagner et al., "Spatial Distribution of Wafer Subsurface Damage Induced by Wire Sawing," in *Proceedings of the 25th EUPVSEC*, Valencia, 2010, pp. 1267-1271.

[140] W. Wijaranakula, "The Dissolution Mechanism of Oxide Precipitates in Czochralski Silicon Degenerately Doped with Boron During High Temeperature Annealing," *Journal of Electronic Materials*, vol. 22, no. 1, pp. 105-110, 1993.

[141] R. W. Olesinski and G. J. Abbaschian, "The C-Si (Carbon-Silicon) System," *Bulletin of Alloy Phase Diagrams*, vol. 5, no. 5, pp. 486-489, 1984.

[142] O. N. Carlson, "The N-Si (Nitrogen-Silicon) System," *Bulletin of Ally Phase Diagrams*, vol. 11, no. 6, pp. 569-573, 1990.

[143] T. Orellana, K. Mayer, M. Schumann, and F. Granek, "Increase in Mechanical Strength of As-Cut Monocrystalline Silicon Wafers by Alkaline Etching Process," in *24th EUPVSEC*, Hamburg, Germany, 2009.

[144] H. Larsson, J. Gustafsson, H. J. Solheim, and T. Boström, "The Impact of Saw Damage Etching on Microcracks in Solar Cell Production," in *23rd EUPVSEC*, Valencia, 2008, pp. 1961-1964.

[145] J. Bauer et al., "Hot spots in multicrystalline silicon solar cells: Avalanche breakdown due to etch pits," *Physica Status Solidi RRL 3* , vol. 2, pp. 40-42, 2009.

[146] T. Rachow, M. Ledinsky, S. Janz, S. Reber, and A. Fejfar, "µc-Si Solar Cells by Direct Deposition with APCVD," in *27th EU PVSEC*, Frankfurt, 2012.

[147] W. Hsiao and C. Liu, "Influence of Thermal Budget on Phosphosilicate Glass Prepared by High-density Plasma Chemical-vapor Deposition," *Journal of Vacuum Science & Technology B*, vol. 23, no. 5, pp. 2146-2150, 2055.

[148] H. Sunami, Y. Itoh, and K. Sato, "Stress and Thermal Expansion Coefficient of Chemical Vapor Deposited Glass Films," *Journal of Applied Physics*, vol. 41, no. 13, pp. 5115-5117, 1970.

[149] H. Huang et al., "Effect of Deposition Consitions on Mechanical Properties of Low-temperature PECVD Silicon Nitride Films," *Materials Science and Engineering A*, vol. 435-436, pp. 453-459, 2006.

[150] P. Temple-Boyer, C. Rossi, E. Saint-Etienne, and E. Scheid, "Residual Stress in Low Pressure Chemical Vapor Deposition SiN_x Films Deposited from Silane and Ammonia," *Journal of Vacuum Science & Technology A*, vol. 16, no. 4, pp. 2003-2007, 1998.

[151] J. W. Corbett, P. Deák, C. Ortiz-Rodriguez, and L. C. Snyder, "Embrittlement of Materials: Si(H) as a Model System," *Journal of Nuclear Materials*, vol. 169, pp. 179-184, 1989.

[152] V. A. Popovich, M. Janssen, I. M. Richardson, T. van Amstel, and I. J. Bennett, "Microstructure and Mechanical Properties of Aluminum Back Contact Layers," *Solar Energy Materials & Solar Cells*, vol. 95, pp. 93-96, 2011.

[153] C. Kohn, R. Kübler, M. Krappitz, and G. Kleer, "Influence of the Metallization Process on the Strength of Silicon Solar Cells," in *24th European Photovoltaic Solar Energy Conference*, Hamburg, Germany, 2009.

[154] U. Kattner, "Silver-Aluminum-Silicon," in *Ternary Alloys : a Comprehensive Compendium of Evaluated Constitutional Data and Phase Diagrams*, G. Petzow and G. Effenberg, Eds.: VCH, 1988, vol. Ag-Al-Au to Ag-Cu-P Ternary alloys, pp. 71-73.

[155] F. Huster, "Aluminum-back Surface Field: Bow Investigation and Elimination," in *Proceedings of the 20th EUPVSEC*, Barcelona, 2005.

[156] J. J. Hall, "Electronic Effects in the Elastic Constants of n-Type Silicon," *Physical Review*, vol. 161, no. 3, pp. 456-761, 1967.

[157] J. J. Wortman and R. A. Evans, "Young´s Modulus, Shear Modulus, and Poisson´s Ratio in Silicon and Germanium," *Journal of Applied Physics*, vol. 36, no. 1, pp. 153-156, January 1964.

[158] W. A. Brantley, "Calculated Elastic Constants for Stress Problems Associated with Semiconductor Devices," *Journal of Applied Physics*, vol. 44, no. 1, pp. 534-535, January 1973.